Acoustoelectric Properties of Graphene and Graphene Nanostructures

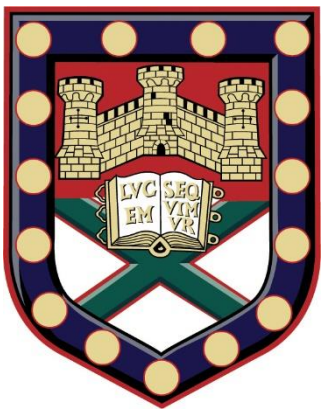

Submitted by Timothy Poole to the University of Exeter
as a thesis for the degree of
Doctor of Philosophy in Engineering
in August 2017.

I certify that all material in this thesis which is not my own work has been identified and that no material has previously been submitted and approved for the award of a degree by this or any other University.

Signature: ……..

Abstract

The acoustoelectric effect in graphene and graphene nanoribbons (GNRs) on lithium niobate surface acoustic wave (SAW) devices was studied experimentally. Monolayer graphene produced by chemical vapour deposition was transferred to the SAW devices. The photoresponse of the acoustoelectric current (I_{ae}) was characterised as a function of SAW frequency and intensity, and illumination wavelength (using 450 nm and 735 nm LEDs) and intensity. Under illumination, the measured I_{ae} increased by more than the measured decrease in conductivity, while retaining a linear dependence on SAW intensity. The latter is consistent with the piezoelectric interaction between the graphene charge carriers and the SAWs being described by a relatively simple classical relaxation model. A larger increase in I_{ae} under an illumination wavelength of 450 nm, compared to 735 nm at the same intensity, is consistent with the generation of a hot carrier distribution.

The same classical relaxation model was found to describe I_{ae} generated in arrays of 500 nm-wide GNRs. The measured acoustoelectric current decreases as the nanoribbon width increases, as studied for GNRs with widths in the range 200 – 600 nm. This reflects an increase in charge carrier mobility due to increased doping, arising from damage induced at the nanoribbon edges during fabrication.

Lastly, the acoustoelectric photoresponse was studied as a function of graphene nanoribbon width (350 – 600 nm) under an illumination wavelength of 450 nm. Under illumination, the nanoribbon conductivity decreased, with the largest percentage decrease seen in the widest GNRs. I_{ae} also decreased under illumination, in contrast to the acoustoelectric photoresponse of continuous graphene. A possible explanation is that hot carrier effects under illumination lead to a greater decrease in charge carrier mobility than the increase in acoustoelectric attenuation coefficient. This causes the measured decrease in I_{ae}.

Acknowledgments

Throughout my studies, I have been fortunate enough to work with some exceptional people. Their support and advice have been instrumental in making this work possible. First and foremost, I want to extend my gratitude to my supervisor Professor Geoffrey R. Nash. There is no doubt that under the supervision of anyone else, I wouldn't have reached this point. Geoff is a great motivator, always enthusiastic, and very knowledgeable. These qualities alone are enough to make him an excellent supervisor. Most importantly for me, however, he is also extremely understanding. Whenever I've felt overwhelmed by my research or by personal difficulties, he has always made time to listen to my concerns and help me get back on my feet. I sincerely hope that there will be opportunities to work together again in the future, and that some of his scientific aptitude and enthusiasm for research has rubbed off on me.

I would also like to thank the members of my research group for their guidance. I'd particularly like to acknowledge Dr. Lokeshwar Bandhu for his help with device fabrication, demonstrations in the clean room, and for developing my experimental technique. His insights have helped immeasurably with my own research. Thanks also to Ben Ash for his many engaging discussions on surface acoustic waves and sharing in the challenges of SAW experiments. Additionally, while I did not work with them directly, Dr. Lorreta Lawton, Dr. Isaac Luxmoore,

Dr. Prarthana Vadegadde Dakappa, Dr. Penglei Li, Dr. Choon How Gan, Dr. Nathan Mahlmeister, Oliver Higbee, Cheng Shi and Kishan Menghrajani have all been great colleagues.

Away from research, I owe considerable thanks to my family and friends. My parents and sisters have been wonderfully supportive, and my visits home have always provided a welcome relief from studying. They have encouraged me to persevere when at times I felt I could not, and it is thanks to their love and kindness that I've been able to reach any landmark in life. Special thanks must also go to Cathy King. She has been extremely understanding, reassuring, and loving, even when I've made it difficult for her, and has helped me struggle through the long hours of writing. She also did me the great service of proof reading this entire thesis, making tremendously helpful recommendations. Additionally, I want to thank Ryan Edginton, Chris Beckerleg, and Lucy Buxton for being great housemates and making our tiny house feel a little more like a home. Lastly, I feel extremely grateful to have the friendship of Des Mansfield, Tom Furnival, Patrick Tompsett, Rachael Morgan, and Jemma Davie. Whether we were walking on Dartmoor, celebrating birthdays or other special occasions, they have helped me create some of the best memories I have of my time in Exeter. My apologies and thanks to all those not named here. I fear that if I listed you all, these acknowledgements would be longer than the body of this work.

Contents

List of Figures

List of Tables

1. Introduction

1.1 Motivation

Surface acoustic waves (SAWs) propagating on piezoelectric substrates have been employed for signal processing since the 1960s. With components including bandpass filters, oscillators, and resonators, SAW devices are used across a broad range of industries [1]. Developments in semiconductor manufacturing during the 1980s brought the interest in high frequency (MHz – GHz) SAWs towards the study of the electronic properties of low-dimensional electron systems (LDESs). The charge carriers of a LDES placed on top of a piezoelectric medium interact with SAWs propagating in the substrate via the acoustoelectric effect, first predicted by Parmenter in 1953 [2]. This leads to energy transfer between the SAW and the charge carriers, manifested as a change in the SAW observables. Wixforth *et al.* [3, 4] provided the first demonstration of this in a two-dimensional (2D) system, observing that Shubnikov-de Haas oscillations in the conductivity of a GaAs/$Ga_{1-x}Al_xAs$ (x = 0.37) heterostructure in a strong magnetic field were mirrored by large oscillations in the SAW attenuation and velocity. Similar effects were later reported in one-dimensional (1D) quantum nanowires [5, 6] and zero-dimensional (0D) quantum dots [7] by Nash *et al*. It is also possible

for SAWs to generate an acoustoelectric current in an LDES in a closed circuit, where the charge carriers become trapped in the electric potential minima and maxima and are transported over macroscopic distances at the acoustic velocity. Individual electron transport by SAWs has even been demonstrated. Talyanskii *et al.* [8] used a 1D split-gate geometry on GaAs/$Ga_{1-x}Al_xAs$ (x = 0.37) heterostructures to transport 1 – 4 electrons per SAW cycle, by tuning the gate voltage. This technology could be highly relevant for metrological and quantum information applications.

Graphene is a 2D allotrope of sp^2-hybridised carbon atoms arranged on a honeycomb lattice [9]. Its discovery in 2004 has led a revolution in materials research, due to its unmatched physical properties. Its charge carriers are predicted to have a mobility exceeding ~200,000 $cm^2\ V^{-1}\ s^{-1}$ [10] and it has no electronic band-gap, readily exhibiting ambipolar transport [10]. It also has an optical absorption coefficient of 2.3%, despite being one atomic layer thick [11, 12], and a Young's modulus of 1.0 TPa for free standing sheets [13]. Graphene's planar structure makes it highly suitable for investigation with surface acoustic waves. This was explored theoretically by Thalmeier *et al.* [14] in 2010 and Zhang and Xu [15] in 2011 and followed experimentally by measurements of an acoustoelectric current in graphene by Miseikis *et al.* [16] in 2012. Subsequent work by Bandhu *et al.* sought a clearer understanding of the SAW frequency and intensity dependence of the acoustoelectric current in graphene at room [17] and low [18] temperature in millimetre-scale devices. This ultimately led to the

development of proof-of-concept chemical sensors [19] and phase shifters [20] based on graphene-SAW hybrids.

Despite these advances, and with graphene's potential as a broadband photodetector [12], no work has so far been reported on the acoustoelectric photoresponse of graphene. Furthermore, the electronic properties of graphene nanoribbons (GNRs), and their photoresponse, have yet to be investigated with surface acoustic waves. These sub-micron wide graphene channels, with high aspect ratios, are envisaged as a key component in future graphene circuitry [21, 22] and when formed into arrays can be used to study graphene plasmonics [23]. The likelihood of graphene-SAW devices being deployed in commercial applications requires a greater understanding of their photoresponse. Additionally, it is important to examine the electronic and optoelectronic properties of GNRs with SAWs, given the growing interest in these structures. The work presented in this thesis seeks to address these gaps.

1.2 Overview

The results presented in this thesis are the first investigation of the photoresponse of the acoustoelectric current in large-area graphene, which has been characterised as a function of SAW frequency and intensity, and illumination wavelength and intensity in the visible range. An acoustoelectric current generated in graphene nanoribbon arrays is reported for the first time, studied as

a function of SAW frequency and intensity, and GNR width for nanoribbon widths in the range of 200 to 600 nm. The photoresponse of the acoustoelectric current in GNR arrays is also studied, as a function of illumination intensity, SAW frequency, and GNR width. The work presented in this thesis has implications for both academic and industrial research, and is structured as follows:

Chapter 2 contains an introduction to graphene and a review of its properties that are relevant to explaining the results in this thesis. This includes discussions on: the band structure of graphene and the tunability of its charge carrier population, both by field effect measurements and surface adsorbates; the electronic properties of GNRs; the optical conductivity of graphene in the visible range; and the generation of a hot carrier distribution under illumination. Graphene production methods are also presented, with specific detail given to chemical vapour deposition, followed by techniques of graphene characterisation. The chapter concludes with a review of relevant applications.

In Chapter 3, the wave equation describing SAW propagation in piezoelectric materials is obtained, along with the functional form of SAWs. The generation of SAWs by interdigital transducers (IDTs) is discussed, including determination of the centre frequency of single-digit IDTs and the effects of IDT apodization, and practical considerations for commercial SAW devices are reviewed. The origin of the acoustoelectric effect in bulk materials is discussed, followed by the special case of its appearance in 2D electron systems, including graphene, integrated

with SAW devices. Some applications of acoustoelectric charge transport are also given.

A comprehensive process for graphene-SAW and GNR-SAW hybrid device fabrication is given in Chapter 4. The manufacturer's data for the as-supplied $LiNbO_3$ SAW devices is shown. The procedures for transferring commercially available CVD graphene to the SAW devices, identifying it on different substrates, and patterning it via electron beam lithography and reactive ion etching, are described. The process of applying electrical contacts to the devices via thermal evaporation, mounting them to custom-designed printed circuit boards, and adding wire bonds, is also outlined. This is followed by a list of the tested devices, their geometries, and the measurements they were used for. The chapter concludes with descriptions of the techniques used for SAW generation and detection, electrical measurements, and controlling the illumination sources.

Chapter 5 contains the results of a study into the photoresponse of the acoustoelectric current generated in, and conductivity of, large-area CVD graphene. The acoustoelectric current and conductivity were first monitored as the measurement chamber was vacuum pumped. A positive current in the direction of SAW propagation was initially observed, corresponding to p-doping. This is consistent with reports of CVD graphene processed following the techniques used here [24]. The resistance was seen to decrease with increasing pump-out time. This is believed to be due to the steady removal of surface adsorbates. Following vacuum pumping over hundreds of hours, the doping

transitioned from p-type to n-type, thought to be caused by the removal of molecular water from the surface. The SAW frequency and intensity dependence of the acoustoelectric current was explained by a classical relaxation model describing the interaction between the SAWs and graphene charge carriers. Under illumination by LED light, an increase in the acoustoelectric current was measured, and was mirrored by a decrease in conductivity. A smaller percentage increase in acoustoelectric current is seen under the same intensity illumination at a longer wavelength. The generation of a hot carrier distribution provides a possible explanation for the observed photoresponse [25]. Lastly, the percentage change in acoustoelectric current was similar at different SAW frequencies, which might be expected if the change in electronic properties were dominated by hot carrier effects. A modified version of this chapter is published in 'Acoustoelectric Photoresponse in Graphene', *Applied Physics Letters*, **106,** 133107 (2015).

The effects on the acoustoelectric current of patterning the graphene into arrays of GNRs is investigated in Chapter 6. First studied in arrays of 500 nm-wide GNRs, the acoustoelectric current was found to be an order of magnitude higher than previously reported in graphene-SAW devices of this scale [17, 18, 20]. This is believed to be due to higher quality, more continuous graphene achieved using a modified transfer technique. This is reflected by a higher conductivity than that measured in the device studied in Chapter 5. The dependence of the acoustoelectric current on SAW frequency and intensity is described by the classical relaxation model used to explain the results in the

previous chapter. The possibility of enhancing the acoustoelectric current by the inclusion of perpendicular 'bridge' nanoribbons in the array is also discussed, with measurements presented for devices with and without these additional structures. The acoustoelectric current generated in neighbouring arrays of GNRs on the same device, with nanoribbon widths in the range 200 – 600 nm, is found to increase with decreasing GNR width. This is thought to be caused by increased p-doping arising from damage to the GNR edges leading to an increase in charge carrier mobility. An adapted form of this chapter is published in 'Acoustoelectric Current in Graphene Nanoribbons', *Scientific Reports*, **7,** 1767 (2017).

In Chapter 7, the results of a study into the acoustoelectric photoresponse in arrays of graphene nanoribbons with GNR widths of 350 - 600 nm are presented. In each array, the largest acoustoelectric currents are observed at a SAW frequency of 355 MHz, compared to 33 MHz. This is consistent with the classical relaxation model describing the measurements presented in Chapters 5 and 6. The GNR conductivity decreases with increasing width, as explained in Chapter 6. Under illumination by a 450 nm LED, a decrease in both acoustoelectric current and conductivity is observed. This contrasts with the measurements in Chapter 5, where the magnitude of acoustoelectric current increased the conductivity decreased. As the GNR width increases, the percentage change in conductivity under illumination also increases. It is believed that, due to the high conductivity of the GNRs compared to the continuous graphene sample studied in Chapter 5,

the decrease in mobility resulting from the generation of a hot carrier distribution overcomes the increase in acoustoelectric attenuation coefficient. This causes the measured decrease in acoustoelectric current under illumination.

Chapter 8 provides a summary of the experimental results presented in this thesis, along with suggestions for future research.

2. Graphene

2.1 Overview

Graphene is a two-dimensional (2D) allotrope of carbon with a honeycomb lattice [9, 10]. It can be derived from a variety of other carbon materials, such as zero-dimensional fullerenes, one-dimensional carbon nanotubes, and three-dimensional (3D) graphite (Figure 2.1). Theoretical and experimental studies suggested that single-atomic-layer materials could not exist outside of bulk 3D structures, as the rapidly rising melting point with decreasing thickness would cause them to decompose or form curved structures [10]. This was disproved in 2004 when graphene was isolated for the first time by Novoselov and Geim [9], who used adhesive tape to extract single-layer graphene (SLG) from graphite.

The ease with which high-quality graphene could be fabricated led to a surge of experimental work to determine its properties. Not only is SLG air-stable, it also exhibits a plethora of desirable engineering attributes, including: an intrinsic charge carrier mobility of ~200,000 $cm^2 V^{-1} s^{-1}$ even for high carrier concentrations (>10^{12} cm^{-2}) [26], surpassing that of any known material [27]; an in-plane thermal conductivity at room temperature of 2000 – 4000 W $m^{-1} K^{-1}$ (depending on crystal quality), higher than that of diamond (2200 W $m^{-1} K^{-1}$ at 300 K) [28]; a high optical

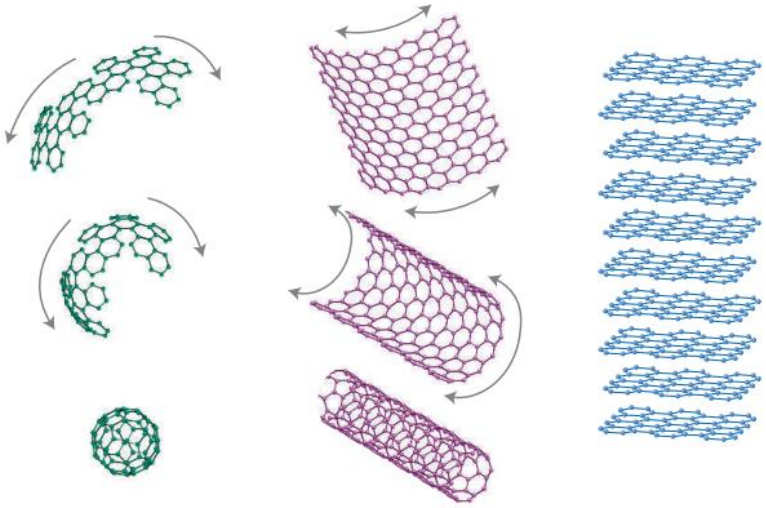

Figure 2.1: *A single layer of graphene can be wrapped into zero-dimensional fullerenes (green), one-dimensional carbon nanotubes (red), and stacked into three-dimensional graphite (blue). Illustration taken from [10].*

absorption of ~2.3%, in spite of its monolayer structure [11]; and a Young's modulus of 1.0 TPa for free-standing sheets, making it the strongest known material [13]. Such is the desire to study graphene, for both pure and applied research, that within a decade of its discovery scalable production methods had developed including wafer-sized sublimation of silicon carbide (SiC) [29, 30, 31, 32, 33] and up to metre-square chemical vapour deposition (CVD) on a variety of transition metals [34, 35, 36, 37, 38, 39]. Advances made in the field of graphene fabrication have facilitated the discovery of a host of other 2D materials [40], too, such as: hexagonal boron nitride (hBN) [41, 42, 43]; molybdenum disulphide (MoS_2) [44, 45]; tungsten diselenide (WSe_2) [46, 47]; silicene; phosphorene; and germanene [48, 49, 50].

Graphene's 2D nature makes it extremely sensitive to surface perturbations. Its charge carrier concentration can be controlled by very low concentrations of gases [51, 52], making it a compelling material for sensing applications. Additionally, its gapless and linear band structure makes it an interesting candidate for broadband optoelectronic applications [53]. The electronic properties of graphene have conventionally been studied with a field effect transistor (FET) configuration. Surface acoustic waves (SAWs), a mechanical vibration propagating along the surface of a material, offer an alternative approach. SAWs on piezoelectric media have been used for many years to probe the band structure of low-dimensional electron systems (LDESs), such as quantum wires [5] and quantum dots [7, 54]. The work in this thesis uses SAWs to study the electronic properties of graphene under illumination, and the electronic properties of graphene nanoribbons. This Chapter will cover the elements of graphene research that will aid interpretation of the measurements presented in Chapters 5 - 7. In Section 2.2, key electronic and optical properties of graphene are discussed. Section 2.3 reviews the popular methods of graphene production, followed by graphene characterisation techniques in Section 2.4. Related applications of graphene are presented in Section 2.5. A summary of the Chapter is given in Section 2.6.

2.2 Properties of Graphene

2.2.1 Electronic Properties

The atoms of graphene are arranged on a trigonal planar lattice with a diatomic basis [55], shown in Figure 2.2. The primitive lattice vectors are given by $\boldsymbol{a_1} = \frac{a}{2}(3, \sqrt{3})$ and $\boldsymbol{a}_2 = \frac{a}{2}(3, -\sqrt{3})$, where $a =$ 1.42 Å is the atomic bond length (in Figure 2.2, $a = |\delta_i|, i =$ 1, 3, 3). The reciprocal lattice vectors are given by $\boldsymbol{b_1} = \frac{2\pi}{3a}(1, \sqrt{3})$ and $\boldsymbol{b_2} = \frac{2\pi}{3a}(1, -\sqrt{3})$. The 2s, $2p_x$, and $2p_y$ valence electrons of carbon undergo sp^2 hybridisation to form strong σ bonds with three neighbouring carbon atoms. These fixed electrons cannot participate in electron transport. On the other hand, the $2p_z$ orbitals (perpendicular to the atomic plane) of neighbouring atoms overlap due to the short σ bond length, forming delocalised π (valence) and π^* (conduction) bands. Applying the tight-binding approach to electrons in the π state, it is possible to calculate the electronic band structure, shown in Figure 2.3.

Intriguingly, the valence and conduction bands meet each other at the edge of the Brillouin zone at points K and K' in reciprocal space, and have a conical shape for low energies (~1 eV). Note that these two points are not connected by a reciprocal lattice vector and arise from the two triangular sub-lattices. Since the curvature of the bands is zero, near the K and K' points the charge carriers have zero effective mass and behave like Dirac fermions, with a Fermi velocity $v_F \sim 10^6$ m s^{-1} and an energy $E = \hbar\kappa v_F$, where $\kappa = |k - K|$ is the wave vector and $\hbar$ is the

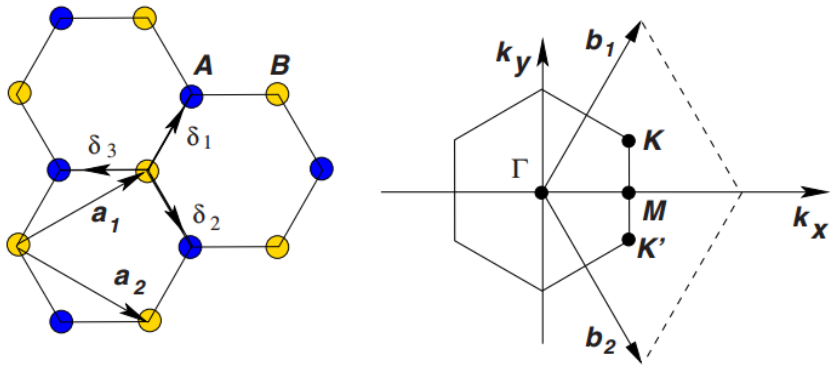

Figure 2.2: *Left: The honeycomb lattice of graphene is made up of two intermeshed triangular lattices, indicated by atoms A (blue) and B (yellow).* $\boldsymbol{a}_1$ *and* $\boldsymbol{a}_2$ *are the primitive lattice vectors, and* δ_i *(*i *= 1, 2, 3) are the nearest-neighbour vectors. Right: The first Brillouin zone and reciprocal lattice vectors* $\boldsymbol{b}_1$ *and* $\boldsymbol{b}_2$*. The Dirac points are located at the* K *and* K' *points. (Illustration taken from [55].)*

reduced Planck's constant. Thus, the K and K' points are commonly referred to as the Dirac points. In undoped graphene, the Fermi level crosses the Dirac points, such that the valence band is completely full and the conduction band is completely empty, rendering graphene a gapless semiconductor or a semi-metal [55, 9]. This unusual band structure gives graphene its unique electronic properties, such as a half-integer quantum Hall effect [56] and non-vanishing conductivity for zero density of states (*i.e.* when the Fermi level lies at the Dirac point) at low temperature, in the absence of defects [10, 57].

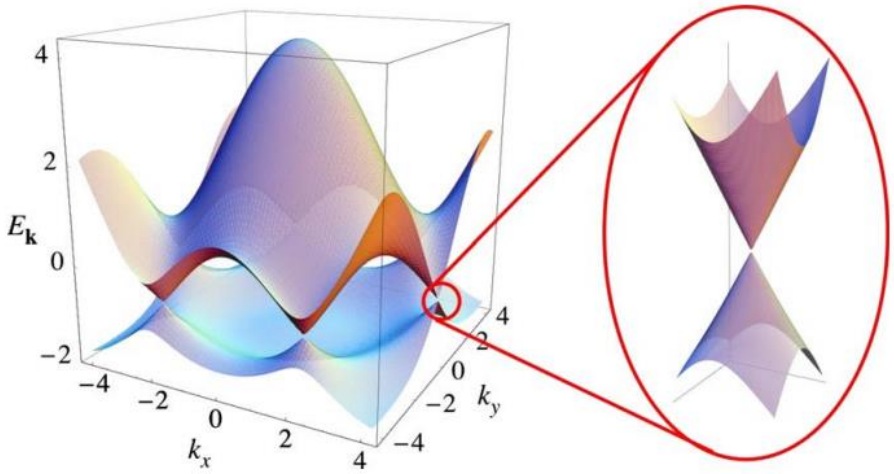

Figure 2.3: *Electronic dispersion of graphene calculated via the tight-binding approach. (Illustration taken from [55].)*

2.2.1.1 Electric Field Effect

The application of an external electric field to a material leads to modulation of the charge carrier concentration, n. This is known as the electric field effect, and enables the band structure of a material to be probed. This effect can be studied in graphene using a device of the geometry shown in Figure 2.4, known as a graphene field effect transistor (GFET) [58], where the external field is provided by a back-gate voltage, V_g. A current I_{SD} is passed from the source (S) contact to the drain (D) contact, while simultaneously the voltage drop along the channel V_{SD} is measured to determine the resistance R_{SD}. In Figure 2.4, the graphene is placed on a doped silicon (Si) substrate (to improve the Si conductivity), which acts as a back gate, with a silicon dioxide (SiO_2) layer, typically 300 nm thick, acting as a dielectric. Application of a positive (or negative) V_g induces electrons

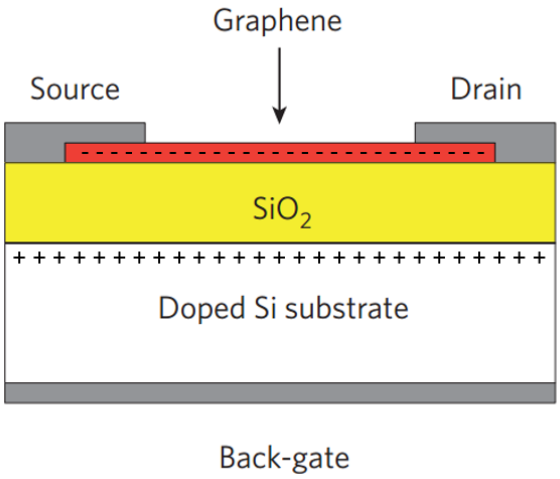

Figure 2.4: *A side-on schematic of a graphene FET. A current I_{SD} is passed from the source (S) to the drain (D). Application of a back-gate voltage V_g can induce charge carriers in the graphene. Illustration modified from [58].*

(or holes) in the graphene, where the whole system can be viewed as a parallel-plate capacitor, the capacitance of which is:

$$C = \frac{Q}{V_g} = \frac{\varepsilon_0 \varepsilon_r A}{d} \tag{2.1}$$

where $Q = eN$ is the charge on the capacitor, e is the charge on an electron, N is the number of charge carriers, ε_0 is the permittivity of free space, ε_r is the relative permittivity of the dielectric ($\varepsilon_r = 3.7$ for SiO_2), A is the surface area, and d is the dielectric thickness. The induced charge carrier concentration is then given by:

$$n_{\text{induced}} = \frac{N}{A} = \frac{\varepsilon_0 \varepsilon_r}{de} V_g \tag{2.2}$$

A schematic gate characteristic is shown in Figure 2.5. A maximum in resistivity is observed as the Fermi energy crosses the Dirac point, where the charge carrier concentration is minimised. This sharp peak is termed the charge neutrality point, as electrons and holes are present in equal concentrations, and is located at a voltage referred to as the Dirac voltage, V_{Dirac}. In intrinsic (undoped, defect-free) graphene, V_{Dirac} is at 0V. Near V_{Dirac}, the conductivity σ depends linearly on V_g, and the charge carrier mobility μ may be extracted from the gradient via:

$$\mu = \frac{1}{C}\frac{\mathrm{d}\sigma}{\mathrm{d}V_g} \tag{2.3}$$

where C is the gate capacitance. Intriguingly, intrinsic graphene's conductivity is non-zero in the limit of vanishing charge carrier concentration [10], and is theoretically predicted to have a minimum value $\sigma_{\mathrm{min}} = 4e^2/h\pi$ as a consequence of its charge carriers behaving as Dirac fermions [59]. In real graphene, inhomogeneous charged impurities (or charge puddles [60]) lead to a lower resistivity of several kiloohms per square at the Dirac point [10].

Graphene's carrier concentration can also be tuned via molecular surface adsorbates [51, 52, 61] due to its high surface area-to-volume ratio. This could enable modulation of n on substrates not compatible with the GFET geometry. For example, water [62] and NO_2 [63, 64] induce p-doping in graphene, whereas ammonia (NH_3) [65] induces n-doping. P-type and n-type doping respectively shift the charge neutrality point towards positive and negative gate voltages. This is

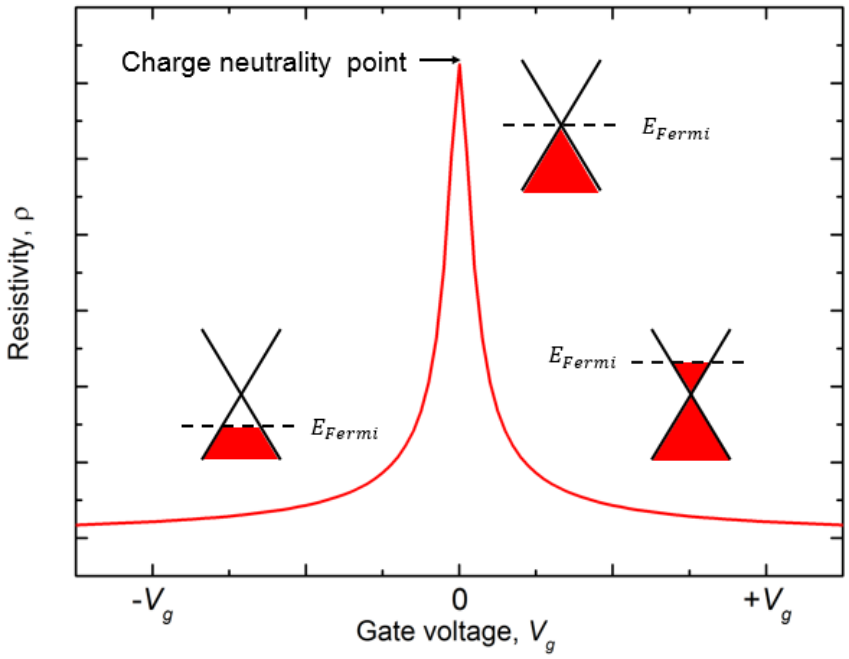

Figure 2.5: *Schematic showing the typical characteristics of source-drain resistance as a function of gate voltage in a GFET. A maximum value of resistance is observed for V_g = 0 V, known as the charge neutrality point. Insets show schematically the position of the Fermi energy as a function of gate voltage.*

due to charge transfer between the adsorbates and the graphene. Solís-Fernandez *et al.* [66] have further demonstrated that piperidine adsorbates can vary the doping level from p-type to n-type with increasing concentration, forming p-n junctions for intermediate concentrations. Currently, poor control over dopant concentrations is a barrier to practical applications. Medina *et al.* [67] have shown that lattice disorder sites induced via plasma etching of graphene can act as 'anchors' for surface adsorbates, to which molecular dopants preferentially

adsorb. This may ultimately open a route towards selective and controllable molecular doping of graphene.

While graphene's ambipolar transport properties are of great interest for pure research, the lack of a band gap is one of the most significant inhibitors to the development of graphene-based electronics. The ability to 'turn off' conduction is a critical aspect of integrated logic circuits. It is presently unlikely that graphene will surpass silicon-based electronics in these applications until methods of opening a band gap reliably and of sufficient magnitude are achieved [68].

2.2.1.2 High Mobility

The electronic quality of a material is often characterized by charge carrier mobility. Graphene is theoretically predicted to exhibit μ exceeding 200,000 $cm^2 V^{-1} s^{-1}$ at room temperature, due to weak electron-phonon scattering, even for a charge carrier concentration $n > 10^{12}$ cm^{-2} [26], and its charge carriers exhibit room temperature ballistic transport (that is, electron transport with negligible resistivity due to scattering) over distances of several hundred nanometres [69, 70], where the mean free path l may be estimated by [69]:

$$l = \frac{\hbar}{e}\mu\sqrt{n\pi} \tag{2.4}$$

Experimentally, however, the charge carrier mobility is much lower [20, 35, 42, 51, 56, 71], with the exfoliated samples on Si/SiO_2 having μ ~ 20,000 $cm^2 V^{-1} s^{-1}$

at room temperature. This is largely attributed to electron scattering from charged impurities on or under the graphene sheet [72, 73, 74, 75], microscopic ripples [76], rips and wrinkles [77, 78], and scattering from substrate phonons [42, 79]. The substrate plays a significant role in limiting the transport properties of graphene. This has been illustrated in experiments by Bolotin *et al.* [80], who measured μ ~ 200,000 $cm^2\ V^{-1}\ s^{-1}$ in thermally-annealed 2 μm-long graphene channels suspended 150 nm above the surface of SiO_2 at room temperature, for a carrier concentration of ~2 x 10^{12} cm^{-2}, at ~5K. Furthermore, Dean *et al.* [42] showed that graphene on insulating hBN substrates can attain a threefold increase in charge carrier mobility, compared to transfer to Si/SiO_2, due to the reduced concentration of charged impurities arising from hBN's resistance to mechanical and chemical manipulation [41]. In graphene produced by chemical vapour deposition (CVD, discussed in Section 2.4.2), the intrinsic polycrystallinity introduces line defects that further deteriorate electronic quality, with typical charge carrier mobilities of 1000 – 5000 $cm^2\ V^{-1}\ s^{-1}$ at 295 K [34, 35, 72]. It is thought that atoms at the grain boundaries undergo chemical reactions with surface adsorbates, disrupting the sp^2 bonded structure [72]. Song *et al.* [72] experimentally confirmed the influential role of the grain boundaries by measuring a threefold increase in mobility within individual grains compared to regions spanning multiple grains. They qualitatively explained this using a potential barrier model. If the length, resistivity, and mobility for the intra-grain region are

l_1, ρ_1, and μ_1, and those for the inter-grain region are l_2, ρ_2, and μ_2, the resistivity and mobility for the whole CVD graphene can be written as:

$$\rho = \rho_1 + \beta\rho_2 \tag{2.5}$$

and:

$$\mu = \left(\frac{\alpha}{\alpha+\beta}\right)(\mu_1 + 2\beta\mu_2) \tag{2.6}$$

where $\alpha = \rho_1/\rho_2$ and $\beta = l_2/l_1$ [72]. With increasing β, the resistivity increases and the mobility decreases according to the above expressions.

2.2.1.3 Graphene Nanoribbons

Graphene nanoribbons (GNRs) are a closely related system to graphene and carbon nanotubes, and have been studied theoretically for many years [81, 82]. GNRs are graphene channels with a high aspect ratio and typical widths of a few hundred nanometres (as studied in this thesis). At these widths, GNRs may be suitable as circuit interconnects in future graphene electronics [21, 22, 83], where their current carrying ability and thermal conductivity (>10^8 A cm^{-2} and 3-5 x 10^3 W mK^{-1} respectively) far surpass those of copper (10^7 A cm^{-2} and ~0.4 x 10^3 W mK^{-1} respectively) [21]. They can also be used to study the plasmonic properties of graphene. For example, Luxmoore *et al.* [23] studied the far-infrared transmission of light through arrays of GNRs with widths from ~200 – ~500 nm. Light polarized perpendicularly to the long-axis of the GNRs induces oscillations in the free charge, exciting plasmons with momentum $q \approx$

$(2\mathrm{x}+1)\pi/w$ (where $\mathrm{x}=0,1,2,...$ and w is the GNR width). This leads to the appearance of absorption features in the transmission spectra, that could have applications in biosensing, communication, and gas detection. At widths below 10 nm, GNRs with specific edge structuring possess an electronic band gap that varies with width W, approximately as $\Delta E \sim 1$ eV nm W^{-1} [84] (i.e. for a GNR width of 1 nm, $\Delta E \sim 1$ eV, whereas for a width of 10 nm, $\Delta E \sim 0.1$ eV). This is due to the confinement of the electrons in the π state to the edges of the GNR [81]. Han *et al.* [85] confirmed this experimentally in lithographically-defined GNRs, where, for channel widths of less than 30 nm, suppressed conductance was observed for certain gate voltages. Reliable control of the GNR edge structuring and scalable production of these devices is anticipated to remain a challenge in the long term, however [68]. Indeed, the on-off ratios attained in graphene modified to include a band gap have so far not exceeded 10^3; this is still significantly smaller than the 10^6 ratio required in today's electronics [68]. Worse still, opening a band gap in graphene by patterning it into GNRs can decrease the mobility [58]. Since the charge carrier mobility in CVD graphene is roughly equal to that of silicon (approximately $1400\ \mathrm{cm^2\ V^{-1}\ s^{-1}}$ at 300 K [86]), graphene's advantage for some applications is likely to be limited. For comparison, silicon's intrinsic bandgap is 1.1 eV [87].

Large (sub-micron) GNRs can easily be fabricated via a combination of electron beam lithography and reactive ion etching (see Chapter 4). High resolution systems have even been used to pattern GNRs with 10 nm widths [88,

89]. Charge carrier mobilities in the range 0.21 – 6000 $cm^2\ V^{-1}\ s^{-1}$ have been reported. Plasma etching can induce significant disorder at the GNR edges [84], to which charged molecules preferentially adsorb [67, 90] and induce doping. The presence of a band gap in the narrowest GNRs is conditional on the quality of the GNR edges. Where this is required, techniques such as the un-zipping of carbon nanotubes [91] or bottom-up synthesis with molecular precursors [84] may be more appropriate.

2.2.2 Optical Properties

2.2.2.1 Linear Optical Absorption

One of the most striking features of graphene is its frequency-independent AC conductivity in the optical range, given by [92]:

$$G_0 \equiv \frac{e^2}{4\hbar} \approx 6.08 \times 10^{-5}\ \Omega^{-1} \tag{2.8}$$

The absence of a dependence of graphene's optical conductivity on material parameters such as carrier mean free time arises from graphene's linear band structure [92]. By applying the Fresnel equations in the thin-film limit [53, 92], the optical transmittance of free-standing SLG is found to be given by:

$$T = \left(1 + {}^{1}/_{2}\,\pi\alpha\right)^{-1/2} \approx 1 - \pi\alpha \approx 97.7\% \tag{2.9}$$

Where $\alpha \approx {}^{1}/_{137}$ is the fine structure constant, determining the interaction strength between charged particles and photons. In other words, graphene absorbs ~2.3% of incident electromagnetic radiation in the visible range [11, 93, 94], with a reflectance of < 0.1% [53]. Nair *et al.* determined this experimentally [11], and found that the absorption scales linearly with increasing layer number for few-layer graphene (FLG) (Figure 2.6). This broadband absorption and high absorption coefficient for a single atomic layer could make graphene suitable as a photodetector across a wide spectral range.

2.2.2.2 Hot Carrier Effects

Under optical illumination, an electron in the valence band can absorb a photon and be excited into the conduction band, creating an electron-hole (e-h) pair [95, 96]. In a semiconductor, charge carrier relaxation proceeds via heat transfer to the lattice and carrier-carrier scattering [97, 98, 99]. However, the relaxation process in graphene is altered [99]. It begins with electron-electron scattering on a sub-picosecond timescale, followed by optical phonon emission over several picoseconds [100]. The relatively high energy of the optical phonon (E_{op} ~ 200 meV) results in cooling by this mechanism quenching rapidly, since the energy of photoexcited carriers quickly falls below E_{op} [12, 99, 100]. Cooling by low-energy acoustic phonons is inefficient, thus energy is redistributed solely among the charge carriers (by carrier-carrier scattering) [101, 102]. By this process, multiple

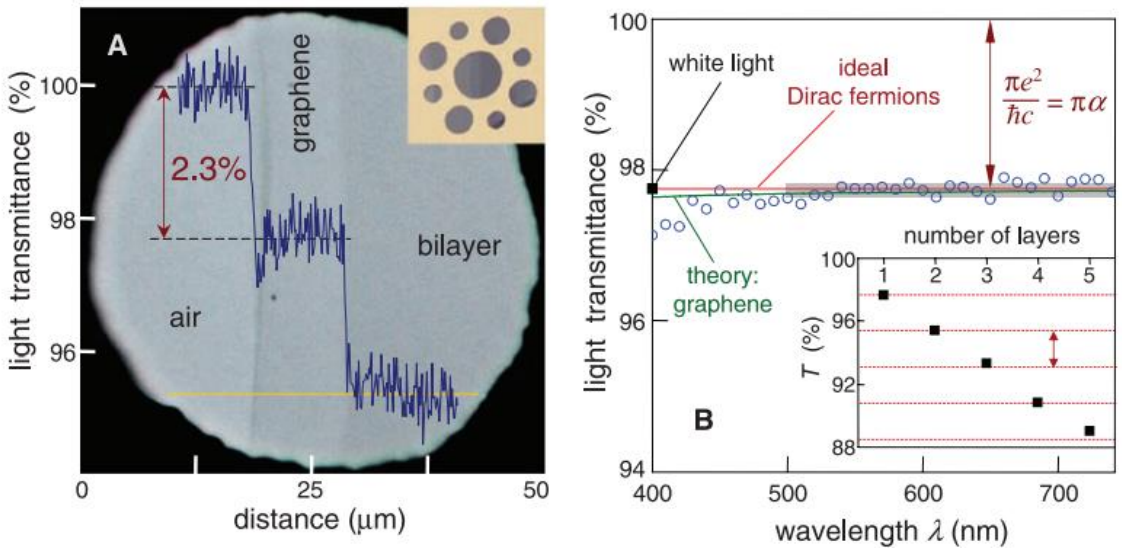

Figure 2.6: *Left: Photograph of a 50 μm-wide aperture, partially covered by graphene and its bilayer. The line scan (yellow line) shows transmittance decreasing with increasing layer number. Right: Transmittance spectrum of graphene in the visible range. The red line is the transmittance according to Equation 2.9. The green line shows the transmittance accounting for band structure warping away from the Dirac point. The inset shows transmittance as a function of layer number. Reproduced from [11].*

secondary hot electrons are generated in the conduction band [12, 25, 102], with the charge carrier distribution having a higher temperature than the lattice [99, 100, 101]. Electron-to-lattice cooling is eventually achieved on a nanosecond timescale, mediated by acoustic phonons [101]. A full, quantitative description of

electronic cooling in graphene is beyond the scope of this thesis. For this, readers may wish to refer to Bistritzer and MacDonald [101] or Winzer *et al.* [102].

Carrier-carrier scattering as the dominant relaxation pathway (rather than optical-phonon emission) was first confirmed by Gabor *et al.* [99] in studies of the photocurrent generated at a graphene p-n junction under illumination by 850 nm laser light. The hot carrier regime was manifested as a strong photothermoelectric effect (Section 2.5.1.2), which resulted in a six-fold photovoltage pattern as a function of top- and back-gate voltage. The relaxation dynamics were further studied in doped graphene by Tielrooij *et al.* [25] using differential-transmission spectroscopy. An optical, pulsed laser was used to photogenerate an e-h pair, and a THz-frequency probe laser was used to examine the carrier relaxation process. The change in transmission is directly proportional to the negative of THz conductivity. A positive fractional increase in transmission corresponded to a decrease in THz conductivity, consistent with the generation of a hot carrier distribution. They also found that the number of hot electrons in the conduction band increased linearly with excitation wavelength.

In practical graphene-based electronics, hot electron cooling can also occur at graphene-metal junctions via the Peltier effect [103, 104] and by electron scattering with substrate phonons [105]. This latter mechanism plays an important role in heat dissipation, as argued by Freitag *et al.* [105] in studying the thermal characteristic of graphene FETs on SiO_2. They found that approximately 77% of heat was dissipated into the substrate, with the remainder through the

electrodes. When the energy of the electrons fell below that of the optical phonon in graphene, energy from the charge carrier distribution could also be dissipated by the direct excitation of substrate phonons of a much lower energy (~60 meV). The original assumption was that the energy of the hot electrons was dissipated by graphene phonons, which in turn coupled to SiO_2 phonons. This was due to the weak van der Waals bonding between the graphene and the substrate, the surface roughness of SiO_2 on the nanometre scale, and the mismatch in energies between the graphene and substrate phonons. The direct generation of phonons in SiO_2 gives the graphene-SiO_2 interface a thermal resistance with a factor of four of that of ideal nanoscopic boundaries ($r_{gr-SiO_2} \sim 4 \times 10^{-8} \mathrm{K\,m^2 W^{-1}}$, compared to $r \sim 10^{-8} \mathrm{K\,m^2 W^{-1}}$).

2.3 Graphene Production

The properties of graphene depend strongly on the material quality and the presence of defects, both of which are influenced by the production methods. In this section, some widely-used procedures for graphene fabrication are reviewed.

2.3.1 Exfoliation

The first graphene samples were fabricated via mechanical exfoliation from highly oriented pyrolytic graphite (HOPG) [9]. An adhesive film is applied to HOPG and peeled away, extracting small mesas with several-hundred-nanometre thickness.

Repeated exfoliation of these mesas eventually yields single-layer graphene (SLG) and few-layer graphene (FLG) flakes of up to 10 μm across, which are commonly pressed against Si with a 300 nm-thick SiO_2 layer to make them visible [106, 107] (see Section 2.4). The flakes adhere to the substrate via van der Waals forces and strong solvents are used to remove adhesive residues before further processing. Exfoliation of graphene is labour intensive and not scalable. Thousands of flakes of different sizes and thicknesses are transferred at once, and careful searching under an optical microscope is needed to identify monolayer samples. Additionally, the positioning of the flakes is uncontrolled. This makes mechanically-exfoliated graphene suitable only for research applications. However, samples fabricated this way exhibit the high charge carrier mobility, with μ ~ 20,000 $cm^2\ V^{-1}\ s^{-1}$ routinely measured [26, 56, 108].

In recent years, liquid-phase/chemical exfoliation has shown promise as a route towards cheap and mass produced graphene. HOPG crystals are dispersed in a solvent and are agitated via ultrasonic vibrations (known as sonication). The resultant shearing force on the graphite splits it into platelets, and prolonged exposure yields graphene flakes of 1 – 5 layers, with diameters in the range 100 – 300 nm [109, 68]. Centrifugation can then be used to separate the SLG and FLG flakes from unexfoliated material [110]. Graphene produced via this approach is suitable for such applications as conductive inks/paints, coatings, energy storage, transparent conductive layers, and bioapplications [68].

2.3.2 Chemical Vapour Deposition

Chemical vapour deposition has emerged as one of the most important methods of graphene fabrication due to its scalability [34, 68, 111, 112, 113]. CVD graphene is commonly grown on nickel [37, 114, 115] or copper foils [34, 36, 112, 116]. The foil is heated to 900 - 1000°C in vacuum, and exposed to methane (CH_4). The metal acts as a catalyst in the decomposition of CH_4, and the carbon atoms dissolve into it. The Ni/Cu is then cooled, resulting in precipitation of carbon on the surface and the formation of graphene. Growth therefore proceeds by nucleation at multiple sites across the metal catalyst, resulting in polycrystalline graphene with single-crystal domains of 100 nm – 10 μm across [117, 118]. Wrinkle-free graphene films can be easily achieved on nickel since their lattice constants are similar, whereas on copper this is generally prevented due to the difference in their thermal expansion coefficients [111]. However, a nickel growth substrate yields graphene films with 1 – 12-layer thickness [119] due to the nickel's polycrystallinity [38, 111, 119]. Copper foils have become preferable principally because the percentage of SLG is high on this substrate (>95% monolayer, 3-4% bilayer, <1% few-layer) due to the lower solubility of carbon in copper [111]. Growth substrate cleanliness and domain size, chamber pressure, temperature, cooling rate, and gas concentration all strongly influence the number of graphene layers and the size of the crystal domains [72, 120].

The graphene is often transferred to arbitrary substrates via a 'wet etch' method [121]. A supporting layer such as poly(methyl methacrylate) (PMMA) is

applied to the top of the graphene and an etchant solution (ammonium persulfate or iron chloride) used to dissolve the underlying metal. The PMMA-graphene layer is then deposited on the target substrate, and the PMMA dissolved [121, 122]. This enables large-area graphene films to be handled relatively easily. However, there are some serious drawbacks. The graphene is frequently contaminated by etchant residues (some of which can be removed via thermal annealing [123]) and incompletely-removed copper [122], and the graphene often has holes, cracks, and ripped sections [34, 77], significantly reducing the charge carrier mobility [77, 123]. PMMA residues are particularly hard to remove as they can become attached to dangling bonds in the graphene [123, 124]. In conjunction with the potential barriers arising from the material's polycrystallinity (discussed in Section 2.2.1.2), charge carrier mobilities of 1000 - 5000 $cm^2\ V^{-1}s^{-1}$ at 295 K are commonly observed [34, 35, 72]. The variation of charge carrier mobilities

Hao *et al.* [125] have shown that exposure to oxygen of the copper substrates suppresses graphene nucleation by preventing the accumulation of hydrocarbons on the surface. At the sites where nucleation does occur, one centimetre-diameter, single-crystal domains can be grown. At 1.7 K, they measured a charge carrier mobility μ ~ 40,000 – 65,000 $cm^2\ V^{-1}\ s^{-1}$ and at room temperature μ ~ 15,000 – 30,000 $cm^2\ V^{-1}\ s^{-1}$, approaching the values measured in exfoliated graphene [42]. However, the coverage was 5 – 10x lower than in conventional CVD graphene, and took place over 12 hours. Wu *et al.* [120] have

increased the growth rate by feeding carbon precursors to specific locations on a copper-nickel alloy substrate. The nuclei can grow into single-crystal graphene monolayers ~1.5” across in 2.5 hours, with room temperature mobilities in the range of 10,000 – 20,000 $cm^2 V^{-1} s^{-1}$. In 2017, Pang *et al.* [126] demonstrated self-terminating CVD graphene growth directly on Si/SiO_x substrates, altogether removing the damaging transfer stage, but the low mobility (410 – 760 $cm^2 V^{-1} s^{-1}$) and small grain size (~200 nm) require improvement to make this approach competitive with conventional CVD. Nonetheless, this is an important development in the production of graphene, since graphene growth on arbitrary substrates is likely to promote its deployment for commercial applications [68].

2.4 Characterisation Techniques

The fabrication of graphene devices relies heavily on its visibility on the substrate [106, 127]. Modern imaging techniques such as atomic force microscopy, scanning-electron microscopy, and tunnelling-electron microscopy are unable to clearly distinguish monolayer samples from thicker ones and have an extremely low throughput at the required atomic resolution [106]. Under certain conditions, optical microscopy can provide a preliminary identification of graphene [106, 127], whereas Raman microscopy can be used to quantitatively confirm the layer number and sample quality [128, 129, 130, 131]. Currently, the only limitations with Raman spectroscopy are that it is low-throughput and has yet to be

automated for SLG identification. In this Section, the optical and Raman characterisation techniques currently in use are reviewed.

2.4.1 Optical Microscopy

Silicon with a 300 nm-thick surface oxide layer (SiO_2) is a commonly used substrate in graphene device fabrication. When viewed under an optical microscope, the increase in optical path length due to the presence of graphene induces a contrast with respect to an empty substrate that is perceptible by the human eye. The contrast scales approximately linearly with layer number for few-layer graphene [121, 127], enabling the distinction of graphene from thicker

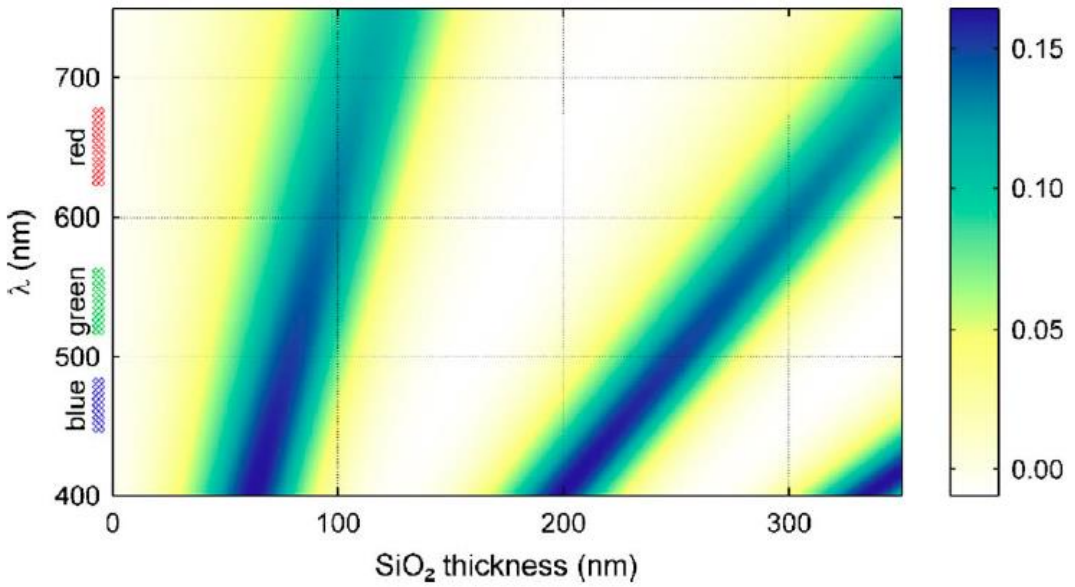

Figure 2.7: *Colour plot of optical contrast as a function of silicon dioxide thickness and illumination wavelength. Taken from [100].*

samples. Blake *et al.* showed that the optical contrast depends strongly on SiO_2 thickness and illumination wavelength, and arises also from the opacity of graphene [106]. Note that surface roughness is assumed to be negligible compared to the thickness of SiO_2. Using a model based on the Fresnel equations, they determined that the highest contrast is obtained for graphene on SiO_2 of thickness 90 nm and 280 nm, illuminated by green light. A colour plot of the contrast as a function of light wavelength and oxide thickness is shown in Figure 2.7. Following the same approach, graphene is most clearly identified on Si_3N_4 of 50 nm thickness under blue light, and PMMA of 90 nm thickness under white light.

2.4.2 Raman Spectroscopy

Raman spectroscopy is a contactless, high-resolution tool for uniquely capturing the electronic spectrum of graphene and conclusively differentiating a monolayer from graphitic structures with up to five layers [131]. It also provides information on the structural quality of graphene [129]. The process is based on the inelastic scattering of monochromatic light [132], typically from a visible-wavelength laser. Electrons in the material absorb incident photons and are excited to higher energy levels. Upon relaxation to the ground state, photons are emitted that may have the same frequency as the incident light (known as Rayleigh scattering), or be colour shifted by an amount Δf to higher or lower frequency (known as Raman scattering). The upshift or downshift in photon frequency/energy is symmetric

about Δf = 0, and is referred to as anti-Stokes and Stokes Raman scattering respectively.

The most prominent features in the Raman spectrum of monolayer graphene are the G-band, with a Raman shift of 1582 cm^{-1}, the 2D- band (or G'-band) at ~2700 cm^{-1}, and the D-band at ~1350 cm^{-1}. The D-band is induced by disorder and is absent in pristine graphene. A Raman spectrum of pristine graphene compared to graphite is shown in Figure 2.8. The G-band is the only band arising from a normal first-order Raman scattering process and is associated with the

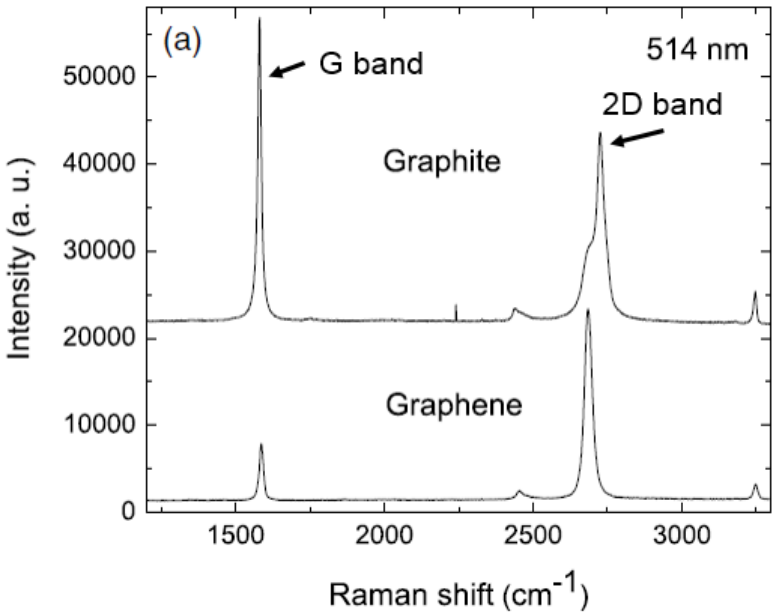

Figure 2.8: *Raman spectra of graphene and graphite, vertically offset, and scaled to give 2D peaks of the same intensity. The absence of the D-peak shows that this graphene sample is of very high quality and is free from structural disorder. Modified from [126].*

doubly-degenerate (transverse optical, TO and longitudinal optical, LO) in-plane phonon mode at the Brillouin zone centre (the Γ point). On the other hand, the 2D- and D-bands originate from a second-order, double-resonance scattering process at the Brillouin zone boundary (the K or K' point). An explanation is given by Malard *et al.* [133], as follows: an electron around the K point in the valence band absorbs a photon of energy E_{Laser} and is excited to the conduction band. It is then elastically scattered by a crystal defect in the case of the D-band, or inelastically scattered by an in-plane TO phonon in the case of the 2D band, to a point around the K' point. For both the D- and 2D-bands, the electron is then inelastically scattered back towards the K point by absorption or emission of an in-plane TO phonon, where it recombines with a hole and emits a photon. A triple-resonance process also occurs that contributes to the 2D-band. Instead of the electron around the K' point being scattered back towards the K point, a hole near the K point is inelastically scattered by a phonon towards the K' point, where a photon is emitted via electron-hole recombination. The scattering processes for the G-, 2D- and D-bands are shown schematically in Figure 2.9.

In a Raman spectrum of monolayer graphene, the 2D- to G-peak intensity ratio is typically in the range ~3 – 4 [129, 131], where the large intensity of the 2D-peak is thought to be due to the triple-resonance scattering process [133]. As the number of graphene layers increases, the 2D-peak broadens and decreases in intensity. The 2D-band broadening is attributed to the splitting of the π and π^* electron bands into four, due to van der Waals bonding between the graphene

layers [131]. This increases the possible number of scattering processes. The 2D-peak continues to evolve towards the graphite 2D-peak as the number of layers increases [131].

Lastly, the frequencies of the 2D- and D-bands in graphene Raman spectra upshift as E_{laser} increases. This dispersive behaviour originates from the double-resonance processes described above. Malard *et al.* [133] describe that for an electron with wave vector k, in-plane TO phonons of wave vector q preferentially

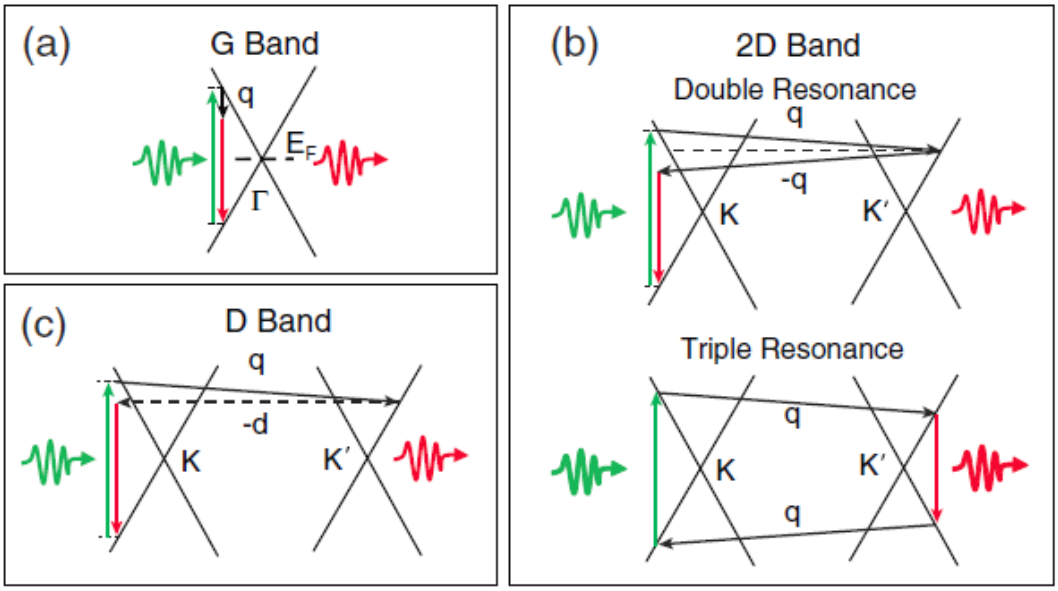

Figure 2.9: *Sketch showing the Raman scattering processes in graphene associated with the (a) G-band (b) top: 2D-band double resonance, bottom: 2D-band triple resonance (c) D-band. Green and right arrows correspond to photons of higher and lower energy respectively. Solid black arrows indicate phonons of momentum q. Elastic scattering by defects is indicated by a change of electron momentum d, dashed line. Diagram taken from [123].*

couple to it such that $q \cong 2k$. This can be seen directly using a Raman spectroscopy system with a tunable laser. The positions of the Raman peaks quoted above are for excitation by photons of energy 2.41 eV (wavelength of 514 nm).

2.5 Relevant Applications

2.5.1 Photodetection

Due to graphene's linear, gapless band structure, graphene-based photodetectors have been fabricated that can absorb a wide range of frequencies (from ultraviolet to the terahertz) [12, 96]. Further, the high charge carrier mobilities enable ultra-fast response times, which could be relevant to future optical switches [12]. Some of the different photodetection mechanisms demonstrated in graphene are reviewed below. Often, more than one mechanism is present simultaneously.

2.5.1.1 Photovoltaic Effect

A photocurrent is generated via the photovoltaic (PV) effect by separating photogenerated electron-hole pairs, which can be achieved by built-in electric fields at a p-n junction. Xia *et al.* [95] were among the first to demonstrate this in graphene, using a double-gate geometry to independently tune the charge carrier concentration in adjacent regions of a ~5 μm-long graphene channel. A

photocurrent was measured for light modulation frequencies up to 40 GHz, with no degradation. The use of mechanically exfoliated graphene ensured the charge carriers had high mobility and could travel out of the ~200 nm-wide p-n junction within ~0.36 ps, to generate a photocurrent. (Electron-hole recombination ordinarily occurs on a timescale of tens of picoseconds). They reported an internal quantum efficiency in the range 6 – 16%. As an alternative material for photovoltaic power generation, this is at best comparable to a hybrid perovskite solar cell (efficiency of 17.9% [134]), but is less than that of commercially-produced silicon PV cells (20 – 25% efficiency). It is thought that the most likely application of graphene in photovoltaics will be as a transparent electrode in place of indium antimonide, rather than as a photodetecting element [135].

2.5.1.2 Photothermoelectric Effect

The photothermoelectric (PTE), or Seebeck, effect exploits the generation of a hot carrier distribution to generate a photovoltage between differently-doped regions of graphene [136]. This is due to the difference in temperature of their electronic distributions [12]. Graphene photodetectors based on the PTE effect can therefore have a very high bandwidth [25]. Graphene-metal junctions can exhibit both PV and PTE effects [137], with the PTE effect dominating for shorter wavelengths.

2.5.1.3 Bolometric Effect

The bolometric effect is associated with a change in electrical conductivity due to heating by incident photons. Via this change, a bolometer can measure the power of electromagnetic radiation by absorbing the incident light and reading out a temperature change [12]. Bolometers are widely used for the detection of mid-infrared light [138, 139] (3 – 10 μm wavelength range), operating at temperatures of a few Kelvin [140]. However, due to the weak temperature dependence of graphene's conductivity, measuring a temperature change via transport measurements is challenging in graphene bolometers [12]. Bilayer graphene does exhibit a temperature-dependent conductivity, and has been used to detect 10.6 μm illumination at temperatures of 5 K [12]. Very recently, Gopalan *et al.* [139] experimentally investigated a room temperature bolometer based on graphene on Z-cut lithium niobate ($LiNbO_3$, cut such that crystal Z-axis was outwardly directed) for the detection of tightly-focussed 6 – 10 μm laser radiation. The illumination induced a temperature change in the $LiNbO_3$ substrate due to its near total absorption of light in this wavelength range [139, 141], which produced a variation in its polarization via the pyroelectric effect. This in turn capacitively tuned the charge carrier concentration in a graphene channel transferred to one of the Z-faces of the $LiNbO_3$, manifested as a change in source-drain current. Note that it was necessary to use Z-cut lithium niobate since, under illumination, charge accumulation only occurs on its +Z and -Z crystal faces, [142, 143]

enabling electrostatic gating of the graphene. Sassi *et al.* [138] observed similar effects in a comparable device.

2.5.2 Sensing

2.5.2.1 Chemiresistors

Graphene's electronic sensitivity to surface adsorbates [51, 52, 61] makes it a good candidate for gas detection systems. For example, Schedin *et al.* [51] and Chen *et al.* [52] have detected individual NO_2 molecules and sub-parts-per-trillion concentrations of NO_2 and NH_3 respectively on graphene flakes through measurements of their resistance. Graphene functionalisation can enable highly targeted sensors [61]. This is the process of chemically bonding species to the graphene sheet which selectively react with the desired analytes. In this way, Tang *et al.* [144] modified a graphene chemiresistor using tetrafluorohydroquinone to selectively detect formaldehyde, a common indoor pollutant, observing a 10% change in resistance for a 1.5 parts-per-million formaldehyde concentration.

2.5.2.2 Optical Gas Detection

Graphene has also been used as a thermal emitter in a mid-infrared gas detection system [24, 145, 146, 147], where gases are identified via their unique absorption spectrum. Lawton *et al.* [145] exploited graphene's low thermal mass to create

mono- and multi-layer graphene infrared sources that could be modulated at frequencies up to 100 kHz. Graphene's broadband absorption of electromagnetic radiation gives it a correspondingly broadband emission spectrum. This was reflected in their measurements, where the emission spectrum peaked at a wavelength of 4 μm, enabling the detection of a variety of important gases, including CO_2 and NO_x. Tungsten micro-bulbs operating on the Joule heating principle are the current prevalent technology in this field. These components are extremely cheap ($1 – 2) [148], but operate at high temperatures, with much of the spectral emission occurring the near-infrared (outside the desired mid-IR range). They also operate with low modulation frequencies (< 10 Hz) due to the high thermal mass of the filament, introducing greater $1/f$ noise. Graphene-based technologies could deliver genuine advantages over existing technologies in the long term.

2.6 Summary

In Section 2.2, the unusual electronic and optical properties arising from graphene's band structure were discussed. In Sections 2.3 and 2.4, the graphene production and characterisation methods currently in use in research and industrial environments were presented. Some potential applications arising from its optoelectronic response and extreme sensitivity to surface adsorbates were considered. As will be discussed in Chapter 3, graphene's 2D nature makes it a natural candidate for investigation via surface acoustic waves (SAWs).

3. Surface Acoustic Waves

3.1 Overview

The controlled use of high-frequency sound waves was first demonstrated over 100 years ago, by Paul Langevin, for the detection of submarines during the first world war [149]. Langevin exploited the piezoelectric effect in quartz to create an electrically-coupled acoustic resonator. This could launch a pulse of elastic waves into the sea and detect the fraction reflected by objects in the acoustic path, and was the world's first SONAR (SOund Navigation And Ranging) system. The powerful concept of echolocation was later extended to electromagnetic radiation to develop RADAR (RAdio Detection And Ranging). However, the far greater velocity of light than sound required the introduction of a delay line to the circuitry, [1] so that signals reflected by different objects could be clearly discriminated. The discovery of new piezoelectric materials and developments in SONAR technology enabled acoustic waves to provide the solution, continuing the dialogue between electronics and sound.

Components based on surface acoustic waves (SAWs) were not seen until the 1960s [150]. SAWs are a form of mechanical vibration guided along the

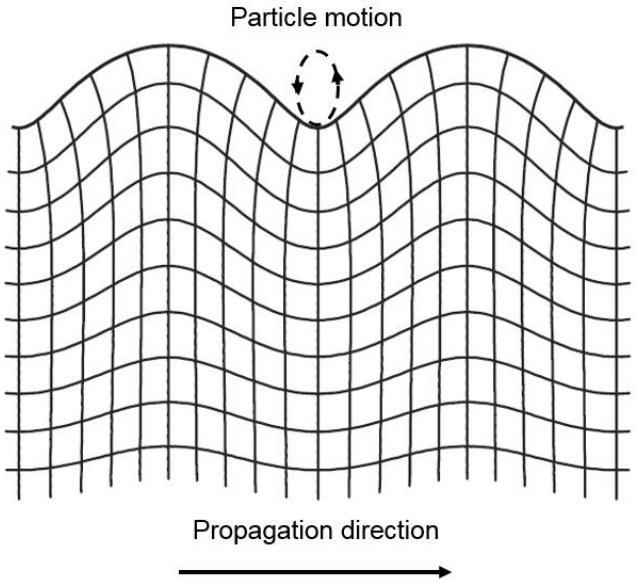

Figure 3.1: *Displacement of a rectangular grid during SAW propagation. Particles have an elliptical trajectory. Diagram modified from [1].*

surface of a material, with an amplitude that decays exponentially into the bulk [1, 151] (see Figure 3.1). This introduces the potential of accessing the wave in its propagation path, with implications for sensing technology and signal processing in a planar structure. White and Voltmer provided a means of generating and detecting SAWs in 1965 with the introduction of the interdigital transducer (IDT) [150]. This metallic, comb-like structure can be fabricated with photolithographic techniques and enabled high-frequency (MHz – GHz) SAWs to be generated cheaply and easily, ultimately leading to the development of bandpass filters, resonators, and oscillators, amongst other components [1] based on SAWs. These are found in everyday technologies including RADAR, mobile phones, and televisions, and annual SAW device output currently exceeds

3 billion devices worldwide [1]. This chapter will discuss: the fundamentals of SAW propagation (Section 3.2); SAW generation by IDTs (Section 3.3); the acoustoelectric effect and the interaction between SAWs and low-dimensional electron systems (Section 3.3); and some of the most recent applications of SAWs for the transportation of charges. A summary of the Chapter is given in Section 3.6.

3.2 Surface Acoustic Wave Propagation

In this section, wave equation for bulk wave propagation in non-piezoelectric media is determined. The piezoelectric case is then considered and the boundary conditions for surface acoustic wave propagation are applied to find the solutions to the wave equation. Lastly, some propagation effects that are important in practical devices are discussed, as well as examples of common SAW device materials. This analysis is a review of that presented by Morgan [1].

3.2.1 Non-piezoelectric Media

The elastic deformation of a solid is described in terms of the displacement of the material from its equilibrium position, the strain S, and the internal forces that act to restore it to its non-deformed state, the stress T. Consider an elemental volume of an anisotropic, homogenous, infinite material, located at a position $\mathbf{x} = (x_1, x_2, x_3)$, that is displaced by an amount $\mathbf{u} = (u_1, u_2, u_3)$. This volume is much

larger than the interatomic distance, but much smaller than $|\mathbf{u}|$. The strain S_{ij} is defined as:

$$S_{ij}(x_1, x_2, x_3) = \frac{1}{2}\left(\frac{\partial u_i}{\partial x_j} + \frac{\partial u_j}{\partial x_i}\right) \qquad i, j = 1, 2, 3 \tag{3.1}$$

where S_{ij} is as a rank-two tensor. In the case of displacement or rotation of the whole material, Equation 3.1 yields a strain of zero, since such movements do not depend on $\mathbf{x}$. The internal forces that act to restore the material to its equilibrium position are similarly described by the stress tensor T_{ij}. For small deformations, the stress and strain are directly proportional and related by the stiffness tensor c_{ijkl}, which characterises the material's physical properties:

$$T_{ij} = \sum_k \sum_l c_{ijkl} S_{kl} \qquad i, j, k, l = 1, 2, 3. \tag{3.2}$$

This is a generalisation of Hooke's law. Consider a small cube of the material with side length δ, centred at $\mathbf{x}' = (x_1', x_2', x_3')$, and surface normal $\hat{\boldsymbol{n}}_{\boldsymbol{i}}$ parallel to coordinate axis x_i $(i = 1, 2, 3)$. Under a stress described by Equation 3.2, the faces at $x_1 = x_1' \pm \delta/2$ experience a force in the x_i direction given by:

$$F_i\left(x_1' \pm \frac{\delta}{2}, x_2, x_3\right) = \pm\delta^2 T_{i1}\left(x_1' \pm \frac{\delta}{2}, x_2, x_3\right) \tag{3.3}$$

where δ^2 is the area of the face of the cube intersecting the x_1 axis. The same approach is used to calculate the forces on the faces intersecting the x_2 and x_3 axes, and the total force on the cube in the x_i direction is the sum of these:

$$F_i = \delta^3 \left(\sum_j \frac{\partial T_{ij}}{\partial x_j} \right)_{\mathbf{x}'} \tag{3.4}$$

In accordance with Newton's second law, F_i is proportional to the acceleration due to the displacement u_i. In terms of the stress T_{ij}, for a material of density ρ this can be written as:

$$\rho \left(\frac{\partial^2 u_i}{\partial t^2} \right) = \sum_j \frac{\partial T_{ij}}{\partial x_j} \qquad i = 1, 2, 3. \tag{3.5}$$

which is the equation of motion.

3.2.2 Piezoelectric Media and Surface Acoustic Waves

Piezoelectricity is the phenomenon whereby the application of a force to a material leads to the generation of a strong internal electric field that influences the material's elastic properties. This is referred to as the 'direct' piezoelectric effect, and is only seen in anisotropic materials. In a reciprocal manner, the application of an electric field will induce strain in a piezoelectric material. The above discussion can be extended to incorporate this.

Now consider a homogeneous piezoelectric insulator. In addition to the strain components S_{ij}, the stress T_{ij} depends on the applied electric field $\mathbf{E}$ and can be written as:

$$T_{ij} = \sum_k \sum_l c^E_{ijkl} S_{kl} - \sum_k e_{kij} E_k \qquad i, j, k, l = 1, 2, 3. \tag{3.6}$$

where the superscript E indicates the stiffness tensor for a constant electric field. Similarly, the displacement vector $\mathbf{D}$ is affected by the strain of the material:

$$D_i = \sum_j \mathcal{E}_{ij}^S E_j + \sum_j \sum_k e_{ijk} S_{jk} \qquad i,j,k = 1,2,3. \tag{3.7}$$

where $\mathcal{E}_{ij}^S$ is the permittivity tensor for constant strain and e_{ijk} is the piezoelectric tensor. The derivation of these relations is beyond the scope of this work and a complete analysis is provided by Royer and Dieulesaint [149].

The electric field can be expressed in terms of the electric potential Φ via $E_i = -\partial\Phi/\partial x_i$. With Equation 3.1 for the strain, the equation of motion becomes:

$$\rho \frac{\partial^2 u_i}{\partial t^2} = \sum_j \sum_k \left\{ e_{ijk} \frac{\partial^2 \Phi}{\partial x_j \partial x_k} + \sum_l c_{ijkl}^E \frac{\partial^2 u_k}{\partial x_j \partial x_l} \right\} \tag{3.8}$$

Since the material is an insulator the enclosed charge is zero, reducing Equation 3.7 to:

$$\sum_i \sum_j \left\{ \mathcal{E}_{ij}^S \frac{\partial^2 \Phi}{\partial x_i \partial x_j} - \sum_k e_{ijk} \frac{\partial^2 u_j}{\partial x_i \partial x_j} \right\} = 0 \tag{3.9}$$

In an infinite medium, the displacements $\mathbf{u}$ and the potential Φ have the form of plane waves:

$$\mathbf{u} = \mathbf{u}_0 \exp[j(\omega t - \mathbf{k} \cdot \mathbf{x})] \tag{3.10}$$

$$\Phi = \Phi_0 \exp[j(\omega t - \mathbf{k} \cdot \mathbf{x})] \tag{3.11}$$

where the wave frequency is ω, the wave vector defining the wave propagation direction is $\mathbf{k} = (k_1, k_2, k_3)$, and $\mathbf{u}_0$ and Φ_0 are constants. Upon substitution into Equations 3.8 and 3.9, four equations in the four variables u_1, u_2, u_3, and Φ are obtained. Four solutions with different values of $\mathbf{k}$ are found by setting the determinant of coefficients to zero. One of these corresponds to the electrostatic solution for an isotropic medium, and the other three are non-dispersive acoustic waves.

To obtain the solutions for surface acoustic waves, define a piezoelectric half-space as shown in Figure 3.2. By convention, the x_3 direction is specified as parallel to the outwardly-directed surface normal, and the wave propagation direction is x_1. The material has infinite extent in the x_1 and x_2 directions. For $x_3 > 0$ the space is vacuum, and the region $x_3 < 0$ is occupied by the material. The (x_1, x_3) plane defined by the surface normal and the propagation direction is known as the sagittal plane, and the wavefronts are parallel to the x_2 axis. It is necessary to impose the boundary condition that there is no net force acting on the surface, such that:

$$T_{13} = T_{23} = T_{33} = 0 \tag{3.12}$$

at $x_3 = 0$.

Due to the material's piezoelectricity, it is necessary to account for the continuity of electric fields. The two scenarios usually considered are the free-surface case, where the region above the material is purely vacuum, and the

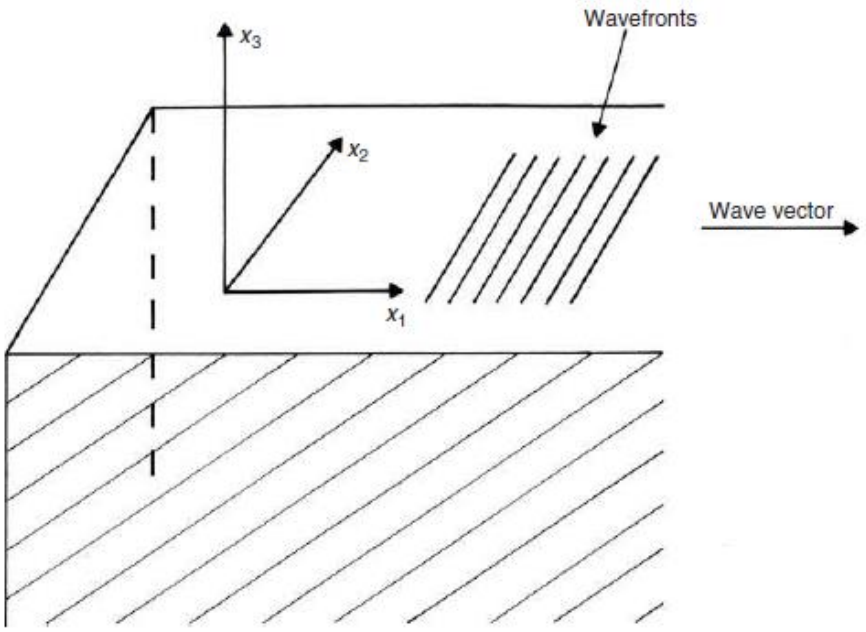

Figure 3.2: *A schematic showing the axes for the piezoelectric half-space. The wavefronts, propagation direction, piezoelectric medium, and free space are shown. Diagram reproduced from [1].*

metallised case, where a thin, infinitely conductive metal film is deposited on the material. The weight of the film is negligible to preserve the condition of Equation 3.12. As will be shown in Section 3.3, the metallised case is particularly important for surface acoustic wave generation. For a free-surface, there will be an electric potential in the vacuum that satisfies Laplace's equation $\nabla^2\Phi = 0$. If the wavenumber is β, Φ may be written as:

$$\Phi = f(x_3)\exp[j(\omega t - \beta x_1)] \tag{3.13}$$

By inserting Equation 3.13 into Laplace's equation, and imposing that Φ vanishes at $x_3 = \infty$, the potential in the vacuum ($x_3 \geq 0$) is given by:

$$\Phi = \Phi_0 \exp(-|\beta| x_3) \exp[j(\omega t - \beta x_1)] \tag{3.14}$$

where Φ_0 is a constant. As there are no free charges D_3 must be continuous at the interface between the vacuum and the medium. Thus, for $x_3 = 0$:

$$D_3 = \varepsilon_0 |\beta| \Phi \tag{3.15}$$

In the metallised case, the stipulation is that $\Phi = 0$ at $x_3 = 0$ since the charges in the metal will screen the electric field.

Surface wave solutions are found by considering partial waves that satisfy the equations of motion in an infinite medium (Equations 3.8 and 3.9), the conditions of either the free surface or the metallised surface, and Equation 3.12. The displacements $\mathbf{u}'$ and potential Φ' of the partial waves take the form:

$$\mathbf{u}' = \mathbf{u}'_0 \exp(j\gamma x_3) \exp[j(\omega t - \beta x_1)] \tag{3.16}$$

$$\Phi' = \Phi'_0 \exp(j\gamma x_3) \exp[j(\omega t - \beta x_1)] \tag{3.17}$$

where β is assumed to be real, and $\gamma = f(V_l, V_t)$ is the x_3 component of the wave vector, where V_l and V_t are the velocities of the longitudinal wave and the transverse wave in the medium respectively. Substituting these expressions for $\mathbf{u}'$and Φ' into Equations 3.8 and 3.9 and solving them numerically, eight values for γ are obtained. The valid solutions are those for which the imaginary component of γ is negative, since $\mathbf{u}' = 0$ and $\Phi' = 0$ when $x_3 = -\infty$. Only four

values for γ meet these criteria, and the corresponding partial waves are written as:

$$\mathbf{u}'_m = \mathbf{u}'_{0m} \exp(j\gamma_m x_3) \exp[j(\omega t - \beta x_1)] \tag{3.18}$$

$$\Phi'_m = \Phi'_{0m} \exp(j\gamma_m x_3) \exp[j(\omega t - \beta x_1)] \tag{3.19}$$

where $m = 1, 2, 3, 4$. It is assumed that, in a half-space, the solution is a linear sum of these, giving:

$$\mathbf{u} = \sum_{m=1}^{4} A_m \mathbf{u}'_m \tag{3.20}$$

$$\Phi = \sum_{m=1}^{4} A_m \Phi'_m \tag{3.21}$$

where the coefficients A_m are such that the boundary conditions are satisfied. Solutions are only valid for values of β that give a determinant of coefficients equal to zero, after substitution of Equations 3.20 and 3.21 into the wave equation. The equations are solved iteratively, changing β until this condition is met. The stiffness, permittivity, piezoelectric characteristics, and orientation of the material strongly influence the values of $\mathbf{u}$ and Φ. The solution most commonly encountered is that for which the displacement $\mathbf{u}$ is in the sagittal plane, corresponding to an elliptical particle motion. This is piezoelectric Rayleigh SAW and the type generated in the measurements presented in Chapters 5 – 7. Henceforth, when using the term ‘surface acoustic wave’ or SAW, it is this type of wave that is being referred to.

An example solution is shown in Figure 3.3 for Y-Z lithium niobate, for SAWs propagating on free and metallised surfaces. The nomenclature 'Y-Z' refers to the crystal Y axis being outwardly directed (parallel to x_3) with SAWs propagating parallel to the crystal Z axis (the x_1 direction). The displacements u_1 and u_3 are very similar in the free-surface and metallised cases (Figure 3.3(a)), and there is a large difference in the electric potential between the free- and metallised-

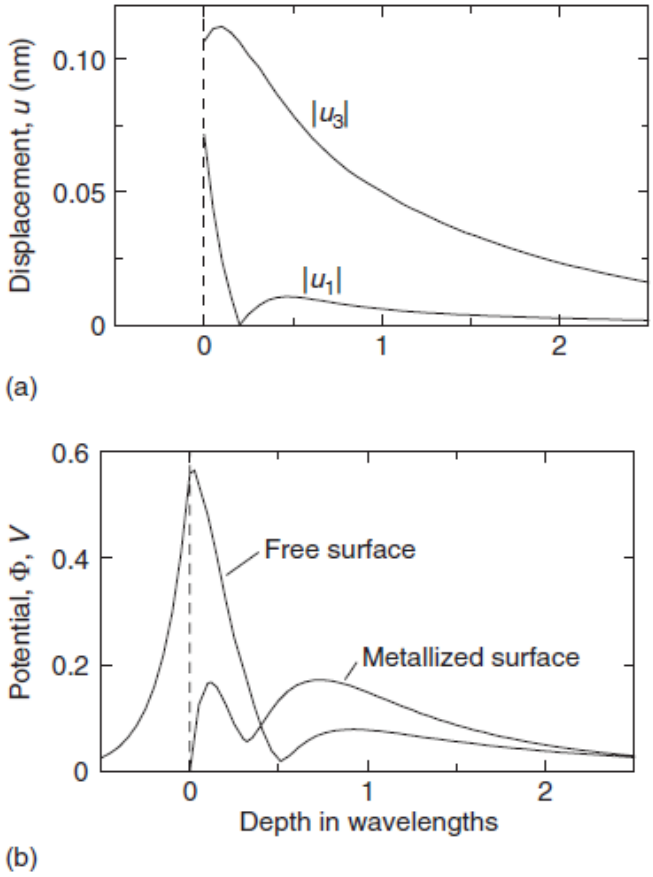

Figure 3.3: *(a) SAW displacement in the x_1 and x_3 directions, and (b) electric potential on the free- and metallised surfaces, as a function of depth into a sample of Y-Z lithium niobate. Figure reproduced from [1].*

surface due to the screening of the electric field by the electrons in the metal (Figure 3.3(b)). The electric potential recovers at a depth of approximately one acoustic wavelength into the bulk.

3.3 SAW Generation

Several methods have been established for SAW generation, including high intensity laser pulses that exploit a material's thermoelastic properties to induce periodic expansion of the crystal [152, 153, 154, 155] and shear wave transducers mechanically coupled to the surface [150]. In electronic applications, interdigital transducers (IDTs) are routinely used as they make it possible to compactly generate and receive SAWs on piezoelectric materials directly [150]. This approach was used for SAW generation and detection in the measurements in this thesis, and here the basic IDT operating principles are discussed. This is followed by some practical considerations that are taken when selecting a piezoelectric substrate for SAW device applications. For more details, please see Morgan [1].

3.3.1 Interdigital Transducers

Devised by White and Voltmer in 1965 [150], IDTs consist of two metal interlocking, comb-like structures (Figure 3.4) defined using photolithography on the surface of the material in which the SAW will propagate. The application of

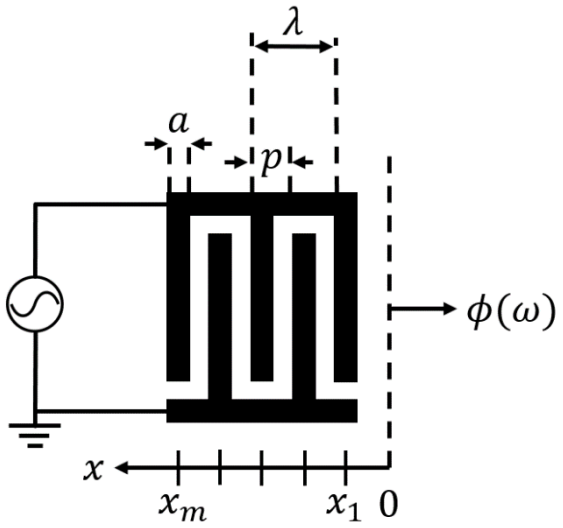

Figure 3.4: *Schematic of a basic IDT. It has m electrodes of width a, on a pitch p, and metallisation ratio of 50%. The distance between alternate electrodes gives the wavelength of the fundamental frequency.*

an AC voltage sets up a periodic electric field, and a corresponding elastic stress is induced in the substrate due to its piezoelectricity. As the field oscillates, vibrations radiate away from the IDT in the direction perpendicular to the long-axis of the electrodes. SAWs are generated strongly at frequencies for which the wavelength of the applied AC voltage matches the periodicity of the IDT. Note that the AC frequency is much higher than the resonant frequency of the crystal due to its dimensions. For a SAW velocity v_{SAW} and a separation distance between alternate electrodes λ, the fundamental SAW frequency f_0 is:

$$f_0 = v_{\mathrm{SAW}}/\lambda \tag{3.22}$$

Higher harmonics may also be generated. By a reciprocal process an IDT can convert a SAW into an electrical signal. A pair of opposing IDTs form an acoustic delay line in which one IDT can be used for SAW generation and the other for SAW detection. Depending on the application, the length of the IDT digits may be as large as a few millimetres, and may include in the range of 20 – 1000 electrodes. The operating frequency is limited only by the fabrication technology; for a typical SAW velocity of ~3000 m/s an electrode width of 0.5 μm, the smallest available in commercial production, a frequency of 1.5 GHz is obtained [1].

We will now determine the IDT frequency response around its fundamental frequency. We assume that there are no SAW reflections from individual electrodes, and that there is no diffraction or loss in propagation. The digit width and pitch are a and p respectively, the metallisation ratio is 50% ($a/p = 1/2$), and there are m digits centred at $x = x_1, x_2, \ldots x_m$. The $x = 0$ position is just outside the IDT. Upon application of a voltage to the IDT, a SAW is launched in both the $+x$ and $-x$ direction, with frequency ω and phase velocity v_{SAW}. We are interested only in SAWs propagating towards the $-x$ direction, where a receiving IDT may be located. Each electrode on the 'live' busbar (connected to the voltage source) acts as a SAW source; those connected to the grounded busbar do not. The amplitude of the SAW generated by the m^{th} digit has the form $\exp[j(k(x - x_m) - \omega t)]$ where k is the wavenumber. We define a digit polarity $\hat{P}_m$ for electrode m, where $\hat{P}_m = 1$ for the live electrodes and $\hat{P}_m = 0$ for the grounded

electrodes. The amplitude of the wave generated by the m^{th} electrode is given by:

$$\phi_m(x,\omega) = VE(\omega)\hat{P}_m \exp[jk(x - x_m)]\exp(j\omega t) \tag{3.23}$$

where V is the applied voltage, and $E(\omega)$ is the element factor representing the response of individual electrodes. The total amplitude at $x = 0$, $\phi(\omega)$, is the sum of the contributions from each electrode:

$$\phi(\omega) = VE(\omega)\exp(j\omega t)\sum_{m=1}^{M} \hat{P}_m \exp(-jkx_m) \tag{3.24}$$

For 'single-digit' and 'double-digit' IDTs, two common types, the polarity sequence is $\hat{P}_m = 0, 1, 0, 1, \ldots$ and $\hat{P}_m = 0, 0, 1, 1, 0, 0, 1, 1, \ldots$ respectively. It is convenient to write the frequency response of the IDT as an array factor $A(\omega)$ that excludes the applied voltage and the element factor. This is defined as:

$$A(\omega) = \sum_{m=1}^{M} \hat{P}_m \exp(-jkx_m) \tag{3.25}$$

For a single-digit IDT, the digit centres are located at $x_m = mp$. We can rewrite Equation 3.25 as a sum of N_p terms with spacing $\Delta x = 2p$, where $N_p = M/2$ is the number of periods and we assume M is even:

$$A(\omega) = \sum_{n=1}^{N_p} \exp(-2jkp) \tag{3.26}$$

Treating the summation as a geometric progression, we obtain:

$$A(\omega) = \frac{\sin(N_p kp)}{\sin(kp)} \exp\left[-j\left(N_p + 1\right)kp\right] \tag{3.27}$$

where Equation 3.27 gives multiple peaks for $kp = n\pi$. Alternatively, this may be written as $2p = n\lambda$, giving the IDT frequency response at the fundamental frequency f_0 for $n = 1$ and $\lambda = 2p$, and the higher harmonics for $n > 1$. The array factor close to f_0 is plotted in Figure 3.5 in arbitrary units. A similar response is seen for double-digit IDTs.

The frequency response of an IDT can be tuned by varying the overlapping length of the active electrodes (apodization). When a SAW pulse propagates beneath the electrode, the strength of the electrical signal generated in it is proportional to the overlap of the electrodes at the location of the pulse. If the IDT aperture is W and the m^{th} electrode extends from the active busbar by an amount u_m, Equation 3.25 can be rewritten as:

$$A(\omega) = \sum_{m=1}^{M} (u_m/W) \exp(-jkx_m) \tag{3.28}$$

where $\hat{P}_m$ has been replaced by the term (u_m/W). Note that if $u_m = 0$ or W, then $(u_m/W) = 0$ or 1 respectively and the original expression for the array factor is

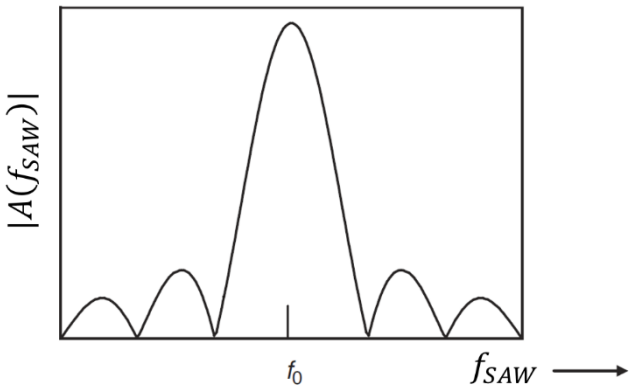

Figure 3.5: *Array factor of a uniform, single-digit IDT close to the fundamental frequency. Diagram adapted from [1].*

recovered. IDT apodization has allowed SAW devices to be developed as band pass filters for communication technologies [1].

3.3.2 Single-Digit and Double-Digit IDTs

Consider a simple SAW device consisting of two opposing single-digit IDTs, where one is used for SAW generation and the other for SAW detection. One of the practical problems of such a device is the presence of unwanted SAW reflections from the two transducers that cause ripples in the amplitude and phase of the output signal. The term ‘triple transit signal’ is used to describe a SAW that traverses the delay line three times, shown schematically in Figure 3.6. This effect can be reduced by lowering the applied input voltage, but this can lead to poor signal-to-noise ratios in the output signal. A more common approach is to use double-digit IDTs, where neighbouring digits are connected to the bus bars in pairs. Single- and double-digit IDTs are compared schematically in Figure 3.7 (a)

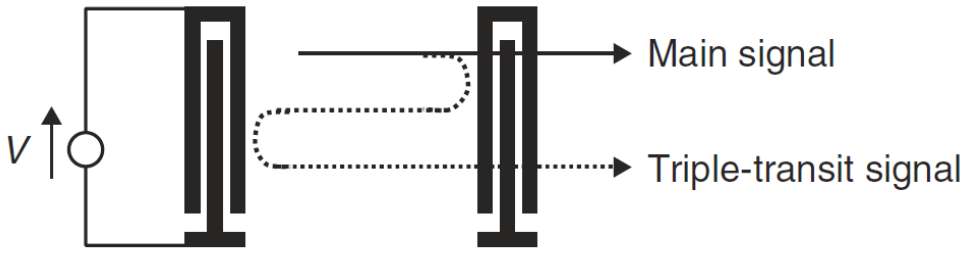

Figure 3.6: *Schematic showing the origin of a triple-transit signal in a two-port SAW device consisting of single-digit IDTs. Diagram from [1].*

and (b) respectively. Neighbouring digits on the single-digit IDT are separated by a distance $p = \lambda_0/2$. Reflections therefore add in-phase with each other at this SAW frequency, subsequently leading to triple-transit signals as the reflected SAW traverses the delay line. In the case of the double-digit IDT, neighbouring digits are separated by a distance of $p = \lambda_0/4$. Reflected SAWs from adjacent electrodes therefore have a phase difference of 180°, causing them to destructively interfere. Whilst this reduces the operating frequency of the device (since the digit width and spacing is ultimately limited by the resolution of the fabrication system), the elimination of SAW reflections is a worthwhile trade-off

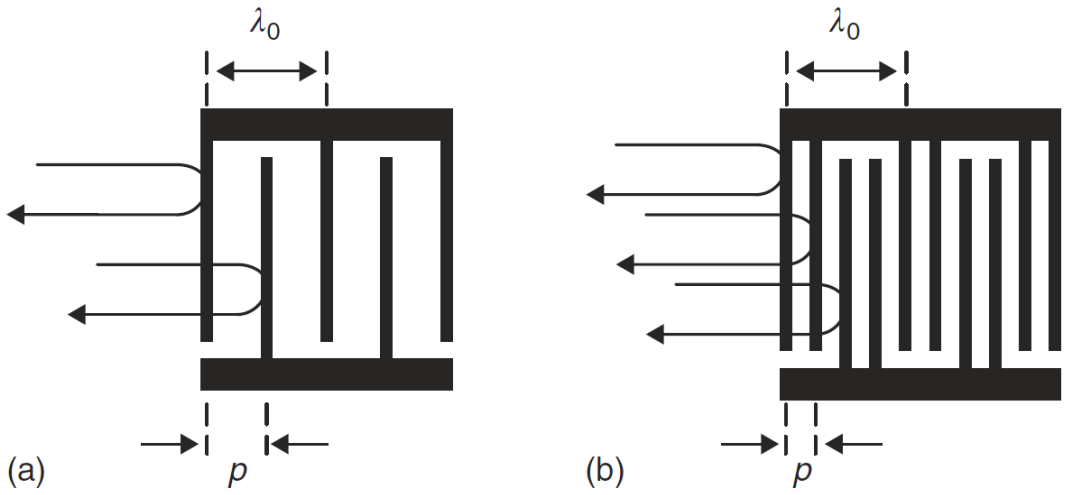

Figure 3.7: *(a) Single- and (b) double- digit IDTs and the SAW reflections from IDT digits. Due to the half-wavelength spacing of neighbouring digits in the single-digit IDT, SAW reflections add in phase and cause distortion of the output signal of a SAW device. The use of quarter-wavelength-spaced digits (the double-digit IDT) ensure reflection add destructively, preventing unwanted triple-transit signals. Diagram from [1].*

for many SAW device applications. The devices used for the measurements presented in this thesis use double-digit IDTs for this reason.

3.3.3 Temperature Effects and Piezoelectric Coupling Coefficient

SAW devices may be required to operate across a broad temperature range whilst retaining precise performance specifications. Temperature effects can be characterised by considering two opposing IDTs separated by a distance l. For a SAW velocity on an unmetallized surface v_f, the SAW transit time is $T = l/v_f$. If the temperature variation of the material constants is known, the resulting variation in v_f can be calculated via the approach in Section 3.2.2. Further, due to the thermal expansion of the material, l also varies with temperature. A 'temperature coefficient of delay' (TCD) α_T is defined:

$$\alpha_T \equiv \frac{1}{T}\frac{\mathrm{d}T}{\mathrm{d}\Theta} = \frac{1}{l}\frac{\mathrm{d}l}{\mathrm{d}\Theta} - \frac{1}{v_f}\frac{\mathrm{d}v_f}{\mathrm{d}\Theta} \tag{3.29}$$

For temperature-sensitive applications, it is preferable to minimise the TCD. ST-X quartz is a common choice since $\alpha_T = 0$ (°C)$^{-1}$ at room temperature, whereas for Y-Z $LiNbO_3$ $\alpha_T = 94 \times 10^{-6}$ (°C)$^{-1}$.

An additional consideration is the difference in the SAW velocity on a metallized and free surface (v_m and v_f respectively). A large difference between v_m and v_m is indicative of strong piezoelectric coupling [1]. The fractional

difference between v_f and v_m is quantified via a piezoelectric coupling coefficient K^2, given by Equation 3.30:

$$\frac{\Delta v}{v} \equiv \frac{(v_f - v_m)}{v_f} = \frac{K^2}{2} \tag{3.30}$$

Where a good signal-to-noise ratio is required, a material with large K^2 is often selected. Examples include Y-Z $LiNbO_3$, 128° Y-X $LiNbO_3$, and 36° Y-X $LiTaO_3$, for which K^2 is 4.8%, 5.6%, 4.8% respectively. For ST-X quartz, $K^2 = 0.12\%$ [1].

The origin of the difference in velocity between a free and metallized surface is explained as follows. If a force F is applied to a piezoelectric medium with an infinitely-conductive, thin, metal film on the surface, the free charge in the metal will short-out the piezoelectric fields generated when SAWs propagate. This effectively removes its piezoelectricity, and the strain in the medium is given by Equation 3.2. However, if F is applied to the medium in the absence of a metallic film, a fraction of the energy input induces a propagating electric potential as well as a mechanical wave. The strain is then given by Equation 3.6. Consequently, the magnitude of the strain is lower for a given force, and the spring constant of the medium appears higher. This is known as piezoelectric stiffening, and leads to $v_f > v_m$.

3.4 SAW Interactions with Electronic Systems

3.4.1 The Acoustoelectric Effect

The effects on the conduction electrons of a crystal due to the presence of a travelling acoustic wave were first discussed by Parmenter in 1953 [2]. A sinusoidal compressional wave traversing the material will generate a sinusoidal electric field that moves through the crystal at the acoustic velocity. He asserted that conduction electrons with a drift velocity component parallel to that of the SAW propagation direction and of similar magnitude to the SAW velocity become trapped in the potential minima of the electric field. The term ‘acoustoelectric current’ was coined to describe the resultant dragging of charge carriers by the wave. Parmenter initially proposed that an acoustoelectric current (or voltage in an open-circuit configuration) would be measurable in metals and *n*-type semiconductors. However, numerical estimates by van den Beukel [156] suggested that the magnitude of the acoustoelectric field in a metal would be 10^3 – 10^4 times smaller than that generated in a semiconductor at room temperature, due to the thermal vibrations of the crystal lattice. The treatments by Parmenter and van den Beukel were later found to be insufficient [157], as they assumed an extremely low charge carrier density (ignoring charge bunching effects) and a mean free path much longer than the acoustic wavelength. However, both contributions were important to the development of the field.

Weinreich was the first to successfully describe the (bulk) acoustoelectric effect in semiconductors, using a purely classical approach [157, 158]. He

proposed that momentum transfer from the acoustic wave to the charge carriers induces charge dragging, leading to a proportional loss of wave energy. The wave provides a spatially varying electric potential, and the charges will tend towards an equilibrium distribution that favours the positions of lowest energy. As the wave is constantly moving, and the particles require a finite time to reach equilibrium, the charges 'lag behind' the wave by a small amount. This is characterised by a relaxation time τ of the distribution. Weinreich showed that for an acoustic wave of frequency ω, as $\omega\tau \rightarrow 0$ and $\omega\tau \rightarrow \infty$ the force on the charge carriers tends to zero. For intermediate cases, due to the lag of the electrons, they are in higher concentration on the forward slope of the potential than on the backward slope, leading to a net average force in the direction of wave propagation [157]. A summary of his analysis [158] is presented below, to better understand the origin of the acoustoelectric effect.

It is assumed that, in general, the acoustic wavelength is much longer than the mean free path of the charge carriers, and the acoustoelectric current j generated by the wave-particle interaction can be described in a macroscopic way as the sum of a diffusion term and a drift term:

$$j = D(F/KT - \nabla)n \tag{3.31}$$

In Equation 3.31 D is the diffusion coefficient, F is the net force exerted on the charge carriers, KT is the thermal energy, ∇ is the Del operator, and n is the particle density. The force F is related to the potential energy of the particles U

by $F = -\partial U/\partial x$ (in the x-direction). Weinreich used the concept of a deformation potential to describe the potential energy of the charged particles due to an acoustic deformation, V, given by:

$$V = -\varepsilon\Delta \tag{3.32}$$

where ε is a constant and Δ is the dilatation of the crystal. There is also the potential energy due to the electric fields resulting from the redistribution of charge to consider. To simplify the difficulty of accounting for this, Weinreich assumes that charge neutrality is always maintained and that the induced electrostatic potential is proportional to the acoustic deformation potential for small sinusoidal disturbances. It can then be shown that U is given by:

$$U = -\sum_i q_i \phi_i \tag{3.33}$$

where q_i is referred to as the acoustic charge, and ϕ_i is the value of the potential of the plane compressional wave ϕ in the semiconducting medium at the position of the i^{th} particle, where ϕ has the form:

$$\phi = \phi_0 \exp(ik(x - ct)) \tag{3.34}$$

where ϕ_0 is a constant, k is the wave vector, and c is the velocity of the acoustic wave moving in the x-direction. If a longitudinal electric field is applied to give the charge carriers a drift velocity βc in the x-direction, the electron and hole acoustoelectric current densities, j_n and j_p respectively, are given by:

$$j_n = n\beta c + \left(\frac{nD_n}{KT}\right)\frac{\partial}{\partial x}(q_n\phi + e\gamma_k\phi) - D_n\frac{\partial n}{\partial x} \tag{3.35}$$

$$j_p = -\frac{p\beta c}{b} + \left(\frac{pD_n}{bKT}\right)\frac{\partial}{\partial x}\left(q_p - e\gamma_k\phi\right) - \frac{D_n}{b}\frac{\partial p}{\partial x} \tag{3.36}$$

where b is the ratio of the electron and hole mobilities, q_n and q_p are the electron and hole acoustic charges respectively, e is the charge on an electron, and $\gamma_k\phi$ is the induced electrostatic potential. The continuity equation takes the form:

$$\frac{\partial n}{\partial t} + \frac{\partial j_n}{\partial x} + \frac{1}{\tau}\left[n - n_0\left(1 + \frac{q}{1+s}\frac{\phi}{KT}\right)\right] = 0 \tag{3.37}$$

$$\frac{\partial p}{\partial t} + \frac{\partial j_p}{\partial x} + \frac{1}{\tau}\left[p - p_0\left(1 + \frac{qs}{1+s}\frac{\phi}{KT}\right)\right] = 0 \tag{3.38}$$

where $s \equiv n_0/p_0$ is the ratio of equilibrium concentrations of electrons and holes, $q \equiv q_n + q_p$, and τ is the lifetime. The last term in Equations 3.37 and 3.38 accounts for the first order change in equilibrium concentrations due to the potential ϕ. Assuming $n - n_0 \ll n_0$ and $p - p_0 \ll p_0$ and let:

$$n = n_0 + n_1\exp(ik(x - ct)) \tag{3.39}$$

$$p = p_0 + p_1\exp(ik(x - ct)) \tag{3.40}$$

By substitution of Equations 3.39 and 3.40 into Equations 3.37 and 3.38 respectively, and invoking charge neutrality ($n_1 = p_1$), we obtain:

$$n_1 = p_1 = \frac{n_0}{1+s}\frac{q\phi_0}{KT}M \tag{3.41}$$

where:

$$M \equiv \frac{1+\omega_0(1+sb)/\omega^2\tau(1+s)}{1+\omega_0(1+sb)\,/\,\omega^2\tau(1+s)-i(\beta_0-\beta)(1-s)\omega_0\,/(1+s)\omega}$$

$$\omega \equiv kc$$

$$\omega_0 \equiv c^2/D_n$$

$$\beta_0 = (1+sb)/(1-s)$$

The dependence of the charge carrier bunching on frequency, applied field, and material properties are accounted for by the factor M. Equation 3.41 can be substituted into Equations 3.39 and 3.40, which in turn can be substituted into Equations 3.35 and 3.36, from which the time-average DC particle currents $\bar{j}_n$ and $\bar{j}_p$ can be obtained. The net acoustoelectric current I_{ae} is given by:

$$I_{\mathrm{ae}} = -e(\bar{j}_n - \bar{j}_p) \tag{3.41}$$

Equation 3.41 only account for charge carrier recombination effects to first-order (via the term in square brackets in Equations 3.37 and 3.38). However, Weinreich argued that for large τ, the whole recombination term is negligible. The final acoustoelectric current is then given by:

$$I_{\mathrm{ae}} = -\frac{1}{2}\frac{en_0c}{(1+s)^2}\left(\frac{q\phi_0}{KT}\right)^2 \frac{(1-s)-\beta(1+s/b)}{1+(\beta_0-\beta)^2[(1-s)/(1+s)]^2(\omega_0/\omega)^2} \tag{3.42}$$

Weinreich and White subsequently observed an acoustoelectric field of 10 μV / cm in a sample of *n*-type germanium [159], in agreement with Weinreich's original work [158].

Acoustoelectric theory was further developed by Hutson and White [160] and Ingebrigsten [161, 162] who considered the influence of the acoustoelectric effect on the acoustic wave properties in piezoelectric semiconductors. The force on the charge carriers leads to a loss of acoustic wave momentum, and a corresponding decrease in wave velocity. Applying a classical relaxation model to the system, in which diffusion effects are neglected and the SAW amplitude is small, the acoustic attenuation per unit length Γ and the velocity shift Δv are given by:

$$\Gamma = \frac{K^2\pi}{\lambda}\frac{(\omega_c/\omega)}{1+(\omega_c/\omega)^2} \tag{3.43}$$

and

$$\frac{\Delta v}{v_0} = \frac{K^2}{2}\frac{1}{1+(\omega_c/\omega)^2} \tag{3.44}$$

where $\omega = kv_0)$ is the acoustic wave frequency, k is the wave vector, v_0 is the wave velocity on a free surface, λ is the wavelength, K^2 is the piezoelectric coupling coefficient, and ω_c is the conductivity relaxation frequency, itself given by $\omega_c = \sigma/\epsilon$, where σ is the conductivity and ϵ is the relative permittivity of the material. This describes the time in which the charge carriers return to their

equilibrium state after perturbation by an electric field. If the acoustic wave frequency is much smaller than the conductivity relaxation frequency ($\omega \ll \omega_c$), the charge carriers will be able to redistribute rapidly enough to screen the piezoelectric field and no charge dragging is observed. As ω increases, the screening becomes less perfect, and for $\omega \gg \omega_c$ the piezoelectric field becomes too dominant and the material effectively behaves as an insulator. Maximum attenuation occurs for $\omega = \omega_c$. In the case of surface acoustic wave propagation, the expression for the conductivity relaxation frequency is given by [4] $\omega_c = \sigma/(\epsilon_1 + \epsilon_2)$, where ϵ_1 and ϵ_2 are the relative permittivity of the piezoelectric substrate and the half-space above it respectively. Please note that the derivation of Equations 3.43 and 3.44 is beyond the scope of this thesis.

3.4.2 SAW Interactions with Low-Dimensional Electron Systems

Acoustoelectric currents may also be generated in two-dimensional electron systems (2DESs) placed directly on top of a piezoelectric material in which SAWs are propagating. Here it is assumed that the thickness of the 2DES d is much smaller than the SAW wavelength λ_{SAW}. Esslinger *et al.* [163] and Fal'ko *et al.* [164] developed an expression for the resulting acoustoelectric current density in the 2DES, which is simply stated:

$$j_{\mathrm{ae}} = \sigma^{\mathrm{2D}} E - \Lambda Q \tag{3.45}$$

where σ^{2D} is the sheet conductivity, E is the applied electric field, Λ is the acoustoelectric tensor, and Q is called the phonon pressure. Q represents the force on the charge carriers due to momentum transfer from the SAW, given by:

$$Q = \frac{I\Gamma}{v} \tag{3.46}$$

where I is the SAW intensity, v is the SAW velocity, and Γ is the attenuation of the SAW per unit length (referred to as the attenuation coefficient). In the absence of an applied electric field, and in a closed-circuit configuration such that no acoustoelectric voltage can build up, we have:

$$j_{ae} = -\Lambda\frac{I\Gamma}{v} \tag{3.47}$$

In the absence of a magnetic field, the acoustoelectric tensor reduces to the charge carrier mobility μ [165], giving:

$$j_{ae} = -\frac{\mu I\Gamma}{v} \tag{3.48}$$

This is an important result, which we will refer to again in discussion of the measurements in Chapters 5 – 7, and is known as the Weinreich relation.

The expressions for the attenuation coefficient and velocity shift for bulk semiconductors given by Equations 3.43 and 3.44 respectively can also be applied to low-dimensional electron systems placed on top of the medium and probed by SAWs. However, in this case the conductivity relaxation frequency exhibits a dependence on the saw wave vector $k = 2\pi/\lambda_{SAW}$ [4]:

$$\omega_c = \frac{k\sigma^{2\mathrm{D}}}{(\epsilon_1+\epsilon_2)} \tag{3.51}$$

It is convenient to express the ratio ω_c/ω in terms of the frequency-independent ratio $\sigma^{2\mathrm{D}}/\sigma_{\mathrm{M}}$, where $\sigma_{\mathrm{M}} = v_0(\epsilon_1 + \epsilon_2)$ is the characteristic conductivity of the substrate, and write Γ and Δv for the 2D case as:

$$\Gamma = \frac{K_{\mathrm{eff}}^2\pi}{\lambda}\frac{(\sigma^{2\mathrm{D}}/\sigma_{\mathrm{M}})}{1+\left(\sigma^{2\mathrm{D}}/\sigma_{\mathrm{M}}\right)^2} \tag{3.52}$$

and

$$\frac{\Delta v}{v_0} = \frac{K_{\mathrm{eff}}^2}{2}\frac{1}{1+\left(\sigma^{2\mathrm{D}}/\sigma_{\mathrm{M}}\right)^2} \tag{3.53}$$

respectively. The (bulk) piezoelectric coupling coefficient has been replaced by an effective piezoelectric coupling coefficient K_{eff}^2 due to the boundary conditions at the surface of the crystal. The attenuation coefficient per unit wave vector Γ/k and fractional change in SAW velocity $\Delta v/v_0$ are plotted as a function of $\sigma^{2\mathrm{D}}/\sigma_{\mathrm{M}}$ in Figure 3.8.

The conductivity dependence of Γ and v has led to the deployment of SAWs as a sensitive probe of the electronic properties of a variety of low-dimensional electron systems. Early experiments by Wixforth *et al.* [3, 4] showed how the Shubnikov-de Haas oscillations in conductivity of a 2DES placed in a strong magnetic field were reflected in measurements of SAW intensity and velocity.

This is shown in Figure 3.9. Nash *et al.* have similarly used SAWs to study the electronic properties of quantum dots and wires [5, 7, 54].

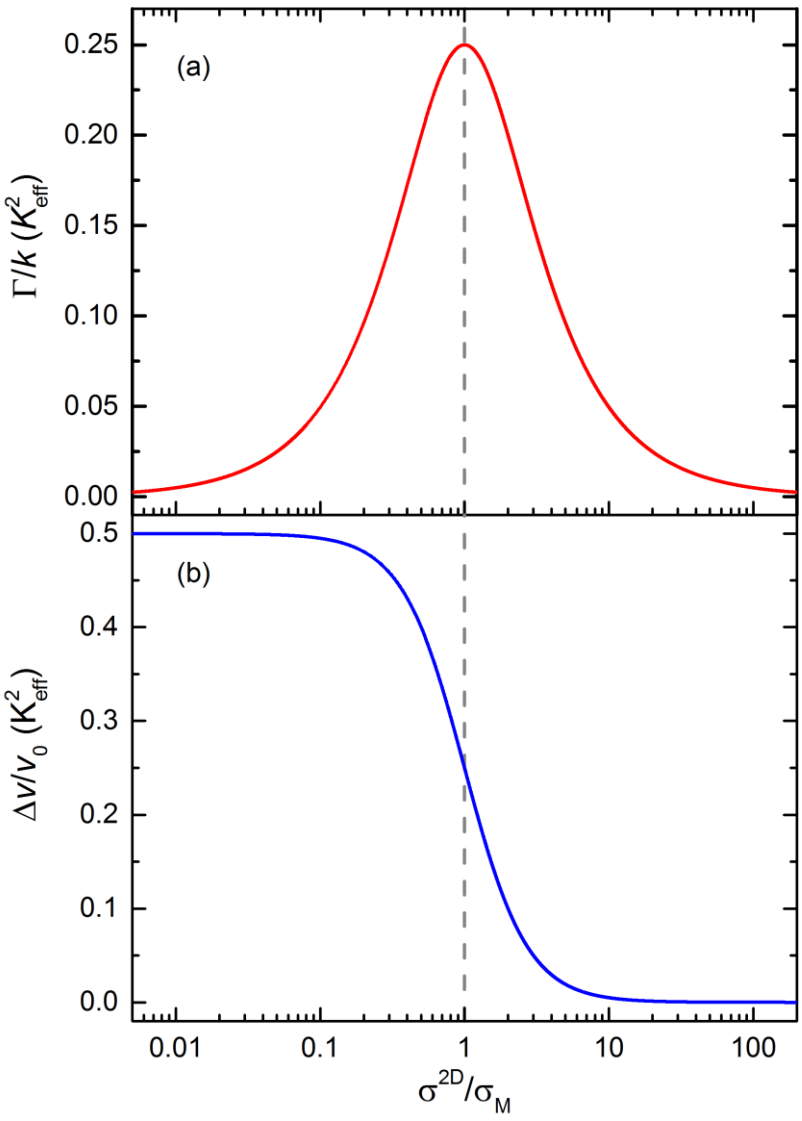

Figure 3.8: *(a) Attenuation coefficient Γ per unit wave vector k and (b) change in acoustic wave velocity $\Delta v/v_0$ in units of K_{eff}^2 as a function of σ^{2D}/σ_M.*

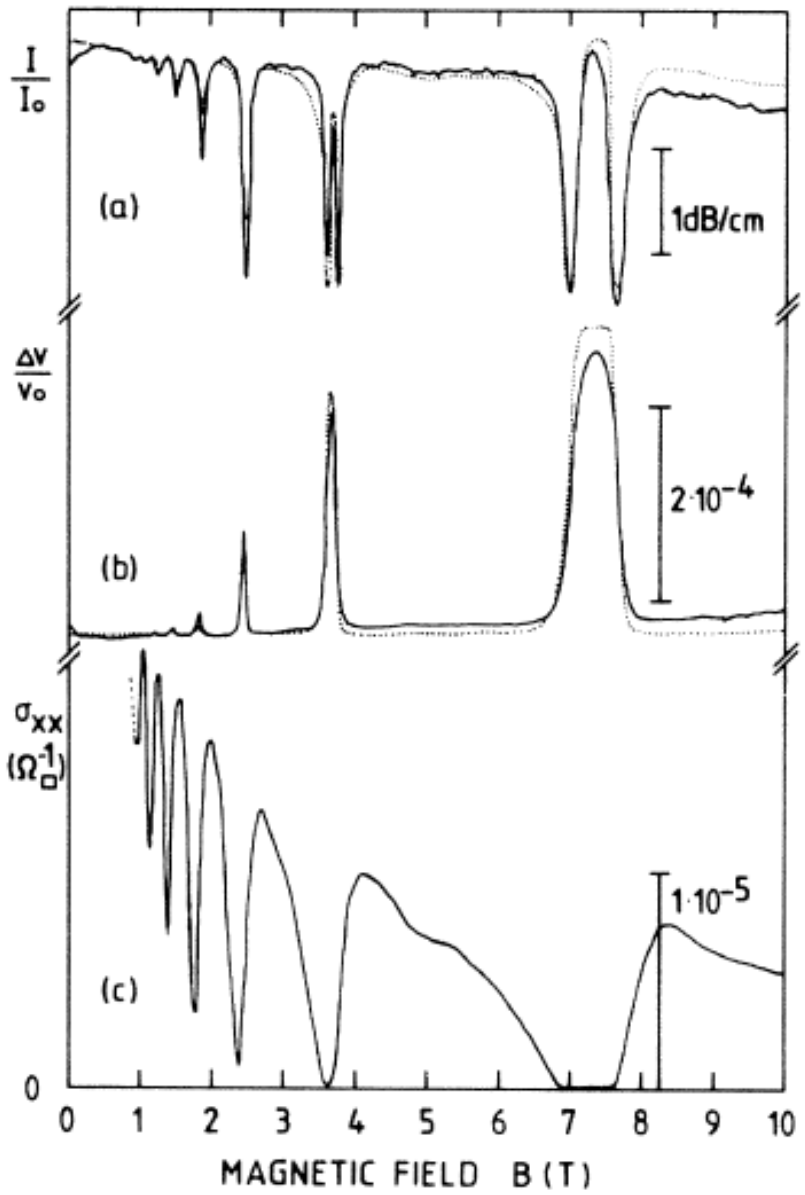

Figure 3.9: *Oscillations in the conductivity of a 2DES in a strong magnetic field are reflected by similar oscillations in SAW attenuation coefficient and velocity shift. Taken from [3].*

3.4.3 SAW Interactions with Graphene

As Chapter 2 shows, graphene possesses extremely desirable electronic properties and has numerous potential applications [10, 68]. Its two-dimensional structure has made it a natural candidate for integration with SAW devices. Theoretical studies by Thalmeier *et al.* [14] and Zhang and Xu [15] have predicted that the coupling of SAWs to graphene charge carriers will lead to measurable changes in SAW observables, such as Landau oscillations in the attenuation and velocity shift in the presence of a magnetic field [14]. Elsewhere, graphene-SAW devices have been developed for sensing of H_2, CO [166], and H_2O [167, 168, 169], where a combination of mass-loading of the delay line and modification of graphene's conductivity by surface adsorbates has induced detectable changes in SAW amplitude and velocity.

It is the acoustoelectric interactions with graphene that have received more attention [16, 17, 18, 20, 170, 171]. This began with the detection of a large (~5 μA) acoustoelectric current in CVD graphene on $LiNbO_3$ by Miseikis *et al.* [16], over a distance of 20 μm. Bandhu and Nash subsequently observed a linear dependence of acoustoelectric current on SAW frequency and intensity both at room [17, 20] and low temperatures [18] in macroscopic devices. This is consistent with Equation 3.47. They also found that SAWs are highly sensitive to the presence of defects and grain boundaries in graphene, raising the prospect of using SAWs as a contactless probe of graphene quality. The possibility for graphene-SAW sensors for a variety of applications has also been considered,

using gases [19], electrolytic solutions [172], and ion gels [20] to modulate the acoustoelectric current. There have also been examinations of DC-biased mono- and multi-layer graphene films for SAW amplification, whereby electron momentum is transferred to the SAW to increase its amplitude [173, 174, 175]. The absence of a band gap in graphene raises the question of how the piezoelectric potential can confine graphene's free charge carriers. Coco *et al.* [176] have reported that a combined shear and uniaxial strain of ~15% can be used to open a band gap of about 0.6 eV, approximately half that of silicon [87]. This strain approaches the breaking strain of graphene (~25%) [176], and it is unlikely that this can be applied with SAWs of the intensity reported in the literature. Interestingly, Thalmeier *et al.* [14] predict that in pristine graphene, for SAWs with wave vector $q < 2k_F$ (where k_{F} is the Fermi wave vector in graphene) and in the absence of a magnetic field, the acoustoelectric attenuation tends to zero. For $q > 2k_{\mathrm{F}}$, acoustoelectric attenuation of the SAWs is observed.

The interesting electronic and optical properties of graphene (Section 2.1) and the numerous potential applications for graphene nanoribbons (Section 2.2.1.3) warrant further investigation using piezoelectric SAWs, which have been demonstrated as sensitive probes of the properties of LDESs. The work in this thesis constitutes the first experimental studies of the photoresponse of the acoustoelectric current generated in graphene monolayers, the effect on the acoustoelectric interaction of patterning graphene into nanoribbons, and the acoustoelectric photoresponse of graphene nanoribbons.

3.5 Acoustoelectric Device Applications

SAW devices are found abundantly in communication technologies [1, 177]. The development of low-dimensional electron systems has seen SAWs deployed for probing their electronic properties [3, 4, 5, 17, 20, 178]. The compactness, affordability, and robustness of the SAW substrates [1] coupled with emergence of atomically-thin materials [9, 10, 68] may yet lead to the development of a new class of wireless chemical [19, 166, 167] and biological sensors [172]. We take this opportunity to review some of the most exciting potential applications of acoustic charge transportation that are relevant to the content of this thesis.

3.5.1 Single Electron/Photon Transport

Since the 1990s there has been a demand in the metrological community for a quantum standard of electrical current [179, 180, 181]. Ideally, such a current standard would be measurable in the nanoampere range with a relative uncertainty of less than one in ten million [181]. Devices using Coulomb blockade of tunnelling operate at low frequencies and subsequently achieve very small current (~1 pA) [181]. Acoustoelectric devices on the other have shown considerable promise in achieving the required accuracy at small SAW wavelengths ($\lambda_{\mathrm{SAW}} < 1$ μm) [181].

Using a one-dimensional (1D) channel defined by a split gate in a GaAs/Al_xGa_{1-x}As heterostructure, operating at 1.3K, Talyanskii *et al.* [8] used SAWs to transfer

electrons between adjacent two-dimensional electron gases (2DEGs). When the 1D channel is pinched off, the SAW potential wells trap and transport the electrons up the potential hill, where the number of electrons in each potential well is defined by SAW potential strength and the shape of the potential hill. By tuning the depth of the SAW potential well (i.e. the SAW power) and the gate voltage, it was found that an acoustoelectric current of the form $I = nef$, where n is an integer number of electrons, e is the electronic charge, and f is the SAW frequency, could be generated for $kL \ll 1$, where k is the SAW vector and L is the length of the 1D channel. As the gate voltage decreases, an increase in the number of electrons is transported per SAW cycle. This is shown in Figure 3.10. Ahlers *et al.* later attained a change in current $\Delta I = ef$ in the low-power regime [179].

As well as single-electron sources, SAWs have been used to create single-photon sources [180, 182, 183]. The dynamics of photo-generated charge carriers in low-dimensional semiconductors have been challenging to study, since the bulk semiconductor band structure dominates their optoelectronic properties [182]. For direct bandgap semiconductors, such as GaAs, electron-hole recombination rates are very short (< 1ns) in comparison to semiconductors possessing an indirect bandgap such as Si. Rocke *et al.* [182] used SAWs to separate electron-hole pairs photo-generated in $In_{0.15}Ga_{0.85}As$ quantum wells. The electrons were stored in the SAW potential minima and the holes were captured in the potential maxima, and transport them over macroscopic (1 mm) distances

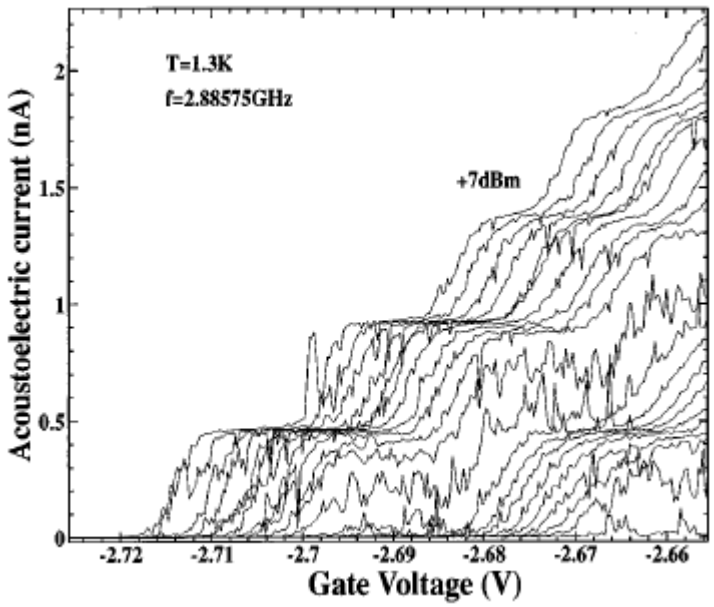

Figure 3.10: *Acoustoelectric current as a function of gate voltage for different SAW powers. The leftmost trace corresponds to a SAW power of 7 dBm. The power level decreases by 0.2 dBm from left to right for each trace. Taken from [8].*

to a neighbouring region for recombination. The half-wavelength spatial separation of the electron and hole dramatically reduces the recombination probability, increasing the exciton lifetime to 350 ns. This is shown in Figure 3.11. The transportation of a single electron-hole pair over long distances is envisaged for optical delay lines operating at sound velocities.

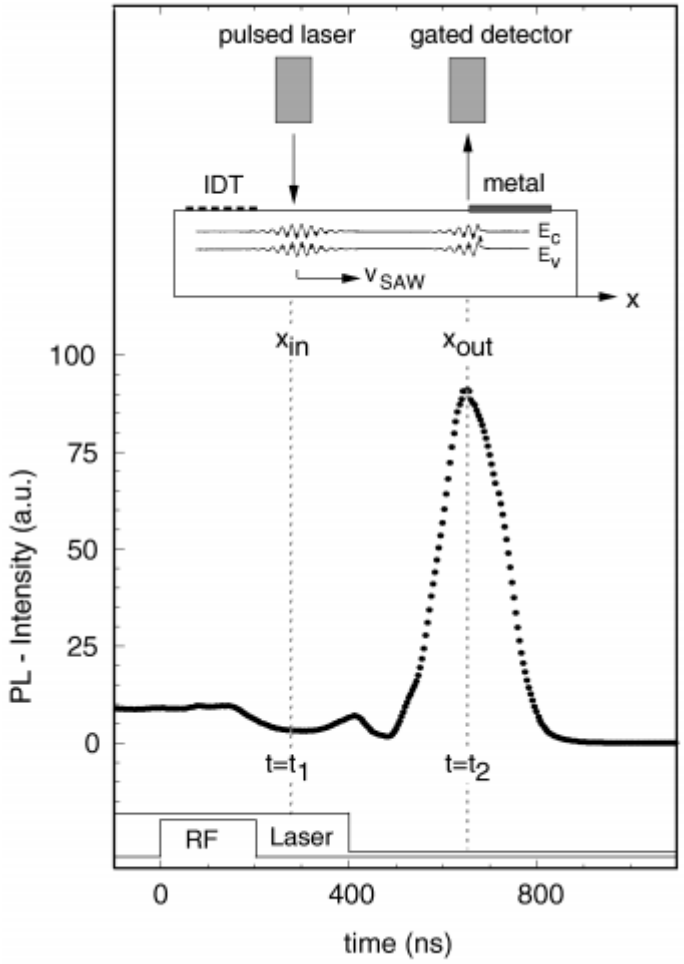

Figure 3.11: *Exciton transport by SAWs. A 200 ns SAW pulse is generated at* $t = 0$*. At* $t = t_1$ *and* $x = x_{in}$*, the potential extrema of the SAW are populated by photoexcited electrons and holes which are transported at the speed of sound to* $x = x_{out}$*, where the semi-metallized region screens the SAW and induces electron-hole recombination at* $t = t_2$*. The RF and laser pulse durations are indicated in the lower part. Taken from [173].*

3.5.2 Chemical Sensing

SAW sensors for gaseous- and liquid-phase chemical detection have inherent advantages of being passive and the potential to be wireless [184]. They are also compact, low cost, and compatible with modern clean-room fabrication processes. A typical device incorporates a selective chemical sensing layer between the opposing IDTs [184] that reacts with or adsorbs target molecules. This can produce a mass loading affect that attenuates and velocity-shifts the SAW [167], or induces a change in conductivity of the sensing layer that modulates the SAW observables [19] (although it may be a combination of both). SAWs of large amplitude are preferred for high signal-to-noise ratios. This is achieved by selecting materials with high piezoelectric coupling coefficients (e.g. $K^2_{\text{eff}} = 0.056$ for 128° YX $LiNbO_3$, versus 0.001 in ST-X quartz [1, 184]) as the substrate. Graphene and related materials have a very high surface to volume ratio, making their electronic properties receptive to surface contaminants [63, 64]. Zheng *et al.* have studied the doping effects on the acoustoelectric effect in graphene-$LiNbO_3$ SAW devices, and observed a 50% increase in sensitivity to NO_2 adsorbates than a conventional DC current measurement [19]. This research could help realise acoustoelectric chemical sensors based on a variety of 2D materials, increasing the versatility of acoustic charge transportation for device applications.

3.6 Summary

In Section 3.2, descriptions of bulk acoustic wave propagation in non-piezoelectric and piezoelectric media were presented. By applying appropriate boundary conditions, the expressions for the displacement and electric potential due to surface acoustic wave propagation in a piezoelectric material were obtained. The use of interdigital transducers for SAW generation was discussed in Section 3.3, along with considerations of the temperature stability and piezoelectric coupling strength for practical devices. The acoustoelectric effect describing the acoustic transportation of charge, and a review of recent studies on the interactions between SAWs and graphene, was given in Section 3.4. In Section 3.5, some of the novel potential applications for SAW technology were presented.

4. Device Fabrication and Experimental Setup

4.1 Overview

This chapter describes the process for fabricating the graphene-SAW and graphene nanoribbon (GNR)-SAW hybrid devices, the experimental setup, and the measurement techniques used in later chapters. The overall objective of the fabrication process is outlined in Section 4.2. In Section 4.3 the lithium niobate ($LiNbO_3$) SAW devices are discussed, including the interdigital transducer (IDT) structures and the manufacturer's data. The process for transferring a graphene monolayer between the IDTs is described in Section 4.4. In Section 4.5, the approach for patterning the graphene into rectangles or GNRs using electron beam lithography and reactive ion etching is presented. This is followed by the application of chromium-gold (Cr/Au) electrodes to the graphene for electrical measurements using a thermal evaporation system (Section 4.6). The graphene quality is then assessed using Raman spectroscopy (Section 4.7). Samples are mounted to electroplated printed circuit boards (PCBs), and gold wire bonds are used to make interconnections between the PCB and the gold electrodes/IDTs (Section 4.8). Section 4.9 contains a full list of the completed devices and the measurements they were

used for, and the details of the measurement setup and techniques are given in Section 4.10.

4.2 Overall Aim of Fabrication

The acoustoelectric effect in 2DESs can be studied by positioning them between the two opposing IDTs of a SAW delay line [3, 17, 19]. Using this layout, the aim was to measure the acoustoelectric effect in graphene- and GNR-SAW hybrids with metal contacts positioned on top of the graphene/GNRs. To maximise the acoustoelectric attenuation of the SAW per unit length, monolayer graphene films with a length comparable to the IDT separation distance were used. By Equations 3.48 and 3.52, this would increase the magnitude of the acoustoelectric current. Metal electrodes would therefore be spaced with large (millimetre-scale) separation distances. Furthermore, large-area CVD graphene routinely exhibits holes and cracks. Such damage is introduced during the process of transferring the graphene to the target substrate [24, 147]. This can lead to an incomplete conduction pathway between the metal electrodes on the graphene, which is much harder to detect on lithium niobate (as will be discussed in Section 4.4.3). To reduce this risk, the graphene and GNR arrays were defined with widths comparable to the IDT aperture. Lastly, by Equation 3.52, graphene with a very high conductivity would be expected to cause the acoustoelectric current to tend to zero, since the piezoelectric fields would be immediately screened by the graphene charge carriers. It is therefore preferable to use CVD graphene with

such defects as wrinkles and cracks, compared to exfoliated graphene, as the conductivity is more similar to the characteristic conductivity of lithium niobate.

4.3 SAW Device Properties and Manufacturer's Data

Commercially-available 128° Y-cut X-propagating lithium niobate SAW delay lines were used to investigate acoustoelectric effects in graphene and graphene nanoribbons in all measurements presented here. Two opposing, double-digit aluminium interdigital transducers had been pre-deposited on the surface of the $LiNbO_3$ crystal by the manufacturer (MESL Microwave/COM DEV International) for SAW generation and detection. The IDT separation distance and acoustic aperture were measured at 5.4 mm and 3.25 mm respectively, shown schematically in Figure 4.1. SAWs propagating on 128° YX $LiNbO_3$ experience little diffraction [1], which enables IDTs with millimetre-scale apertures to be applied. The large separation distance allowed graphene monolayers to be placed on the delay line with reduced probability of shorting out the IDTs. The IDT

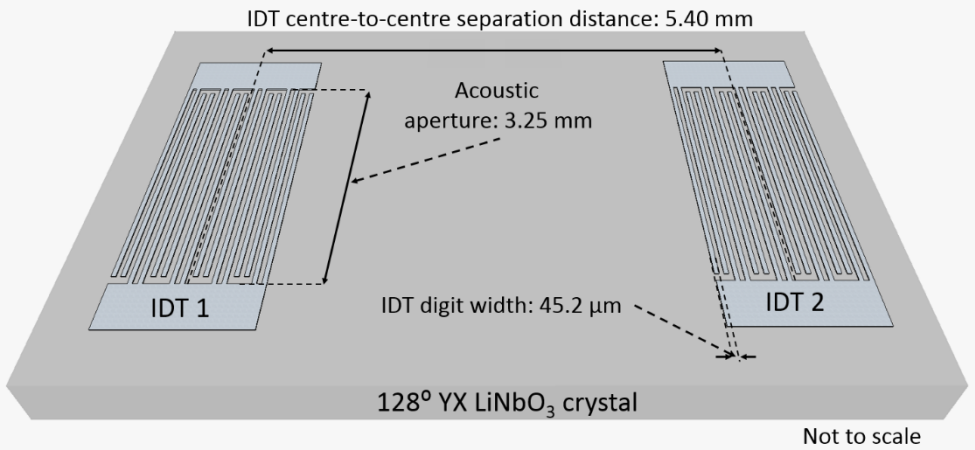

Figure 4.1: *Schematic of a blank SAW device as supplied by the manufacturer.*

metallisation ratio was 50%, with all digits having the same length and a width of 45.2 μm. The speed of SAWs in 128° YX $LiNbO_3$ is $v = 3979$ m/s [1]. The fundamental frequency of the IDTs is $f_0 = 11$ MHz (corresponding wavelength $\lambda_0 = 361.7$ μm).

Figure 4.2 shows the relative SAW amplitude (in decibels) as a function of frequency in a bare SAW device as measured by the manufacturer in the frequency range 1 – 500 MHz. For convenience, such measurements are termed the 'frequency response'. The prominent peaks in relative amplitude correspond to the resonant frequencies of the IDTs,

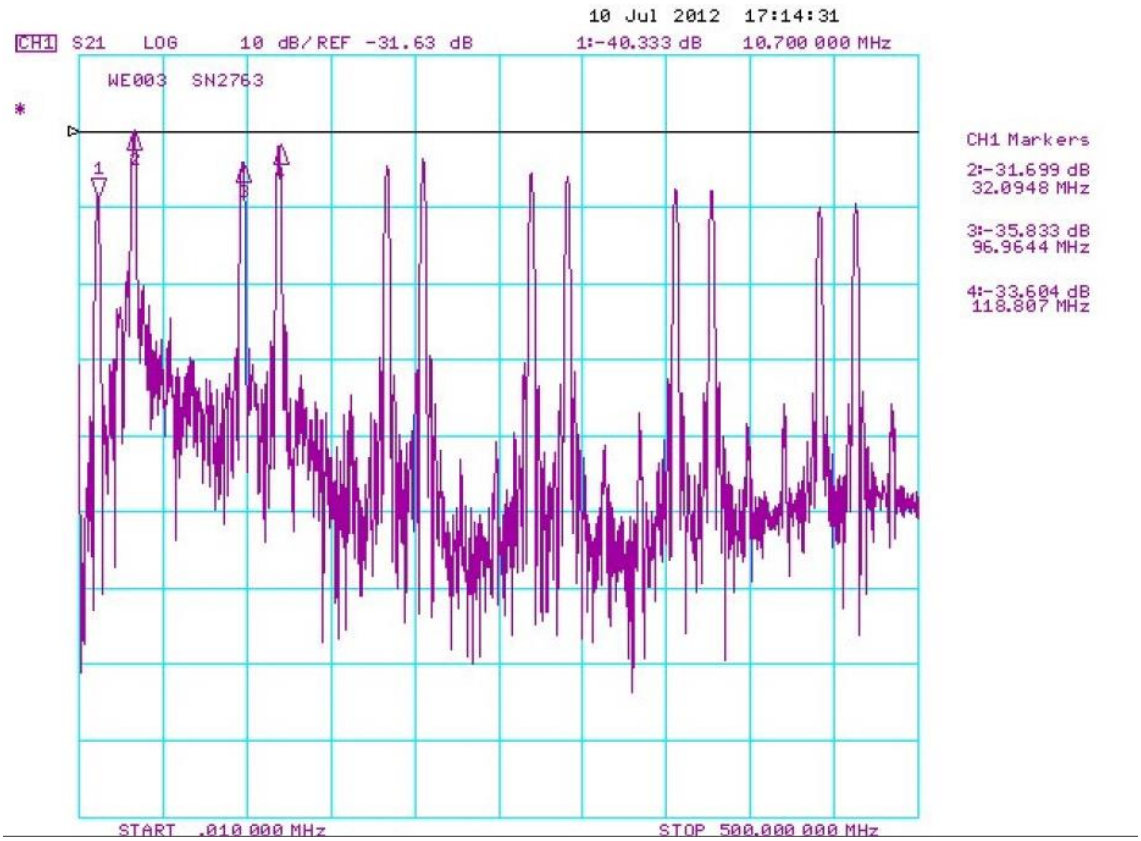

Figure 4.2: *Manufacturer's data showing the relative amplitude of SAWs as a function of frequency for a bare lithium niobate SAW device.*

at: 11, 33, 97, 119, 184, 205, 270, 291, 356, 377, 442, and 463 MHz. The relative amplitudes of frequencies 11, 33, 97, and 119 MHz are (in dB): -40.33, -31.70, -35.83, and -33.60, as measured by the manufacturer (note that no manufacturer data is provided for any higher resonant frequencies).

4.4 Graphene Transfer Process

Commercially available graphene for research purposes is most commonly grown by chemical vapour deposition (CVD) on either copper [111, 112, 116] or nickel [37, 115, 119] foils. This is due to the relatively low cost of the substrates and the scalable production techniques [35, 36]. In this work all the devices were fabricated using CVD graphene on copper, since the growth process on this substrate is self-terminating at a single layer [112] (whereas neighbouring regions of graphene on nickel can have thicknesses ranging from 1-12 layers [119], due to inhomogeneities introduced by the nickel grain boundaries [112, 113, 119]). The manufacturer (Graphene Supermarket) quoted a graphene domain size of no larger than 10 μm.

4.4.1 PMMA Coating and Reactive Ion Etching

Graphene was positioned between the two IDTs using the poly-methyl methacrylate (PMMA) transfer technique, developed by Ruoff [34, 121] and others [119]. PMMA is a transparent thermoplastic that is typically dissolved in

anisole. Ruoff's approach is to use a spin coater to deposit a PMMA membrane onto the graphene, which it will adhere to via van der Waals forces, and a chemical etchant to remove the metal growth substrate. This allows centimetre-scale, continuous graphene samples to be placed on arbitrary substrates relatively easily. To transfer the graphene to the $LiNbO_3$, a 200 nm-thick layer of PMMA 950K A4 was deposited onto a ~5mm x ~5mm section of graphene on copper foil. 950K refers to the molecular weight of the polymer chain in Daltons and A4 refers to a PMMA dilution in anisole (A) of 4% by weight (4). The spin coater operated for 50 s at a rotation rate of 3500 RPM. The PMMA-graphene-Cu-graphene stack was baked at 150°C for 8 minutes on a hotplate so that the PMMA would set as a semi-rigid support layer following the contours of the underlying foil. Since graphene grows on both sides of the copper, it was necessary to etch away the uncoated graphene layer before the foil could be removed. This was done via reactive ion etching (RIE), the process of using a chemically reactive plasma to remove unwanted materials and contaminants from substrates. A potential difference of several hundred volts across the RIE chamber causes ionised atoms to collide with the target material at high speed, displacing atoms and molecules via transfer of kinetic energy. A 10 W, 50 s argon etch was used, with a flow rate of 15 standard cubic centimetres per minute (SCCM) at a pressure of 20 mTorr. This process was repeated two to three times to fully remove the bottom layer of graphene. The copper could then be dissolved from the remaining PMMA-graphene-copper stack via a wet-etch process.

4.4.2 Etchant Chemicals and Transfer

The most commonly used chemicals for copper etching in CVD graphene processing are iron chloride ($FeCl_3$) [114] and ammonium persulphate ($(NH_4)_2S_2O_8$) [35], dissolved in deionised water. A 0.1 Molar solution of ammonium persulphate was used to remove the copper at room temperature over the course of 8 hours. Ammonium persulphate was selected based on results of energy dispersive spectroscopy studies performed by Bandhu [178] revealing that it leaves fewer unwanted etchant salts on the graphene. The PMMA-graphene stack appears as a thin, transparent layer floating on the surface of the etchant solution that can be extracted with a glass spoon and rinsed in deionised water. The sample was rinsed five to six times, each time in fresh water to reduce contamination of the graphene, and transferred to the lithium niobate. The sample was left to dry at room temperature for 12 hours to ensure good adhesion between the graphene and the substrate. Once dry, the PMMA layer was dissolved in acetone at room temperature for at least 12 hours.

4.4.2.1 Modified PMMA Transfer

During the fabrication of the devices characterised in Chapters 6 and 7, a modification to the above process was introduced after the PMMA-graphene bilayer had dried on the $LiNbO_3$. The cured PMMA retains some of the contours of the copper, causing the graphene to make imperfect contact with the substrate after transfer. When the PMMA is dissolved in acetone, any graphene that is not

in contact with the $LiNbO_3$ is more susceptible to damage during the subsequent stages of device fabrication. Li *et al.* [185] found that a second PMMA layer applied by drop casting helps re-dissolve the existing PMMA. This allows the underlying graphene to relax, increasing its contact area with the substrate. Optical microscopy images showing the improved coverage are presented in Section 4.4.1, where a droplet of PMMA was applied to the dried PMMA-graphene stack for 30 minutes at room temperature before being washed in acetone for several hours.

4.4.2.2 Substrate Cleaning

The $LiNbO_3$ substrates were thoroughly cleaned to remove any residues just before the graphene was transferred. SAW devices were cleaned via sonication for 10 minutes in acetone then isopropyl alcohol, to dissolve any organic chemical residues. Trace inorganic chemicals were then removed by sonication in deionised water. The substrates were blow-dried with nitrogen and placed on a hotplate at 120°C for 15 minutes to remove any remaining water droplets. Finally, the substrates underwent two to three rounds of an oxygen-argon RIE process (O_2 and Ar flow rate of 10 SCCM each; 15 W power for 30 s; chamber pressure of 30 mTorr). Oxygen plasma etching can be used to chemically break down carbon-hydrogen, carbon-carbon, and carbon-oxygen bonds in any trace species on the surface. Such chemicals may be present following device processing in organic solvents. An argon plasma enhances cleaning via a physical

bombardment process, whereby kinetic energy transfer from the argon ions to surface contaminants displaces them from the substrate, and can assist with the removal of inorganic chemical residues.

4.4.3 Optical Microscopy

The fabrication of graphene-based devices still relies heavily on its visibility on the substrate under optical microscopy [106, 127]. Most experimental work on graphene is performed using a silicon (Si) substrate with a 300 nm-thick surface oxide layer (SiO_2), on which transferred graphene monolayers are discernible due to the increase in optical path changing their interference colour with respect to an empty substrate [9, 106]. Lithium niobate does not have an oxidised surface, rendering monolayer graphene invisible. To conserve the relatively expensive SAW devices, in this thesis the PMMA transfer method was practiced on Si/SiO_2 wafer sections. A typical transfer is shown in Figure 4.3 (a) and (b), imaged with an optical microscope. In Figure 4.3 (a) a relatively large, continuous graphene island of ~300 μm x ~250 μm is visible in the top right-hand corner of the image as a slightly darker patch. Elsewhere there are small, disconnected graphene pieces, impurities, and rolled-up multilayer sections. Another region in Figure 4.3 (b), imaged at a higher magnification, shows the rips, discontinuities, and wrinkles that are easily introduced during the PMMA transfer technique. The difference in colour between the two images arises from a change in illumination intensity, rather than a change in thickness of the SiO_2 layer. The images show the difficulty

of transferring continuous graphene monolayers on the scale of hundreds of microns to millimetres. Devices fabricated from CVD graphene on Si/SiO_2 can be easily shaped and electrically contacted with the assistance of optical microscopy, and it is straightforward to select homogeneous regions of the type in Figure 4.3 (a). The inability to be so selective when the graphene is placed on lithium niobate makes it difficult to assess the coverage of graphene without techniques such as Raman spectroscopy, which typically have very low throughput. Graphene films transferred onto Si/SiO_2 via the modified PMMA transfer process [185] described in Section 4.3.2.1 showed significantly greater coverage under optical microscopy (Figure 4.4 (a) and (b)). Approximately five test transfers were made using the modified PMMA transfer technique, with each compared to one made using the conventional approach. Whilst this provides only anecdotal evidence of an improvement of graphene coverage using the modified PMMA transfer technique, Raman studies of defects in graphene transferred via this method support the notion that it leads to enhanced graphene quality [185].

Due to the visibility of the PMMA membrane on lithium niobate, optical microscopy can at least be used to determine the maximum extent of the graphene and the region to which electrical contacts can be applied. A typical SAW device with a PMMA-graphene bilayer on the surface is shown in Figure 4.5. The chequered effect arises from stitching smaller images together. The multi-coloured regions (e.g. in the red rectangle) of the PMMA have slightly different thicknesses, caused by the film wrinkling when it was positioned on the

substrate. Pink circles show regions where the PMMA-graphene stack overlaps the IDTs, which can be removed later (Section 4.4). A rip in the PMMA is shown in the blue square, and wrinkles and cracks in the PMMA are labelled. When designing the layout of the electrical contacts to deposit on top of the graphene or GNRs, it was assumed that a graphene monolayer fully covered the region beneath the PMMA. Following the process of graphene patterning and electrode application, the quality of the graphene in each device was assessed quantitatively using Raman spectroscopy (Section 4.6).

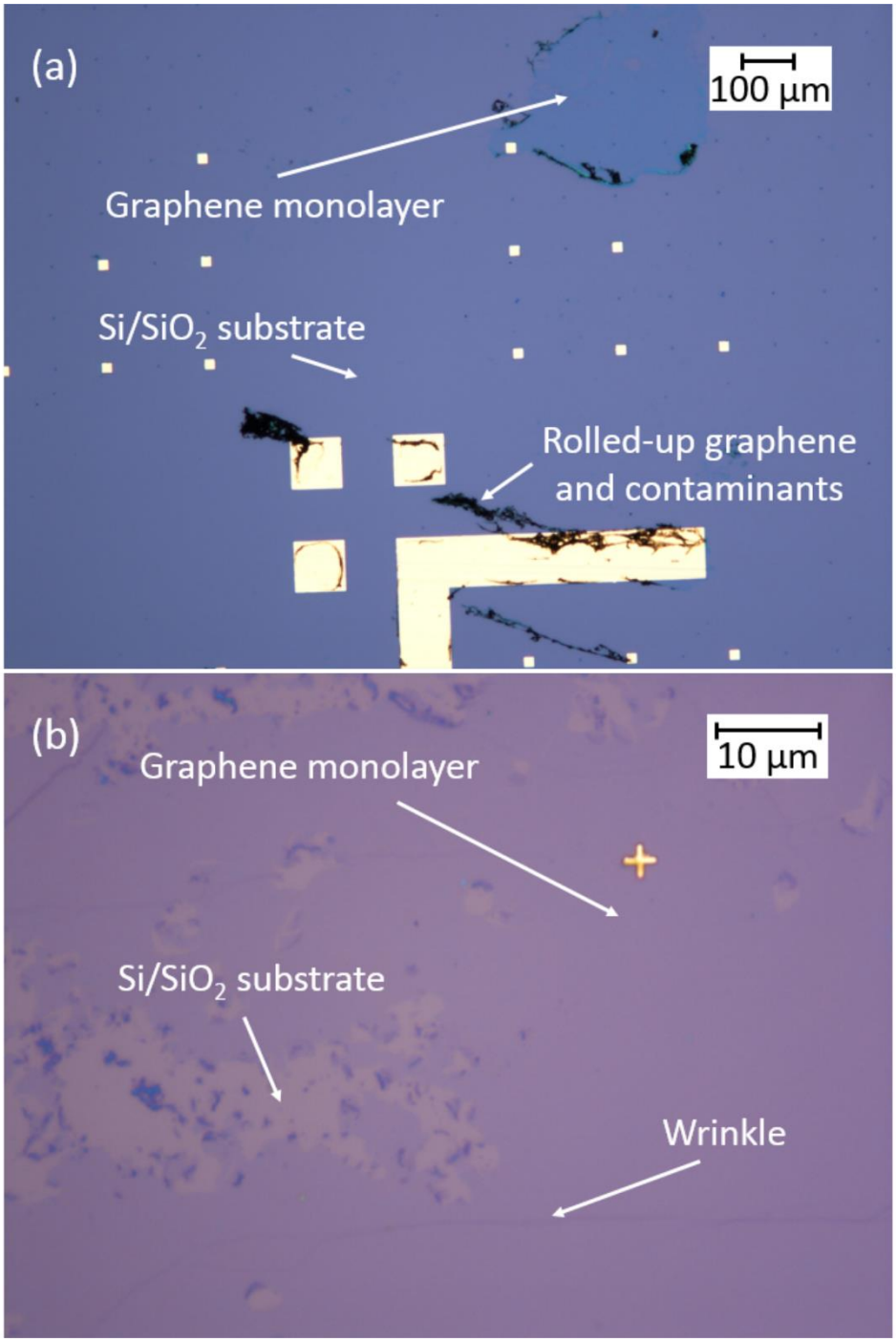

Figure 4.3: *(a) Optical micrograph of a CVD graphene monolayer on a Si/SiO_2 wafer, transferred via the PMMA transfer technique. (b) Zooming in on a similar region, holes and wrinkles in the graphene become visible.*

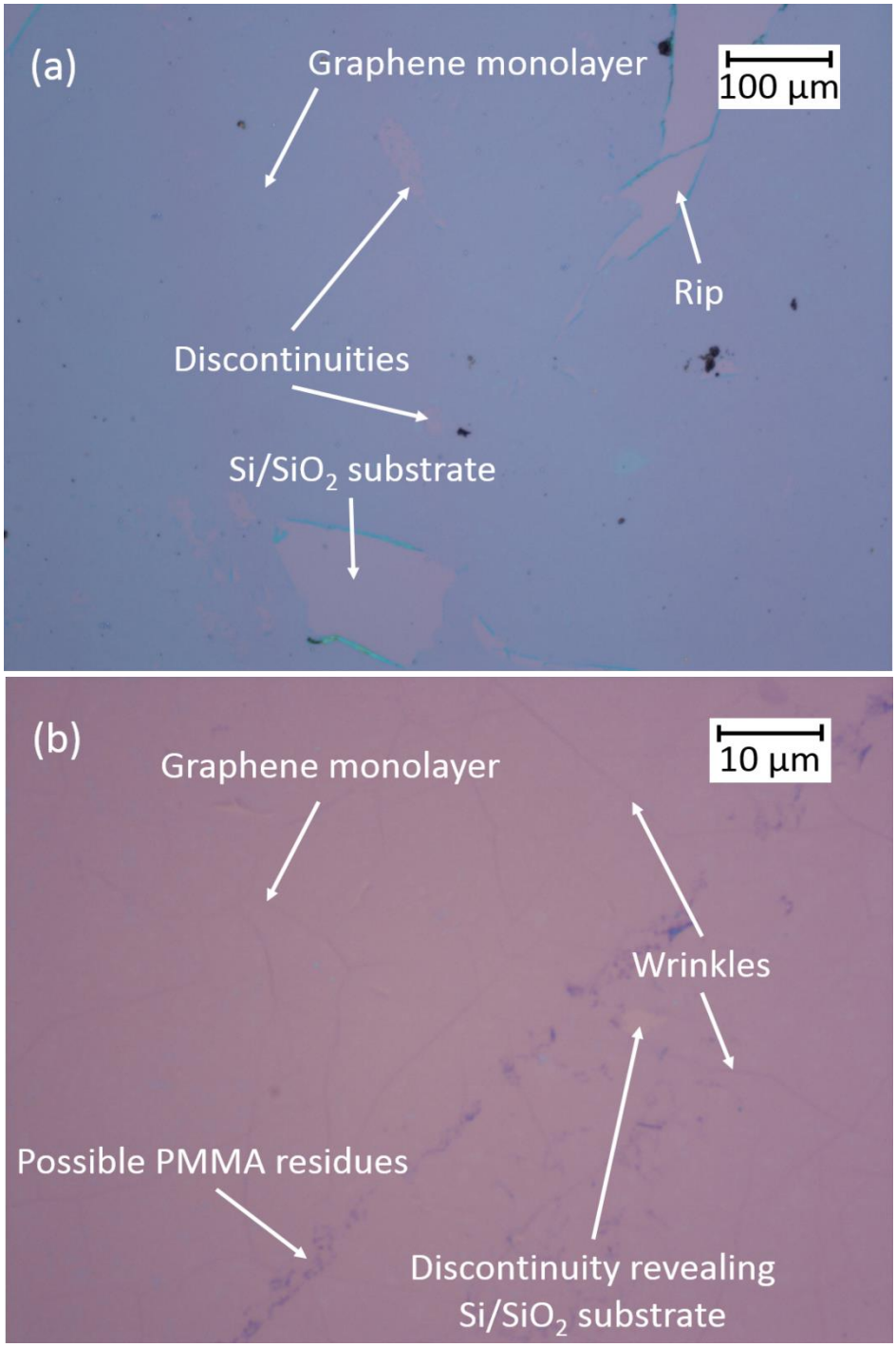

Figure 4.4: *(a) Optical micrograph of a CVD graphene monolayer on a Si/SiO₂ wafer, transferred via the modified PMMA transfer technique. (b) A similar region at higher magnification shows good quality graphene with few discontinuities.*

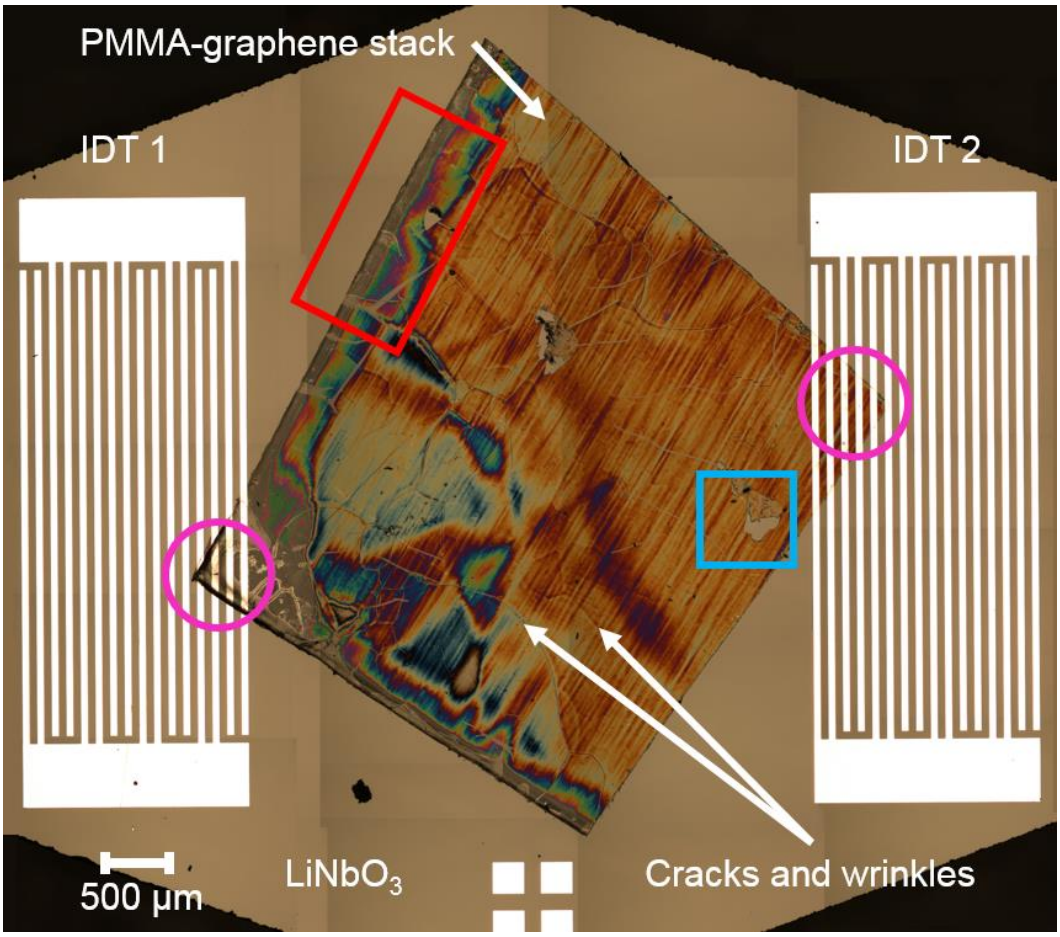

Figure 4.5: *An optical micrograph of a PMMA-graphene stack transferred to a lithium niobate SAW device. Multi-coloured regions (e.g. red rectangle) correspond to nonuniform PMMA thickness. The pink circles show regions where the graphene overlaps the IDTs, potentially shorting them out. A small rip is indicated by the blue square. Other defects are labelled.*

4.5 Patterning Graphene

The acoustoelectric current was studied in graphene samples of several different geometries, the full details of which are given in the relevant chapters.

Irrespective of size, the procedure for patterning the graphene relies on two technologies: electron beam (e-beam) lithography and reactive ion etching. The implementation of each is described in the following sections.

4.5.1 Electron Beam Lithography

E-beam lithography is the process of using a focussed beam of electrons to draw custom shapes on surfaces covered with an electron-sensitive chemical known as a resist. The technique is similar to photolithography, in which a laser or UV light is used to create shapes, but can achieve a resolution of tens of nanometres versus hundreds of nanometres. PMMA is a positive e-beam resist. When exposed to electrons its solubility changes due to the scission of polymer chains. The cut/exposed regions can be removed by immersion in a developer solution, leaving behind a mask of the unexposed areas. Materials not covered by the mask can be removed via RIE. Here, e-beam lithography is used to define large squares of graphene or arrays of GNRs. The advantage of this is that the same chemical for graphene transfer and patterning can be used, simplifying the device fabrication process and reducing the graphene contamination. However, e-beam lithography has a lower throughput than photolithography. The full procedure for shaping the graphene is described below.

A 200 nm-thick layer of PMMA 950K A4 resist was deposited on the surface of the graphene-SAW hybrid device via spin coating, and cured at 150°C for 8

minutes on a hotplate. Since $LiNbO_3$ is an insulator, exposure to the electron beam will cause charge build-up on the surface of the device. As the surface charge increases, the beam of electrons becomes more and more deflected and will lead to a distorted version of the pattern being drawn. To prevent this, a 12 – 13 nm-thick layer of aluminium (Al) was deposited on top of the PMMA via thermal evaporation (Section 4.5). The high-energy electrons of the e-beam can penetrate this layer with their path relatively unchanged. The aluminium was electrically grounded to the sample stage using a small quantity of silver conductive paint. The patterns were produced using AutoCAD.

After the e-beam exposure, the aluminium top-layer was removed by immersion in Microposit MF 319 developer (97 – 98 % deionised water, 2.45 % tetramethylammonium hydroxide) at room temperature for approximately 2 minutes. Samples were then rinsed in deionised water and dried in a nitrogen stream. The PMMA developer solution was mixed in the ratio 1:5:15 of methyl ethyl ketone, methyl isobutyl ketone, and isopropyl alcohol (IPA) respectively. The device was immersed in the solution for 30 s to remove the exposed PMMA, then rinsed in IPA and blow-dried with nitrogen.

4.5.2 Reactive Ion Etching

An argon RIE process is used to remove graphene that is not protected by the PMMA mask (10 W, 50 s duration; Argon flow rate of 15 SCCM; chamber pressure of 20 mTorr). Raman spectroscopy studies showed that one etch process is sufficient to remove the unwanted graphene. The sample was then placed in room temperature acetone for approximately 12 hours to remove the PMMA, and subsequently rinsed in IPA and dried with nitrogen. Figure 4.6 shows a detailed schematic of the lithography and RIE processes up to this stage. Figure 4.7 (a) and (b) schematically show the unpatterned and patterned device respectively.

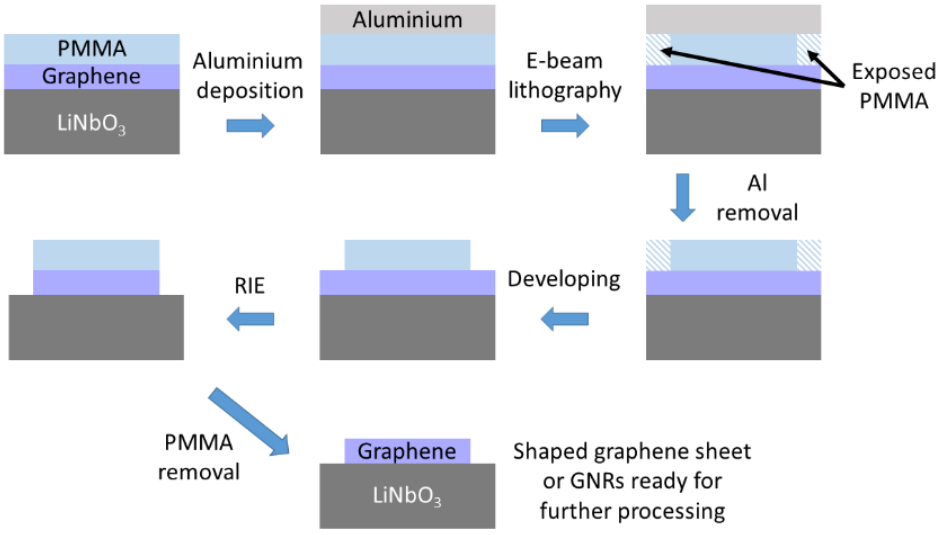

Figure 4.6: *Schematic showing the stages involved in shaping or patterning the transferred graphene monolayer via e-beam lithography and reactive ion etching.*

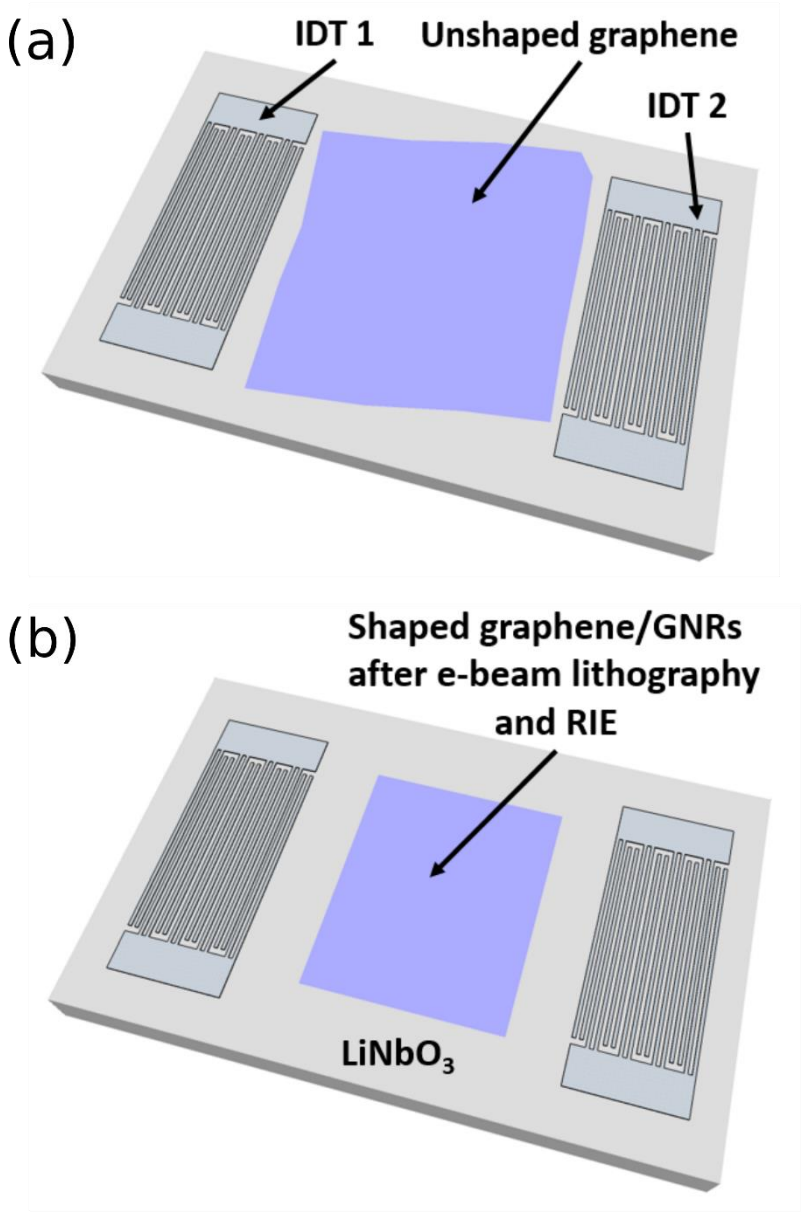

Figure 4.7: *Schematic showing monolayer graphene (a) before and (b) after it has been shaped using electron beam lithography and reactive ion etching.*

4.6 Metallization of Gold Electrodes

A second stage of e-beam processing was used to draw the pattern for the electrical contacts that would be applied to the graphene/GNR arrays. A thermal evaporator was used for the deposition of chromium (Cr) and gold (Au) electrodes (and Al when performing e-beam lithography). Metals were placed in tungsten baskets to which a large electrical current was applied, causing them to evaporate. The SAW device was placed directly above the basket, where the metal vapour condensed. The evaporation chamber pressure was initially held at ~1.2 x 10^{-6} Torr to prevent the metals from oxidising and the deposition rate was kept in the range 0.5 – 1.0 Å/s. Each of the devices had contacts with thicknesses of 5 nm and 50 nm of Cr and Au respectively, with the Cr providing greater adhesion of the contact to the substrate. Contacts had a width of 20 μm and a length of up to 3 mm. The unwanted metal was removed via ‘lift-off’. This is the process of dissolving the PMMA mask in an aggressive solvent, thereby removing the excess metal on top of it, leaving behind only the required Cr/Au. Lift-off was performed using room temperature acetone, after which the sample was rinsed in fresh acetone and IPA, then dried with nitrogen. The stages of the Cr/Au contact deposition are shown schematically in Figure 4.8. Figure 4.9 shows a schematic of a device after the metal contacts have been deposited. Note that the metal contact separation distance was chosen such that it did not coincide with a resonant frequency of the IDTs.

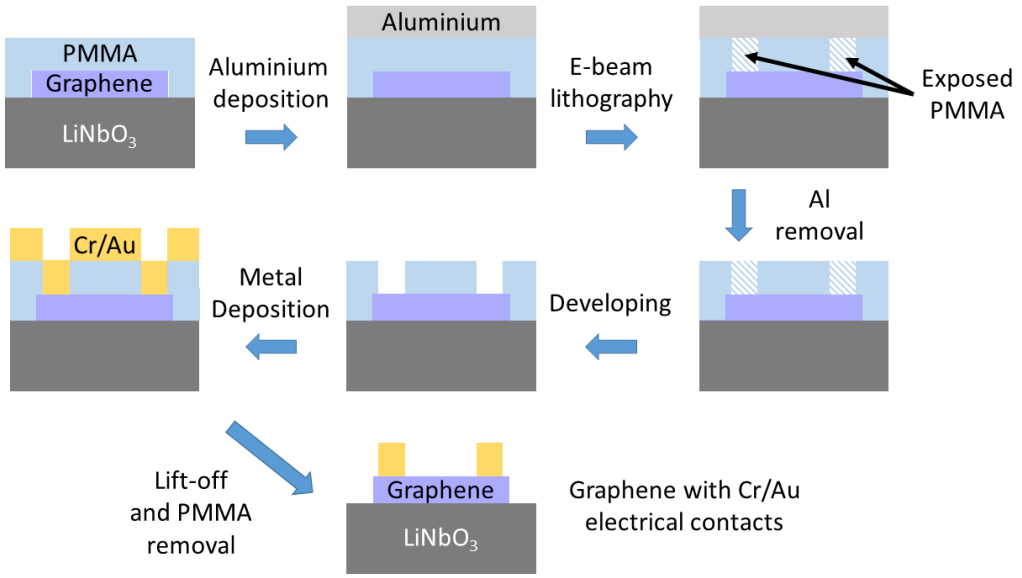

Figure 4.8: *Schematic showing the stages involved in applying Cr/Au electrical contacts to the graphene, via e-beam lithography and thermal evaporation of metals. Unwanted metals removed via lift-off in acetone.*

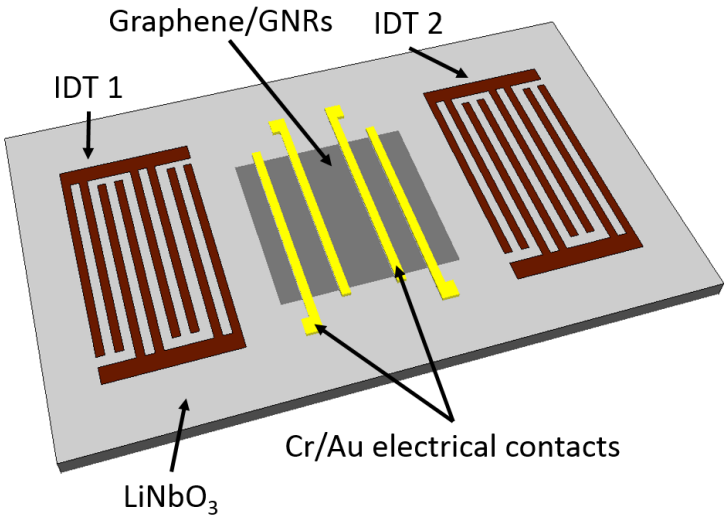

Figure 4.9: *Schematic showing a SAW device with graphene or a GNR array on the surface, along with the Cr/Au electrical contacts.*

4.7 Raman Spectroscopy

After contact metallization, Raman spectroscopy studies of the devices were performed. It is a non-destructive optical characterisation technique that can be used to determine the number of graphene layers, information on its electronic properties, and an assessment of graphene's structural quality on materials where visible light microscopy cannot be used (as here) [128, 129, 130, 131, 133]. Pristine monolayer graphene's Raman-active modes are found at ~1580 cm^{-1} (G band) and ~2670 cm^{-1} (2D band or G' band) [186]. The D band at ~1350 cm^{-1}, visible in 'real' graphene, is indicative of disorder such as cracks, wrinkles and impurities [133]. The Raman shift of the 2D and D bands quoted above are for illumination by a 532 nm laser (photon energy 2.33 eV). Full details of Raman spectroscopy in graphene, including the origin of the excitation wavelength dependence of the 2D- and D-peak positions, are given in Section 2.4.2.

The Raman spectrum of the device used for the measurements in Chapter 5, consisting of a lithium niobate SAW device with a continuous ~3 mm x ~3 mm graphene sheet on the surface, was obtained using a Renishaw 100 mW continuous wave 532 nm laser as the illumination source. Backscattered light is collected with a lens and sent into a spectrophotometer. A series of notch filters separate the unwanted Rayleigh-scattered photons, which have the same energy as the incident light, from the small number (approximately 1 in 10 million [132]) of Raman-scattered photons, which are colour shifted compared to the incident photons due to their interaction with the lattice of the material under test. The

Raman-scattered photons are then counted by a thermoelectrically-cooled charge-coupled device (CCD). The response is shown in Figure 4.10 in the range 1200 – 3000 cm^{-1}, as measured by Bandhu [178]. The lower, black curve corresponds to the Raman spectrum of the lithium niobate substrate, used as a control, and the upper, red curve shows the Raman spectrum in a region of graphene-on-lithium niobate. The two curves have been vertically offset to more clearly show the differences between them. Since this Raman spectroscopy

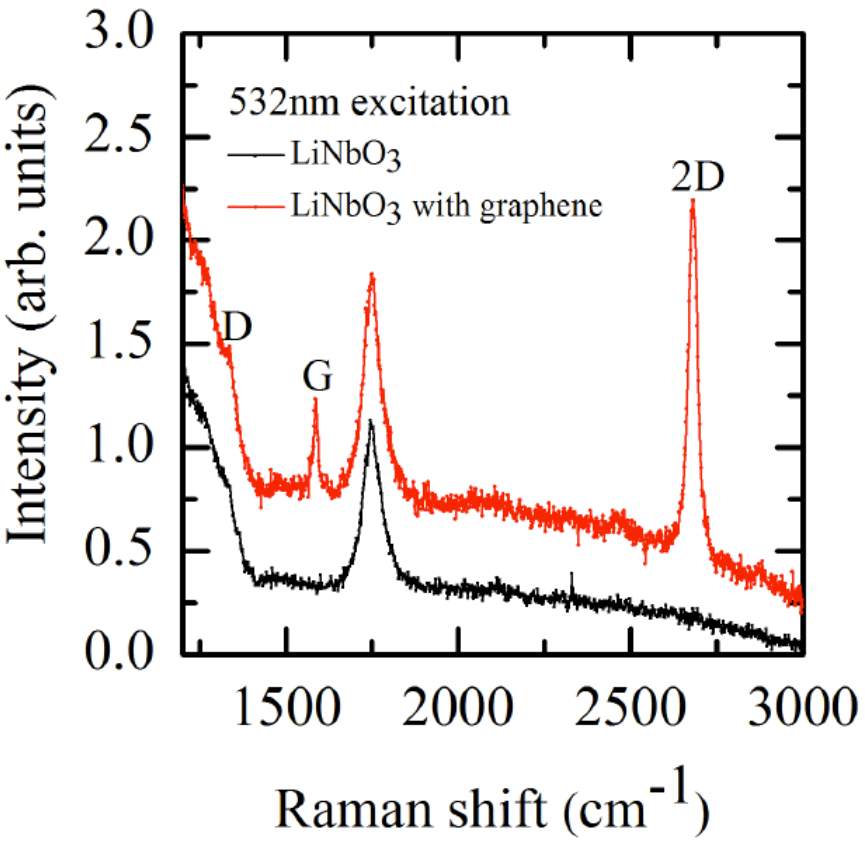

Figure 4.10: *Raman spectra of the bare lithium niobate substrate (black curve) and the graphene transferred onto it (red curve), for the device used for measurements in Chapter 5. The curves are vertically offset to show the difference between them. Figure reproduced from [169].*

system provides only single-point analysis, rather than a two-dimensional spatial map, 25 spectra from randomly distributed points on the sample were averaged together to produce the red curve in Figure 4.10 and assess the average graphene quality. The shifts of the G, 2D, and D bands are 1585 cm^{-1}, 2680 cm^{-1}, and 1337 cm^{-1} respectively. The relative intensity of the 2D and G bands (I_{2D} / I_G) of 3.5 is consistent with literature reports of Raman spectra of monolayer graphene [129, 131, 187]. The low intensity of the D band suggests that the average quality of the graphene film is high, with relatively few defects. The slight blue shift of the 2D and G bands is indicative of p-doping of the graphene [90], probably arising from molecular water adsorbates on the surface [64, 63, 188] [63, 64, 188]. (The Raman spectra are taken under atmospheric conditions with non-zero relative humidity.)

Raman spectra for all the SAW devices supporting graphene nanoribbons used for the measurements in Chapters 6 and 7 were obtained using a WITec Alpha300 confocal Raman microscope equipped with a thermoelectrically cooled CCD detector, capable of producing two-dimensional spatial maps of the Raman bands. These provide greater insight into the graphene coverage and any structural damage, and are shown in Section 6.2.2. Excitation was performed with a 532 nm wavelength laser, and the backscattered light was collected with a 50x objective lens with a lateral resolution of 388 nm. The laser power incident on the sample was approximately 2.3 mW. The Raman spectrum of a GNR-SAW hybrid device fabricated using the modified PMMA transfer method is shown in Figure

4.11. The spectrum represents the mean of 10 Raman spectra of 500 nm-wide graphene nanoribbons. Cosmic ray removal and background subtraction of the lithium niobate signal were performed to help better interpret the measurements. The Raman shifts of 2691 cm^{-1} and 1588 cm^{-1} of the 2D and G peaks respectively are consistent with reports by Gupta *et al.* [187] in studies of monolayer graphene films on Si/SiO_2, and the blue shift of the peaks is consistent with p-doping of graphene nanoconstrictions [90]. The 2D to G peak intensity ratio I_{2D} / I_G = 6.91

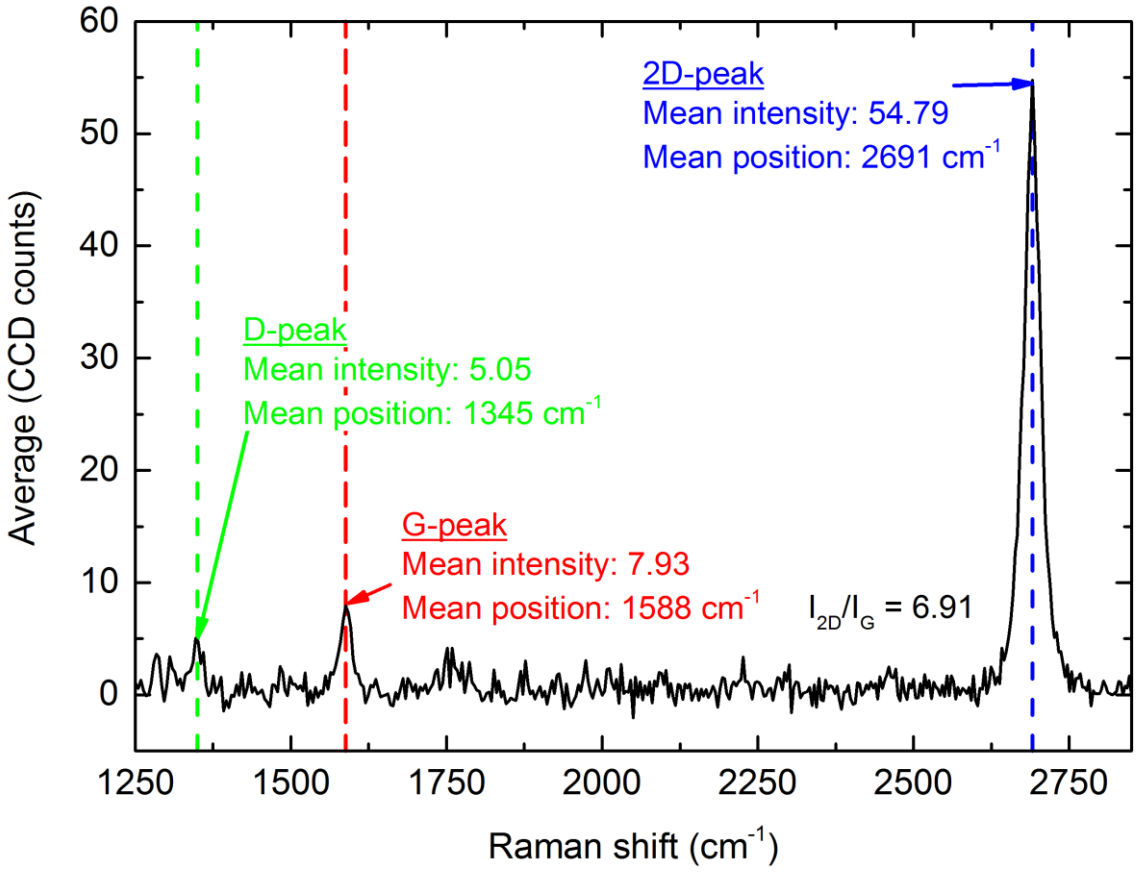

Figure 4.11: *Ten-point average Raman spectrum of the GNR-SAW device used for measurements in Section 6.3.1 (GNR1). The background lithium niobate spectrum has been removed.*

is higher than the typical values reported in the literature [129, 131]. However, the influence of the lithium niobate substrate on the peak heights is unclear (even after removing the lithium niobate Raman spectrum), and others suggest that $I_{2D} / I_G \geq 2$ is sufficiently characteristic of monolayer graphene [189]. The full-width-half-maximum of 30 cm^{-1} for the 2D band is also consistent with monolayer graphene, and the low intensity D band implies that the quality of the graphene is high. This is further evidence that the modified PMMA transfer technique leads to good quality graphene films.

4.8 Sample Mounting, PCB Electroplating, and Wire Bonding

Devices with satisfactory graphene coverage were mounted on copper printed circuit boards (PCBs). A router was used to create the tracks in the PCB, and sharp corners were avoided to reduce reflection of the radio frequency (RF) signal used for SAW generation (Section 4.10.1). A ~1 μm-thick layer of gold was deposited via electroplating on the surface of the PCB so that gold wire bonds could be made to the electrodes on the device. A commercially-available (Intertronics) system was used for this purpose, and a mask of Kapton tape was used to ensure the gold was deposited only in the required regions. The PCB was connected to the negative terminal of a 6V DC power supply sourcing a 100 mA current, forming the cathode. A gold electroplating pen was connected to the positive terminal of the power supply, forming the anode. The circuit is completed by touching the pen to the PCB, depositing the gold cations. Once complete,

excess chemicals were washed with deionised water and the PCB placed in acetone for several hours to remove adhesive resides from the mask.

SAW devices were mounted on the PCBs using an epoxy. The epoxy was mixed in a ratio of 1:1 with a hardener to cross-link the polymers, and cured on a hotplate at 120°C for 15 minutes. This method of binding the device to the PCB was found to be the cleanest, most permanent approach. A wire bonding system was used to connect the IDTs and the Cr/Au electrodes to the appropriate tracks on the electroplated PCB. Wire bonding is the process of making interconnections between components ultrasonically. A gold wire (diameter as small as 15 μm) threaded through a wedge made from silicon carbide was pressed against the PCB and vibrated at high frequency for a few milliseconds until it melted. After the vibrations stopped, the wire cooled and solidified. The required length of wire was unwound from a spool and the wedge reapplied to make a similar connection at the contact/IDT on the device. Creating durable wire bonds was extremely challenging. The presence of organic chemical residues (including graphene) caused the Cr/Au contact to slip upon application of the ultrasonic pulse. This effect was minimised by shaping the graphene with e-beam lithography, and it was found that bonding to the gold electrodes was easier if the sample was heated to 150°C. Bonding to the aluminium IDTs, however, proved more difficult. It is a recognised problem that aluminium-gold alloys formed during wire bonding can lead to mechanical failure of the bond [190]. In contrast to wire bonding to the gold contacts, bonding to the IDTs had a higher success rate when performed

at room temperature. It was occasionally necessary to stick the wire bonds to the IDTs with a small quantity of silver conductive paint, applied at ~100°C, although this is not an ideal solution as the IDTs can easily become shorted out. SMA connectors were then soldered to the PCB tracks leading to the input and output IDTs, and wires were soldered to each track for electrical characterisation of the graphene.

4.9 Summary of Devices Tested

Table 4.1 contains a full list of the completed devices and the measurements they were used for. Device Graphene1 was fabricated by Dr. Lokeshwar Bandhu.

Table 4.1: *A list of the completed devices, the graphene structuring, and the measurements they were used for.*

Sample ID	**Graphene Dimensions**	**Measurements**
Graphene1	Continuous graphene, 3 mm x 3 mm Contact separation: 300 μm (A – B) 200 μm (B – C) 500 μm (C – D)	Examining the photoresponse of the acoustoelectric current in graphene (Chapter 5).

GNR1	500 nm-wide GNRs, 2 mm x 3 mm array. Every 10 μm, perpendicular 'bridge' GNR inserted of width 500 nm. Contact separation: 300 μm (A – B) 200 μm (B – C) 500 μm (C – D)	Examining the acoustoelectric current generated in GNR arrays (Chapter 6).
GNR2	Identical to GNR1.	As above.
GNR3	Similar to GNR1, but without bridge structures.	As above.
GNR4	Identical to GNR3.	As above.
GNR5	Arrays of 200 – 600 nm-wide GNRs on the same SAW delay line. Each array 400 μm wide. Every 10 μm, perpendicular 'bridge' GNR inserted of width 500 nm. Contact separation / GNR width: 200 μm / 200 nm (A – B) 260 μm / 350 nm (A – C) 320 μm / 400 nm (A – D) 380 μm / 600 nm (A – E) 480 μm / 500 nm (A – F) 420 μm / 300 nm (A – G) 360 μm / 100 nm (A – H)	Examining the width dependence of the acoustoelectric current in GNR arrays (Chapter 6). Examining the photoresponse of the acoustoelectric current in GNR arrays, as a function of GNR width (Chapter 7).

Device fabrication proved challenging for several reasons. The devices listed above are those successfully fabricated from 40 – 50 SAW device substrates, representing a yield of 12 – 15 %. Positioning of the graphene monolayer on the SAW device such that it did not short out the IDTs was difficult, since it is not possible to touch the graphene/PMMA layer using fine-nose tweezers without destroying it. Additionally, PMMA delamination frequently occurred during the removal of the aluminium film after electron-beam lithography. It is unclear what lead to this, and it is speculated that there is weaker van der Waals bonding between PMMA and $LiNbO_3$, compared to PMMA and Si/SiO_2, or that there is a higher bond energy between aluminium and PMMA than $LiNbO_3$ and PMMA. PMMA adhesion to the substrate may be improved by varying the PMMA thickness and bake duration, as has been explored when it is deposited on silicon [191]. However, this would require significantly further work. Even among the completed devices listed in Table 4.1, not all contacts pairs had continuous graphene between them, with such damage likely arising during the PMMA transfer process. Wire bonding between the aluminium IDTs and the electroplated gold on the circuit board typically required 10-20 bonding attempts before a successful bond was formed (as discussed in Section 4.8), and future work should optimise this procedure.

Following completion of the measurements presented in this thesis, a conductive protective coating under the trade name Electra 92 has been brought to market to enable e-beam lithography on insulating substrates. It is applied via

spin coating on top of a cured PMMA layer, and removed with deionised water. This would remove the need to deposit an aluminium layer on top of the PMMA prior to e-beam lithography, which could resolve the issue of PMMA delamination. Further, MF319 aluminium developer would no longer be required, the effects of which on graphene are unreported.

4.10 Experimental Setup

During all measurements, the device under test was placed in a vacuum chamber at a pressure of 6.3 x 10^{-6} mbar at room temperature. Continuous vacuum pumping helped prevent the accumulation of dopants such as water [63, 188] (the effects of which are discussed in detail in Section 5.3), as well as reducing SAW attenuation via mass loading by air. A schematic of the measurement system is shown in Figure 4.12.

4.10.1 Generation and Detection of SAWs

Surface acoustic waves were generated using a Hewlett-Packard 8648C RF signal generator with a maximum output power of +20.0 dBm (100 mW). The signal was applied to the input IDT via a SMA vacuum feedthrough to the connector soldered to the PCB. The IDT converts this into SAWs which propagate in both directions perpendicular to the IDT aperture. Therefore, 50% of the input power does not contribute towards measurable SAWs, known as insertion loss.

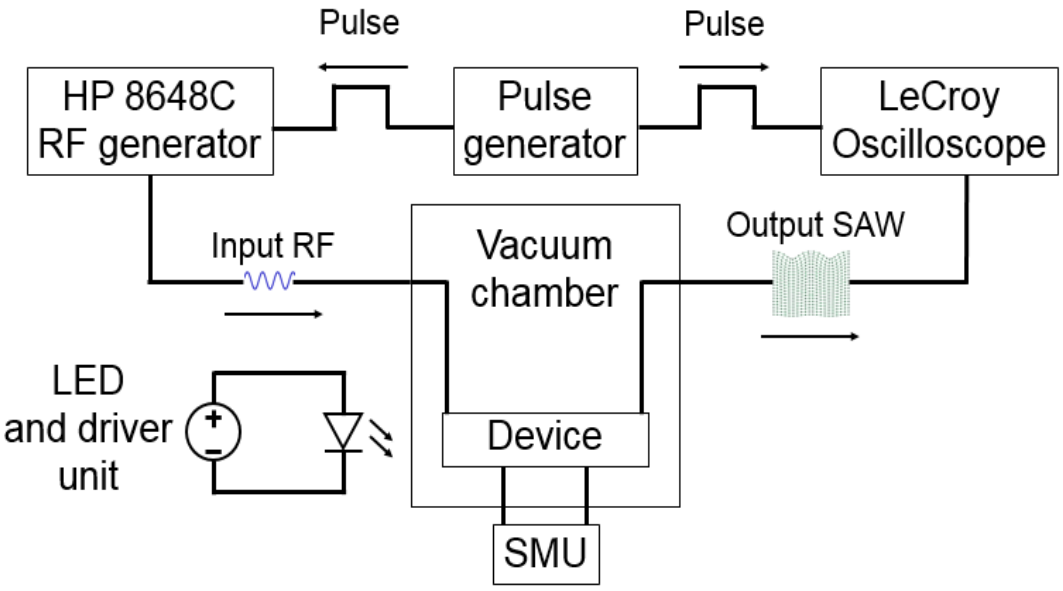

Figure 4.12: *Schematic diagram of the measurement system.*

The SAWs propagating in the direction of the output IDT interact with the graphene or GNR arrays. A LeCroy WaveRunner 204Xi-A digital oscilloscope connected to the output transducer was used to determine their amplitude. This enabled the SAW intensity and relative SAW amplitude to be estimated, discussed below.

4.10.2 SAW Intensity and Relative Amplitude Measurements

For consistency with literature reports (see, for example, [17, 18]), the measured acoustoelectric current was characterised as a function of SAW intensity. It can be shown (Appendix A) that the SAW intensity I_{SAW} is given by:

$$I_{\mathrm{SAW}} = \frac{1[\mathrm{mW}]}{\sqrt{2}} \times 10^{P_{\mathrm{in}}[\mathrm{dBm}]/10} \times \frac{V_{\mathrm{out}}}{V_{\mathrm{in}}} \times \frac{1}{d} \quad (4.1)$$

where P_{in} is the power of the RF signal generator in dBm, V_{in} is the voltage of the signal applied to the input IDT, V_{out} is the voltage measured across the output IDT, and d is the transducer aperture in metres. When determining I_{SAW}, the RF signal was modulated using a 300 ns pulse with a repetition period of 1.5 μs (20% duty cycle). The SAWs had a transit time between the input and output IDTs of ~1.4 μs, enabling sequential pulses to be distinguished from each other and V_{out} to be measured more accurately. Each measurement of V_{out} represented the mean of 128 waveform acquisitions by the oscilloscope. It was necessary to calculate I_{SAW} as a function of SAW frequency as well as input power, to account for frequency-dependent transduction losses of the RF signal. It was confirmed that SAWs could only be generated when the frequency of the RF signal coincided with a resonance of the IDTs by measuring V_{out} at randomly-selected, non-resonant frequencies. In each of these cases, $V_{\mathrm{out}} = 0$ V.

The relative SAW amplitude can be calculated and compared with the manufacturer's frequency response data shown in Figure 4.1, via Equation 4.2:

$$\text{Relative amplitude (dB)} = 20 \log_{10}\left(\frac{V_{\mathrm{out}}}{V_{\mathrm{in}}}\right) \quad (4.2)$$

Frequency response measurements can provide an assessment of device performance and give insight into the effect of graphene patterning on the acoustoelectric interaction (Section 6.3.2).

4.10.2.1 Frequency Response – Graphene1

SAWs of frequency 33 MHz and 355 MHz were used for acoustoelectric current generation in device Graphene1 for the measurements in Chapter 5. This allows the graphene's conductivity to be examined on different length scales (~60 and ~6 μm respectively). Via Equation 4.2, the relative SAW amplitudes at these frequencies were respectively calculated as -37.4 dB and -63.2 dB. The lower amplitude SAWs measured in Graphene1 compared to the values reported by the manufacturer could be caused by several mechanisms. The device has undergone several additional stages of processing that may have introduced some surface roughness. Since SAWs are inherently sensitive to surface damage, sources of SAW reflection or scattering will reduce the measurable voltage across the output IDT. Also, any difference in ambient pressure and temperature between the two measurements could lead to mass loading of the substrate, resulting in SAW damping. Furthermore, impedance mismatches between the PCB and the SMA connectors, for example, would cause RF reflection, leading to the generation of lower-amplitude SAWs. Lastly, the SAWs propagating in Graphene1 have interacted with the graphene monolayer, which leads to SAW attenuation via the acoustoelectric effect [164, 165]. A full frequency response for Graphene1 was reported by Bandhu in Refs. [178, 17], where it was also confirmed that acoustoelectric currents could only be generated when the frequency of the signal applied to the input IDT was equal to one of its resonances.

4.10.2.2 Frequency Response – GNR1-5

In measurements of the acoustoelectric effect in graphene on identical SAW substrates, Bandhu [178] found that between similar SAW devices the SAW intensity was approximately the same, for a given frequency and applied RF power. This was confirmed in the devices studied here by measuring the frequency response of GNR3 and GNR4 (Section 6.3.2). Unfortunately, device GNR1 was damaged before a frequency response measurement could be taken. Assuming that the frequency response of identical devices is approximately the same, the frequency response and SAW intensity values calculated for device GNR2 were used to interpret the measurements made on GNR1. Lower SAW amplitudes were measured in all devices compared to those reported by the manufacturer, as with Graphene1. Poor signal-to-noise ratios in measurements of V_{out} for device GNR5 are thought to be caused by the numerous Cr/Au electrodes on the delay line with spacing on the scale of the SAW wavelength acting as resonant structures that attenuate, or introduce RF noise into, propagating SAWs. Therefore, SAW intensity and frequency response measurements were not made for this device.

4.10.3 Detection of Acoustoelectric Current

For the generation of a continuous acoustoelectric current, continuous-wave SAWs were applied to the input IDT. A Keithley K2400 source-measurement unit (SMU) was used to measure the acoustoelectric current, in the absence of a bias voltage. During each measurement, background current sources were accounted for by recording the acoustoelectric current in the absence of SAWs, and

subtracting the mean value (measured over approximately 2 hours) from those measurements conducted in the presence of SAWs. These were in the range of a few nanoamperes.

A similar configuration was used for measurements of the graphene/GNR array conductivity; a current was applied in the range -10 μA to +10 μA, and current-voltage characteristics obtained via the two-probe technique. Currents of higher magnitude could potentially cause permanent damage to the device. Given the size of the gold electrodes, their contact resistance was assumed to be negligible [192] compared to the resistance of the large-area graphene/GNRs. However, future work should investigate the possibility of using the four-probe method to determine the contact resistance. There is presently conflicting information whether graphene-metal contact resistance is dominated by a difference in graphene and metal work function [193], or the area of the graphene-metal interface [194]. Note that the current-voltage measurements were performed in the absence of SAWs.

4.10.4 Photoresponse Measurements

The photoresponse of the acoustoelectric current was characterised under illumination by Thorlabs MCWHL2 and M735L2 LEDs, which had peak emission wavelengths at 450 nm and 735 nm respectively. These wavelengths were selected due to graphene's high optical absorption coefficient in the visible

wavelength range [11], as discussed in Section 2.2.2.1. A schematic of the measurement geometry for the photoresponse measurements is shown in Figure 4.13. A CaF_2 window in the vacuum chamber allowed the device under test to be illuminated. A motorised shutter was used to modulate the illumination, and the illumination intensity was controlled using a Thorlabs DC2100 LED driver unit.

The optical output power as a function of drive current, the normalised emission spectrum, and normalised emission profile as a function of viewing angle, are shown in Figure 4.14 (a) – (c) and Figure 4.15 (a) – (c) for the Thorlabs MCWHL2 (450 nm) and M375L2 (735 nm) LEDs respectively. The lines in Figure 4.14 (a) and Figure 4.15 (a) were determined by interpolating between manufacturer-quoted values of optical output power for given LED drive currents (square markers). Normalised emission spectra were provided by the manufacturer, and the lines in the emission profile are nonlinear fits to manufacturer-quoted values of relative intensity as a function of viewing angle (circular

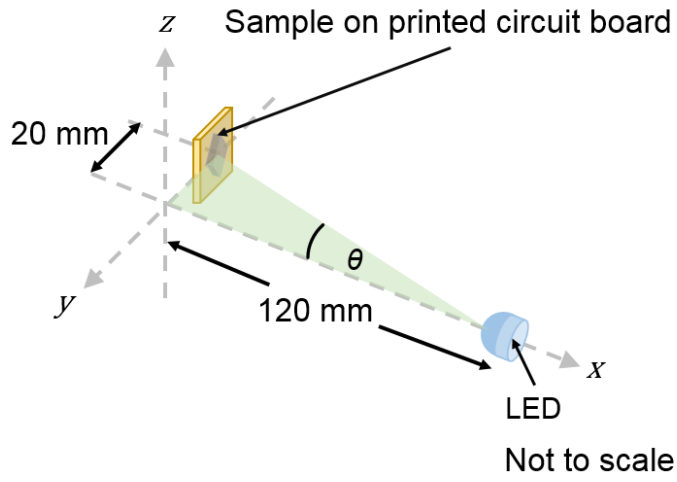

Figure 4.13: *Schematic showing the position of the sample with respect to the illumination source.*

markers). These figures enable estimates of incident light intensity and photon number to be made, as will be discussed in Sections 5.4.3 and 5.5 respectively.

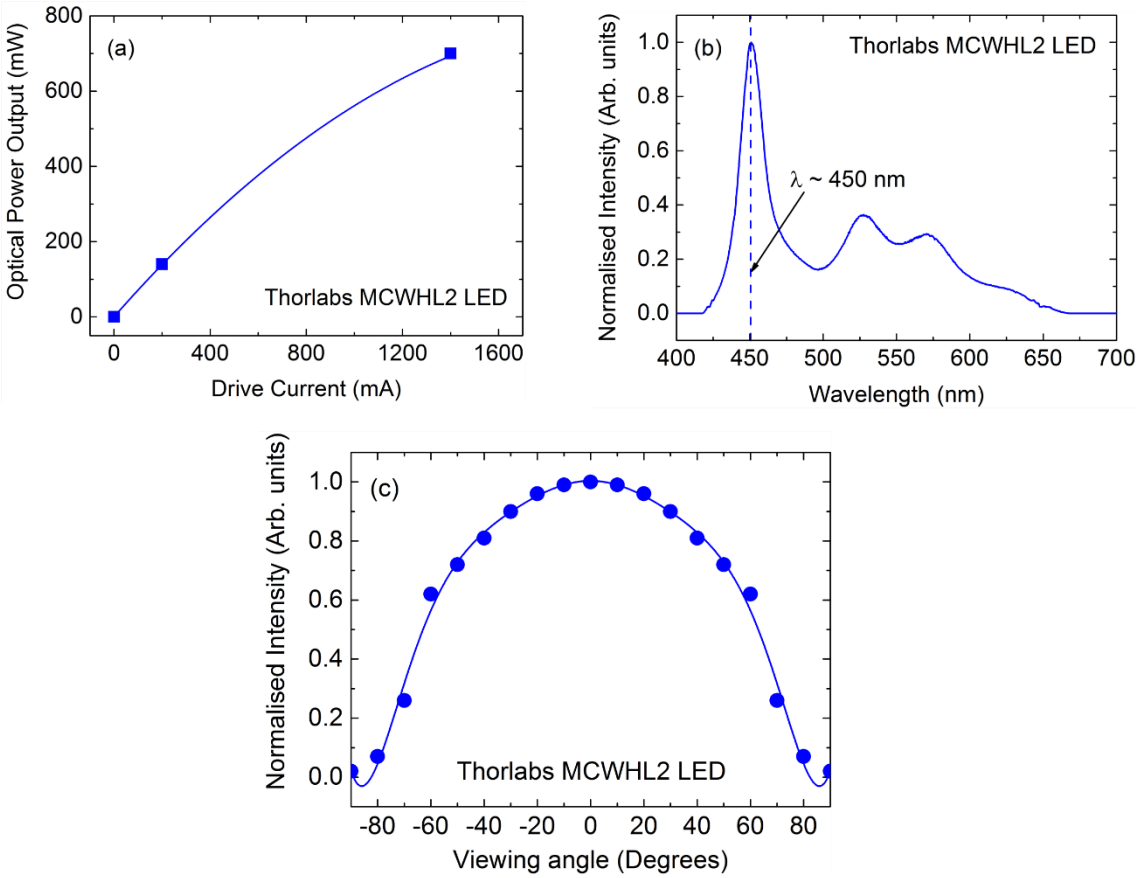

Figure 4.14: *MCWHL2 (a) optical output power as a function of drive current (b) normalised emission spectrum (c) beam profile as a function of viewing angle.*

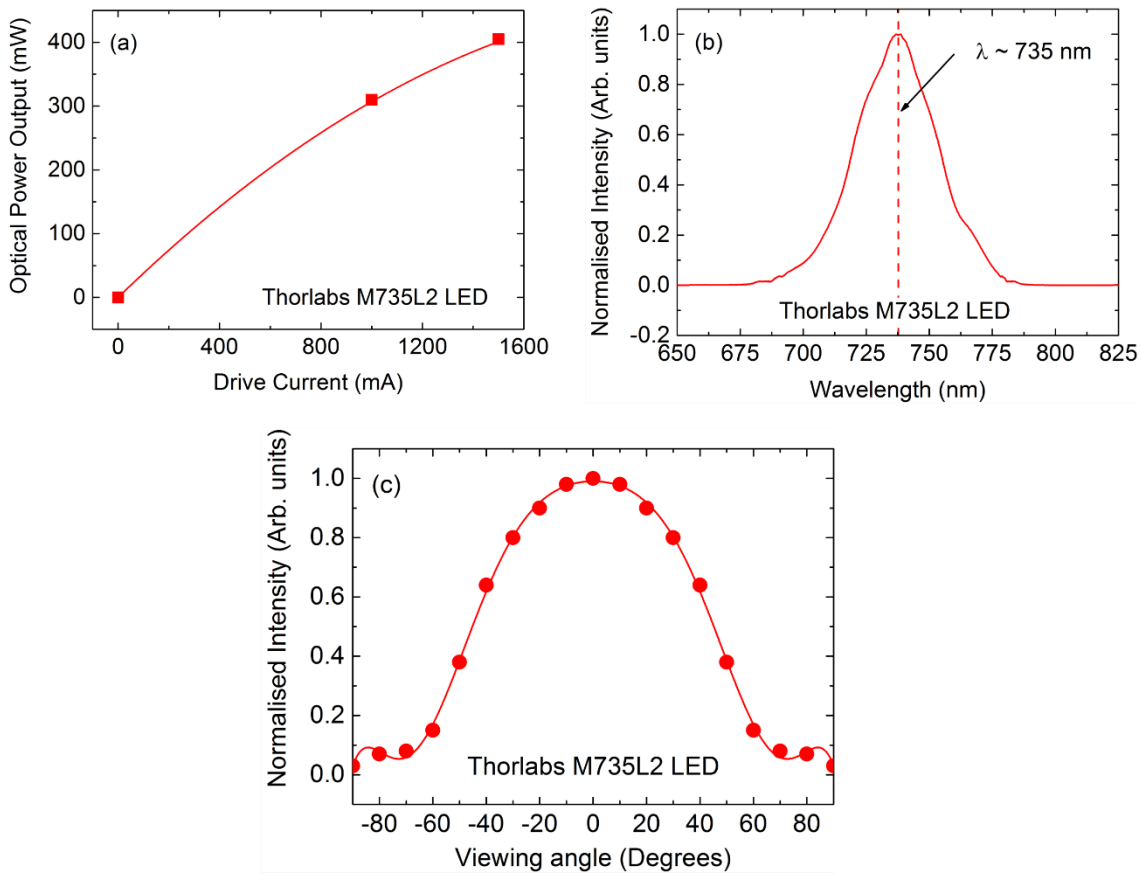

Figure 4.15: *M735L2 (a) optical output power as a function of drive current (b) normalised emission spectrum (c) beam profile as a function of viewing angle.*

4.11 Summary

Section 4.2 provided an overview of the intended outcome of the device fabrication process. In Section 4.3, the properties of the as-supplied SAW devices were discussed. The process of adding monolayer CVD graphene to the device surface using the PMMA transfer method was described (Section 4.4), and the procedure for patterning the graphene into rectangles or nanoribbons via electron

beam lithography and reactive ion etching shown (Section 4.5). In Section 4.6, the use of thermal evaporation of metals to add electrodes to the graphene/GNRs was discussed. Example Raman spectra were shown in Section 4.7. The process of mounting the devices on printed circuit boards using a silver epoxy and adding gold wire bonds to the electrodes and IDTs was outlined in Section 4.8. A summary of the devices used for the measurements in later chapters was given in Section 4.9. Lastly, the experimental setup and methods were discussed in Section 4.10.

5. Acoustoelectric Photoresponse in Graphene

5.1 Overview

In recent years, interest has grown significantly in the interactions between surface acoustic waves (SAWs) and graphene. The electric fields associated with SAWs propagating on piezoelectric materials have been exploited for acoustic charge transportation. Such acoustoelectric currents (I_{ae}) have been generated over micron- [16, 195] to millimetre-scale distances under a range of conditions in graphene [17, 18, 19, 20, 172], and could lead to the development of robust, wireless devices for use as biological and chemical sensors [19, 172], or as velocity shifters in resonator circuits [19, 20, 175]. Chivukula *et al.* [196] considered the effects on SAWs of illumination by 633 nm laser light of randomly stacked graphene flakes on $LiNbO_3$, and attributed the measured velocity shift to an increase in surface temperature due to optical energy absorption by the graphene. However, no work has been reported on the electronic properties of graphene-SAW devices under illumination, even against the backdrop of graphene and related materials being deployed for optoelectronic applications [12]. The work in this chapter, reported in Applied Physics Letters [197], marks the first exploration in this exciting field.

In Section 5.2 the device geometry and its electrical characteristics are described. The reproducibility of measurements of the resistance and acoustoelectric current under the influence of vacuum pumping is discussed in Section 5.3. In Section 5.4, the photoresponse of the resistance and acoustoelectric current is studied. The photoresponse of I_{ae} is characterised as a function of SAW intensity and frequency, as well as illumination wavelength and intensity. In Section 5.5, the classical relaxation model discussed in Section 3.4.2 is shown to successfully describe the dependencies of the acoustoelectric current on SAW intensity and frequency. The measured photoresponse is also discussed, and is attributed to the generation of a hot carrier distribution in graphene. A summary of the chapter is found in Section 5.6.

5.2 Device Characteristics

A schematic of the device used in the experiments described in this chapter is shown in Figure 5.1, designated Graphene1. This device was fabricated by Dr. Lokeshwar Bandhu. Contact pairs A-B, B-C, and C-D were separated by 300 μm, 200 μm, and 500 μm respectively. Full details of the device fabrication process are provided in Sections 4.2 to 4.7. All measurements presented in this chapter were made between contact pair A-B, due to difficulty maintaining a wire-bond on the bond pads of electrodes C and D. This is likely due to organic chemical residues causing the wire-bonder wedge to slip on the gold contact [190].

The resistance of the graphene was measured following the technique outlined in Section 4.10.3. Since the electrical contacts were of large size (3 mm x 20 µm), contact resistance was assumed to be negligible [192]. A 10 µA DC current was sourced between electrodes A and B, and the voltage measured in the absence of SAWs. A resistance of R = 28.8 kΩ was extracted via Ohm's law, corresponding to a conductivity σ^{2D} = 3.47 x 10^{-6} Ω^{-1}. This value was measured in the absence of illumination. The resistance measured here is considerably higher than the values previously reported for large-area CVD graphene monolayers on Si/SiO_2 [24] (up to ~7 kΩ at the Dirac point). There are currently no detailed studies on any detrimental effects $LiNbO_3$ may have on graphene's electrical conductivity. Rips, wrinkles, and charged impurities are known to degrade the electrical quality of graphene films [72, 74, 73, 124]. They are easily introduced during a

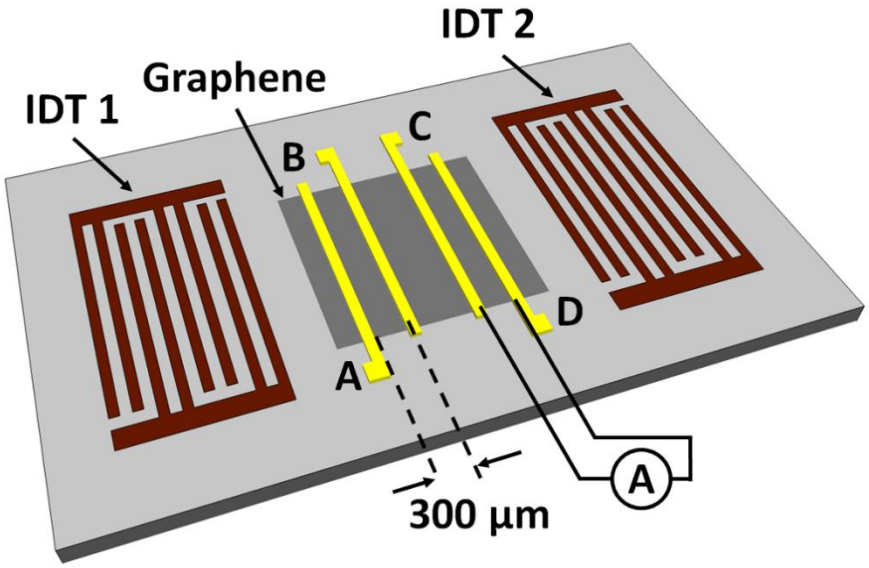

Figure 5.1: *The schematic of a device used in measuring the acoustoelectric photoresponse of graphene. SAWs propagate from IDT 1 to IDT 2.*

multi-stage device fabrication process and are the probable cause of the comparatively high resistance of the graphene on Graphene1. The polycrystalline nature of CVD graphene also introduces potential barriers that limit charge carrier mobility [198], and, because the graphene film is of such a large area, it is possible that sections have become disconnected during the fabrication process. This introduces narrow physical channels that increase the resistance of the device [199] and cannot be accounted for when calculating its conductivity.

5.3 Vacuum Dependence

Due to its 2D structure, the conductivity of graphene is readily modified by the presence of charged surface adsorbates [200, 201] or contaminants between the graphene and the substrate [9]. Polymer residues from the transfer process [123, 202], ionized impurities, or polar molecules such as H_2O and NH_3 [19, 51, 52, 63, 188, 203, 204] can lead to increased Coulomb scattering of the graphene charge carriers [74, 75], decreasing its conductivity. While thermal annealing can be used to remove such contaminants [123, 202], this approach was not preferable since, during trial graphene transfer to SiO_2/Si, water droplets trapped beneath the graphene had been found to evaporate and rupture the graphene film when heated to temperatures above 100°C. Since the graphene-SAW devices are challenging to fabricate, vacuum pumping of the measurement chamber was explored as a route towards sample cleaning prior to measurements of the acoustoelectric photoresponse. Decreasing the ambient pressure can cause

desorption of surface dopants [51, 188], and the resultant changes in conductivity have been exploited to achieve graphene-based gas sensors with up to single-molecule detection limits [51]. The influence of vacuum pumping on the electrical characteristics of Graphene1 was therefore monitored until consistent behaviour was observed.

5.3.1 Resistance

In Figure 5.2 the electrical resistance measured in Graphene1 has been plotted as a function of time, where each data point corresponds to the resistance

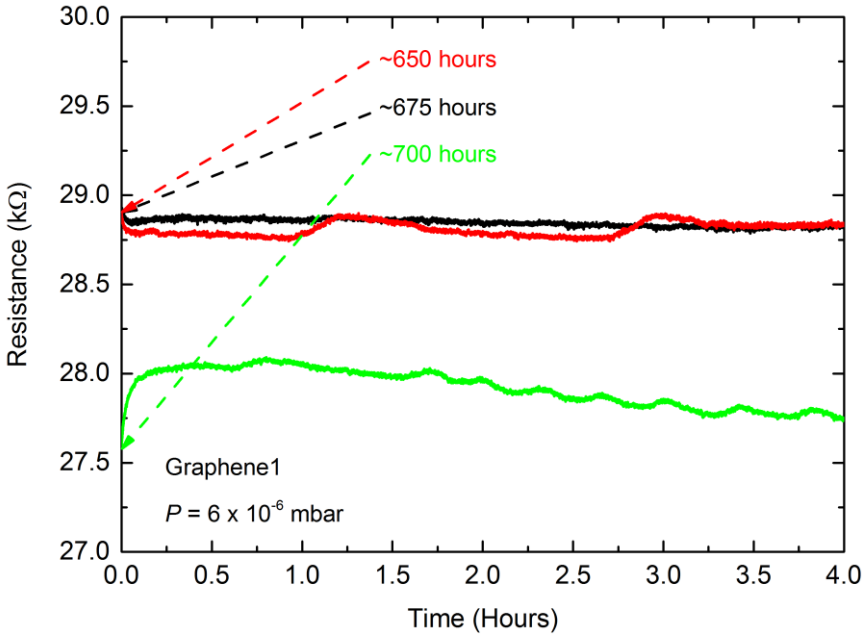

Figure 5.2: *Electrical resistance of Graphene1 over time due to vacuum pumping of the measurement chamber. The origin of the sharp change in resistance after 50 hours of vacuum pumping is unclear, nor is the modulation of the resistance in the green curve.*

measured at one second intervals when a 10 μA current was applied to the sample (see Section 4.10.3). The red, black, and green lines represent vacuum pump times of 650, 675, and 700 hours respectively. The resistance decreased by ~1 kΩ over the course of 50 hours, consistent with a decrease in the concentration of charged impurities [205]. However, the step-like change in resistance suggests that the removal of molecular surface adsorbates is not the only mechanism driving the change in the graphene's electrical characteristics. If it were, the adsorbate concentration might be expected to decrease exponentially with time, with the decreasing chamber pressure. This would be manifested as a continuous change in device resistance. A possible explanation for this is the removal of water droplets trapped between the graphene and the substrate, which are easily introduced during the fabrication process. This has been investigated by Lee *et al.* [206] in graphene-on-SiO_2/Si substrates, where a high relative humidity lead to significant wrinkle formation of the graphene. They found that the ice-like bi-layers of water molecules between the graphene and hydrophilic substrate enabled liquid water to diffuse between them due to the relatively rough morphology, elevating the graphene by 0.8 nm (compared to its 0.3 nm thickness). These water droplets formed under high-humidity conditions (up to 90% humidity was studied, with changes in thickness observed from 40% humidity), and persisted under ambient conditions for several weeks after exposure to water-rich environments. The diffusion of water in this way was proposed as a method of modulating the graphene's electrical characteristics for

humidity sensors, due to doping of the graphene by the water and a change in conductivity caused by the introduction of structural defects as water droplets grew. The formation of droplets was dependent on the hydrophilicity of the substrate, however, and such water droplet growth under graphene on $LiNbO_3$ has not been studied. Further work would be required to understand whether such changes in water concentration could cause step-like changes in resistance of the magnitude measured here. Lastly, the source of the modulation of resistance (green curve) is unclear, occurring on timescales of approximately 1 hour, but is likely caused by electrical interference.

5.3.2 Acoustoelectric Current

Since the piezoelectric interaction between SAWs and a nearby charge carrier system is implicitly dependent on its conductivity (see Section 3.4.2), a change in resistance is expected to be reflected in measurements of I_{ae}. This was explored by measuring the acoustoelectric current over time as the measurement chamber was vacuum pumped. Initially, the sign of the measured I_{ae} in Graphene1 was positive in the direction of SAW propagation, corresponding to p-type doping of the graphene [62, 64]. A typical example is shown in Figure 5.3, where I_{ae} generated by SAWs of frequency 33 MHz and intensity $I_{\mathrm{SAW}} = 0.30$ W/m has been plotted as a function of time at one second intervals, for a chamber pressure P = ~2.6 x 10^{-5} mbar. At $t \approx 1$ hour and $t \approx 3$ hours, plateaus are seen in the acoustoelectric current, and there is an underlying modulation with a period of

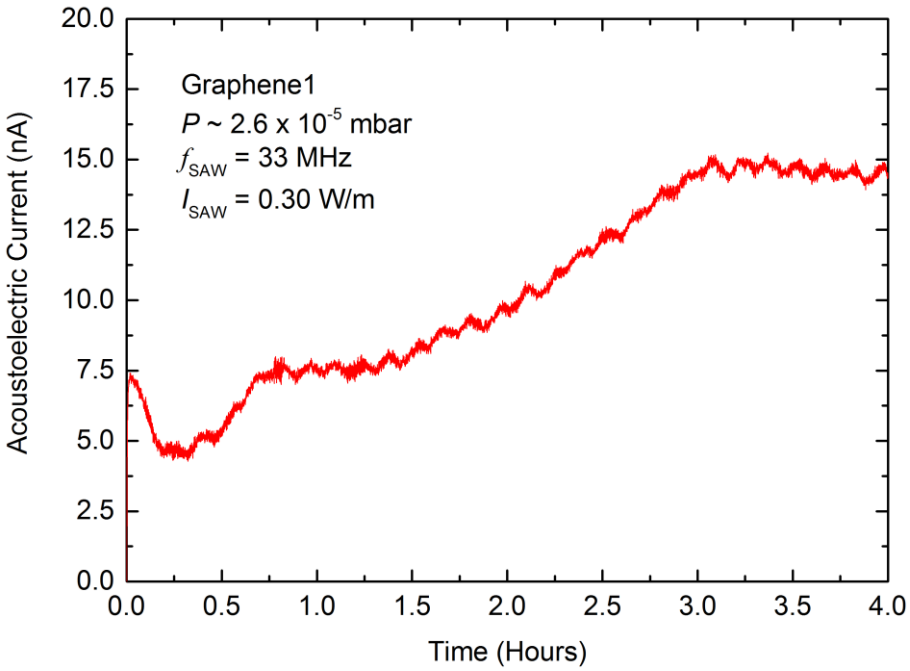

Figure 5.3: *Acoustoelectric current as a function of time in Graphene1, induced by 33 MHz SAWs. Plateaus occur in I_{ae} at t = ~1 hour and t = ~3 hours, and there is an underlying modulation of the acoustoelectric current with a period of ~15 minutes.*

approximately 15 minutes. These vanished in subsequent measurements, suggesting that they may be due to DC and low-frequency electrical interference. Measurements of the acoustoelectric current using continuous-wave SAWs are inherently sensitive to such noise. Attempts were made to drive an acoustoelectric current using a pulsed SAW, where the measured I_{ae} was fed into a low-noise current preamplifier (Stanford Research Systems SR570). The output voltage from the preamplifier was the measured on an oscilloscope, but the signal-to-noise ratio was consistently too small to obtain a repeatable

measurement of the current. For this reason, continuous-wave SAWs were used for acoustoelectric current generation.

Following extended vacuum pumping (~380 hours) the magnitude of the acoustoelectric current increased, mirroring the decrease in resistance observed in Figure 5.2. Additionally, the sign of I_{ae} became negative, indicating that the doping of the graphene switched from p-type to n-type. This is shown for consecutive measurements of acoustoelectric current in Figure 5.4 for the same SAW intensity and frequency. Repeatability of measurements of I_{ae} was assessed

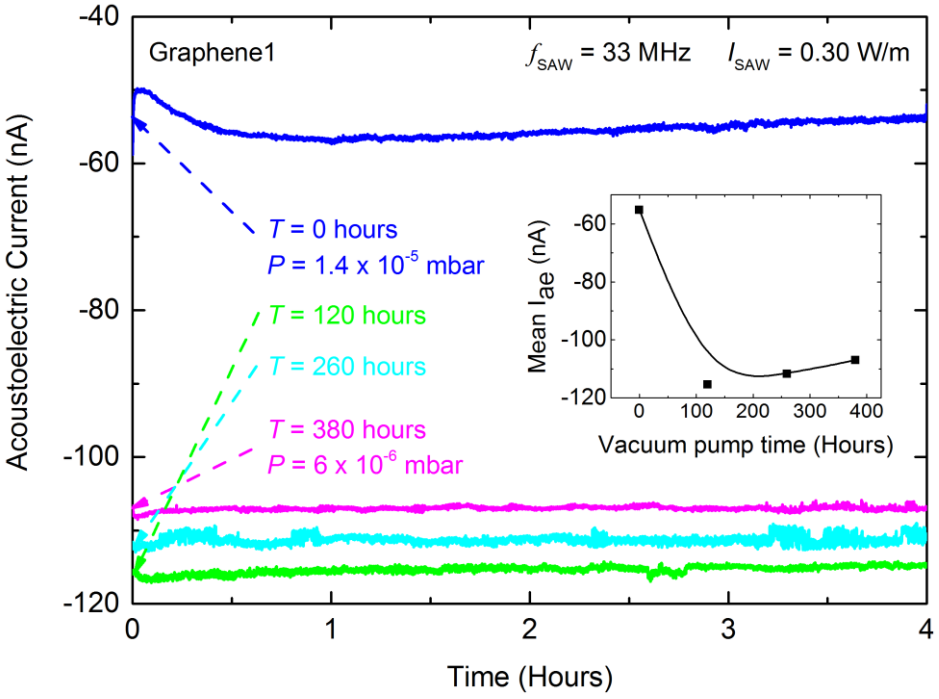

Figure 5.4: *Acoustoelectric as a function of time measured in Graphene1.* f_{SAW} *= 33 MHz. The magnitude of the current generally increases with increase pumping. Inset: Mean acoustoelectric current as a function of vacuum pump time.*

by calculating the rate of change of the mean acoustoelectric current as a function of time, using the data from the inset to Figure 5.4, which shows the mean acoustoelectric current as a function of vacuum pump time. The rate of change of acoustoelectric current in the first 120 hours was -0.50 nA / hour. In the following 260 hours, the rate of change in I_{ae} was approximately 3×10^{-2} nA / hour. Therefore, an increase in vacuum pump time is correlated with increased stability of the acoustoelectric current. Subsequent measurements of the acoustoelectric current in all devices characterised in this thesis were obtained only after at least 120 hours of vacuum pumping of the measurement chamber, based on these datasets, with continuous pumping to prevent dopant accumulation on the graphene [62].

In devices that have been prepared under atmospheric conditions and have not been thermally annealed, as here, it is believed that molecular water adsorbed to the surface is a major source of p-doping [62, 188, 202] as well as water trapped between the graphene and the substrate. Pinto and Markevich propose that surface adsorbates dope graphene either by direct exchange of charge or by participating in redox reactions [188]. In the case of molecular water, the latter mechanism can lead to the hysteresis effects commonly observed in resistance measurements of graphene field effect transistors (FETs) as the gate voltage is swept [207]. Such effects can be suppressed by annealing samples at 473 K, or vacuum pumping for at least 50 hours [188]; the considerable pumping duration necessary to remove water molecules indicates they are strongly bound

to the graphene, and is consistent with the measurements in Figure 5.4 Upon exposure to air the graphene recovered its initial p-doped configuration, probably caused by water molecules preferentially re-adsorbing to permanent defect sites such as wrinkles and rips in the graphene [208, 209, 90, 210, 202].

Lastly, it is important to note that while n-type behaviour in graphene can be achieved by chemical coating [211] or processing [212], exposure to polar molecules [213], especially ammonia [65], is a more common approach. For example, Lohmann *et al.* have demonstrated that NH_3 adsorbates lead to n-type doping in a similar fashion to p-doping by water [208], where the dipole moment due to the electron lone pair on the nitrogen atom acts as the electron source. As with water, the concentration of NH_3 molecules is inhomogeneous on the surface and p-type behaviour is recovered in air. Wang *et al.* [214] showed that electrothermal annealing of graphene FETs in a NH_3 environment induces n-doping at the edges of graphene nanoribbons and at defect sites, as the carbon atoms at these locations are much more chemically reactive than those in pristine graphene. Graphene1 was not characterised under such conditions and it is possible that the $LiNbO_3$ substrate plays a role in the observed doping. Baeumer *et al.* have spatially modulated the carrier density in graphene by creating up- and down-polarized domains in a lithium niobate substrate [215], exploiting its ferroelectric properties. However, such effects in Graphene1 would require significantly further work to understand and are beyond the scope of this thesis.

5.3.3 Contamination Rate of a Surface in Vacuum

In the preceding sections, the variation in dependence of the acoustoelectric current and device resistance was seen to evolve over timescales of tens to hundreds of hours. While molecular water trapped beneath the graphene may play an important role in modifying its electronic properties, it is interesting to estimate the rate of contamination of the surface of the device in vacuum due to water vapour in the measurement chamber. Following the analysis presented by Davies [216], the number of molecules striking a unit area in a unit time is given by:

$$F = \frac{1}{4} n \bar{c} \tag{5.1}$$

where n is the number of molecules per unit volume and $\bar{c}$ is their mean velocity. The chamber pressure p and temperature T are related to n via the ideal gas law:

$$p = n k_{\mathrm{B}} T \tag{5.2}$$

where k_{B} is the Boltzmann constant. The average velocity of a molecule is related to the thermal energy by:

$$\frac{1}{2} m c_{\mathrm{rms}}^2 = \frac{3}{2} k_{\mathrm{B}} T \tag{5.3}$$

where c_{rms}^2 is the route-mean-square velocity, which is related to the mean velocity by:

$$\bar{c} = \sqrt{8/3\pi}\, c_{\mathrm{rms}} \tag{5.4}$$

which can be combined to write:

$$p = \frac{1}{3} n m c_{\mathrm{rms}}^2 \tag{5.5}$$

Rearranging Equation 5.3 for c_{rms}^2 and inserting this into Equation 5.4, we have

$$\bar{c} = \sqrt{\frac{8 k_{\mathrm{B}} T}{m \pi}} \tag{5.6}$$

Replacing $\bar{c}$ in Equation 5.1 with the above expression, and rearranging Equation 5.2 for n, we rewrite the flux of molecules onto a surface F as:

$$F = \frac{1}{4} \sqrt{\frac{8 k_{\mathrm{B}} T}{m \pi}} \frac{p}{k_{\mathrm{B}} T} \tag{5.7}$$

Water vapour occupies approximately 4% of air at sea level for a temperature of 300 K. Therefore, when the chamber is reduced to 6.3 x 10^{-6} mbar (as in the measurements presented here), the partial pressure due to water is approximately 2.5 x 10^{-7} mbar. If 50% of incident water molecules adhere to the graphene (to account for molecules desorbing) we find F ≈ 5.0 x 10^{17} molecules per unit area per second. Water molecules have a diameter of approximately 0.3 nm and might therefore be expected to cover an area of ~3 mm x ~3 mm (the size of the graphene) almost instantly under these conditions. However, this estimate does not account for graphene's hydrophobicity [217] or the presence of other surface contaminants. It also does not account for the density of physical defects in graphene, and how atmospheric water molecules react at these sites

to induce graphene doping. The removal of molecular water under similar vacuum conditions continues to be regarded as an important mechanism for the control of graphene's electronic properties (see, for example, [63, 218]).

5.4 Photoresponse

5.4.1 Resistance

The photoresponse of the resistance of the graphene-SAW hybrid was examined following the technique described in Section 4.10.4. A Thorlabs MCWHL2 LED with a peak emission wavelength at 450 nm was used as the illumination source, giving an incident light intensity on the sample of 1.10 mW/mm^2 after correcting for the measurement geometry (The method of estimating the incident light intensity is presented in Section 5.4.3). A motorised shutter was used to modulate the exposure of the sample to the LED.

In Figure 5.5, the resistance is plotted as a function of time, measured at one second intervals. The grey, dashed lines indicate the times at which the motorised shutter is opened or closed. Upon illumination, the measured resistance rapidly increases by as much as 6%. When the shutter is closed again, the resistance quickly approaches its value prior to illumination. Such a photoresponse suggests that illumination induces a change in the electronic properties of the graphene. Since the acoustoelectric attenuation is modulated by the conductivity, change in the acoustoelectric current under illumination might therefore be expected.

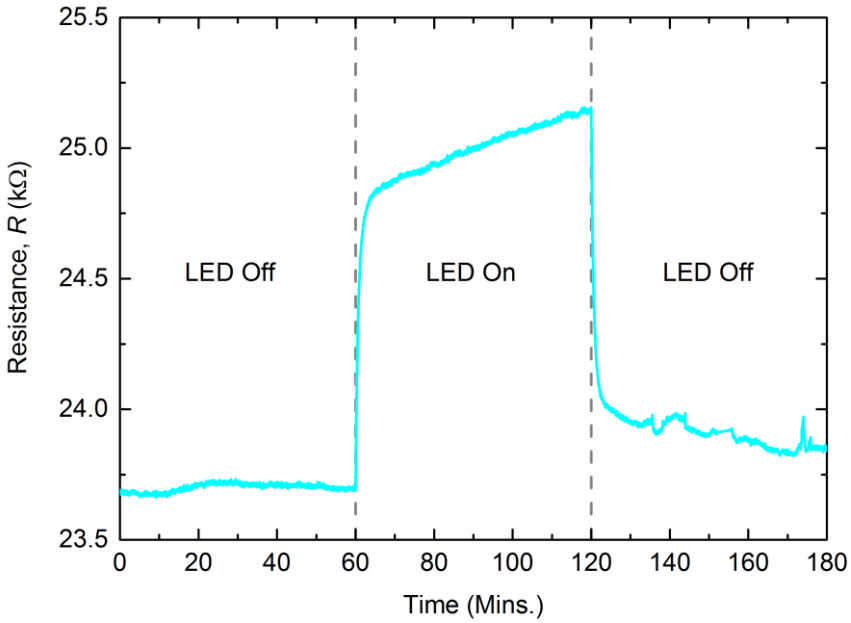

Figure 5.5: *Device resistance is plotted as a function of time at one second intervals. Under illumination, up to a 6% increase in resistance is observed.*

5.4.2 Acoustoelectric Current

The acoustoelectric current was measured over the same period, under the same illumination source, for SAW frequencies of 33 MHz and 355 MHz, plotted in Figure 5.6 (a) and (b) respectively. The RF signal generator in both cases was set to +17.8 dBm, giving a SAW intensity of (a) ~0.16 W/m and (b) ~8.00 mW/m.

The standard deviation as a percentage of the mean during the first hour of the measurements, prior to illumination, was equal to 0.34% at both SAW frequencies. This reflects the underlying stability of the graphene's electrical characteristics. Upon opening the shutter, the measured I_{ae} increased rapidly by 2.4% and 1.9% within the first 20 seconds for f_{SAW} = 33 MHz and 355 MHz

respectively, following which the rate of change of acoustoelectric current decreased. For 33 MHz SAWs the maximum increase in the magnitude of I_{ae} was 14%, while for 355 MHz SAWs it was 10%. This is mirrored by a decrease in the conductivity by up to 6%, indicated in Figure 5.6 (c) by the pink, dashed line, where σ^{2D} has been calculated from the measurements of R in Figure 5.5. A measurement of the photoresponse of the acoustoelectric current is therefore more sensitive than a simple measurement of device conductivity. The solid, blue line in Figure 5.6 (c) shows the attenuation coefficient Γ calculated from the measurements of conductivity for a SAW frequency of 355 MHz (via Equation 3.52), where a value of $\sigma_M = 1.25 \times 10^{-6}\ \Omega^{-1}$ has been used for the characteristic conductivity of lithium niobate [165]. The increase in Γ under illumination corresponds to an increase in energy transfer from the SAWs to the charge carrier system, and will be discussed further in Section 5.5. Upon closing the shutter, the acoustoelectric current generated at both SAW frequencies rapidly decreases, approaching their values prior to illumination.

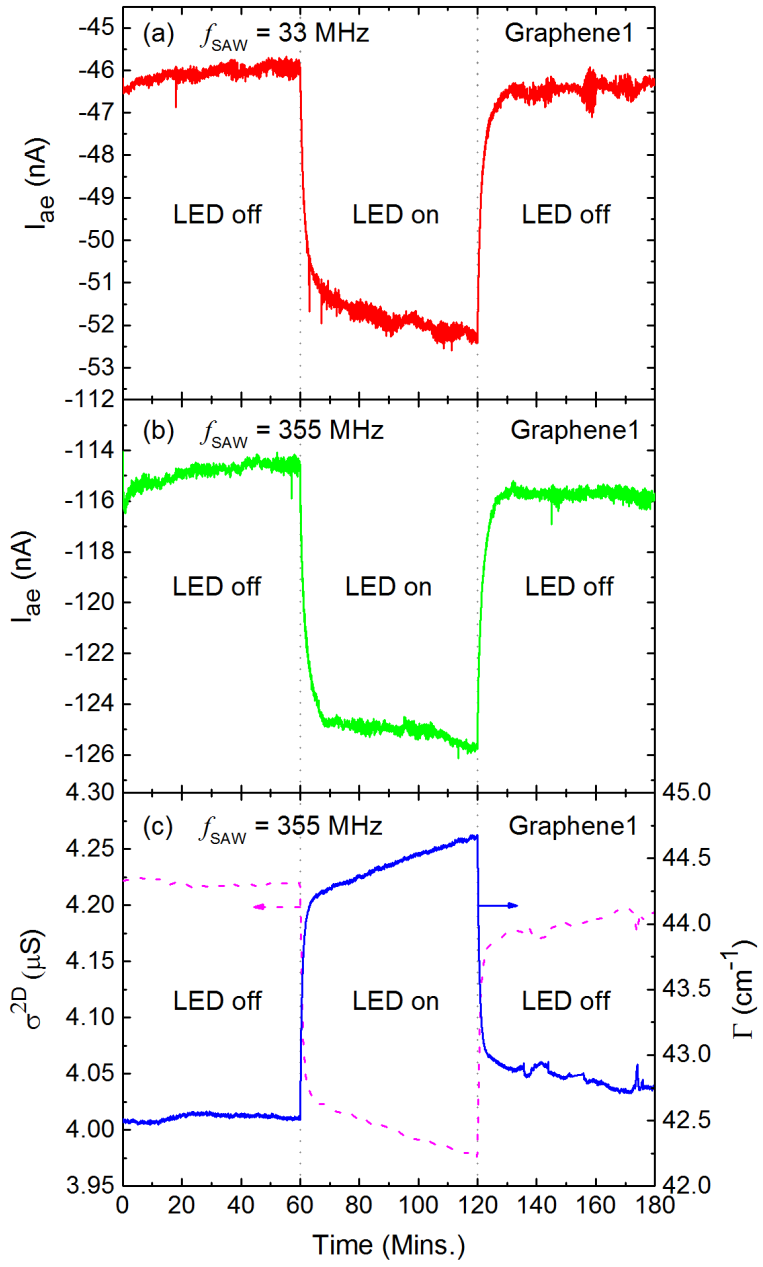

Figure 5.6: *Acoustoelectric current recorded as a function of time in Graphene1 at SAW frequencies of (a) 33 MHz and (b) 355 MHz. Illumination was provided by a 450 nm-wavelength LED of intensity 1.1 mW/mm^2. In (c) the sample conductivity (pink, dashed line) is used to calculated the attenuation coefficient (solid, blue line) via Equation 3.52.*

To determine whether the change in the measured acoustoelectric current was due to a change in the electronic properties of the graphene, the measurements were repeated for a range of SAW intensities. The magnitude of I_{ae} as a function of SAW intensity is shown in Figure 5.7 for (a) f_{SAW} = 33 MHz and (b) f_{SAW} = 355 MHz, where the SAW intensities have been estimated via the technique in Section 4.10.2. Circular points indicate the measured current when the sample was illuminated, whereas triangular points show the case in the absence of illumination. The solid lines are linear regression fits to the data, where Γ in Equation 3.52 was calculated from the classical relaxation model used to describe this interaction (discussed in Section 5.5) using the recorded values of sample conductivity in the presence and absence of illumination. At both SAW frequencies there is a clear linear dependence of acoustoelectric current on SAW intensity, with an increase in the gradient under illumination mirroring an increase in the attenuation coefficient Γ in Figure 5.6 (c). In the case of Figure 5.7 (a), the Pearson's product-moment correlation coefficient (*p*) for the acoustoelectric current as a function of SAW intensity is p = 0.999, for measurements under illumination and in the absence of illumination. In Figure 5.7 (b), it was necessary to exclude data points for SAW intensities of ~12 – 16 mW m^{-1} to attain a satisfactory linear fit (that is, where p = 0.999). The sub-linearity in the data may be due to an overestimation of the SAW intensity.

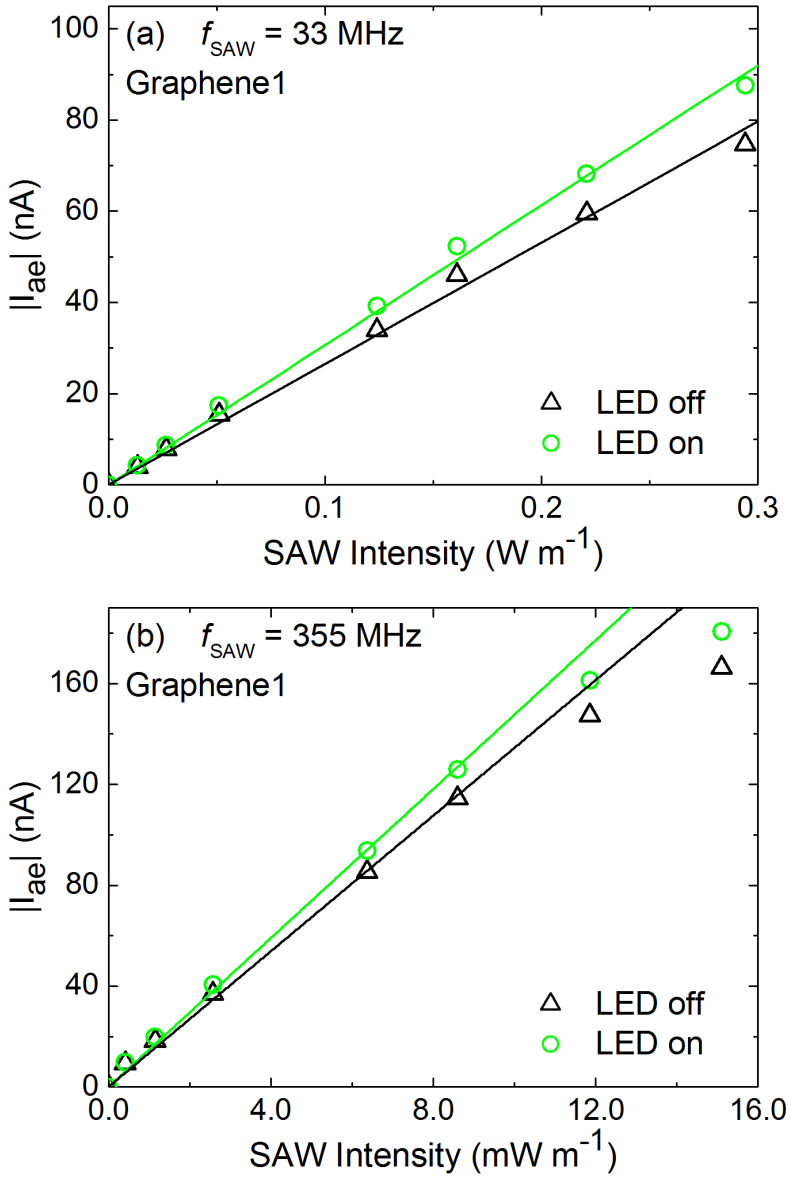

Figure 5.7: *Acoustoelectric current measured in Graphene1 as a function of SAW intensity at SAW frequencies (a) 33 MHz and (b) 355 MHz. Current measured when Graphene1 was illuminated is shown by green circles; black triangular points show the case without illumination. The sublinearity observed in Figure 5.7 (b) for SAW intensities of ~12 – 16 mW m^{-1} may be due to an overstimation of SAW intensity.*

5.4.3 Illumination Wavelength Dependence

To further probe the mechanism of the photoresponse of the acoustoelectric current, the measurements were repeated under illumination by a Thorlabs M735L2 LED, for which peak emission occurred at a much longer wavelength of 735 nm. The percentage change in I_{ae} [$\Delta I_{ae}(\%) = (I_{ae}^{\text{LED off}} - I_{ae}^{\text{LED on}})/I_{ae}^{\text{LED off}}$] was then characterised as a function of incident light intensity. The incident optical power on the sample P_0 was determined using each LED emission profile $f(\theta')$ (Figure 4.14 (c) and Figure 4.15 (c) for the 450 nm and 735 nm LEDs respectively). This was integrated over the viewing angle θ', where $f(\theta')$ has units of mW / °:

$$P_0 = 2\int_0^{\pi/2} \eta . f(\theta')\, \mathrm{d}\theta' \tag{5.8}$$

where the constant η is chosen such that Equation 5.8 yields a value of P_0 equal to the optical power output in Figure 4.14 (a) and Figure 4.15 (a) for an arbitrary LED drive current. From the schematic of the measurement geometry in Figure 4.13, the centres of the sample and LED have (x, y, z) coordinates, in millimetres, of (0, -20, 0) and (120, 0, 0) respectively. They form a viewing angle of $\theta = 1.65 \text{ x } 10^{-1}$ radians in the x-y plane. For a graphene square of width 3 mm in the y direction, the extreme faces are located at (0, -18.5, 0) and (0, -21.5, 0), forming angles of $\theta_1 = 1.53 \text{ x } 10^{-1}$ radians and $\theta_2 = 1.77 \text{ x } 10^{-1}$ radians respectively with the centre of the LED. The incident power on the sample P_{incident} is therefore estimated as:

$$P_{\text{incident}} = \int_{\theta_1}^{\theta_2} \eta . f(\theta')\, \mathrm{d}\theta' \tag{5.9}$$

For a graphene sheet of area A, the incident light intensity on the sample I is approximately given by:

$$I = \frac{P_{\text{incident}}}{A} \tag{5.10}$$

$\Delta I_{ae}(\%)$ is plotted as a function of incident light intensity in Figure 5.8 for (a) f_{SAW} = 33 MHz and (b) f_{SAW} = 355 MHz respectively. The blue squares indicate the photoresponse under illumination by the blue LED, and the red triangles show the change caused by the red LED. As with the measurements presented in Figure 5.6, the RF generator was set to +17.8 dBm, giving SAW intensities of ~0.16 W/m and ~8.00 mW/m at each SAW frequency. The percentage change in acoustoelectric current increases approximately linearly with increasing light intensity at both SAW frequencies for both LEDs. The dashed lines are intended only as a guide to the eye. In Figure 5.8 (a) and (b), over most of the intensity range the percentage change in acoustoelectric current is much greater under illumination by the blue (450 nm) LED than the red (735 nm) LED. For f_{SAW} = 33 MHz, for example, it is approximately 3x larger for an incident intensity of 0.8 mW/mm^2. The origins of this illumination wavelength dependence are discussed in the next section.

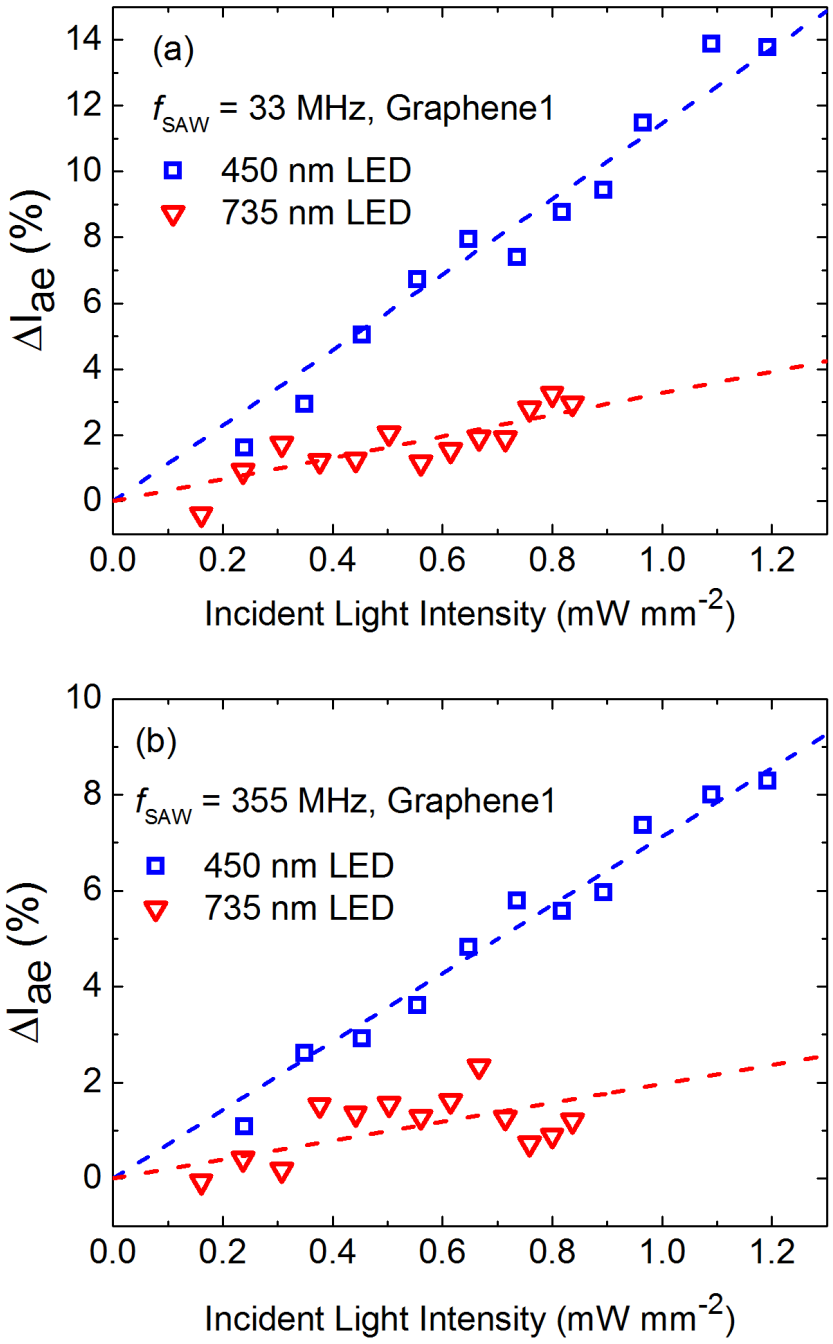

Figure 5.8: *The percentage change in acoustoelectric current under illumination by the blue and red LEDs, at SAW frequencies (a) 33 MHz and (b) 355 MHz. Dashed lines are intended only as a guide to the eye.*

5.5 Classical Relaxation Model

In Section 3.4.2, a classical relaxation model was described that explained the dependence of acoustoelectric current on SAW wavelength. In this model, the SAW attenuation per unit length, Γ, due to the piezoelectric interaction with the graphene charge carriers was given by:

$$\Gamma = \frac{K_{\mathrm{eff}}^2 \pi}{\lambda}\left[\frac{\sigma^{2\mathrm{D}}/\sigma_{\mathrm{M}}}{1+\left(\sigma^{2\mathrm{D}}/\sigma_{\mathrm{M}}\right)^2}\right] \tag{5.11}$$

where K_{eff}^2 is the effective piezoelectric coupling coefficient (0.056 in $LiNbO_3$), λ is the SAW wavelength, $\sigma^{2\mathrm{D}}$ is the graphene conductivity, and the attenuation has a maximum value for a characteristic conductivity σ_{M}. For a hybrid system based on $LiNbO_3$, this is given by:

$$\sigma_{\mathrm{M}} = \upsilon\varepsilon_0\left(\sqrt{\varepsilon_{xx}^S \varepsilon_{zz}^S}+1\right) = 1.25\times10^{-6}\ \Omega^{-1} \tag{5.12}$$

where ε_0 is the permittivity of free space, and ε_{xx}^S and ε_{zz}^S are the dielectric constants of $LiNbO_3$ at constant stress [165]. In Section 3.3.3, the effective piezoelectric coupling coefficient K_{eff}^2 was defined as the fractional difference in SAW velocity between a free surface and a metallised surface. The thin metallic layer was assumed to preserve the condition there was no net force acting on the surface. Graphene is the strongest material ever characterised, with a Young's modulus of $E = 1.0$ TPa [13]. This raises the question whether under deformation by a SAW, the condition of no stress on the surface of the piezoelectric material

due to the presence of graphene is preserved, since the graphene will resist changes to its dimensions. This may lead to a difference in SAW velocity in the case of a metallised surface, which will change the value of K_{eff}. Graphene intrinsically exhibits ripples of up to a nanometre in amplitude [219] (comparable to the SAW amplitude [195]), with a period on the order of a micron. For comparison, the SAW wavelengths applied here are on the scale of tens to hundreds of microns. Since the SAWs do not strain the graphene more than it intrinsically exhibits, we assume that the value of K_{eff} is not modified by the presence of graphene.

The attenuation decreases the energy of the SAW, leading to a proportional loss of momentum [165]. This appears as a force on the charge carrier system, leading to the dragging of charges. The resulting current density, in a closed circuit and in the absence of a magnetic field, was described by Fal'ko *et al.* [164] and Rotter *et al.* [165] as:

$$j = -\frac{\mu I \Gamma}{v} \tag{5.13}$$

where j is the acoustoelectric current density, μ is the charge carrier mobility, I is the SAW intensity, Γ is the attenuation per unit length, and v is the SAW velocity (3979 $m.s^{-1}$ in $LiNbO_3$ [1]).

The strong linear dependence of acoustoelectric current on SAW intensity observed in Figure 5.7 is consistent with Equation 5.13, where the linear fits to

the data are made using values of Γ calculated from the measured conductivity. This demonstrates the applicability of this classical relaxation model in describing the acoustoelectric effect in graphene. However, in the absence of an electrostatic gate, it is not possible to extract a value for the charge carrier mobility from measurements of the conductivity (see the parallel plate capacitor model, Section 2.2.1.1). Since the measured conductivity is much larger than σ_{M}, the attenuation coefficient may be approximated as:

$$\Gamma \approx K_{\mathrm{eff}}^2 \frac{\pi}{\lambda} (\sigma_{\mathrm{M}}/\sigma^{2\mathrm{D}}) \tag{5.14}$$

as $\sigma^{2\mathrm{D}}/\sigma_{\mathrm{M}} \gg 1$. Since $\sigma^{2\mathrm{D}} = ne\mu$, where n is the charge carrier concentration and e is the charge on an electron, the mobility dependence of the acoustoelectric current density disappears from Equation 5.13. This means that μ cannot be extracted from the gradient of the linear fit either. Despite this, the measurements in Figure 5.6 (b) show that, even for SAW intensities much smaller than those achieved when f_{SAW} = 33 MHz, the acoustoelectric current is larger for SAWs of higher frequency (smaller wavelength). This again is consistent with the acoustoelectric effect in graphene being described by the above model.

The increase in acoustoelectric current seen under illumination in Figure 5.6, mirrored by the decrease in conductivity, suggests that the photons induce a change in the electronic properties of the graphene. Figure 5.9 shows schematically the change in attenuation coefficient due to the change in conductivity under illumination. The attenuation is maximised when $\sigma^{2\mathrm{D}} = \sigma_{\mathrm{M}}$, as is the acoustoelectric current density

(Equation 5.10). As the conductivity of the graphene approaches σ_M, there will be an accompanying decrease in charge carrier concentration or charge carrier mobility.

A possible explanation of the measured photoresponse is provided by Tielrooij *et al.* [25] in recent studies of the energy relaxation process of photoexcited electron-hole pairs in doped graphene monolayers. Employing an ultrafast optical pump terahertz probe measurement technique, they observed that the energy relaxation process of photoexcited charge carriers is dominated by carrier-carrier scattering, as opposed to the emission of optical phonons, where energy is transferred to multiple secondary hot electrons in the conduction band to create a hot carrier distribution. This is an intraband electron process. The electron-hole pairs originate from an interband process; electrons are promoted from the valence band to the conduction band via photon absorption. The number of hot electrons generated increases (linearly) with increasing energy of the pump photons [220]. This is consistent with the measurements in Figure 5.8 where, for a fixed illumination intensity, a greater change in acoustoelectric current is seen under illumination by photons of higher energy (2.8 eV for the blue LED, 1.7 eV for the red LED). The hotter carrier distribution causes a decrease in graphene conductivity [12], due to a reduction in the mobility. This manifests itself in Graphene1 as change in the acoustoelectric current. The number of charge carriers in the conduction band (that is, with energy above the Dirac point) does not change due to carrier-carrier scattering, but the number of electrons with high kinetic energy increases [25]. While the photoexcited charge carrier energy relaxation process takes place on femtosecond timescales [25, 220, 221, 222], the continuous illumination of the graphene in these measurements [197]

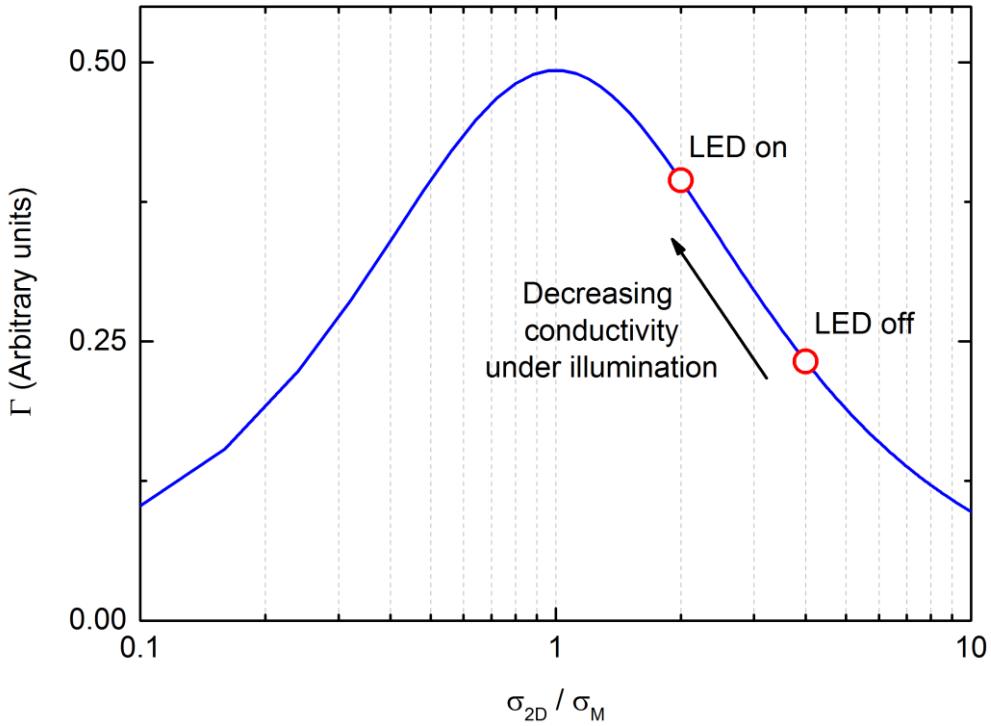

Figure 5.9: *A schematic representation of the increase in attenuation coefficient under illumination. The arrow indicates the decrease in conductivity. Γ has been calculated using Equation 5.11.*

maintains the hot carrier distribution. Once the source of illumination is removed (as suggested by Winzer *et al.* [102]), the acoustoelectric current and graphene conductivity rapidly approach their original values.

A further consideration is whether the observed illumination wavelength dependence in the photoresponse of I_{ae} arises from a significant difference in the number of photons absorbed by the graphene per second, N_{absorbed}. To estimate the number of incident photons, consider the emission spectrum (Figure 4.14 (b) and Figure 4.15 (b)) $g(\lambda)$ in

units of mW / nm, and integrate it with respect to the illumination wavelength λ in nm. A scaling factor χ is included, which is varied until the integral is equal to P_{incident} as computed by Equation 5.9:

$$P_{\text{incident}} = \int_{\lambda_1}^{\lambda_2} \chi . g(\lambda)\, \mathrm{d}\lambda \tag{5.15}$$

where λ_1 and λ_2 are the lower and upper limits of the emission spectrum respectively. If the energy of a photon of wavelength λ is given by $E = hc/\lambda$, where h is Planck's constant and c is the speed of light (the speed of light in air and vacuum are approximately equal), then the number of photons incident on the sample per second N_{incident} is:

$$N_{\text{incident}} = \frac{1}{hc} \int_{\lambda_1}^{\lambda_2} \chi . \lambda . g(\lambda)\, \mathrm{d}\lambda \tag{5.16}$$

In the range 400 nm < λ < 800 nm, the absorption coefficient of graphene $\alpha = 0.023$ [11]. Thus, the number of photons absorbed by the graphene per second N_{absorbed} is:

$$N_{\text{absorbed}} = \alpha N_{\text{incident}} \tag{5.17}$$

For an illumination intensity of approximately 0.80 mW/mm^2, the number of absorbed photons is estimated as N_{absorbed} = 7.74 × 10^{16} s^{-1} and 5.41 × 10^{16} s^{-1} for the blue and red LEDs respectively. This corresponds to an absorption of ~1.4x more photons under illumination by the blue LED. In comparison, the measured change in acoustoelectric current is ~2.7x and ~6.3x greater when the sample is illuminated by the blue LED, for SAW frequencies of 33 MHz and 355 MHz respectively. This suggests that the photoresponse is dominated by the incident photon energy.

Additionally, low-temperature characterisation of the acoustoelectric current in graphene [18] found that the length scale over which the SAW probes the graphene conductivity (approximately half of the SAW wavelength) was important. It reflected, for example, the effects of grain boundaries on conductivity due to the polycrystalline nature of the CVD graphene [72]. In Figures 5.6 – 5.8, the effect of illumination on the acoustoelectric current measured at SAW frequencies of 33 MHz and 355 MHz is very similar, up to a 14% and 8% change respectively. This might be expected if the conductivity of the graphene is dominated by a hot carrier distribution.

To discount the bolometric effect dominating the measured photoresponse, it is helpful to make a comparison to the graphene on Z-cut $LiNbO_3$ pyroelectric bolometers reported by Sassi *et al.* [138] and Gopalan *et al.* [139]. Their devices operate under illumination in the 6 – 10 μm wavelength range, where $LiNbO_3$ absorbs almost all incident light [139, 141], inducing a large temperature change in the substrate. In the visible range (400 – 750 nm), as in the measurements presented here, it has a transmittance of 70 – 75% [141]. Additionally, pyroelectrically-induced surface charge is only observed on the +Z and -Z crystal faces of lithium niobate [142, 143]. Since Graphene1 uses a Y-cut $LiNbO_3$ substrate, electrostatic gating of the graphene via a change in substrate polarization under illumination is not expected. This could be checked by applying electrodes to the top and bottom faces of the crystal and measuring any voltage generated under illumination. Lastly, the maximum illumination intensity used in the measurements presented here was 1.2×10^3 W m^{-2}. Both Sassi *et al.* [138] and Gopalan *et al.* [139] used tightly focussed

laser radiation to induce a temperature change in the $LiNbO_3$. In the case of Ref. [138], the incident power density on the graphene was up to 7.92 x 10^6 W m^{-2}.

Finally, we note that under illumination, the photoresponse of the acoustoelectric current and device resistance are seen to develop over timescales of tens of minutes. Following closure of the shutter, there is also an offset of ~1-2 nA in I_{ae} compared to the value prior to illumination (Figure 5.6 (a) and (b)) at both SAW frequencies. The conductivity too has decreased by approximately 5×10^{-8} μS. The long timescale over which these changes occur suggests that, in addition to the generation of a hot carrier distribution, the measured photoresponse is driven by non-electronic effects. The origin of these observations is not well understood, and a complete investigation is beyond the scope of this thesis. An initial consideration was charge trapping in graphene, but this persists over microsecond timescales (in graphene-on-SiO_2 [223]), and is therefore too short to explain the trends seen here. A possible explanation is the heating of the graphene under illumination, leading to heating of the substrate. This may evolve over long timescales, causing a change in graphene conductivity (in turn leading to the observed deviation in acoustoelectric current and conductivity following illumination), which is distinct from the photoresponse due to hot carrier effects.

5.6 Summary

The effect of vacuum pumping on resistance and acoustoelectric current was studied in 3 mm x 300 μm monolayer CVD graphene. Continuous vacuum pumping over hundreds of hours resulted in the doping of the graphene switching from p-type to n-type, believed to be due to the steady removal of water surface adsorbates. The photoresponse of the acoustoelectric current generated in the same sample was studied as a function of SAW intensity and frequency, and illumination wavelength and intensity. The measured linear dependence of the acoustoelectric current on SAW intensity, and the increase in the current with SAW wavelength, is consistent with a relatively simple classical relaxation model describing the piezoelectric interaction between the SAWs and the graphene charger carriers. Under illumination the acoustoelectric current was observed to increase, more than the measured decrease in graphene conductivity, while retaining a linear dependence on SAW intensity. This suggests that illumination induces a change in the graphene's electronic properties. The greater increase in I_{ae} under illumination by a blue (450 nm) LED compared to a red (735 nm) LED is consistent with the creation of a hot electron distribution. A similar response was observed at SAW frequencies of 33 MHz and 355 MHz, further supporting the idea that the graphene conductivity is being dominated by hot carrier effects.

6. Acoustoelectric Effects in Graphene Nanoribbons

6.1 Overview

Graphene nanoribbons (GNRs) are sub-micron-wide channels of graphene that can be fabricated via electron beam lithography [22, 224]. They have been demonstrated for such applications as interconnects in integrated circuits [21, 22, 83], where their current carrying ability and thermal conductivity (>10^8 A/cm^2 and 3-5 x 10^3 W/mK respectively) far exceed those of copper (10^7 A/cm^2 and ~0.4 x 10^3 W/mK respectively) [21]. Moreover, graphene plasmonics can be studied in sub-micron wide GNRs via infrared transmission measurements [23], potentially applicable to biosensing, communication, and gas sensing applications. At widths of tens of nanometres and below [84], GNRs possess an electronic bandgap that varies as a function of ribbon width, enabling their use in digital electronics where high on-off ratios are typically required [84, 68]. While electron beam lithography is suitable for processing large batches of nanoribbons, the damaged edges generated by etching through resist masks can modify the electronic properties of the nanoribbons by introducing dopants or defects [224, 225, 226]. Such changes can be probed by measurements of the acoustoelectric current in GNRs, which implicitly depends on GNR conductivity. Given the variety of potential applications of GNRs, and

the sensitivity of an acoustoelectric current to changes in conductivity, it is of interest to examine the crossover between these two fields. The measurements in this chapter mark the first steps in this direction, and have been published in Scientific Reports [227].

The acoustoelectric current was investigated in monolayer CVD-graphene nanoribbons on lithium niobate SAW devices, as a function of SAW intensity and frequency, and GNR width ranging from 200 – 600 nm. The acoustoelectric current was found to be described by the same classical relaxation model used to explain the measurements in Chapter 5. It depends linearly on SAW intensity for a given SAW frequency, and linearly on SAW frequency for a given SAW intensity, as measured in arrays of 500 nm-wide GNRs. It was also found that perpendicular 'bridge' nanoribbon structures inserted into the array with a periodicity approximately equal to the SAW wavelength could enhance the acoustoelectric interaction. As the width of the GNRs decreased, the acoustoelectric current was found to increase, under most conditions. However, for high SAW frequencies, currents measured in arrays with large spatial inhomogeneities decreased with decreasing ribbon width, indicative of the ability of the SAWs to probe electron systems on different scales, depending on the wavelength.

The electrical characteristics of the studied devices are discussed in Section 6.2, and two-dimensional spatial maps of the GNR Raman 2D and G peaks are shown. In Section 6.3, the acoustoelectric current measurements are presented, the intensity and frequency dependence is studied, and comparisons are made to a classical relaxation model describing the interaction. The GNR width dependence is also investigated, and anomalies in the current generated at high frequency in the narrowest nanoribbons are

discussed in the context of information revealed by the Raman spatial maps. A summary of the chapter is given in Section 6.4.

6.2 Device Characteristics

To study the acoustoelectric effect in graphene nanoribbons, GNR-SAW devices of two distinct designs were produced. Both were based on a 128° YX $LiNbO_3$ SAW delay line with a monolayer CVD graphene film positioned on the surface (Section 4.4). In the first design, the graphene was patterned into nanoribbons of 500 nm width, in a 2 mm x 3 mm array, shown in Figure 6.1. To help maintain electrical conductivity [23], perpendicular bridge nanoribbons were included in the array every 10 µm with a width of 500 nm. Note that the long axis of the bridge is perpendicular to the SAW wave vector. This is shown schematically in Figure 6.2. Two devices of this type were fabricated (GNR1 and GNR2).

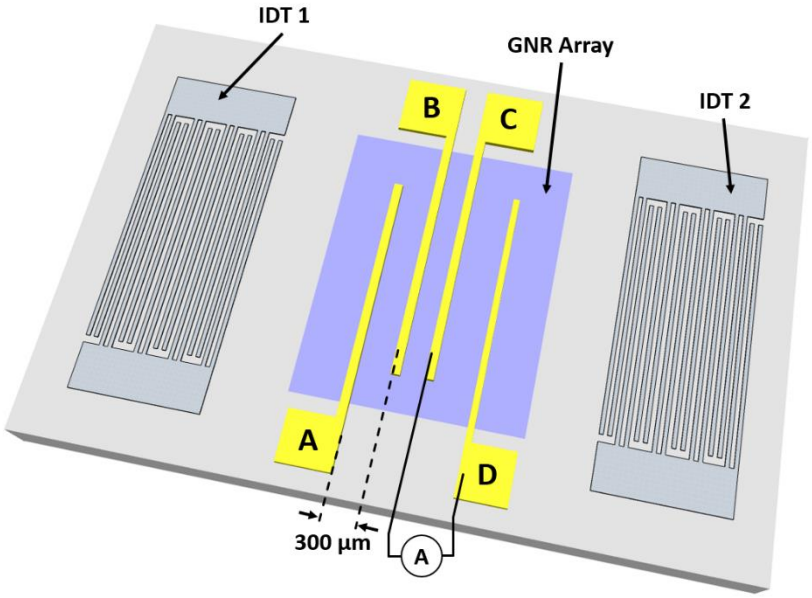

Figure 6.1: *The schematic of a device used in measuring the acoustoelectric current in arrays of 500 nm-wide graphene nanoribbons.*

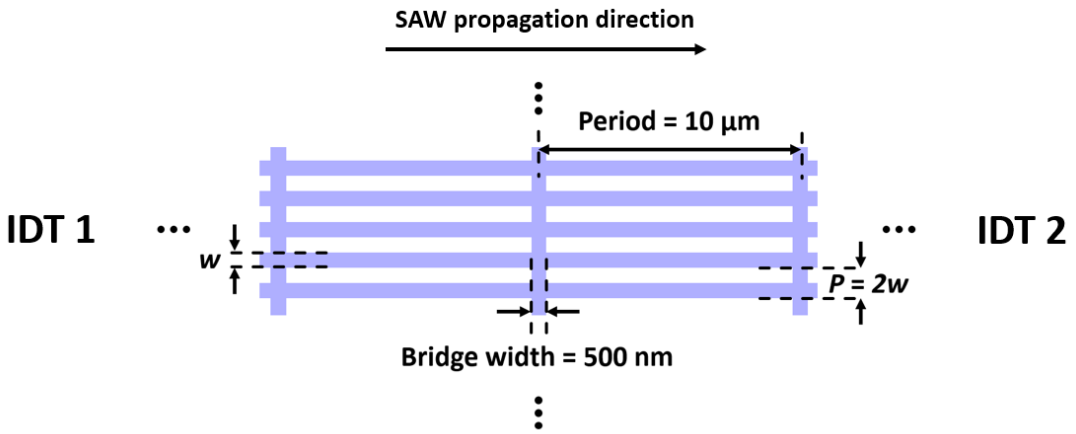

Figure 6.2: *Schematic showing the graphene nanoribbons and perpendicular bridge structures. In all cases, the bridges had a width of 500 nm. The GNR width w was varied between 100 and 600 nm. The nanoribbon repeat period P was always equal to $2w$.*

Devices that did not include the bridge structures were also fabricated (GNR3 and GNR4) to determine if bridges influenced the piezoelectric interaction between the SAWs and the GNRs. On each device, Cr/Au electrical contact pairs A-B, B-C, and C-D were separated by distances of 300 µm, 200 µm, and 500 µm respectively. All contacts had dimensions of 20 µm x 3 mm.

The second design enabled the study of the width dependence of the acoustoelectric effect in GNRs on a single substrate. CVD graphene is well known to exhibit inconsistent electrical properties between samples [10]. Subtle differences in fabrication processes can lead to different concentrations of etchant salts and PMMA residues, which can further affect performance. This approach reduced the variation in graphene quality between different GNR arrays, as each had undergone an identical fabrication process.

This also ensured that all GNRs experienced the same SAW intensity, and a more reliable comparison between the acoustoelectric measurements could be made. The design is shown schematically in Figure 6.3. Arrays of 400 µm width were defined in the acoustic beam path, laterally spaced by 20 µm from their nearest neighbours. The width of the nanoribbons in each array is indicated in colour, and were selected to evenly span the range 100 – 600 nm. Note that the physical ordering of the nanoribbon arrays on the substrate was varied by width from top to bottom, to avoid misinterpretation of the measurements due to, for example, defects that varied continuously across the graphene film. Due to the compact size of the $LiNbO_3$ SAW devices, and the desire to study a broad range of GNR widths, neighbouring Cr/Au electrical contacts were fabricated with a separation as little as 40 µm between them. This presented significant challenges during the lift-off process, and of four devices fabricated only one did not have shorted electrical

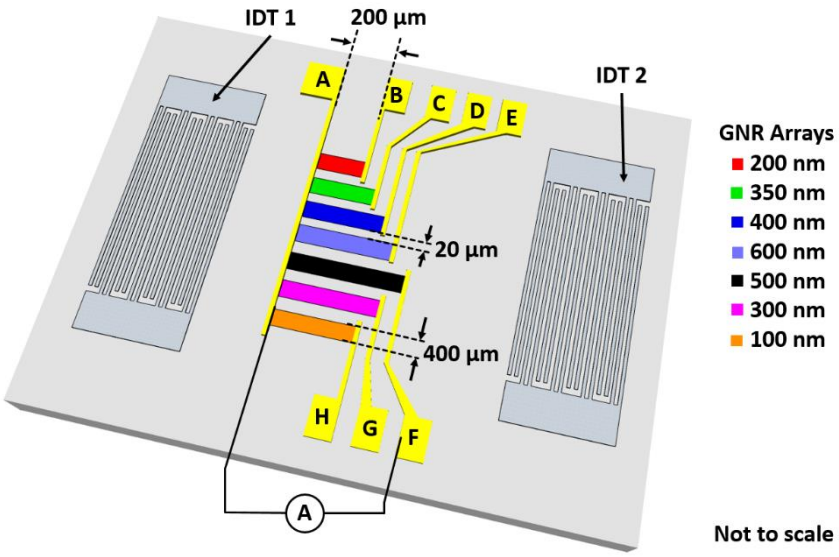

Figure 6.3: *Schematic of GNR5, used to study the width dependence of the acoustoelectric current generated in graphene nanoribbons.*

contacts (determined by inspection under an optical microscope). Further processing was undertaken only for this sample, designated GNR5. As with GNR1 and GNR2, bridge structures were included in each nanoribbon array on GNR5. For each array, a different nanoribbon width *w* was chosen, but the width of the bridges was maintained at 500 nm. The GNR arrays shared a common electrode of size 20 μm x 3 mm (contact A). Contacts B to H had a width of 20 μm, but the lengths differed to contact individual GNR arrays.

Unless otherwise stated, all measurements of devices GNR1-5 were performed under a vacuum pressure of 6.3×10^{-6} mbar, maintained via continuous pumping, to prevent the accumulation of dopants on the surface. Based on the initial instability in the measured resistance and acoustoelectric current reported in Section 5.3, devices were not characterised until at least 120 hours of vacuum pumping of the measurement chamber had elapsed.

6.2.1 Current-Voltage Measurements

The resistance of the GNR arrays was measured following the technique described in Section 4.10.3. To reduce the risk of damaging them via Joule heating, the magnitude of the source current was in the microampere range. The current-voltage characteristics of GNR1 are shown in Figure 6.4. The measured resistance of the GNRs between contacts A and B, $R_{A\text{-}B}$ = 2.11 kΩ, is significantly lower than the values for arrays on GNR2 and GNR3, for which $R_{B\text{-}C}$ = 43.10 kΩ and 0.91 MΩ respectively. In both devices, contact pairs A-B and C-D were open circuit (I-V plots not shown). There was no continuous graphene

between any of the electrode pairs on GNR4. The inconsistency of the resistance between devices indicates the challenges of obtaining continuous, consistent graphene over such large areas. The GNR conductivity measured in Graphene1 is approximately 4% of the highest values obtained for GNR1, reflecting the improved quality of the graphene transferred via the modified PMMA transfer method (Section 4.4.2.1). In Section 5.2, defects that limit the electrical performance of graphene and GNRs were discussed. These included wrinkles, tears, residues, and charged impurities [72, 73, 74, 75], among other sources. The relatively high resistance of the GNRs between contact pair C-D in GNR1, and B-C in GNR2 and GNR3, probably arises from such defects.

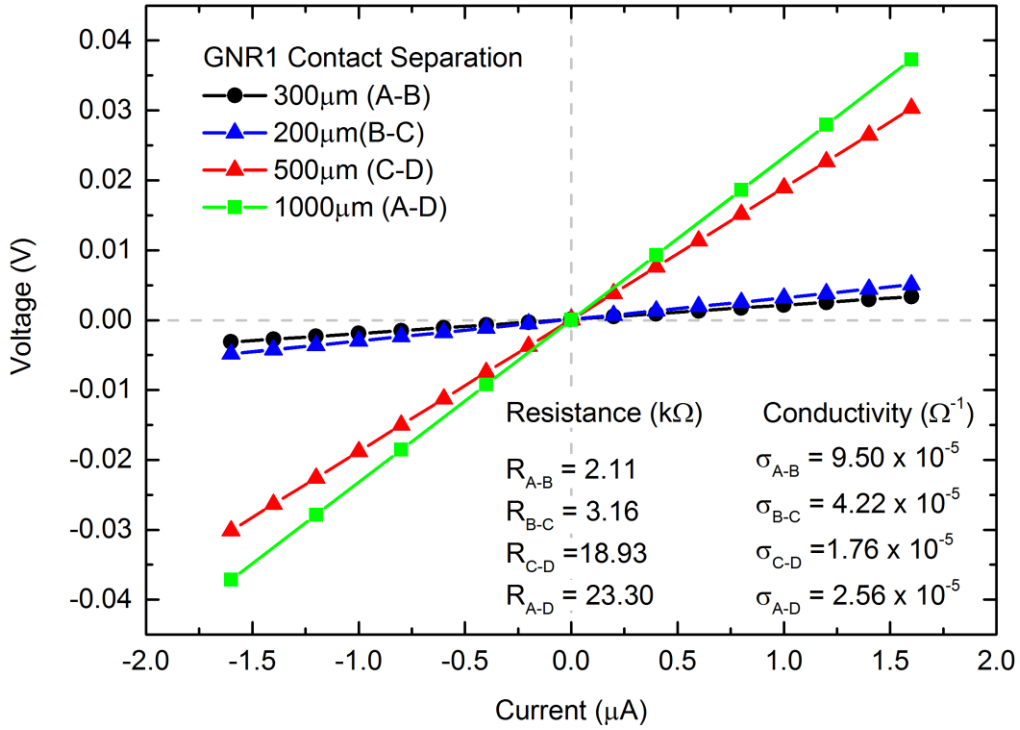

Figure 6.4: *Current-voltage measurements of the graphene nanoribbon arrays in GNR1. The electrode separation distance associated with each dataset is indicated.*

It is well known that field effect measurements of the resistance of graphene exhibit hysteresis as the gate voltage is swept [228] due to the trapping of charges in defect states. To confirm that charge transfer to and from surface adsorbates or other defects was not a significant issue, the current-voltage measurements were made by gradually increasing the magnitude of the applied current in intervals of 0.2 μA, before returning to 0.0 μA via decrements of 0.2 μA. The range was extended by 0.2 μA for each sweep. There was 0% difference in the measured voltage as a function of the applied current for consecutive current sweeps, suggesting that the effects (if any) of charge transfer to impurities at room temperature in these devices were negligible.

The current-voltage characteristics of the GNR arrays on device GNR5 were taken in a similar fashion. The measurements are plotted in Figure 6.5, and the associated conductivity has been calculated and tabulated in **Error! Reference source not found.**. I n Figure 6.5, the ordering of the plot legend reflects the physical ordering of the nanoribbon arrays on the sample. The array of 100 nm-wide GNRs was found to be open circuit and is not included in the figure or the table. The arrays of 200 nm-wide and 300 nm-wide GNRs were found to have low conductivities compared to the others on the device. Generally, however, the conductivities are similar to those observed in Graphene1 and GNR1 - 3.

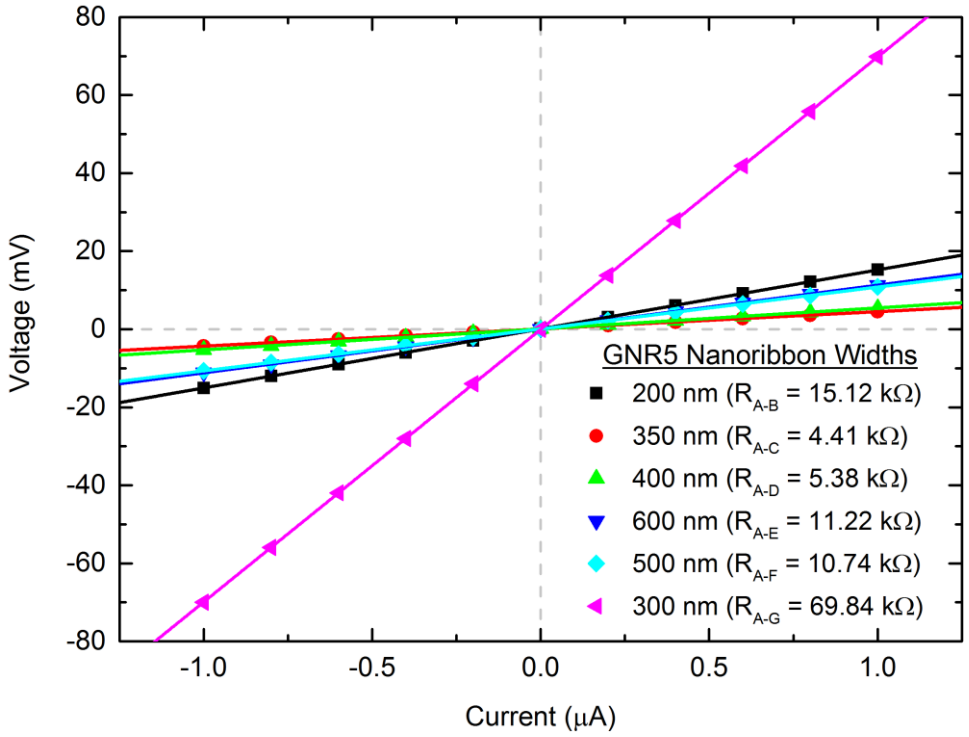

Figure 6.5: *Current-voltage characteristics of the GNR arrays on GNR5. The widths of the constituent GNRs and the associated array resistance extracted from the gradients are indicated.*

Table 6.1: *Calculated resistance, sheet resistance, and conductivity for each GNR array on GNR5.*

GNR Width (nm)	Resistance (kΩ)	Sheet Resistance (kΩ / □)	Conductivity (Ω^{-1})
200	15.12	15.12	6.61×10^{-5}
300	69.84	38.83	2.87×10^{-5}
350	4.41	3.67	2.72×10^{-4}
400	5.38	3.84	2.60×10^{-4}
500	10.74	5.37	2.05×10^{-4}

6.2.2 Raman Spectroscopy

In Section 4.7, a Raman spectrum of GNR1 was shown (Figure 4.11) that indicated the high quality of graphene attainable when the modified PMMA transfer technique is employed, which was further supported by the current-voltage measurements in Section 6.2.1. Here, two-dimensional Raman spatial maps of devices GNR1 and GNR5 are shown, as they are a useful visual aid in assessing the quality of the graphene, and will later be used in interpreting measurements presented in Section 6.3. Full details of the Raman spectroscopy technique, performed using a WITec Alpha300 system, are provided in Section 4.7.

An optical image of GNR1 is shown in Figure 6.6. The green rectangle indicates a patch of damaged graphene, visible as black marks where the graphene has rolled into

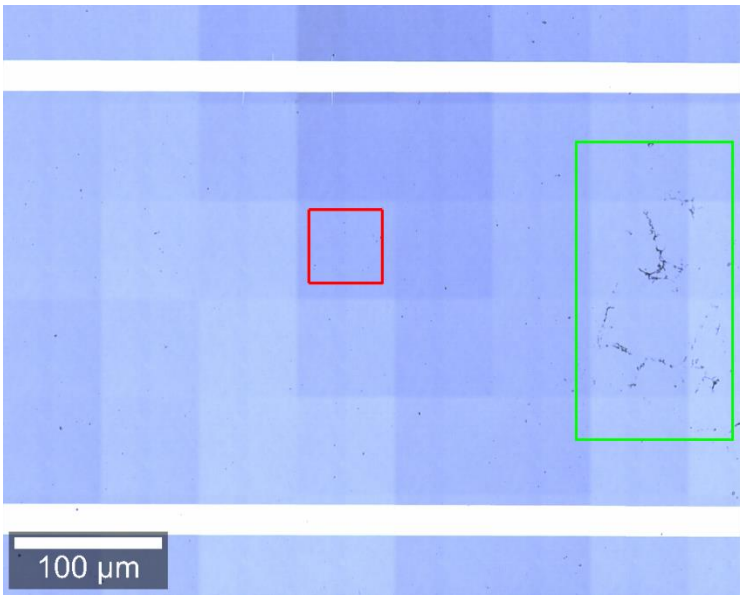

Figure 6.6: *Optical image of a region between electrodes A and B on device GNR1. The contacts appear as white bands at the top and bottom of the image.*

multi-layers, and the red square is the randomly selected region in which the Raman spatial maps of the 2D and G peaks were taken. These are shown in Figure 6.7 (a) and (b) respectively. Consistent with Raman studies of monolayer graphene on Si/SiO_2 by Gupta *et al.* [187], the 2D and G peak shifts are 2691 cm^{-1} and 1588 cm^{-1} respectively (see Figure 4.11), and the blue shift is consistent with the p-doping of graphene nanoconstrictions [90].

The bright, horizontal lines at intervals of 10 μm (pink squares) are the perpendicular bridges. The increased ratio of the 2D to G peaks at the bridges is likely due to under-dosing of the PMMA in these regions during fabrication (see Section 4.5), resulting in wider strips of graphene than intended. Bright vertical lines (green circles) are caused by stitching errors in the electron beam lithographer; the spacing of 20 μm corresponds to the size of the sub-field in our system. The blue rectangle indicates a piece of graphene that has rolled into a multi-layer structure. Associated with this feature is a high intensity D

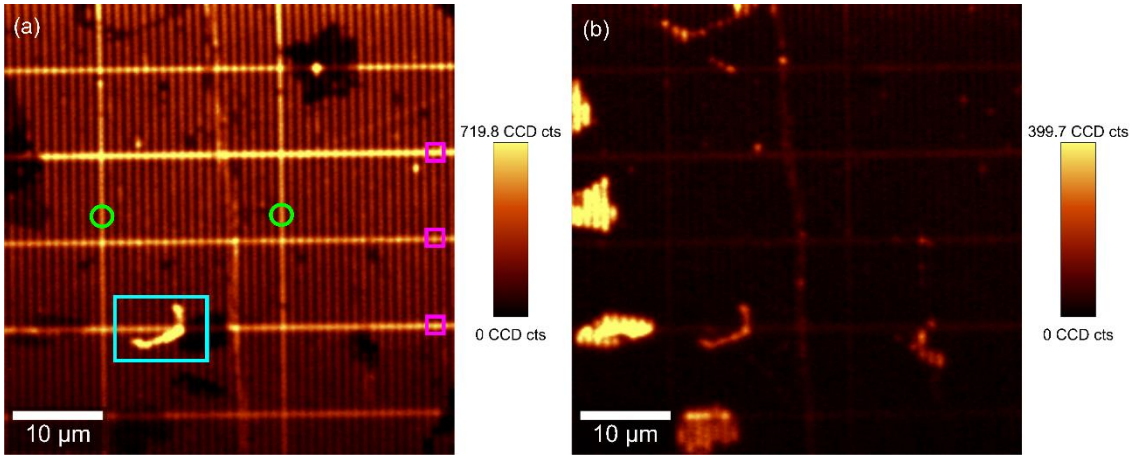

Figure 6.7: *The Raman shift (a) 2D and (b) G peaks are spatially mapped in a randomly selected region of GNR1, between contacts A and B.*

peak, consistent with disorder and defects in graphene [189]. Disconnected GNRs are visible as dark patches at identical locations in both images, and a wrinkle can be seen running vertically in both images (also associated with a strong D peak). However, the array contains few large (~10 µm) discontinuities, metallic residues, or rips. This suggests that the graphene quality is high.

In contrast, Raman spatial maps of the array of 200 nm-wide GNRs on GNR5 indicate some damage. An optical image of the device is shown in Figure 6.8 and two-dimensional spatial maps of the Raman 2D and G peaks are plotted in Figure 6.9 (a) and (b) respectively. The Raman shift associated with each peak is 2689 cm^{-1} and 1590 cm^{-1}. As in Figure 6.7 (a) and (b), horizontal lines spaced 10 µm apart correspond to the location of the bridges. Individual nanoribbons are smaller than the probe laser spot size (388 nm) and cannot be resolved, resulting

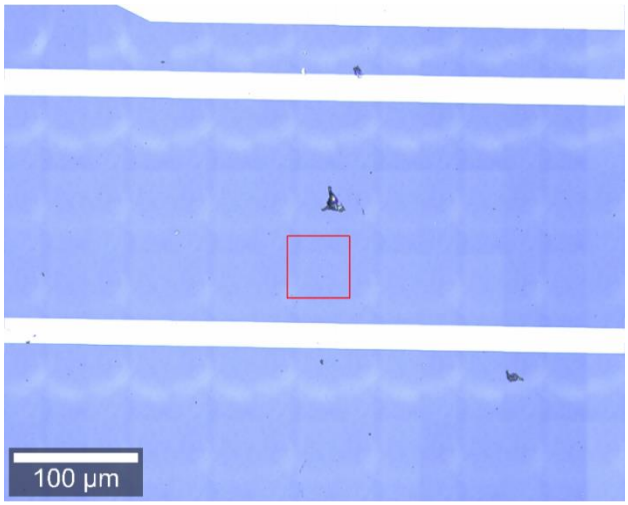

Figure 6.8: *Optical image of GNR5 between contacts A and B, connected to the array of 200 nm-wide GNRs. The red square indicates the region in which a Raman spectrum was taken.*

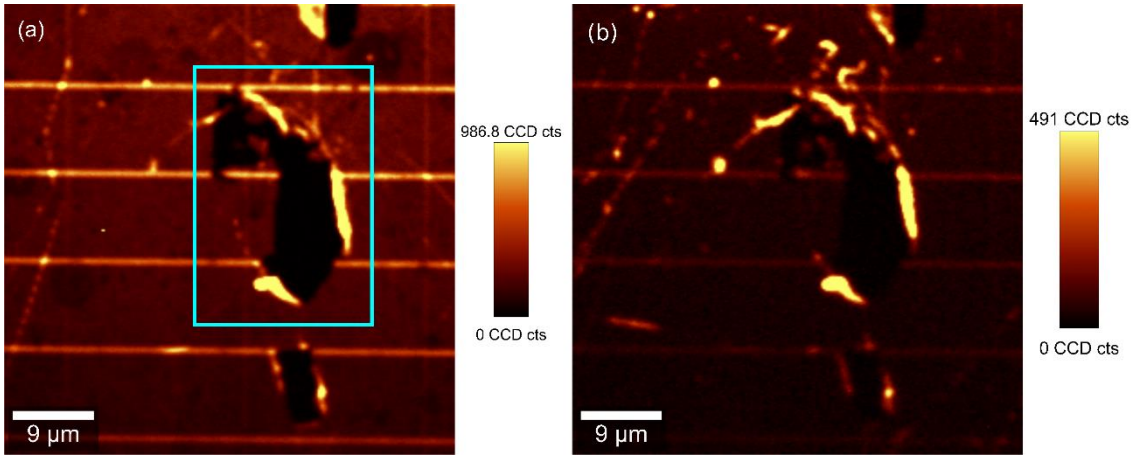

Figure 6.9: *Raman (a) 2D and (b) G peaks in the array of 200 nm-wide GNRs on GNR5.*

in lower intensity 2D and G peaks in these regions than those seen in GNR1. The blue rectangle in Figure 6.9 (a) highlights a significant spatial discontinuity of ~15 µm across, as well as cracks, wrinkles and scratches. This inhomogeneous conduction pathway leads to a lower conductivity compared to the other arrays on the device, as determined from Figure 6.5. The impact of this on acoustoelectric current measurements will be discussed in Section 6.3.3.

6.3 Acoustoelectric Current

6.3.1 SAW Frequency and Intensity Dependence

Devices GNR1-3 were used to study the dependence of the acoustoelectric current (I_{ae}) in graphene nanoribbons on SAW frequency and intensity. Many of the measurements of I_{ae} discussed in this section are those made between contact pair A-B in GNR1

(defining a 3 mm x 300 μm area, made up of 500 nm-wide GNRs) due to the high conductivity of the GNR array. Full details of the experimental set-up and technique for measuring the acoustoelectric current are provided in Section 4.10.

The acoustoelectric current was measured as a function of SAW frequency in the range 1 – 500 MHz, with frequency intervals of 1 MHz, for several applied RF powers, and is plotted in Figure 6.10. Each data point represents the mean of five measurements of I_{ae}. The peaks in the measured current coincide with the resonances of the IDTs identified in the manufacturer's data for the bare $LiNbO_3$ SAW devices (Figure 4.2) and those observed in Section 5.4, confirming its acoustoelectric nature. I_{ae} up to 5.5 μA was measured at a SAW frequency of 442 MHz and applied RF power of +20.0 dBm. Between contact pairs B-C and C-D, currents of a similar magnitude were observed. The positive sign of I_{ae} corresponds to the transportation of holes, which is consistent with the theory that PMMA residues, etchant salts [124], and water molecules adsorbed to the surface [62] p-dope the graphene, and the blue shift of the Raman 2D and G peaks [90]. Upon reversal of the SAW direction, the sign of I_{ae} became negative. In GNR2 the results were qualitatively similar; I_{ae} up to 80 nA was measured for $f_{\mathrm{SAW}} = 205$ MHz and RF power +20.0 dBm. The lower magnitude of the current is associated with the relatively high sheet resistance of the GNR array on GNR2. In comparison to measurements in the literature, the maximum $|I_{ae}|$ measured in GNR1 is nearly two orders of magnitude larger than that reported by Bandhu and Nash in 3 mm x 300 μm monolayer graphene sheets on the same SAW substrates [18, 17], at a SAW frequency of 291 MHz for similar SAW intensities, and Okuda *et al.* [172] reported currents of similar magnitude in continuous

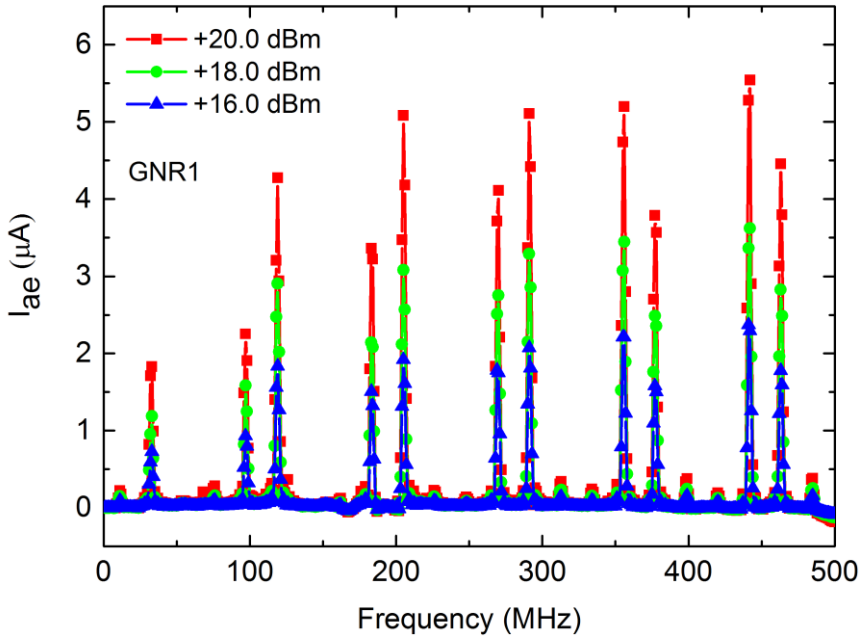

Figure 6.10: *Acoustoelectric current generated in an array of 500 nm-wide GNRs as a function of SAW frequency, measured between contacts A and B in GNR1, for several SAW intensities.*

graphene films of width 5 mm and length 20 μm in solution. The large acoustoelectric currents measured in GNR1 likely arise from the high quality GNR array, supported by the Raman spatial maps (Figure 6.7).

Figure 6.10 also shows that the magnitude of I_{ae} decreases with decreasing applied RF power. The acoustoelectric current generated in GNR arrays was measured as a function of SAW intensity to quantify this dependency, and has been plotted in Figure 6.11. RF power in the range 0.0 – +20.0 dBm was applied to the input IDT in intervals of +2.0 dBm for several SAW frequencies, and the SAW intensity I_{SAW} estimated via the technique outlined in Section 4.10.2 (Equation 4.1). The SAW intensities accessible at

each frequency are comparable with those of Graphene1 (Section 5.4.2). The solid lines in Figure 6.11 are linear fits to the data. The SAW frequencies selected enable comparison with measurements in Chapter 5 [197] and similar studies [18, 17]. In Chapter 3, the acoustoelectric current density j generated in a two-dimensional electron system (in the absence of a magnetic field and in a closed circuit [164, 165]) was described by:

$$j = -\frac{\mu I_{\mathrm{SAW}} \Gamma}{v_{\mathrm{SAW}}} \tag{6.3}$$

where μ is the charge carrier mobility, Γ is the attenuation per unit length, and v_{SAW} is the SAW velocity on a free surface (3973 m s^{-1} in 128° YX $LiNbO_3$ [1]). The attenuation per

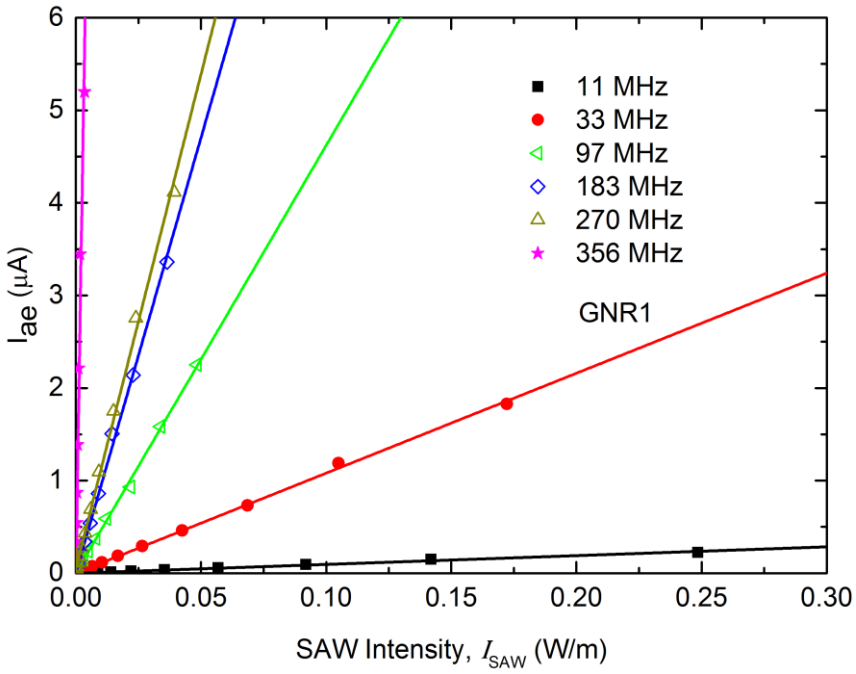

Figure 6.11: *Acoustoelectric current as a function of SAW intensity for several SAW frequencies, as measured in GNR1 between contact pair A-B.*

unit length is described by a classical relaxation model and is a non-monotonic function of the diagonal component of the conductivity tensor, σ^{2D} [4]:

$$\Gamma = K_{\text{eff}}^2 \frac{\pi}{\lambda}\left[\frac{\sigma^{2D}/\sigma_M}{1+(\sigma^{2D}/\sigma_M)^2}\right] \quad (6.4)$$

where K_{eff}^2 is the effective piezoelectric coupling coefficient (0.056 in 128° YX $LiNbO_3$), λ is the SAW wavelength, and the attenuation is maximised at a characteristic conductivity σ_M of lithium niobate. The strong linear dependence of I_{ae} on I_{SAW} in Figure 6.11 is consistent with Equation 6.3 at all frequencies. However, in the absence of an electrostatic gate, a value for μ cannot be directly extracted from gradient. Further, as in Section 5.4.2, note that $\sigma^{2D} \gg \sigma_M$ ($\sigma^{2D}/\sigma_M \sim 1000$), reducing Equation 6.4 to:

$$\Gamma \approx K_{\text{eff}}^2 \frac{\pi}{\lambda}\left(\frac{\sigma_M}{\sigma^{2D}}\right) \quad (6.5)$$

as $\sigma^{2D}/\sigma_M \gg 1$. Since $\sigma^{2D} = f(\mu) = ne\mu$, where n is the charge carrier concentration and e is the electronic charge, the mobility dependence of j in Equation 6.3 disappears. It should be noted that the SAW attenuation induced by the GNR charge carriers is determined by the conductivity of the graphene nanoribbons on the scale of approximately half the SAW wavelength [229] and is highly sensitive to surface defects. The polycrystalline nature of CVD graphene [198], in addition to physical damage, leads to an inhomogeneous conduction pathway, which in turn may lead to a frequency dependent mobility and one which is different to that obtained from a field effect measurement.

Equations 6.3 and 6.4 show that I_{ae} is directly proportional to SAW frequency for a given SAW intensity. Values of I_{ae} were extracted from the linear fits in Figure 6.11 for a fixed SAW intensity and plotted as a function of SAW frequency (Figure 6.12). The strong linear dependence up to SAW frequencies of 270 MHz confirms the applicability of this model to acoustoelectric currents generated in GNRs.

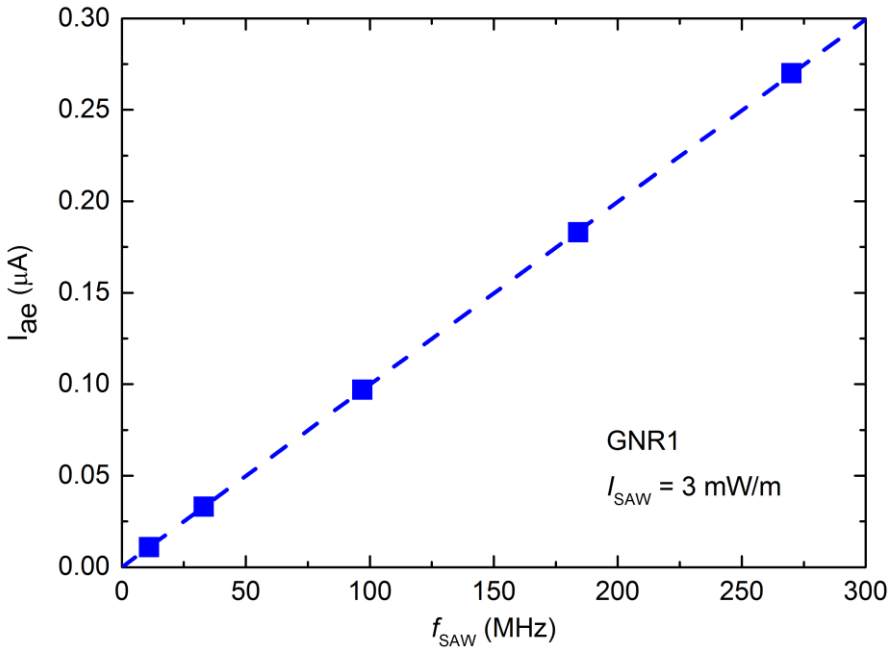

Figure 6.12: *Acoustoelectric current extracted from linear fits in Figure 6.11, for a SAW intensity of 3mW/m, as a function of SAW frequency.*

6.3.2 Influence of Bridge Structures

If the acoustoelectric current for a fixed intensity is plotted as a function of SAW frequency up to 463 MHz, a sharp increase in acoustoelectric current is seen, which peaks at 356 MHz (Figure 6.13. Similar behaviour is seen in GNR2, Figure 6.14). The enhanced piezoelectric interaction between the GNRs and the SAWs at this frequency is believed to arise from the commensuration of the SAW wavelength (~11.2 μm) with the periodicity (10 μm) of the perpendicular graphene bridges in the array. This is similar to the recent study by Mayarov *et al.* [230], in which IDTs were formed from graphene on $LiNbO_3$ for

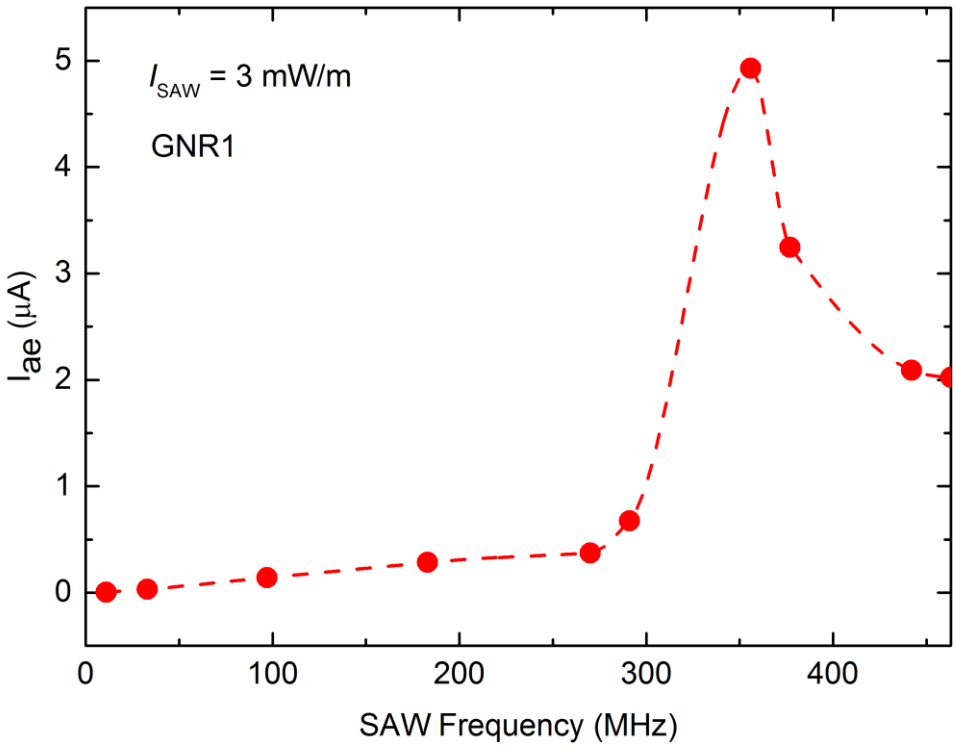

Figure 6.13: *Acoustoelectric current as a function of SAW frequency, extracted from fitting to raw data. Spline (dashed line) is a guide to the eye. A sharp increase in measured acoustoelectric current is observed at* $f_{SAW} = 356$ *MHz.*

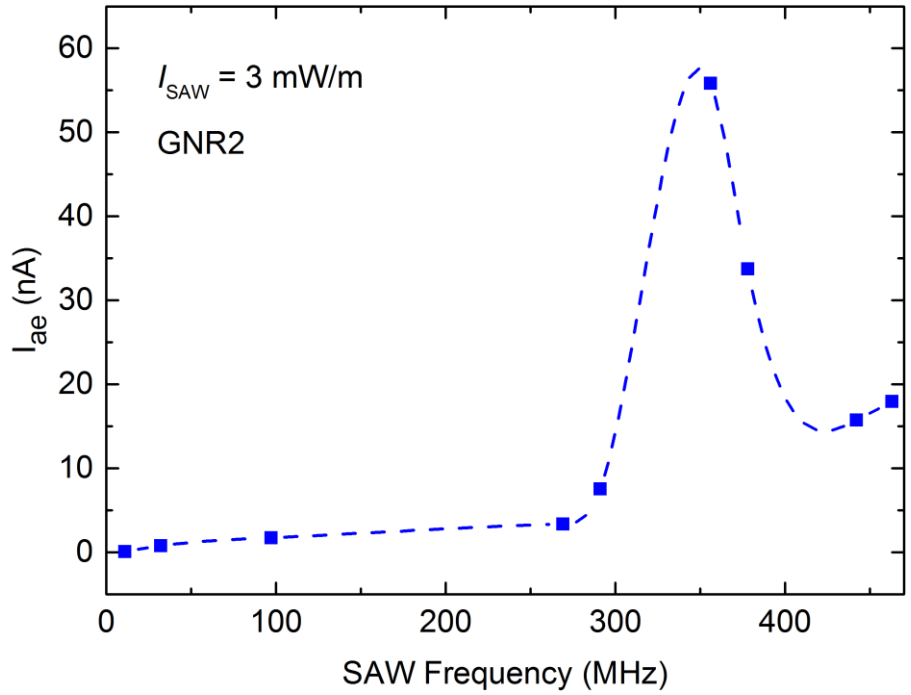

Figure 6.14: *Acoustoelectric current as a function of SAW frequency, extracted from fitting to raw data. Spline (dashed line) is a guide to the eye. As with GNR1, a sharp increase in acoustoelectric current is seen at* $f_{SAW} = 356$ *MHz.*

the purpose of SAW generation and detection. This coupling could explain the extremely low SAW intensity and relatively large acoustoelectric currents measured in devices GNR1 and GNR2 at these frequencies. The acoustoelectric current measured in GNR3, fabricated without any bridge structures, does not exhibit this behaviour when plotted as a function of SAW frequency (Figure 6.15). This is reflected in measurements of the relative amplitude of SAWs in Figure 6.16, where the orange curve with square symbols and the green curve with triangular symbols correspond to measurements of GNR2 (with bridges) and GNR3 (without bridges) respectively. The error bars represent plus-minus

one standard deviation from ten measurements of relative amplitude. The relative SAW amplitude decreases in GNR2 at SAW frequencies of 355 – 377 MHz (SAW wavelength ~11.2 – 10.6 μm) compared to GNR3. Acoustoelectric current measurements for GNR4 could not be made since the nanoribbon array was discontinuous between the electrodes.

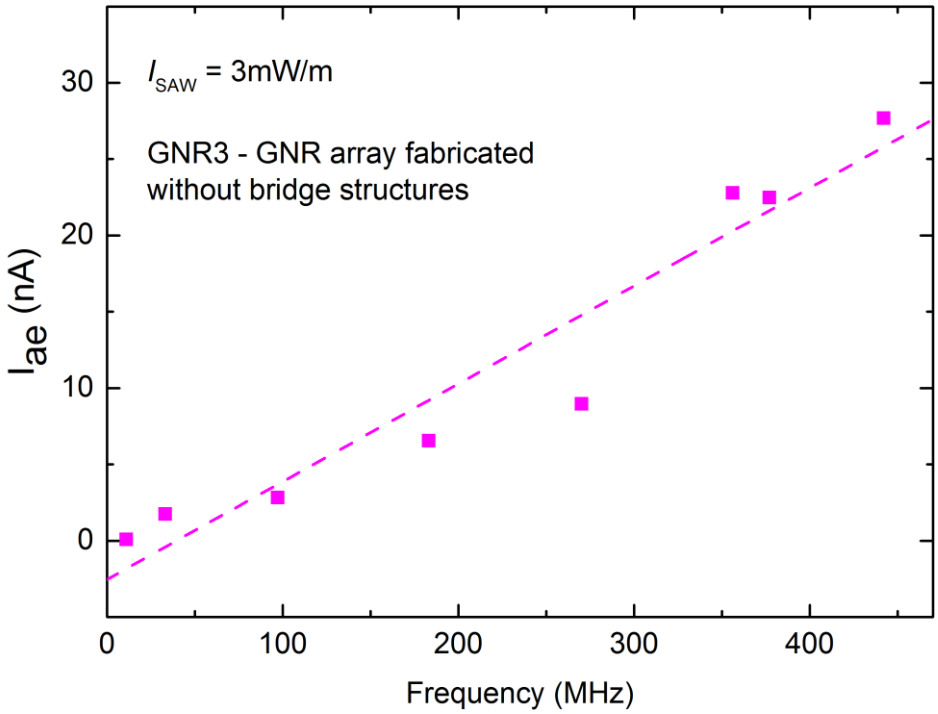

Figure 6.15: *Acoustoelectric current as a function of SAW frequency for a SAW intensity of 3 mW/m. No increase in current seen at 356 or 377 MHz, believed to be due to absence of bridge structures.*

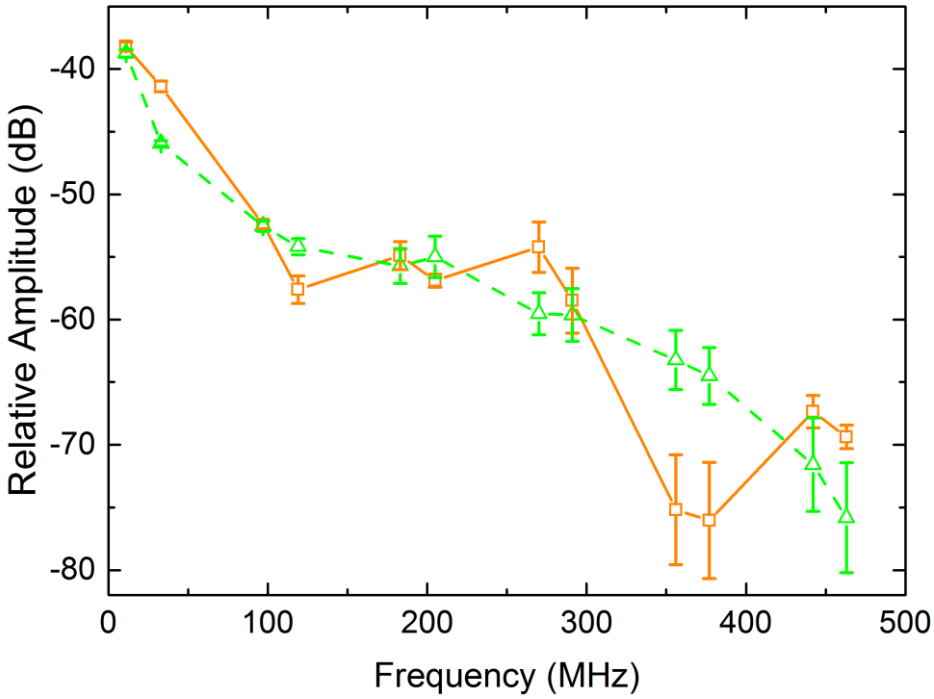

Figure 6.16: *The relative amplitude of the output voltage measured on the oscilloscope is plotted as a function of SAW frequency for GNR2 (in orange) and GNR3 (in green). Error bars are one standard deviation from ten measurements.*

6.3.3 Graphene Nanoribbon Width Dependence

The channel width dependence of I_{ae} in GNRs was studied with device GNR5 as a function of SAW frequency up to 377 MHz, for a fixed SAW intensity (applied RF power of +20.0 dBm). At higher frequencies, the signal-to-noise ratio in the current was too high to obtain repeatable measurements. In Figure 6.17 the measured acoustoelectric current has been plotted as a function of GNR width, where each data point represents the mean of five repeat measurements. Dashed lines are to aid interpretation of the results. The I-V measurements in Section 6.2.1 revealed that the sheet resistance of the array comprised of 300 nm-wide GNRs was ~150% and 1000% greater than that of the

200 nm and 350 nm-wide nanoribbons respectively, and for this reason has not been included in the figure.

The positive sign of the current corresponds to the transportation of holes and is indicative of p-doping of the graphene. As expected from Equations 6.3 and 6.4, for a given GNR width I_{ae} increases approximately linearly with SAW frequency, suggesting that the classical relaxation model discussed previously is applicable to GNRs of the widths considered here. Additionally, for all GNR widths the highest acoustoelectric current is measured at $f_{\mathrm{SAW}} = 356$ MHz, consistent with the measurements of GNR1 and GNR2, and again believed to be due to enhanced momentum transfer from the SAWs to the GNR charge carriers when λ coincides with the periodicity of the bridge structures in the arrays. This is the case even without accounting for the frequency response of the device.

For SAW frequencies of 11, 33, 97, and 119 MHz, the acoustoelectric current generally decreases as the ribbon width increases, so that the largest current is measured in the narrowest ribbons. At SAW frequencies above 205 MHz, I_{ae} decreases significantly when the ribbon width is decreased from 350 nm to 200 nm. The Raman spatial maps of the array of 200 nm-wide GNRs in Figure 6.9 revealed spatial discontinuities of ~15 μm across. As the attenuation of the SAWs by the charge carriers is determined by the conductivity of the graphene on the scale of half the SAW wavelength [229], and for $f_{\mathrm{SAW}} = 205$ MHz the SAW wavelength is ~20 μm, the inhomogeneous conduction path in the 200 nm array leads to lower conductivity, lower SAW attenuation, and correspondingly lower acoustoelectric currents at high SAW

frequencies, where the dimensions of the inhomogeneities are similar to the SAW wavelength. At frequencies below 205MHz, where the SAW wavelength is much larger than the scale of the discontinuities, the acoustoelectric current increases when the nanoribbon width decreases from 350 nm to 200 nm, consistent with the overall trend of increasing current with decreasing ribbon width. Note that the results at 11 MHz are included for completeness; the comparatively low acoustoelectric current in this case means that the changes in acoustoelectric current with ribbon width are not experimentally significant.

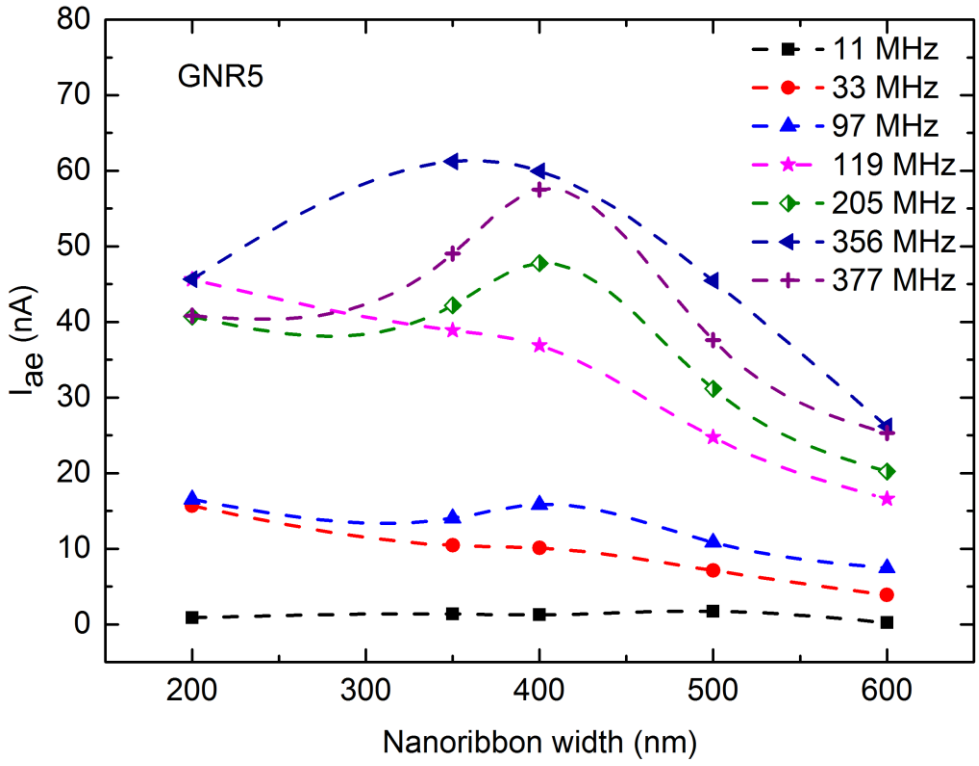

Figure 6.17: *The acoustoelectric current is plotted as a function of nanoribbon width at several SAW frequencies.*

The attenuation coefficient Γ for $f_{\mathrm{SAW}} = 33$ MHz was calculated using Equation 6.4 and is plotted in Figure 6.18 as a function of $\sigma^{2\mathrm{D}}/\sigma_{\mathrm{M}}$ (orange line), where $\sigma_{\mathrm{M}} = 1 \times 10^{-7}$ Ω^{-1} has been recently determined for graphene-lithium niobate hybrids [20]. The symbols in this plot correspond to the value of Γ calculated for each array (indicated by the coloured, dashed vertical line), again using Equation 6.4, and using the conductivity calculated from the current-voltage measurements, with the assumption that the arrays contained no breakages and fully covered the intended area. Due to the discontinuities

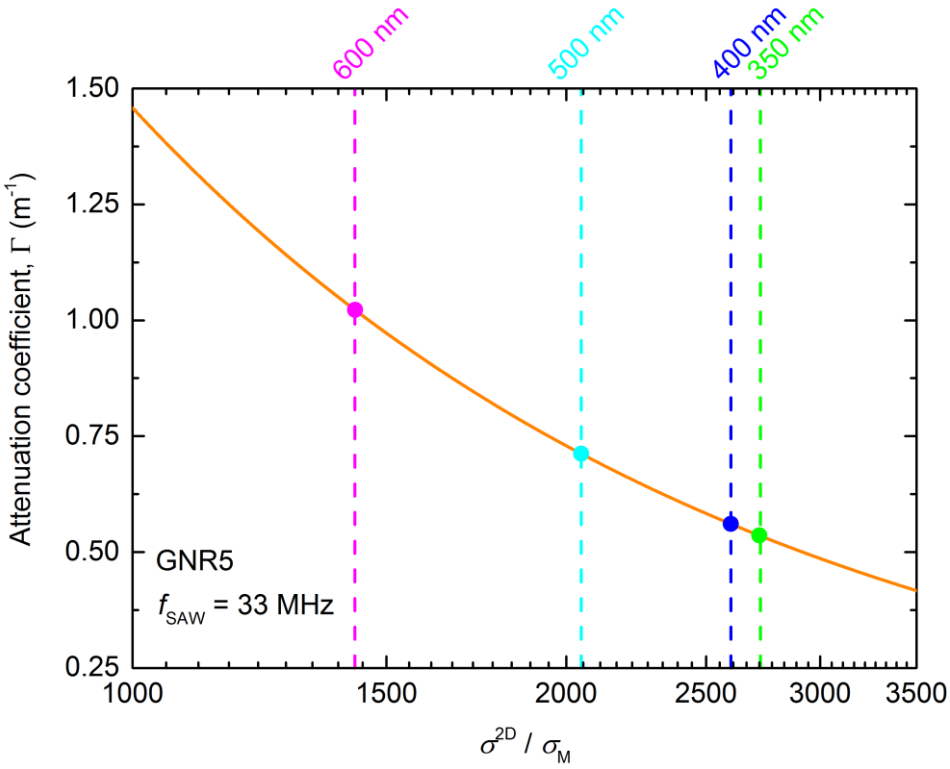

Figure 6.18: *Calculated attenuation coefficient as a function of σ^{2D}/σ_M, for a SAW frequency of 33 MHz. For each GNR array, a value of Γ has been calculated from the estimated conductivity (coloured dashed line) and is indicated by a point of the same colour.*

observed in the Raman map, the attenuation coefficient for the 200 nm array has not been plotted. The increase in conductivity as the GNR width decreases from 600 to 350 nm leads to the attenuation coefficient approximately halving. This contrasts with the acoustoelectric current, which increases as the nanoribbon width decreases. From Equation 6.3, this implies that as the ribbon width decreases, both the conductivity and mobility in the ribbons rises.

The increase in conductivity with decreasing GNR width is consistent with measurements made in graphene nanoconstrictions on Si/SiO_2 fabricated from monolayer CVD graphene, and patterned with plasma etching to similar widths as studied here [90]. In the study by Iqbal *et al.* [90], significant p-doping was observed as the width of the nanoconstrictions decreased. This was attributed to the oxidation of the edges of the nanoconstriction introduced during fabrication. The increased p-doping in their devices was reflected by an increase of the Dirac voltage V_{Dirac}, with a shift of approximately 3V between 600 nm- and 300 nm-wide constrictions in devices that had not been annealed (as here). Using a capacitor model for the graphene on 300 nm-thick SiO_2, on Si, (the closest approximation to this system from the literature) the Fermi energy E_F (in eV) in the graphene can be approximated as [23]:

$$|E_F| = 0.031\sqrt{\left|V_{\mathrm{Dirac}} - V_{\mathrm{gate}}\right|} \tag{6.6}$$

where V_{gate} is the voltage applied to the gate electrode. Setting $V_{\mathrm{gate}} = 0$V and computing E_F for the 300 nm-wide and 600 nm-wide constrictions, for which $V_{\mathrm{Dirac}} = 12.06$ V and 9.16 V respectively, a considerable shift in the Fermi energy of ~15 meV is obtained. CVD

graphene's conductivity is known to be limited by rips, wrinkles, charge puddles and grain boundaries [72, 198], and in previous measurements of the temperature dependence of the acoustoelectric current in graphene [18], the charge carrier mobility was found to be thermally activated, described by an Arrhenius relationship:

$$\mu \propto \exp\left(\frac{-E_a}{k_B T}\right) \tag{6.7}$$

where E_a is the activation energy (determined to be 60 meV), k_B is the Boltzmann constant, and T is the temperature. Although it is not possible to measure the Fermi energy or carrier concentration in these devices directly, an increase in Fermi energy of 15 meV would cause the mobility to more than double (assuming the activation energy is 60 meV) as the GNR ribbon width decreased from 600 nm to 350 nm. This is broadly consistent with the measurements presented here, where an increase in mobility of this order is required to explain the measured increase in acoustoelectric current. Lee *et al.* [231] also showed how the non-uniform charge carrier concentration in graphene channels, due to the presence of defects and charge puddles, can lead to a channel width-dependent charge carrier mobility.

Although the mobility in these devices cannot be directly measured, the magnitude of the currents measured in GNR5 are similar to those observed in samples with μ ~ 5 – 10 cm^2 / V.s [17, 18, 20]. Finally, it is believed that the relatively large acoustoelectric currents measured in the array of 200 nm-wide GNRs arise from the dominant effect of poor conductivity, rather than the increased mobility arising from p-doping of the GNR edges seen in the other arrays. As shown in Table 6.1, the conductivity of the 200 nm-wide

GNRs is approximately half that of the array 600 nm-wide GNRs. Via Equation 6.4, this leads to a more-than two-fold increase in momentum transfer from the SAW to the graphene charge carriers compared to the 600 nm-wide GNRs.

6.4 Summary

The dependence of the acoustoelectric current (I_{ae}) in CVD-graphene nanoribbons on lithium niobate SAW devices was investigated as a function of SAW intensity and frequency, and nanoribbon width (from 200 nm to 600 nm), for the first time. The measured acoustoelectric current in 300 μm x 3 mm arrays of 500 nm-wide GNRs was found to be consistent with the description of this interaction by a relatively simple classical relaxation model, depending linearly on SAW frequency and intensity. I_{ae} up to ~5.5 μA was measured at a SAW frequency of 442 MHz, far higher than has been previously measured in similar systems, attributed to the high-quality graphene afforded by using the modified PMMA transfer method. Enhanced acoustoelectric currents were observed when a perpendicular bridge nanoribbon was inserted into the array, with a periodicity similar to the SAW wavelength. The increasing acoustoelectric current with decreasing nanoribbon width is thought to be due to increased p-doping along the nanoribbon edges introduced during the fabrication process. This leads to a higher charge carrier mobility by raising the Fermi level, enabling conduction across grain boundaries and charge puddles. At SAW frequencies of 205 MHz and above, in nanoribbons of 200 nm width, discontinuities on the scale of the

SAW wavelength overcome the effect of greater p-doping on mobility, and cause the current to decrease. This highlights the ability of the SAWs to probe the conductivity of GNRs on different length scales. These measurements provide a stepping stone towards the eventual use of single charge carrier manipulation in graphene channels, for such applications as metrology and sensing.

7. Acoustoelectric Photoresponse in Graphene Nanoribbons

7.1 Overview

There is a growing range of potential applications for graphene nanoribbons, due to their desirable electronic and optical properties [21, 22, 23, 83]. Recently, there has been particular interest in the development of visible to mid-infrared GNR photodetectors [232, 233], predicated on the presence of a bandgap in nanoribbons with widths below ten nanometres [84, 85, 68]. Furthermore, arrays of GNRs with widths of several hundred nanometres can be used to study the plasmonic properties of graphene via infrared transmission measurements [23], which could be useful in sensing applications. Building on the measurements from Chapters 5 and 6, the photoresponse of the acoustoelectric effect in arrays of graphene nanoribbons is considered for the first time. The decrease in conductivity of continuous graphene under illumination due to hot carrier effects led to an increase in acoustoelectric current [197]. The conductivity of lithographically-defined GNRs is strongly influenced by the presence of dopants at the GNR edges [227]. Since SAWs are intrinsically sensitive to changes in conductivity of a nearby 2DES, examining the acoustoelectric photoresponse

GNRs may provide further insight into their optoelectronic properties. This may be useful for future nanoribbon-based photodetectors.

In Section 7.2, the electrical characteristics of the studied nanoribbons are described. Measurements of the photoresponse of the acoustoelectric current generated in the GNRs at different SAW frequencies are presented in Section 7.3.1. In Section 7.3.2, the effect of illumination on the nanoribbon conductivity is considered, and a classical relaxation model (Section 3.4.2) is used to calculate the acoustoelectric attenuation coefficient in each case. The nanoribbon width dependence of the acoustoelectric current, conductivity and attenuation coefficient are discussed in Section 7.3.3. The measured photoresponse is consistent with the generation of a hot carrier distribution in the GNRs, and comparisons are made to the measurements reported in Chapter 5. A summary of the chapter is found in Section 7.4.

7.2 Device Characteristics

Device GNR5 was used for the measurements presented in this Chapter. This enabled the photoresponse of the acoustoelectric effect in graphene nanoribbons to be studied as a function of GNR width. Nanoribbon widths of 350, 400, 500, and 600 nm were characterised, due to the spatial discontinuities in the array of 200 nm-wide GNRs (Section 6.2.2) and the comparatively high resistance of the array of 300 nm-wide GNRs (Section 6.2.1). Measurements were undertaken at

room temperature and under a pressure of 6.3 x 10^{-6} mbar, maintained via continuous vacuum pumping to prevent the accumulation of dopants on the device.

Resistance measurements were taken following vacuum pumping over approximately 500 hours, using a 1.0 μA current to reduce the possibility of device breakdown. Measurements were taken in the absence of illumination. The conductivity of each nanoribbon array was calculated from the resistance measurements and is listed in Table 7.1. The conductivity increases as the GNRs become narrower, as seen in the characterisation of GNR5 in Section 6.2.1. However, in each case σ^{2D} is approximately one third of the value reported in the previous chapter. A possible explanation for this is the longer vacuum pumping duration before these measurements were made leading to the desorption of nanoribbon edge dopants [188]. Since the conductivity of GNRs is highly dependent on the concentration of dopants at the damaged edges [90, 227], a reduction in dopant concentration following extended vacuum pumping may lower the Fermi energy. This in turn reduces the charge carrier mobility, leading to a decrease in conductivity.

Table 7.1: *Calculated resistance, sheet resistance, and conductivity for each GNR array on GNR5.*

GNR Width (nm)	Resistance (kΩ)	Sheet Resistance (kΩ / □)	Conductivity (Ω^{-1})
350	14.45	11.13	8.98×10^{-5}
400	19.38	12.11	8.26×10^{-5}
500	34.06	14.19	7.05×10^{-5}
600	40.77	21.46	4.66×10^{-5}

7.3 Photoresponse

7.3.1 Acoustoelectric Current

A Thorlabs MCWHL2 LED (peak emission wavelength of 450 nm) was used to study the acoustoelectric photoresponse in GNRs. This light source was found to induce a greater percentage change in acoustoelectric current in continuous graphene sheets than one with a peak emission of 735 nm, for a given light intensity (Section 5.4.3). LED drive currents of 0.2 A and 1.4 A were used, respectively producing an incident light intensity on the sample of 0.24 mW mm^{-2} and 1.20 mW mm^{-2} after correcting for the measurement geometry. A motorised shutter was used to control the exposure of the sample to the LED.

The acoustoelectric current is plotted as a function of time for nanoribbon widths of 350, 400, 500, and 600 nm in Figures 7.1 – 7.4 respectively (pp. 212 - 215), recorded for SAW frequencies of (a) 33 MHz and (b) 355 MHz over the

same period as the measurements in Chapter 5. An RF power of +20.0 dBm (100 mW) was applied to the input IDT at both SAW frequencies to improve the signal to noise ratio in measurements of I_{ae}. The photoresponse of I_{ae} due to each illumination intensity is shown. The vertical, grey dashed lines indicate the time at which the motorised shutter was opened or closed. A negative current in the direction of SAW propagation was observed in all nanoribbon arrays, corresponding to n-type doping (compared to p-doping in Chapter 6). I_{ae} was seen to transition from positive to negative following pumping of the measurement chamber over several hundred hours. This was also observed when characterising the vacuum dependency of the acoustoelectric current in Graphene1 (Section 5.3.2). This may reflect the increased vacuum pump-out time in these measurements compared to those in Chapter 6 leading to the removal of surface adsorbates that p-dope graphene, such as molecular water [63, 62, 64]. The magnitude of the acoustoelectric current was largest for a SAW frequency of 355 MHz in each nanoribbon array. This SAW frequency dependence of I_{ae} was also reported in Chapters 5 and 6, despite the decreasing relative SAW amplitude as the SAW frequency increases (see Figure 6.15, for example).

Upon illumination, a rapid decrease in magnitude of the acoustoelectric current is observed at both SAW frequencies in all GNR arrays. Closing the shutter again causes the current to approach its original value, but in the narrowest GNRs (350 nm and 400 nm) there is an offset in I_{ae} by as much as 10

nA when the illumination intensity is 1.20 mW mm^{-2}. Additionally, transient features become prominent in I_{ae} at this illumination intensity (Figures 7.1 – 7.3, panel (b)). Similarly, the photoresponse of the measured conductivity is also unstable in the arrays of 350 nm-wide and 400 nm-wide GNRs. In contrast, I_{ae} and σ^{2D} as measured in the array of 600 nm-wide GNRs are much more stable. At the moments when the LED is turned on and off, the acoustoelectric current and conductivity reach stable values within a few minutes. The decrease in acoustoelectric current under illumination contrasts with the acoustoelectric photoresponse of continuous graphene sheets reported in Chapter 5, where the magnitude of the current increased upon exposure to optical radiation. A larger change in acoustoelectric current (ΔI_{ae}) was measured due to illumination at the higher incident light intensity, and at the higher SAW frequency. This was also the case in Graphene1.

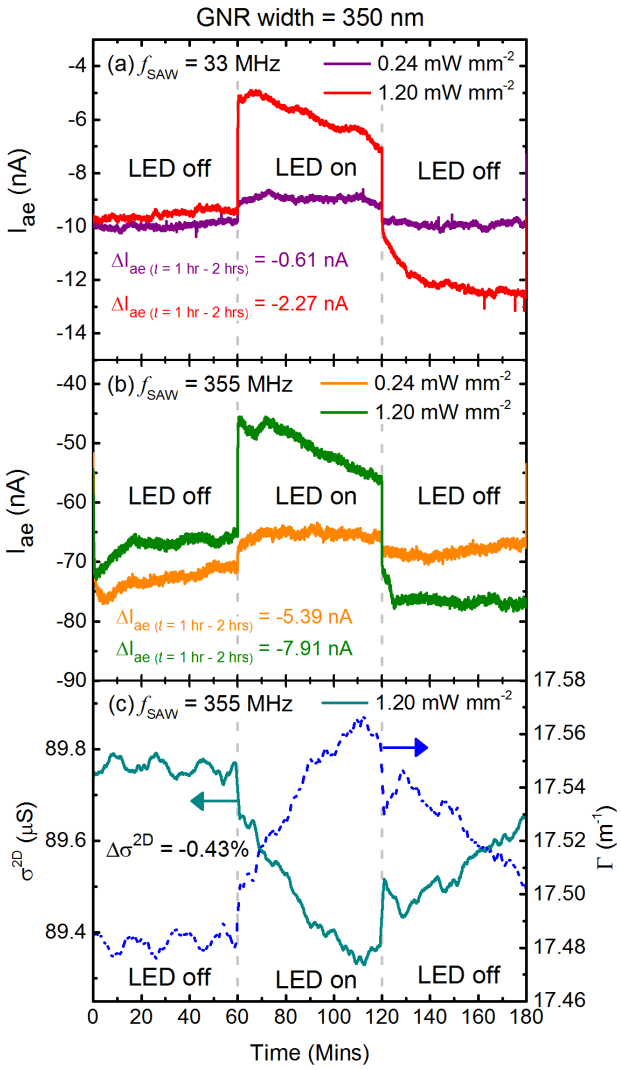

Figure 7.1: *Acoustoelectric current recorded as a function of time in the array of 350 nm-wide GNRs on GNR5 at SAW frequencies of (a) 33 MHz and (b) 355 MHz. Illumination intensity in each case is indicated in the legend. In (c), the conductivity (solid line) is used to calculate the attenuation coefficient (dashed line) via Equation 3.52 for a SAW frequency of 355 MHz. The transient features in acoustoelectric current become more prominent with increasing illumination intensity, but their origin is unclear. Additionally, for the highest illumination intensity, the current is offset by as much as 10 nA (panel (b), green curve).*

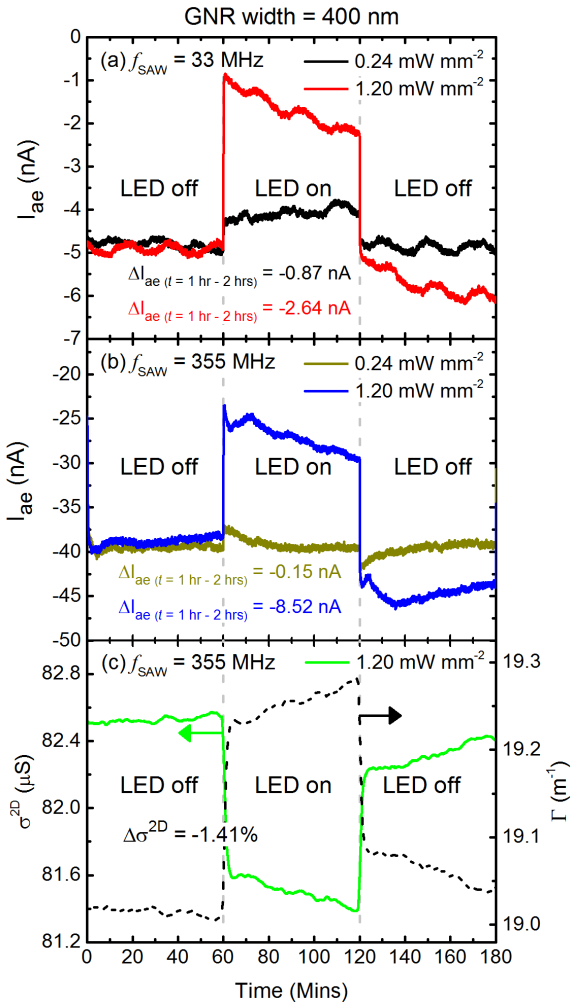

Figure 7.2: *Acoustoelectric current recorded as a function of time in the array of 400 nm-wide GNRs on GNR5 at SAW frequencies of (a) 33 MHz and (b) 355 MHz. Illumination intensity in each case is indicated in the legend. In (c), the conductivity (solid line) is used to calculate the attenuation coefficient (dashed line) via Equation 3.52 for a SAW frequency of 355 MHz. The transient features in acoustoelectric current become more prominent with increasing illumination intensity, but their origin is unclear. For highest illumination intensity, the acoustoelectric current drifts from its initial value by ~5-10 nA when the LED is switched off (panel (b), blue curve).*

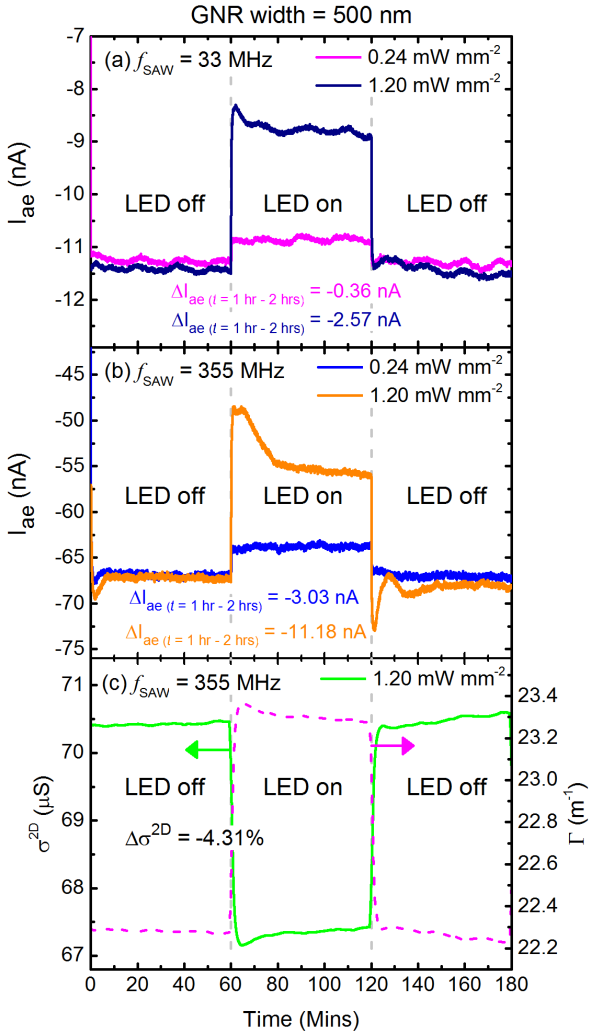

Figure 7.3: *Acoustoelectric current recorded as a function of time in the array of 500 nm-wide GNRs on GNR5 at SAW frequencies of (a) 33 MHz and (b) 355 MHz. Illumination intensity in each case is indicated in the legend. In (c), the conductivity (solid line) is used to calculate the attenuation coefficient (dashed line) via Equation 3.52 for a SAW frequency of 355 MHz. For an incident light intensity of* $1.20\ mW/mm^2$*, transient features in acoustoelectric current appear. In panel (b), this also appars when the LED is turned off. In contrast, the conductivity and attenuation coefficient do not show such features.*

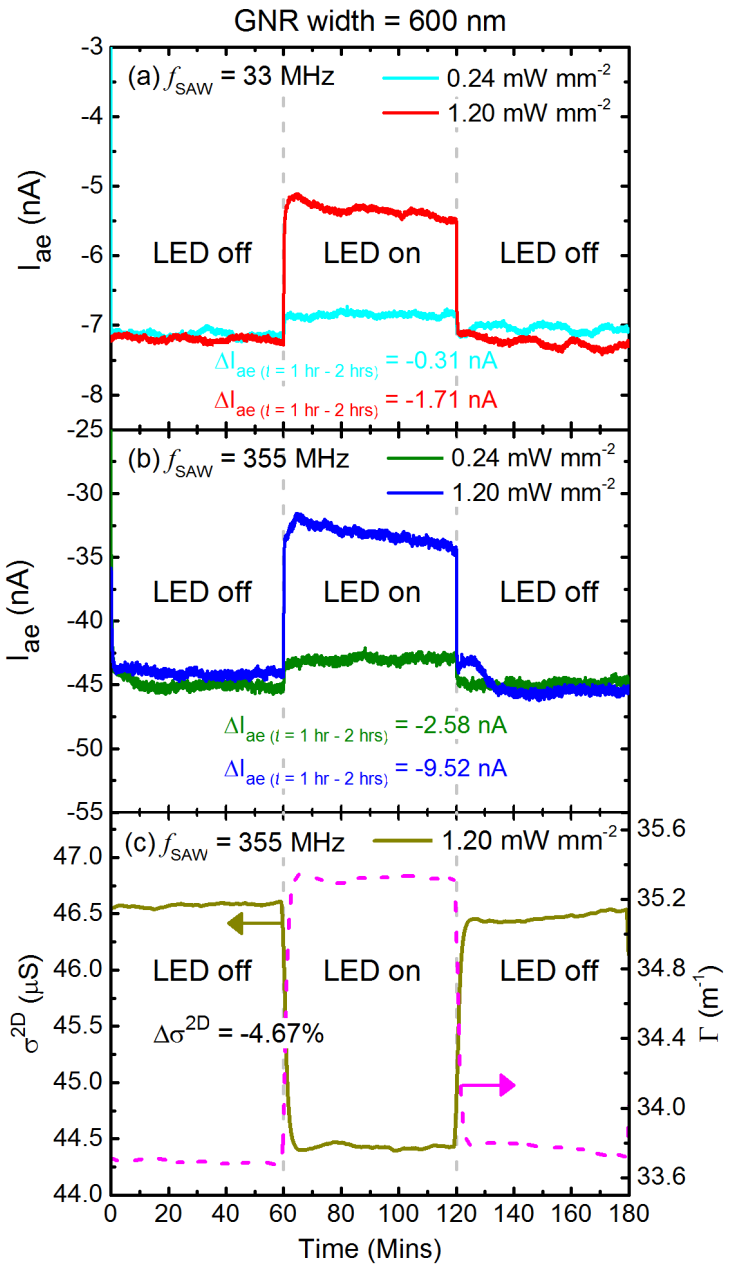

Figure 7.4: *Acoustoelectric current recorded as a function of time in the array of 600 nm-wide GNRs on GNR5 at SAW frequencies of (a) 33 MHz and (b) 355 MHz. Illumination intensity in each case is indicated in the legend. In (c), the conductivity (solid line) is used to calculate the attenuation coefficient (dashed line) via Equation 3.52 for a SAW frequency of 355 MHz.*

7.3.2 Conductivity and Attenuation Coefficient

The conductivity of the GNRs was recorded as a function of time and is plotted as the solid line in Figures 7.1 – 7.4 (c) for each nanoribbon width. For consistency with Figure 5.6 (c), the photoresponse of the conductivity is shown for an illumination intensity of 1.20 mW mm^{-2}. Measurements of I_{ae} are highly susceptible to small leakage currents due to their small magnitude. Since the conductivity measurements are made using a Keithley K2400 SMU sourcing a much larger, constant current of 1.0 μA, it is possible to determine a percentage change in σ^{2D} under illumination. Upon exposure to the light, the conductivity quickly decreases, by as much as 4.67% in the case of the array of 600 nm-wide GNRs. When the shutter is closed, the conductivity increases again towards its value prior to illumination. For comparison, a decrease of up to 6% was measured in the conductivity of Graphene1 under the same illumination (Section 5.4.2).

The decrease in conductivity is mirrored by an increase in the SAW attenuation per unit length, Γ (the attenuation coefficient). In Figures 7.1 – 7.4 (c), Γ is indicated by the coloured dashed line, for a SAW frequency of 355 MHz. This enables easier comparison with the measurements in Figure 5.6 (c). Γ has been calculated from the conductivity using the classical relaxation model describing the acoustoelectric interaction between the SAWs and the GNR charge carriers used in Chapter 6:

$$\Gamma = \frac{K_{\mathrm{eff}}^2 \pi}{\lambda}\left[\frac{\sigma^{2\mathrm{D}}/\sigma_{\mathrm{M}}}{1+\left(\sigma^{2\mathrm{D}}/\sigma_{\mathrm{M}}\right)^2}\right] \tag{7.1}$$

where $K_{\mathrm{eff}}^2 = 0.056$ is the effective piezoelectric coupling coefficient in $LiNbO_3$, λ is the SAW wavelength), and σ_{M} is the characteristic conductivity of lithium niobate. A value of $\sigma_{\mathrm{M}} = 1 \times 10^{-7}\ \Omega^{-1}$ was used, as determined by Bandhu and Nash for graphene-$LiNbO_3$ SAW devices [20].

7.3.3 Graphene Nanoribbon Width Dependence

In Section 6.3.3, the acoustoelectric current was found to increase as the GNR width decreased, for a given SAW frequency. This was attributed to increased doping at the damaged nanoribbon edges in the narrowest GNRs leading to an increase in Fermi energy and charge carrier mobility. Due to an untraced source of drift in the measurements of I_{ae}, this trend is not observed in the measurements in Figures 7.1 – 7.4 (not plotted). Furthermore, the absolute change in acoustoelectric current as a function of GNR width shows no clear width-dependence, shown in Figure 7.5. This is also believed to be due to the underlying drift in I_{ae}.

The percentage change in conductivity has been plotted as a function of nanoribbon width in Figure 7.6, to further understand the change in electronic properties of the GNRs under illumination. The left and right vertical axes show $\Delta\sigma^{2\mathrm{D}}$ for illumination intensities of 0.24 mW mm^{-2} and 1.20 mW mm^{-2} respectively. Dashed splines are used to aid interpretation of the measurements. As the nanoribbon width increases, a larger percentage change in conductivity is

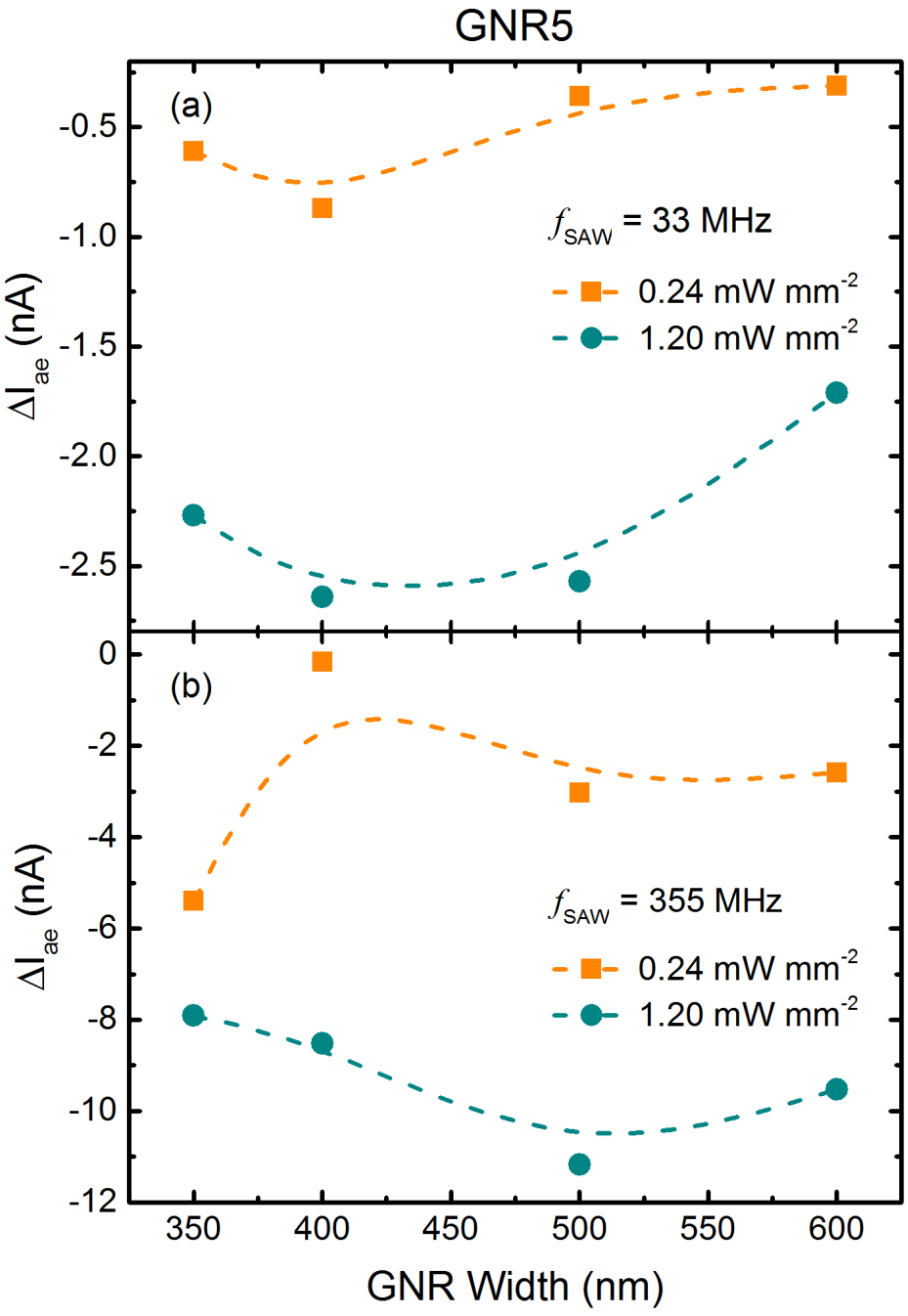

Figure 7.5: *Absolute change in acoustoelectric current for SAW frequencies of (a) 33 MHz and (b) 355 MHz. The incident light intensity is indicated in each figure. Dashed splines are used to aid interpretation of the measurements.*

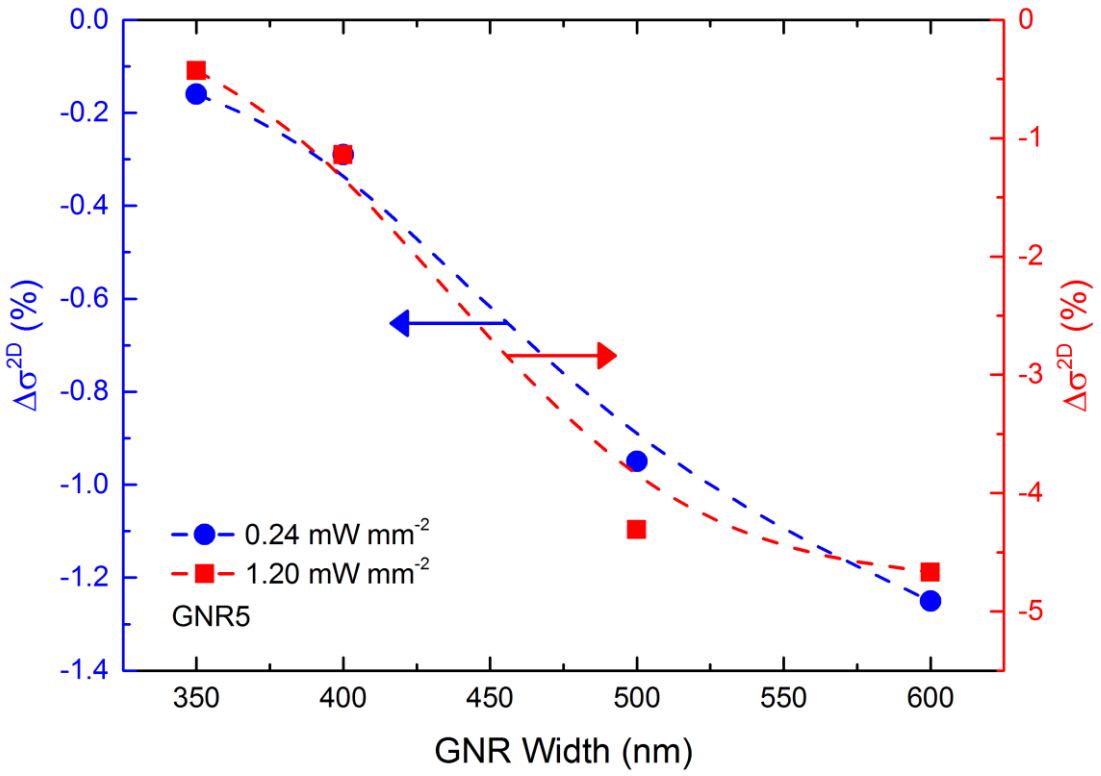

Figure 7.6: *Percentage change in conductivity as a function of GNR width, under illumination intensities of 0.24 mW mm^{-2} (blue circular markers, left axis) and 1.20 mW mm^{-2} (red square markers, right axis). Dashed splines are to aid interpretation of the measurements.*

observed for both incident light intensities. Furthermore, $\Delta\sigma^{2D}$ has the same dependence on GNR width for the two illumination intensities, with approximately a five times greater change seen for an incident light intensity of 1.20 mW mm^{-2} than at 0.24 mW mm^{-2}. This may simply reflect the five-fold increase in illumination intensity. The dependence of $\Delta\sigma^{2D}$ on illumination intensity should be studied further.

In Figure 7.7, the percentage change in attenuation coefficient is plotted as a function of GNR width, for SAW frequencies of (a) 33 MHz and (b) 355 MHz. As the GNR width increases, ΔΓ (%) increases for both illumination intensities. This

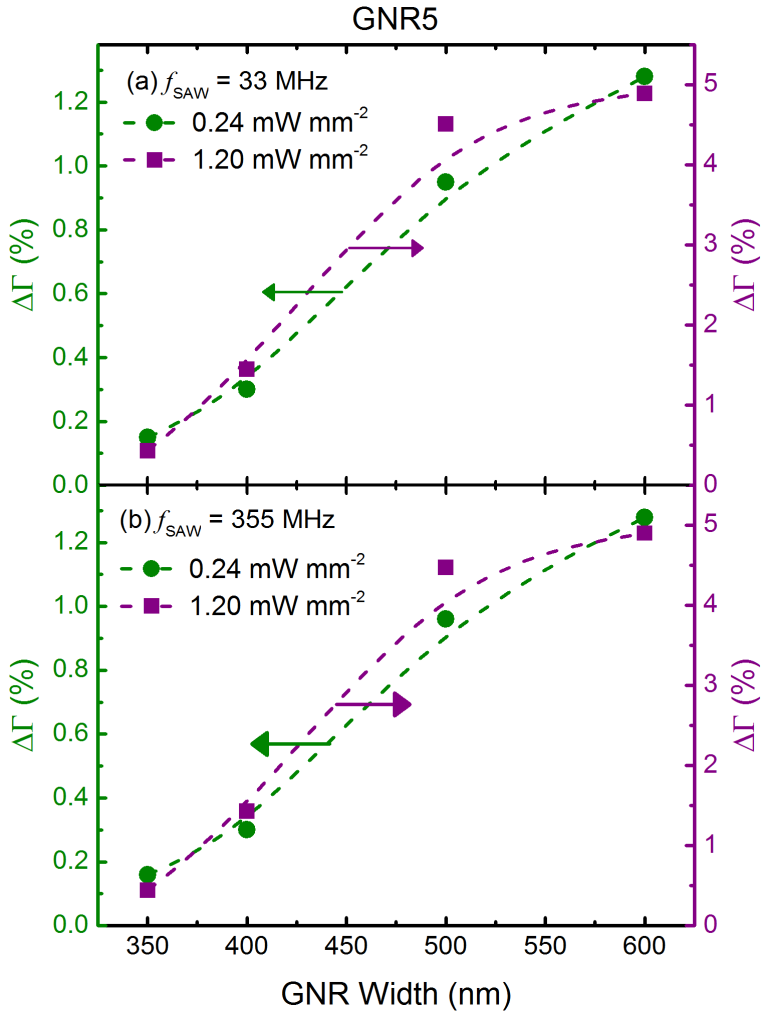

Figure 7.7: *Percentage change in attenuation coefficient for SAW frequencies of (a) 33 MHz and (b) 355 MHz, plotted as a function of GNR width. Incident light intensities on the sample of 0.24 mW mm^{-2} (green circular markers, left axis) and 1.20 mW mm^{-2} (purple square markers, right axis) were used. Dashed splines are used to aid interpretation of the measurements.*

reflects the trend in Figure 7.6, where a greater percentage change in conductivity under illumination is seen with increasing GNR width. Since $\sigma^{2D} \gg \sigma_M$ in all GNR arrays (in the case of the 350 nm-wide GNRs, $\sigma^{2D} \sim 900\sigma_M$), Γ is approximately inversely proportional to the nanoribbon conductivity. Additionally, $\Delta\Gamma$ is roughly the same for both SAW frequencies under both illumination intensities. This is to be expected, since the SAW wavelength differs by only one order of magnitude.

When studying the photoresponse of the acoustoelectric current in continuous graphene sheets, the increase in acoustoelectric current under illumination was attributed to the generation of a hot carrier distribution [197]. The relaxation process of photoexcited carriers in graphene is dominated by carrier-carrier scattering, leading to a decrease in the conductivity or charge carrier mobility μ. This in turn caused the attenuation coefficient to increase, resulting in an increase in the magnitude of the acoustoelectric current according to [164, 165]:

$$j = -\frac{\mu I \Gamma}{v} \tag{7.2}$$

where j is the acoustoelectric current density, I is the surface acoustic wave intensity, and v is the SAW velocity (3979 m s^{-1} in 128° YX $LiNbO_3$ [1]). As seen in Figures 7.1 – 7.4, in all GNR arrays a decrease in the magnitude of acoustoelectric current is associated with a decrease in σ^{2D}. A decrease in σ^{2D} in turn corresponds to an increase in Γ under illumination. From the classical relaxation model, this might be expected to induce a greater acoustoelectric current, as was seen in Chapter 5. A possible explanation for the decrease in I_{ae}

in the nanoribbons under illumination is obtained by considering the large difference in conductivity between the continuous graphene on device Graphene1 and the GNRs on device GNR5. The arrays of 600 nm-wide and 350 nm-wide GNRs have conductivities ~11x and 21x greater than that of Graphene1 respectively. Therefore, the decrease in $\sigma^{2\mathrm{D}}$ in the GNRs under illumination leads to a smaller change in attenuation coefficient than that seen in the continuous graphene (via Equation 7.1). For an illumination intensity of 1.20 mW mm^{-2} and a SAW frequency of 355 MHz, the percentage increase in attenuation coefficient in the arrays of 350 nm-wide and 600 nm-wide GNRs is 0.44% and 4.90% respectively. This compares to an increase of 6.16% in Graphene1, characterised in Chapter 5, where Γ was calculated using $\sigma_{\mathrm{M}} = 1$ x 10^{-7} Ω^{-1}. It was necessary to re-determine the values of the attenuation coefficient calculated from the conductivity of Graphene1 using the value of σ_{M} provided by Bandhu and Nash [20] to enable a fair comparison of the photoresponse measurements from the two devices. The increasing nanoribbon conductivity with decreasing width means that as the GNR width increases, $\Delta\sigma^{2\mathrm{D}}$ (%) and $\Delta\Gamma$ (%) decrease. This is shown schematically in Figure 7.8, where the calculated attenuation coefficient is shown for device Graphene1, the 600 nm-wide and 350 nm-wide GNRs. The reduction in mobility of the charge carriers due to the generation of a hot carrier distribution overcomes the increase in Γ in the GNRs, owing to their high conductivity compared to that of Graphene1. This causes the measured decrease in acoustoelectric current under illumination, via Equation 7.2. It would therefore

be interesting to explore the photoresponse of GNRs with widths greater than 600 nm. This may help determine if there is a threshold GNR width for which the

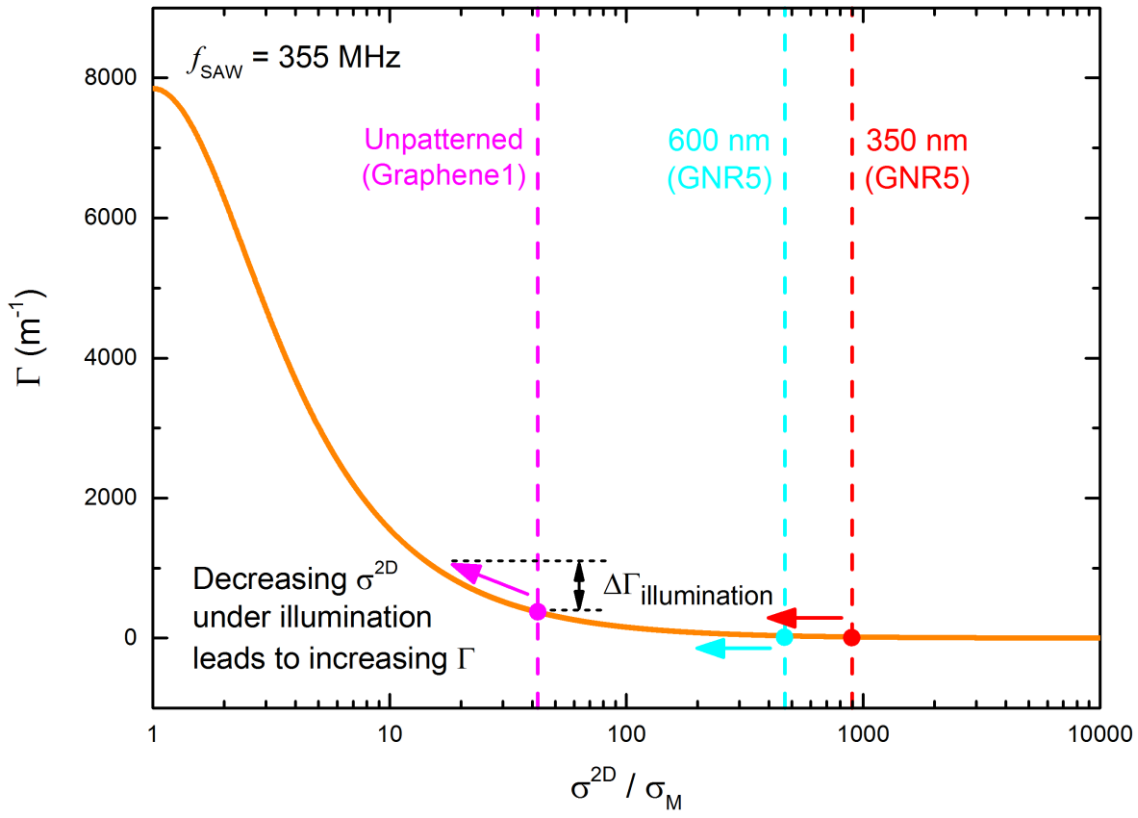

Figure 7.8: *Acoustoelectric attenuation coefficient as a function of conductivity for f_{SAW} = 355 MHz, where σ^{2D} normalised to σ_M = 1 x 10^{-7} Ω^{-1}. The attenuation coefficient calculated from the conductivity of the unpatterned graphene (Graphene1) and arrays of 600 nm-wide and 350nm-wide GNRs (GNR5) are shown in pink, blue, and red respectively. Arrows indicate schematically the decrease in conductivity under illumination. $\Delta\Gamma_{illumination}$ indicates schematically the change in attenuation coefficient resulting from the decrease in conductivity., in this case for the continuous graphene on device Graphene1.*

increase in Γ exactly compensates the decrease in μ under illumination, causing no net change in acoustoelectric current.

Lastly, the acoustoelectric current measured in each GNR array under illumination slowly decreases over time before the motorised shutter is closed and the light source obscured. These transients may provide further insight into the acoustoelectric photoresponse of GNRs on $LiNbO_3$. Future work would include an investigation of their dependence on GNR width and illumination intensity. The origin of these features remains unclear.

7.4 Summary

The photoresponse of the acoustoelectric effect was studied in arrays of monolayer CVD graphene nanoribbons with GNR widths in the range 350 – 600 nm. The negative sign of the acoustoelectric current in the direction of SAW propagation corresponds to n-type doping, reflecting the extended vacuum pump-out duration and consistent with the removal of molecular water from the surface of the GNRs. In each GNR array, the magnitude of the acoustoelectric current was largest when generated by a SAW frequency of 355 MHz, compared to 33 MHz. This is consistent with a relatively simple classical relaxation model describing the piezoelectric interaction between the GNR charge carriers and the SAWs. The conductivity of the GNRs increased as their width decreased, possibly due to increased doping at the damaged GNR edges raising the Fermi

level. Under illumination by a blue (450 nm) LED, both the acoustoelectric current and the conductivity were seen to decrease. This contrasts with the photoresponse of continuous graphene of lower conductivity, where the magnitude of I_{ae} increased under illumination. For a given incident light intensity, the percentage change in conductivity increased with increasing nanoribbon width. This was reflected by a larger percentage increase in acoustoelectric attenuation coefficient as the GNRs became wider. The decrease in conductivity under illumination is consistent with the generation of a hot carrier distribution. Due to the high conductivity of the GNRs, the reduction in mobility due to increased carrier-carrier scattering under illumination overcomes the increase in acoustoelectric attenuation coefficient, causing the acoustoelectric current to decrease.

8. Conclusions and Outlook

The work presented in this thesis focusses on: the acoustoelectric photoresponse of monolayer graphene films; the generation of an acoustoelectric current in graphene nanoribbons (GNRs); and the photoresponse of acoustoelectric charge transport in GNRs. The devices characterised here were prepared in a clean room environment. Graphene produced via chemical vapour deposition (CVD) was transferred to lithium niobate ($LiNbO_3$) surface acoustic wave (SAW) delay lines and patterned using electron beam lithography and reactive ion etching. SAWs were generated with a Hewlett-Packard 8648C radio-frequency signal generator, and the acoustoelectric current measured using a Keithley K2400 source-measurement unit. Illumination was provided by Thorlabs MCWHL2 cold white and M735L2 red light emitting diodes (LEDs), the intensity of which was controlled via a Thorlabs DC2100 LED driver, with a motorised shutter used to control the exposure. All measurements were performed in a vacuum environment to prevent the accumulation of surface dopants on the graphene.

The purpose of this chapter is to summarise the experimental measurements from this thesis and present suggestions for future work. Section 8.1 provides a review of measurements of the acoustoelectric current and conductivity as a

function illumination wavelength and intensity, studied at different SAW frequencies and intensities. In Section 8.2, an evaluation of the SAW wavelength and intensity dependence of the acoustoelectric current generated in GNR arrays is presented, followed by a description of the effect on the acoustoelectric current of varying GNR width. The role of the bridge structure in enhancing the piezoelectric interaction between the SAWs and GNR charge carriers is also considered. In Section 8.3, the photoresponse of the acoustoelectric current in arrays of GNRs as a function of illumination intensity, SAW frequency, and GNR width is summarised, and the effect of illumination on GNR conductivity is discussed. Lastly, Section 8.4 provides suggestions for future research on graphene- and GNR-SAW hybrid structures.

8.1 Acoustoelectric Photoresponse in Graphene

The acoustoelectric current in 3 mm x 300 μm (width x length) graphene on $LiNbO_3$ was measured as a function of SAW frequency (33 and 355 MHz) and SAW intensity (up to ~3.0 mW/mm). The acoustoelectric current was found to be well described by a Weinreich relation, depending linearly both on SAW frequency and intensity. The linear dependence on SAW frequency arises from a classical relaxation model describing the attenuation of the SAW by the charge carriers, which results in a decrease of SAW velocity and amplitude. The SAW velocity and amplitude are in turn nonlinearly dependent on the conductivity of the charge carrier system. The model predicts an increase in acoustoelectric

current when the conductivity approaches the characteristic conductivity of lithium niobate. The effect of illumination on acoustoelectric current and conductivity was first studied using a Thorlabs MCWHL2 LED, with a peak emission wavelength at 450 nm, and an incident intensity of up to 1.2 mW mm^{-2} after correcting for the measurement geometry. When the motorised shutter was opened, the magnitude of the measured acoustoelectric current rapidly increased, by 2.4% and 1.9% for SAW frequencies of 33 and 355 MHz respectively, within the first 20 seconds. A maximum increase of 14% and 10% was observed for SAW frequencies of 33 and 355 MHz respectively, compared to a decrease in conductivity by 6%, after one hour of illumination, suggesting that the electronic properties of the graphene changed under illumination. Per the classical relaxation model describing the acoustoelectric effect, a decrease in conductivity led to an increase in attenuation coefficient (as calculated from the measurements of resistance) and an increase in acoustoelectric current. Further, for a given illumination intensity, the acoustoelectric current retained a linear dependence on SAW intensity. The photoresponse was explored in more detail by measuring the the acoustoelectric current under illumination by a 735 nm LED light. The percentage change in acoustoelectric current was found to depend linearly on the illumination intensity for both LEDs, with a greater percentage for higher photon energies. This is consistent with the generation of a hot carrier distribution under illumination [25]; the increase in carrier-carrier-scattering due to the increased kinetic energy of the electrons in the conduction band leads to a

decrease in conductivity, in turn leading to greater acoustoelectric attenuation, and an increase in acoustoelectric current.

8.2 Acoustoelectric Effects in Graphene Nanoribbons

Graphene transferred to $LiNbO_3$ SAW delay lines was patterned into arrays of graphene nanoribbons, with individual GNR widths ranging from 200 – 600 nm, and the acoustoelectric current measured as a function of SAW frequency (in the range 11 – 463 MHz) and intensity (up to ~3.0 mW/mm) for the first time. The arrays had a 50% fill factor, and all devices exhibited p-doping. The acoustoelectric current measured in 3 mm x 300 μm arrays of 500 nm-wide GNRs was found to be well described by the Weinreich relation and classical relaxation model used to describe the measurements taken in Chapter 5, depending linearly on SAW frequency and intensity. The acoustoelectric current of up to ~5.5 μA at a SAW frequency of 442 MHz was over an order of magnitude larger than that reported in the literature [17, 20], for devices up this scale, and is attributed to the higher quality graphene resulting from a modified PMMA transfer process, leading to an increase in charge carrier mobility. Enhanced acoustoelectric currents were measured at a SAW frequency of 356 MHz, for a given SAW intensity, when 500 nm-wide GNRs lying perpendicular to the SAW wave vector, spaced with a period similar to the SAW wavelength, were included in the array (referred to as ‘bridge’ structures). This was reflected by a decrease in relative SAW amplitude at 356 MHz. The acoustoelectric current measured in devices

without periodic bridge structures increased linearly with SAW frequency, for a fixed SAW intensity, as expected. In order to gain clearer insight into the width dependence of acoustoelectric current, neighbouring arrays of GNRs of different widths were fabricated on the same SAW delay line, ensuring that each had undergone identical preparation and were subject to the same SAW intensity. The acoustoelectric current was studied at SAW frequencies up to 377 MHz. For a given SAW frequency and intensity, the acoustoelectric current was observed to increase with decreasing GNR width. This is believed to be due to increased p-doping along the disordered GNR edges (which act as ‘anchors’ for dopant molecules) introduced during the fabrication process [90, 67]. This raises the Fermi energy in the samples and enables conduction across inhomogeneous charged impurities and grain boundaries, arising from the CVD graphene’s polycrystalline nature. At SAW frequencies of 205 MHz and above, in the array of GNRs with 200 nm width, spatial discontinuities on the scale of the SAW wavelength overcome the effect of greater p-doping on mobility, and cause the current to decrease, further demonstrating the ability of SAWs to probe the conductivity of low-dimensional electron systems on different length scales. Lastly, identical bridge structures to those studied previously were included in each GNR array while studying the width dependence. For a given GNR width, the highest acoustoelectric currents were measured at SAW frequencies of 356 MHz, even without accounting for SAW intensity, additionally supporting the notion that bridge structures commensurate with the SAW wavelength can

increase the piezoelectric interaction between the SAWs and GNR charge carriers.

8.3 Acoustoelectric Photoresponse of Graphene Nanoribbons

Using one of the devices characterised in Chapter 6, the photoresponse of the conductivity and acoustoelectric current was studied as a function of GNR width. Nanoribbons in the range 350 – 600 nm were measured, due to the spatial discontinuities in the array of 200 nm-wide GNRs and the relatively high resistance of the 300 nm-wide nanoribbons. The measured conductivity of each nanoribbon array was approximately 1/3 of the value measured in Chapter 6. This may reflect the increased vacuum pump-out time prior to these measurements being made, leading to the desorption of edge-dopants. This in turn lowers the Fermi energy, reduces charge carrier mobility, and increases the device resistance. For the measurements of acoustoelectric current, a power of +20.0 dBm was applied to the input IDT at SAW frequencies of 33 MHz and 355 MHz. Initially, a positive acoustoelectric current was observed in the direction of SAW propagation, corresponding to p-type doping. This transitioned to a negative current (n-type doping), which was also observed in Chapter 5 and is again consistent with the removal of molecular surface adsorbates such as water that p-dope graphene. The largest magnitude I_{ae} in each GNR array was measured for the higher SAW frequency, despite the decreasing relative SAW amplitude at higher SAW frequencies. This is in accordance with a classical relaxation model

describing the interaction between the GNR charge carriers and the SAWs. An untraced source of drift in the measurements of I_{ae} means it is not possible to compare I_{ae} as a function of GNR width. Under illumination by the same blue (450 nm) LED as used for the measurements in Chapter 5, both the acoustoelectric current and conductivity are seen to decrease. Furthermore, the percentage change in conductivity and attenuation coefficient increased with decreasing GNR width for a given SAW frequency. The maximum measured change in conductivity was 4.67%, in the array of 600 nm-wide GNRs. This is in comparison to a 6% decrease seen in continuous graphene with a ~11x lower conductivity under the same illumination intensity. It is believed that the generation of a hot carrier distribution under illumination leads to a reduction in conductivity and charge carrier mobility due to increased carrier-carrier scattering. Since the conductivity of the GNRs is nearly three orders of magnitude greater than the characteristic conductivity of the lithium niobate substrate, there is only a small increase in acoustoelectric attenuation coefficient. This is overcome by the decrease in mobility, leading to the measured decreased in acoustoelectric current under illumination.

8.4 Suggestions for Future Work

Graphene's ambipolar transport characteristics are at the heart of many potential applications, where a back-gate in graphene FETs can be used to change the Fermi energy. While the thick substrates used for the measurements in this thesis

precluded the use of a back-gate, Bandhu and Nash [20] used an ion-gel dielectric applied via drop-casting to top-gate large-area graphene monolayers on identical $LiNbO_3$ delay lines. They demonstrated p-type and n-type behaviour, and the ability to switch off the acoustoelectric current entirely as the Fermi energy crossed the charge neutrality point. Controllable modulation of the charge carrier concentration by top-gating could further elucidate the mechanism behind the measured photoresponse of the acoustoelectric current, and conductivity, in SLG and GNRs on $LiNbO_3$. It could also provide a clearer understanding of the influence of edge dopants on the electronic transport characteristics of GNRs. Six GNR-on-$LiNbO_3$ devices with an ion-gel top-gate were fabricated, but none exhibited electrical continuity. Small quantities of ion-gel dielectric will be required to prevent significant SAW damping by mass loading.

The estimated charge carrier mobilities of the graphene- and GNR-SAW hybrids characterised here were consistently lower than values typically reported for graphene on Si/SiO_2 [24, 23]. This may partly be due to the large area of the devices, introducing more physical defects and charged impurities that decrease the conductivity. It is also possible that the $LiNbO_3$ substrate influences the electronic properties of graphene, which has yet to be explored. A possible approach to reducing such effects would be encapsulation of the graphene and GNRs between few-layer hexagonal boron nitride (hBN) sheets. Dean *et al.* [42] observed a large improvement in mobility in graphene supported by hBN, compared to positioning directly on a Si/SiO_2 substrate. They attributed this to the

high degree of lattice-matching between hBN and graphene, and hBN's chemical inertness, respectively resulting in fewer graphene wrinkles and a lower concentration of charged impurities.

The presence of bridge GNRs, perpendicular to the SAW wave vector, in arrays of graphene nanoribbons, led to an increase in measured acoustoelectric current when the bridge period was commensurate with the SAW wavelength ($f_{\mathrm{SAW}} = 355$ MHz, bridge period 10 μm). This is similar to the study by Mayarov *et al.* [230], in which graphene interdigital transducers were used for SAW generation and detection. An increased piezoelectric interaction between the SAW and GNR charge carriers results in a higher signal-to-noise ratio in measurements of the acoustoelectric current, which could be useful in a variety of GNR-SAW applications. It would be interesting to further explore the role of the bridge structures by tuning their periodicity to more closely match different SAW wavelengths. This would be quite challenging, as delamination of the graphene from the $LiNbO_3$ frequently occurred during PMMA development, following GNR patterning via e-beam lithography.

GNR arrays are a powerful tool for studying the plasmonic properties of graphene, as shown by Luxmoore *et al.* [23] via mid-infrared (MIR) differential transmission measurements. Lithium niobate strongly absorbs MIR radiation, making it an unsuitable substrate to investigate graphene plasmons via this approach. On the other hand, it would be interesting to see if the presence of graphene plasmons could be inferred by a change in the acoustoelectric current

or SAW observables under illumination. Schiefele *et al.* [234] and Farhat *et al.* [235] separately proposed that surface acoustic waves propagating beneath a graphene sheet could form a diffraction grating, via which laser light could couple to graphene plasmons, negating the need for complex patterning. Again, measurements of the acoustoelectric current may indicate the presence of graphene plasmons. Aluminium nitride and zinc oxide were proposed as piezoelectric substrates, since they have large piezoelectric coupling coefficients and can be deposited on a variety of substrates via sputtering, with a back-gate to tune the charge carrier concentration.

Appendix A.
Estimation of SAW Intensity

The amplitude of surface acoustic waves measured at the output transducer has undergone transduction losses in SAW generation and detection, attenuation due to propagation in the supporting medium, and acoustoelectric attenuation due to the presence of a nearby charge carrier system. The SAW intensity was estimated based on the assumptions that:

1. SAW attenuation due to propagation in the medium was negligible compared to the transduction losses.
2. The input and output IDTs have the same efficiency x, and for an input power P_{in} the input transducer transmits SAWs of equal amplitude across the substrate in directions perpendicular to its apertures, with an intensity proportional to $xP_{\mathrm{in}}/2$.

Thus, the SAW power P at the centre of the substrate is:

$$P = xP_{\mathrm{in}}/2 \tag{A.1}$$

And the SAW power at the output transducer P_{out} is:

$$P_{\text{out}} = x^2 P_{\text{in}}/2 \tag{A.2}$$

Recognising that:

$$\frac{P_{\text{in}}}{P_{\text{out}}} = \left(\frac{V_{\text{in}}}{V_{\text{out}}}\right)^2 \tag{A.3}$$

which may be rearranged for P_{out}:

$$P_{\text{out}} = P_{\text{in}} \left(\frac{V_{\text{out}}}{V_{\text{in}}}\right)^2 \tag{A.4}$$

Combining this with Equations A.1 and A.2, an expression for x can be obtained:

$$x = \sqrt{2} \left(\frac{V_{\text{out}}}{V_{\text{in}}}\right) \tag{A.5}$$

that can be substituted into Equation A.1 to obtain:

$$P = \frac{1}{\sqrt{2}} P_{\text{in}} \left(\frac{V_{\text{out}}}{V_{\text{in}}}\right) \tag{A.6}$$

While V_{in} and V_{out} may be directly measured on an oscilloscope, P_{in} for the RF generator used in these measurements is given in dBm. Equation A.7 is used to convert P_{in} into mW:

$$P_{\text{in}}\,[\text{mW}] = 1[\text{mW}] \times 10^{P_{\text{in}}[\text{dBm}]/10} \tag{A.7}$$

Substituting Equation A.7 into Equation A.6, the SAW power in mW is given by:

$$P = \frac{1\,[\text{mW}]}{\sqrt{2}} \times 10^{P_{\text{in}}[\text{dBm}]/10} \times \frac{V_{\text{out}}}{V_{\text{in}}} \tag{A.8}$$

Finally, the SAW intensity I_{SAW} encountered by the graphene for an arbitrary input power P_{in} is:

$$I_{\mathrm{SAW}} = \frac{P}{d} = \frac{1\ [\mathrm{mW}]}{\sqrt{2}} \times 10^{P_{\mathrm{in}}[\mathrm{dBm}]/10} \times \frac{V_{\mathrm{out}}}{V_{\mathrm{in}}} \tag{A.9}$$

where d = 3.5 mm is the size of the transducer aperture.

Bibliography

[1] D. Morgan, Surface acoustic wave filters with appliactions to electronic communications and signal processing (2nd edition), London: Academic Press, 2007.

[2] R. H. Parmenter, “The acousto-electric effect,” *Physical Review,* vol. 89, no. 5, pp. 990 - 998, 1953.

[3] A. Wixforth, J. P. Kotthaus and G. Weimann, “Quantum oscillations in the surface-acoustic-wave attenuation caused by a two-dimensional electron system,” *Physical Review Letters,* vol. 56, no. 19, pp. 2104 - 2106, 1986.

[4] A. Wixforth, J. Scriba, M. Wassermeier, J. P. Kotthaus, G. Weimann and W. Schlapp, “Surface acoustic waves on GaAs/AlxGa1-xAs heterostructures,” *Physical Review B,* vol. 40, no. 11, pp. 7874 - 7887, 1989.

[5] G. R. Nash, S. J. Bending, M. Boero, P. Grambow, K. Erbel and Y. Kershaw, “Anisotropic surface acoustic wave scattering in quantum-wire arrays,” *Physical Review B,* vol. 54, no. 12, pp. R8337 - R8340, 1996.

[6] M. Boero, G. R. Nash, S. J. Bending, J. C. Inkson, P. Grambow, K. Erbel and Y. Kershaw, “Surface acoustic wave scattering in quantum wire arrays: theory and experiment,” in *Surface Science*, Genova, 1997.

[7] G. R. Nash, S. J. Bending, M. Boero, M. Riek and K. Eberl, “Surface-acoustic-wave absorption by quantum-dot arrays,” *Physical Review B,* vol. 59, no. 11, pp. 7649 - 7655, 1999.

[8] V. I. Talyanskii, J. M. Shilton, M. Pepper, C. G. Smith, C. J. B. Ford, E. H. Linfield, D. A. Ritchie and G. A. C. Jones, “Single-electron transport in a one-dimensional channel by high-frequency surface acoustic waves,” *Physical Review B,* vol. 56, no. 23, pp. 15180 - 15184, 1997.

[9] K. S. Novoselov, A. K. Geim, S. V. Mayarov, D. Jiang, Y. Zhang, S. V. Dubonos, I. V. Grigorieva and A. A. Firsov, “Electric field effect in atomically thin carbon films,” *Science,* vol. 306, no. 5696, pp. 666 - 669, 2004.

[10] A. K. Geim and K. S. Novoselov, “The rise of graphene,” *Nature Materials,* vol. 6, pp. 183 - 191, 2007.

[11] R. R. Nair, P. Blake, A. N. Grigorenko, K. S. Novoselov, T. J. Booth, T. Stauber, N. M. R. Peres and A. K. Geim, “Fine structure constant defines visual transparency of graphene,” *Science,* vol. 320, p. 1308, 2008.

[12] F. H. L. Koppens, T. Mueller, P. Avouris, A. C. Ferrari, M. S. Vitiello and M. Polini, “Photodetectors based on graphene, other two-dimensional materials and hybrid systems,” *Nature Nanotechnology,* vol. 9, pp. 780 - 793, 2014.

[13] C. Lee, X. Wei, J. W. Kysar and J. Hone, “Measurement of the elastic properties and intrinsic strength of monolayer graphene,” *Science,* vol. 321, no. 5887, pp. 385 - 388, 2008.

[14] P. Thalmeier, B. Dora and K. Ziegler, “Surface acoustic wave propagation in graphene,” *Physical Review B,* vol. 81, no. 4, p. 041409(R), 2010.

[15] W. Zhang and W. Xu, “Absorption of surface acoustic waves by graphene,” *AIP Advances,* vol. 1, no. 2, p. 022146, 2011.

[16] V. Miseikis, J. E. Cunningham, K. Saeed, R. O'Rorke and A. G. Davies, “Acoustically induced current flow in graphene,” *Applied Physics Letters,* vol. 100, no. 13, p. 133105, 2012.

[17] L. Bandhu, L. M. Lawton and G. R. Nash, “Macroscopic acoustoelectric charge transport in graphene,” *Applied Physics Letters,* vol. 103, p. 133101, 2013.

[18] L. Bandhu and G. R. Nash, “Temperature dependence of the acoustoelectric current in grapene,” *Applied Physics Letters,* vol. 105, p. 263106, 2014.

[19] S. Zheng, H. Zhang, Z. Feng, Y. Yu, R. Zhang, C. Sun, J. Liu, X. Duan, W. Pang and D. Zhang, “Acoustic charge transport induced by the surface acoustic wave in chemical doped graphene,” *Applied Physics Letters,* vol. 109, no. 18, p. 183110, 2016.

[20] L. Bandhu and G. R. Nash, “Controlling the properties of surface acoustic waves using graphene,” *Nano Research,* vol. 9, no. 3, pp. 685 - 691, 2015.

[21] R. S. Duryat, “Graphene nanoribbons (GNRs) for future interconnect,” *IOP Conf. Series: Materials Science and Engineering,* vol. 131, p. 012018, 2016.

[22] C. Xu, H. Li and K. Banerjee, “Graphene nano-ribbon (GNR) interconnects: a genuine contender or a delusive dream,” in *Electron Devices Meeting*, San Francisco, 2008.

[23] I. J. Luxmoore, C. H. Gan, P. Q. Liu, F. Valmorra, P. Li, J. Faist and G. R. Nash, “Strong coupling in the far-infrared between graphene plasmons and the surface of optical phonons,” *ACS Photonics,* vol. 1, no. 11, pp. 1151 - 1155, 2014.

[24] I. J. Luxmoore, C. Adlem, T. Poole, L. M. Lawton, M. H. Mahlmeister and G. R. Nash, “Thermal emission from large area chemical vapor deposited graphene devices,” *Applied Physics Letters,* vol. 103, no. 13, p. 131906, 2013.

[25] K. J. Tielrooij, J. C. W. Song, S. A. Jensen, A. Centeno, A. Pesquera, A. Zurutuza Elorza, M. Bonn, L. S. Levitov and F. H. L. Koppens, “Photoexcitation cascade and multiple hot-carrier generation in graphene,” *Nature Physics,* vol. 9, pp. 248 - 252, 2013.

[26] S. V. Morozov, K. S. Novoselov, M. I. Katsnelson, F. Schedin, D. C. Elias, J. A. Jaszczak and A. K. Geim, “Giant intrinsic carrier mobilities in graphene and its bilayer,” *Physical Review Letters,* vol. 100, no. 1, p. 016602, 2008.

[27] L. Liao and X. Duan, “Graphene for radio frequency electronics,” *Materials Today,* vol. 15, no. 7 - 8, pp. 328 - 338, 2012.

[28] E. Pop, V. Varshney and A. K. Roy, “Thermal properties of graphene: fundamentals and applications,” *MRS Bulletin,* vol. 37, no. 12, pp. 1273 - 1281, 2012.

[29] G. R. Yazdi, T. Iakimov and R. Yakimova, “Epitaxial graphene on SiC: a review of growth and characterization,” *Crystals,* vol. 6, no. 53, 2016.

[30] N. Mishra, J. Bockel, N. Motta and F. Iacopi, “Graphene growth on silicon carbide: a review,” *Physica Status Solidi A,* vol. 213, no. 9, pp. 2277 - 2289, 2016.

[31] Y.-M. Lin, C. Dimitrakopoulos, K. A. Jenkins, D. B. Farmer, Y.-H. Chiu, A. Grill and P. Avouris, “100-GHz transistors from wafer-scale epitaxial graphene,” *Science,* vol. 327, p. 662, 2012.

[32] M. Kruskopf, K. Pierz, S. Wundrack, R. Stosch, T. Dziomba, C.-C. Kalmbach, A. Müller, J. Baringhaus, C. Tegenkamp, F. J. Ahlers and H. W. Schumacher, “Epitaxial graphene on SiC: modification of structural and electron transport properties by substrate pretreatment,” *Journal of Physics: Condensed Matter,* vol. 27, no. 18, p. 185303, 2015.

[33] K. V. Emtsev, A. Bostwick, K. Horn, J. Jobst, G. L. Kellogg, L. Ley, J. L. McChesney, T. Ohta, S. A. Reshanov, J. Röhrl, E. Rotenberg, A. K. Schmid, D. Waldmann, H. B. Weber and T. Seyeller, “Towards wafer-size graphene layers by atmospheric pressure graphitization of silicon carbide,” *Nature Materials,* vol. 8, no. 1, pp. 203 - 207, 2009.

[34] X. Li, W. Cai, J. An, S. Kim, J. Nah, D. Yang, R. Piner, A. Velamakanni, I. Jung, E. Tutuc, S. K. Banerjee, L. Colombo and R. S. Ruoff, “Large-area synthesis of high-quality and uniform graphene films on copper foils,” *Science,* vol. 324, no. 5932, pp. 1312 - 1314, 2009.

[35] S. Bae, H. Kim, Y. Lee, X. Xu, J.-S. Park, Y. Zheng, J. Balakrishnan, T. Lei, H. R. Kim, Y. I. Song, Y. J. Kim, K. S. Kim, B. Ozyilmaz, J.-H. Ahn, B. H. Hong and S. Iijima, “Roll-to-roll production of 30-inch graphene films for transparent electrodes,” *Nature Nanotechnology,* vol. 5, pp. 574 - 578, 2012.

[36] S. Gottardi, K. Muller, L. Bignardi, J. C. Moreno-Lopez, T. A. Pham, O. Ivashenko, M. Yablonskikh, A. Barinov, J. Bjork, P. Rudolf and M. Stohr, “Comparing graphene growth on Cu(111) versus oxidized Cu(111),” *Nano Letters,* vol. 15, no. 2, pp. 917 - 922, 2015.

[37] L. Huang, Q. H. Chang, G. L. Guo, Y. Liu, Y. Q. Xie, T. Wang, B. Ling and H. F. Yang, “Synthesis of high-quality graphene films on nickel foils by rapid thermal chemical vapor deposition,” *Carbon,* vol. 50, no. 2, pp. 551 - 556, 2012.

[38] H. C. Lee, W.-W. Liu, S.-P. Chai, A. R. Mohamed, C. W. Lai, C.-S. Khe, C. H. Voon, U. Hashim and N. M. S. Hidayah, “Synthesis of single-layer

graphene: a review of recent development," *Procedia Chemistry,* vol. 19, pp. 916 - 921, 2016.

[39] J. Nam, D.-C. Kim, H. Yun, D. H. Shin, S. Nam, W. K. Lee, J. Y. Hwang, S. W. Lee, H. Weman and K. S. Kim, "Chemical vapor deposition of graphene on platinum: Growth and substrate interaction," *Carbon,* vol. 111, pp. 733 - 740, 2017.

[40] D. Jariwala, T. J. Marks and T. J. Hersam, "Mixed-dimensional van der Waals heterostructures," *Nature Materials,* vol. 16, pp. 170 - 180, 2017.

[41] K. S. Novoselov, A. Mishchenko, A. Carvalho and A. H. Castro Neto, "2D materials and van der Waals heterostructures," *Science,* vol. 353, no. 6298, p. 9439, 2016.

[42] C. R. Dean, A. F. Young, I. Meric, C. Lee, L. Wang, S. Sorgenfrei, K. Watanabe, T. Taniguchi, P. Kim, K. L. Shepard and J. Hone, "Boron nitride substrates for high-quality graphene electronics," *Nature Nanotechnology,* vol. 5, no. 1, pp. 722 - 726, 2010.

[43] A. K. Geim and I. V. Grigorieva, "Van der Waals heterostructures," *Nature,* vol. 499, pp. 419 - 425, 2013.

[44] H. S. Lee, S.-W. Min, Y.-G. Chang, M. K. Park, T. Nam, H. Kim, J. H. Kim, S. Ryu and S. Im, "MoS2 nanosheet phototransistors with thickness-modulated optical energy gap," *Nano Letters,* vol. 12, no. 7, pp. 3695 - 3700, 2012.

[45] B. Radisavljevic, A. Radenovic, J. Brivio, V. Giacometti and A. Kis, "Single-layer MoS2 transistors," *Nature Nanotechnology,* vol. 6, pp. 147 - 150, 2011.

[46] Q. H. Wang, K. Kalantar-Zadeh, A. Kis, J. N. Coleman and M. S. Strano, "Electronics and optoelectronics of two-dimensional transition metal dichalcogenides," *Nature Nanotechnology,* vol. 7, pp. 699 - 712, 2012.

[47] M. Yankowitz, F. Larentis, K. Kim, J. Xue, D. McKenzie, S. Huang, M. Paggen, M. N. Ali, R. J. Cava, E. Tutuc and B. J. LeRoy, "Intrinsic disorder in graphene on transition metal dichalcogenide heterostructures," *Nano Letters,* vol. 15, no. 3, pp. 1925 - 1929, 2015.

[48] L. Tao, E. Cinquanta, D. Chiappe, C. Grazianetti, M. Fanciulli, M. Dubey, A. Molle and D. Akinwande, “Silicene field-effect transistors operating at room temperature,” *Nature Nanotechnology,* vol. 10, pp. 227 - 231, 2015.

[49] A. Molle, J. Goldberger, M. Houssa, Y. Xu, S.-C. Zhang and D. Akinwande, “Buckled two-dimensional Xene sheets,” *Nature Materials,* vol. 16, pp. 163 - 169, 2017.

[50] J. Zhao, H. Liu, Z. Yu, R. Quhe, S. Zhou, Y. Wang, C. C. Liu, H. Zhong, N. Han, J. Lu, Y. Yao and K. Wu, “Rise of silicene: a competitive 2D material,” *Progress in Materials Science,* vol. 83, pp. 24 - 151, 2016.

[51] F. Schedin, A. K. Geim, S. V. Morozov, E. W. Hill, P. Blake, M. I. Katsnelson and K. S. Novoselov, “Detection of individual gas molecules adsorbed on graphene,” *Nature Materials,* vol. 6, pp. 652 - 655, 2007.

[52] G. Chen, T. M. Paronyan and A. R. Harutyunyan, “Sub-ppt gas detection with pristine graphene,” *Applied Physics Letters,* vol. 101, no. 5, p. 053119, 2012.

[53] F. Bonaccorso, Z. Sun, T. Hasan and A. C. Ferrari, “Graphene photonics and optoelectronics,” *Nature photonics,* vol. 4, pp. 611 - 622, 2010.

[54] G. R. Nash, S. J. Bending, Y. Kershaw, K. Eberl, P. Grambow and K. von Klitzing, “Surface acoustic wave studies of quantum nanostructures,” *Surface Science,* Vols. 361 - 362, no. 1996, pp. 668 - 672, 1996.

[55] A. H. Castro Neto, F. Guinea, N. M. R. Peres, K. S. Novoselov and A. K. Geim, “The electronic properites of graphene,” *Reviews of Modern Physics,* vol. 81, no. 1, pp. 109 - 162, 2009.

[56] K. S. Novoselov, A. K. Geim, S. V. Morozov, D. Jiang, M. I. Katsnelson, I. V. Grigorieva, S. V. Dubonos and A. A. Firsov, “Two-dimensional gas of massless Dirac fermions in graphene,” *Nature,* vol. 438, pp. 197 - 200, 2005.

[57] G. L. Klimchitskaya and V. M. Mostepanenko, “Conductivity of pure graphene: theoretical aproach using the polarization tensor,” *Physical Review B,* vol. 93, no. 24, p. 245419, 2016.

[58] F. Schwierz, “Graphene transistors,” *Nature Nanotechnology,* vol. 5, pp. 487 - 496, 2010.

[59] M. I. Katsnelson, “Zitterbewegung, chirality, and minimal conductivity in graphene,” *The European Physical Journal B,* vol. 51, no. 2, pp. 157 - 160, 2006.

[60] S. Samaddar, I. Yudhistira, S. Adam, H. Courtois and C. B. Winkelmann, “Charge puddles in graphene near the Dirac point,” *Physical Review Letters,* vol. 116, no. 12, p. 126804, 2016.

[61] O. Moldovan, B. Iniguez, M. J. Deen and L. F. Marsal, “Graphene electronic sensors - review of recent developments and future challenges,” *IET Circuits, Devices & Systems,* vol. 9, no. 6, pp. 446 - 453, 2015.

[62] T. O. Wehling, A. I. Lichtenstein and M. I. Katsnelson, “First-principles studies of water absorption on graphene: The role of the substrate,” *Applied Physics Letters,* vol. 93, no. 20, p. 202110, 2008.

[63] T. O. Wehling, K. S. Novoselov, S. V. Morozov, E. E. Vdovin, M. I. Katsnelson, A. K. Geim and A. I. Lichtenstein, “Molecular doping of graphene,” *Nano Letters,* vol. 8, no. 1, pp. 173 - 177, 2008.

[64] T. O. Wehling, M. I. Katsnelson and A. I. Lichtenstein, “Adsorbates on graphene: impurity states and electron scattering,” *Chemical Physics Letters,* vol. 476, no. 4-6, pp. 125 - 134, 2009.

[65] X. Li, T. Tang, M. Li. and X. He, “Nitrogen-doped graphene films from simple photochemical doping for n-type field-effect transistors,” *Applied Physics Letters,* vol. 106, no. 1, p. 013110, 2015.

[66] P. Solís-Fernandez, S. Okada, T. Sato, M. Tsuji and H. Ago, “Gate-tunable Dirac point of molecular doped graphene,” *ACS Nano,* vol. 10, no. 2, pp. 2930 - 2939, 2016.

[67] H. Medina, Y.-C. Lin, D. Obergfell and P.-W. Chiu, “Tuning of charge densities in graphene by molecule doping,” *Advanced Functional Materials,* vol. 21, no. 14, pp. 2687 - 2692, 2011.

[68] K. S. Novoselov, V. I. Fal'ko, L. Colombo, P. R. Gellert, M. G. Schwab and K. A. Kim, “A roadmap for graphene,” *Nature,* vol. 490, pp. 192 - 200, 2012.

[69] S. Weingart, C. Bock, U. Kunze, F. Speck, T. Seyller and L. Ley, “Low-tmperature ballistic transport in nanoscale epitaxial graphene cross junctions,” *Applied Physics Letters,* vol. 95, no. 26, p. 262101, 2009.

[70] X. Du, I. Skachko, A. Barker and E. Y. Andrei, “Approaching ballistic transport in suspended graphene,” *Nature Nanotechnology,* vol. 3, pp. 491 - 495, 2008.

[71] Y. Zhang, Y.-W. Tan, H. L. Stormer and P. Kim, “Experimental observation of the quantum Hall effect and Berry's phase in graphene,” *Nature,* vol. 438, pp. 201 - 204, 2005.

[72] H. S. Song, S. L. Li, H. Miyazaki, S. Sato, K. Hayashi, A. Yamada, N. Yokoyama and K. Tsukagoshi, “Origin of the relatively low transport mobility of graphene grown through chemical vapor deposition,” *Scientific Reports,* vol. 2, no. 337, pp. 1 - 6, 2012.

[73] M. Hofmann, Y. P. Hsieh, K. W. Chang, H. G. Tsai and T. T. Chen, “Dopant morphology as the factor limiting graphene conductivity,” *Scientific Reports,* vol. 5, no. 17393, pp. 1- 7, 2015.

[74] Y. Zhang, V. W. Brar, C. Girit, A. Zetti and M. F. Crommie, “Origin of spatial charge inhomogeneity in graphene,” *Nature Physics,* vol. 5, pp. 722 - 726, 2009.

[75] J. Martin, N. Akerman, G. Ulbricht, T. Lohmann, J. H. Smet, K. von Klitzing and A. Yacoby, “Observation of electron-hole puddles in graphene using a scanning single-electron transistor,” *Nature Physics,* vol. 4, pp. 144 - 148, 2008.

[76] M. I. Katsnelson and A. K. Geim, “Electron scattering in microscopic corrugations in graphene,” *Philosophical Transactions of the Royal Society A,* vol. 366, pp. 195 - 204, 2008.

[77] X. Liang, B. A. Sperling, I. Calizo, G. Cheng, C. A. Hacker, Q. Zhang, Y. Obeng, K. Yan, H. Peng, Q. Li, X. Zhu, H. Yuan, A. R. Hight Walker, Z. Liu, L.-M. Peng and C. A. Richter, “Toward clean and crackless transfer of graphene,” *ACS Nano,* vol. 5, no. 11, pp. 9144 - 9153, 2011.

[78] M. Ishigami, J. H. Chen, W. G. Cullen, M. S. Fuhrer and E. D. Williams, “Atomic structure of graphene on SiO2,” *Nano Letters,* vol. 7, no. 6, pp. 1643 - 1648, 2007.

[79] S. Fratini and F. Guinea, “Substrate-limited electron dynamics in graphene,” *Physical Review B,* vol. 77, p. 195415, 2008.

[80] K. I. Bolotin, K. J. Sikes, Z. Jiang, M. Klima, G. Fudenberg, J. Hone, P. Kim and H. L. Stormer, “Ultrahigh electron mobility in suspended graphene,” *Solid State Communications,* vol. 146, no. 9 - 10, pp. 351 - 355, 2008.

[81] K. Nakada, M. Fujita, G. Dresselhaus and M. S. Dresselhaus, “Edge state in graphene ribbons: nanometer size effect and edge shape dependence,” *Physical Review B,* vol. 54, no. 24, p. 17954, 1996.

[82] K. Wakabayashi, M. Fujita, H. Ajiki and M. Sigrist, “Electronic and magnetic properties of nanographite ribbons,” *Physical Review B,* vol. 59, no. 12, p. 8271, 1999.

[83] A. Maffucci and G. Miano, “Electrical properties of graphene for interconnect applications,” *Applied Sciences,* vol. 4, no. 2, pp. 305 - 317, 2014.

[84] A. Celis, M. N. Nair, A. Taleb-Ibrahimi, E. H. Conrad, C. Berger, W. A. de Heer and A. Tejeeda, “Graphene nanoribbons: fabrication, properties and devices,” *Journal of Physics D: Applied Physics,* vol. 49, no. 14, p. 143001, 2016.

[85] M. Y. Han, B. Ozyilmaz, Y. Zhang and P. Kim, “Energy band-gap engineering of graphene nanoribbons,” *Physical Review Letters,* vol. 98, no. 20, p. 206805, 2007.

[86] C. Canali, C. Jacoboni, F. Nava, G. Ottaviani and A. Alberigi-Quaranta, “Electron drift velocity in silicon,” *Physical Review B,* vol. 12, no. 4, pp. 2265 - 2284, 1975.

[87] B. G. Streetman and S. K. Banerjee, Solid State Electronic Devices, New Jersey, USA: Prentice Hall, 2000.

[88] S. E. Bryan, Y. Yang and R. Murali, “Conductance effects of epitaxial graphene nanoribbons: influence and size effects and substrate morphology,” *Journal of Physical Chemistry C,* vol. 115, no. 20, pp. 10230 - 10235, 2011.

[89] W. S. Hwang, P. Zhao, K. Tahy, L. O. Nyakiti, V. D. Wheeler, R. L. Myers-Ward, C. R. Eddy, Jr., D. K. Gaskill, J. A. Robinson, W. Haensch, H. Xing, A. Seabaugh and D. Jena, “Graphene nanoribbon field-effect transistors on wafer-scale epitaxial graphene on SiC substrates,” *APL Materials,* vol. 3, no. 1, p. 011101, 2015.

[90] M. W. Iqbal, M. Z. Iqbal, X. Jin, C. Hwang and J. Eom, “Edge oxidation effect of chemical-vapor-deposition-grown graphene nanoconstriction,” *ACS Applied Materials and Interfaces,* vol. 6, no. 6, pp. 4207 - 4213, 2014.

[91] B. Xiao, X. Li, X. Li, B. Wang, C. Langford, R. Li and X. Sun, “Graphene nanoribbons derived from the unzipping of carbon nanotubes: controlled synthesis and superior lithium storage performance,” *Journal of Physical Chemistry C,* vol. 118, no. 2, pp. 881 - 890, 2014.

[92] A. B. Kuzmenko, E. van Heuman, F. Carbone and D. van der Marel, “Universal optical conductance of graphite,” *Physical Review Letters,* vol. 100, no. 11, p. 117401, 2008.

[93] L. A. Falkovsky, “Optical properties of graphene,” *Journal of Physics: Conference Series,* vol. 129, p. 012004, 2008.

[94] M. K. Kavitha and M. Jasiwal, “Graphene: a review of optical properties and photonic applications,” *Asian Journal of Physics,* vol. 25, no. 7, pp. 809 - 831, 2016.

[95] F. Xia, T. Mueller, Y. Lin, A. Valdes-Garcia and P. Avouris, “Ultrafast graphene photodetector,” *Nature Nanotechnology,* vol. 4, pp. 839 - 843, 2009.

[96] C.-H. Liu, Y.-C. Chang, T. B. Norris and Z. Zhong, “Graphene photodetectors with ultra-broadband and high responsivity at room temperature,” *Nature Nanotechnology,* vol. 9, pp. 273 - 278, 2014.

[97] K.-C. Je and Y. Kim, “Ultrafast relaxation of photexcited carriers in semiconductor superlattices,” *Japanese Journal of Applied Physics,* vol. 37, no. 10, pp. 5490 - 5492, 1998.

[98] R. Rota, F. Rossi, P. Lugli and E. Molinari, “Ultrfast relaxation of photoexcited carriers in semiconductor quantum wires: a Monte Carlo approach,” *Physical Review B,* vol. 52, no. 7, pp. 5183 - 5201, 1995.

[99] N. M. Gabor, J. C. W. Song, Q. Ma, N. L. Nair, T. Taychatanapat, K. Watanabe, T. Taniguchi, L. S. Levitov and P. Jarillo-Herrero, “Hot carrier-assisted intrinsic photoresponse in graphene,” *Science,* vol. 334, pp. 648 - 652, 2011.

[100] J. C. W. Song, M. S. Rudner, C. M. Marcus and L. S. Levitov, “Hot carrier transport and photocurrent response in graphene,” *Nano Letters,* vol. 11, no. 11, pp. 4688 - 4692, 2011.

[101] R. Bistritzer and A. H. MacDonald, “Electronic cooling in graphene,” *Physical Review Letters,* vol. 102, no. 20, p. 206410, 2009.

[102] T. Winzer, A. Knorr and E. Malic, “Carrier multiplication in graphene,” *Nano Letters,* vol. 10, no. 12, pp. 4839 - 4843, 2010.

[103] I. J. Vera-Marun, J. J. van den Berg, F. K. Dejene and B. J. van Wees, “Direct electronic measurement of Peltier cooling and heating in graphene,” *Nature Communications,* vol. 7, p. 11525, 2016.

[104] K. L. Grosse, M.-H. Bae, F. Lian, E. Pop and W. P. King, “Nanoscale Joule heating, Peltier cooling and current crowding at graphene-metal contacts,” *Nature Nanotechnology,* vol. 6, pp. 287 - 290, 2011.

[105] M. Freitag, M. Steiner, Y. Martin, V. Perebeinos, Z. Chen, J. C. Stand and P. Avouris, “Energy dissipation in graphene field-effect transistors,” *Nano Letters,* vol. 9, no. 5, pp. 1883 - 1888, 2009.

[106] P. Blake, E. W. Hill, A. H. Castro Neto, K. S. Novoselov, D. Jiang, R. Yang, T. J. Booth and A. K. Geim, “Making graphene visible,” *Applied Physics Letters,* vol. 91, no. 6, p. 063124, 2007.

[107] S. Roddaro, P. Pingue, V. Piazza, V. Pellegrini and F. Beltram, “The optical visibility of graphene: interference colours of ultrathin graphite on SiO2,” *Nano Letters,* vol. 7, no. 9, pp. 2707 - 2710, 2007.

[108] M. Woszczyna, M. Friedemann, K. Pierz, T. Weimann and F. J. Ahler, “Magneto-transport properties of exfoliated graphene on GaAs,” *Journal of Applied Physics,* vol. 110, no. 4, p. 043712, 2011.

[109] S. Haar, M. E. Gemayel, Y. Shin, G. Melinte, M. A. Squillaci, O. Ersin, C. Casiraghi, A. Ciesielski and P. Samori, “Enhancing the liquid-phase exfoliatoin of graphene in organic solvents upon addition of n-octylbenzene,” *Scientifc Reports,* vol. 5, p. 16684, 2015.

[110] S. Haar, M. Bruna, J. X. Lian, F. Tomarchio, Y. Oliver, R. Mazzaro, V. Morandi, J. Moran, A. C. Ferrari, D. Beljonne, A. Ciesielski and P. Samori, “Liquid-phase exfoliation of graphite into single- and few-layer graphene

with α-functionalized alkanes," *The Journal of Physical Chemistry Letters,* vol. 7, no. 14, pp. 2714 - 2721, 2016.

[111] Y. Zhang, L. Zhang and C. Zhou, "Review of chemical vapor deposition of graphene and related applications," *Accounts of Chemical Research,* vol. 46, no. 10, pp. 2329 - 2339, 2013.

[112] C. Mattevi, H. Kim and M. Chhowalla, "A review of chemical vapour deposition of graphene on copper," *Journal of Materials Chemistry,* vol. 21, no. 10, pp. 3324 - 3334, 2011.

[113] A. N. Obraztsov, E. A. Obraztsova, A. V. Tyurnina and A. A. Zolotukhin, "Chemical vapor deposition of thin graphite films of nanometer thickness," *Carbon,* vol. 45, no. 10, pp. 2017 - 2021, 2007.

[114] K. S. Kim, Y. Zhao, H. Jang, S. Y. Lee, J. M. Kim, K. S. Kim, J.-. H. Ahn, P. Kim, J.-. Y. Choi and B. H. Hong, "Large-scale pattern growth of graphene films for stretchable transparent electrodes," *Nature,* vol. 457, pp. 706 - 710, 2009.

[115] Q. Yu, J. Lian, S. Siriponglert, H. Li, Y. P. Chen and S.-S. Pei, "Graphene segregated on Ni surfaces and transferred to insulators," *Applied Physics Letters,* vol. 93, no. 11, p. 133103, 2008.

[116] A. Srivastava, C. Galande, L. Ci, L. Song, C. Rai, D. Jariwala, K. F. Felley and P. M. Ajayan, "Novel liquid precursor-based facile synthesis of large-area continuous, single, and few-layer graphene films," *Chemistry of Materials,* vol. 22, no. 11, pp. 3457 - 3461, 2010.

[117] P. Nemes-Incze, K. J. Yoo, L. Tapaszto, G. Dobrik, J. Labar, Z. E. Horbath, C. Hwang and L. P. Biro, "Revealing the grain structure of graphene grown by chemical vapor deposition," *Applied Physics Letters,* vol. 99, no. 2, p. 023104, 2011.

[118] A. W. Tsen, L. Brown, M. P. Levendorf, F. Ghahari, P. Y. Huang, R. W. Havener, C. S. Ruiz-Vargas, D. A. Muller, P. Kim and J. Park, "Tailoring electrical transport across grain boundaries in polycrystalline graphene," *Science,* vol. 336, pp. 1143 - 1146, 2012.

[119] A. Reina, X. Jia, J. Ho, D. Nezivh, H. Son, V. Bulovic, M. S. Dresselhaus and J. Kong, "Large area, few-layer graphene films on arbitrary substrates by chemical vapor deposition," *Nano Letters,* vol. 9, no. 1, pp. 30 - 35, 2009.

[120] T. Wu, X. Zhang, Q. Yuan, J. Xue, G. Lu, Z. Liu, H. Wang, H. Wang, F. Ding, Q. Yu, X. Xie and M. Jiang, “Fast growth of inch-sized single-crystalline graphene from a controlled single nucleus on Cu-Ni alloys,” *Nature Materials,* vol. 15, no. 1, pp. 43 - 47, 2016.

[121] J. W. Suk, A. Kitt, C. W. Magnuson, Y. Hao, S. Ahmed, J. An, A. K. Swan, B. B. Goldberg and R. S. Ruoff, “Transfer of CVD-grown monolayer graphene onto arbitrary substrates,” *ACS Nano,* vol. 5, no. 9, pp. 6916 - 6924, 2011.

[122] Y. Chen, X.-L. Gong and J.-G. Gai, “Progress and challenges in transfer of large-area graphene films,” *Advanced Science,* vol. 3, p. 1500343, 2016.

[123] Y.-C. Lin, C.-C. Lu, C.-H. Yeh, C. Jin, K. Suenaga and P.-W. Chiu, “Graphene annealing: how clean can it be?,” *Nano Letters,* vol. 12, no. 1, pp. 414 - 419, 2011.

[124] A. Pirkle, J. Chan, A. Venugopal, D. Hinojos, C. W. Magnuson, S. McDonnell, L. Colombo, E. M. Vogel, R. S. Ruoff and R. M. Wallace, “The effect of chemical residues on the physical and electrical properties of chemical vapor deposited graphene transferred to SiO2,” *Applied Physics Letters,* vol. 99, no. 12, p. 122108, 2011.

[125] Y. Hao, M. S. Bharati, L. Wang, Y. Liu, S. Nie, X. Wang, H. Chou, C. Tan, B. Fallahazad, H. Ramanarayan, C. W. Magnuson, E. Tutuc, B. I. Yakobson, K. F. McCarty, Y. W. Zhang, P. Kim, J. Hone, L. Colombo and R. S. Ruoff, “The role of oxygen in the growth of large single-crystal graphene on copper,” *Science,* vol. 342, pp. 720 - 723, 2013.

[126] J. Pang, R. G. Mendes, P. S. Wrobel, M. D. Wlodarski, H. Q. Ta, L. Zhao, L. Giebeler, B. Trzebicka, T. Gemming, L. Fu, Z. Liu, J. Eckert, A. Bachmatiuk and M. H. Rümmeli, “Self-terminating confinement approach for large-area uniform monolayer graphene directly over Si/SiOx by chemical vapor deposition,” *ACS Nano,* vol. 11, no. 2, pp. 1946 - 1956, 2017.

[127] D. S. L. Abergel, A. Russell and V. I. Fal'ko, “Visibility of graphene flakes on a dielectric substrate,” *Applied Physics Letters,* vol. 91, no. 6, p. 063125, 2007.

[128] R. Beams, L. G. Cancado and L. Novotny, “Raman characterization of defects and dopants in graphene,” *Journal of Physics: Condensed Matter,* vol. 27, no. 8, pp. 1 - 27, 2015.

[129] A. C. Ferrari, “Raman spectroscopy of graphene and graphite: Disorder, electron-phonon coupling, doping and nonadiabatic effects,” *Solid State Communications,* vol. 143, no. 1-2, pp. 47 - 57, 2007.

[130] A. C. Ferrari and D. M. Basko, “Raman spectroscopy as a versatile tool for studying the properties of graphene,” *Nature Nanotechnology,* vol. 8, pp. 235 - 246, 2013.

[131] A. C. Ferrari, J. C. Meyer, V. Scardaci, C. Casiraghi, M. Lazzeri, F. Mauri, S. Piscanec, D. Jiang, K. S. Novoselov, S. Rother and A. K. Geim, “Raman spectrum of graphene and graphene layers,” *Physical Review Letters,* vol. 97, no. 18, p. 187401, 2006.

[132] H. A. Szymanski, Raman Spectroscopy: Theory and PRactice, New York: Springer US, 1967.

[133] L. M. Malard, M. A. Pimenta, G. Dresselhaus and M. S. Dresselhaus, “Raman spectroscopy in graphene,” *Physics Reports,* vol. 473, no. 5 - 6, pp. 51 - 87, 2009.

[134] F. H. Alharbi and S. Kais, “Theoretical limits of photovoltaics efficiency and possible improvements by intuitive approaches learned from photosynthesis and quantum coherence,” *Renewable and Sustainable Energy Reviews,* vol. 43, pp. 1073 - 1089, 2015.

[135] W. S. Koh, C. H. Gan, W. K. Phua, Y. A. Akimov and P. Bai, “The potential of graphene as an ITO replacement in organic solar cells: an optical perspective,” *IEEE Journal of Selected Topics in Quantum Electronics,* vol. 20, no. 1, pp. 36 - 42, 2914.

[136] M. C. Lemme, F. H. L. Koppens, A. L. Falk, M. S. Rudner, H. Park, L. S. Levitov and C. M. Marcus, “Gate-activated photoresponse in a graphene-p-n junction,” *Nano Letters,* vol. 11, no. 10, pp. 4134 - 4137, 2011.

[137] X. Xu, N. M. Gabor, J. S. Alden, A. M. van der Zande and P. L. McEuen, “Photo-thermoelectric effect at a graphene interface junction,” *Nano Letters,* vol. 10, no. 2, pp. 562 - 566, 2010.

[138] U. Sassi, R. Parret, S. Nanot, M. Bruna, S. Borini, D. De Fazio, E. Lidorikis, F. H. L. Koppens, A. C. Ferrari and A. Colli, “Graphene-based mid-infrared room temperature pyroelectric bolometers with ultrahigh temperature coefficient of resistance,” *Nature Communications,* vol. 8, p. 14311, 2017.

[139] K. K. Gopalan, D. Janner, S. Nanot, R. Parret, M. B. Lundeberg, F. H. L. Koppens and V. Pruneri, “Mid-infrared pyroresistive graphene detector on LiNbO3,” *Advanced Optical Materials,* vol. 5, no. 4, p. 1600723, 2017.

[140] Q. Han, T. Gao, R. Zhang, Y. Chen, J. Chen, G. Liu, Y. Zhang, Z. Liu, X. Wu and D. Yu, “Highly sensitive hot electron bolometer based on disordered graphene,” *Scientific Reports,* vol. 3, p. 3533, 2013.

[141] P. Loza-Alvarez, C. T. A. Brown, D. T. Reid, W. Sibbett and M. Missey, “High-reperition-rate ultrashort-pulse optical parametric oscillator continuously tunable from 2.8 - 6.8 μm,” *Optics Letters,* vol. 24, no. 21, pp. 1523 - 1525, 1999.

[142] M. Esseling, A. Zaltron, C. Sada and C. Denz, “Charge sensor and particle trap based on z-cut lithium niobate,” *Applied Physics Letters,* vol. 103, no. 6, p. 061115, 2013.

[143] E. M. Bourim, C.-W. Moon, S.-W. Lee, V. Sidorkin and I. K. Yoo, “Pyroelectric electron emission from -z face polar surface of lithium niobate monodomain single crystal,” *Journal of Electroceramics,* vol. 17, no. 2 - 4, pp. 479 - 485, 2006.

[144] X. Tang, N. Mager, B. Vanhorenbeke, S. Hermans and J.-P. Raskin, “Defect-free functionalized graphene sensor for formaldehyde detection,” *Nanotechnology,* vol. 28, no. 5, p. 055501, 2016.

[145] L. M. Lawton, N. H. Mahlmeister, I. J. Luxmorre and G. R. Nash, “Prospective for graphene based thermal mid-infrared light emitting devices,” *AIP Advances,* vol. 4, no. 8, p. 087139, 2014.

[146] N. H. Mahlmeister, L. M. Lawton, I. J. Luxmoore and G. R. Nash, “Modulation characteristics of graphene-based thermal emitters,” *Applied Physics Express,* vol. 9, no. 1, p. 012105, 2015.

[147] H. R. Barnard, E. Zossimova, N. H. Mahlmeister, L. M. Lawton, I. J. Luxmoore and G. R. Nash, “Boron nitride encapsulated graphene infrared emitters,” *Applied Physics Letters,* vol. 108, no. 13, p. 131110, 2016.

[148] S. D. Smith, H. R. Hardaway and J. G. Crowder, “Recent developments in the applications of mid-infrared lasers, LEDs, and other solid state sources to gas detection,” *Proceedings of SPIE,* vol. 4651, pp. 157 - 172, 2002.

[149] D. Royer and E. Dieulesaint, Elastic Waves in Solids I: Free and Guided Propagation, Heidelberg: Springer, 2000.

[150] R. M. White and F. W. Voltmer, “Direct piezoelectric coupling to surface elastic waves,” *Applied Physics Letters,* vol. 7, no. 12, pp. 314 - 316, 1965.

[151] Lord Rayleigh, “On waves propagated along the plane surface of an elastic solid,” *Proceedings of the London Mathematical Society,* Vols. s1 - 17, no. 1, pp. 4 - 11, 1885.

[152] G. Chow, E. Uchaker, G. Cao and J. Wang, “Laser-induced surface acoustic waves: an alternative method to nanoindentation for the mechanical characterization of porous nanostructured thin film electrode media,” *Mechanics of Materials,* vol. 91, no. 2, pp. 333 - 342, 2015.

[153] S. Kitazawa, A. Chiba and E. Wakai, “Laser-induced surface acoustic waves and their detection via diagnostic systems for detection of radiation damage on steel materials of nuclear devices,” *Nuclear Instruments and Methods in Physics Research A,* vol. 786, pp. 47 - 50, 2015.

[154] M. Ochiai, “Laser-induced surface acoustic wave technique for precise depth measurement of stress corrosion cracking,” *Journal of Physics: Conference Series,* vol. 278, no. 1, pp. 1 - 5, 2011.

[155] C. Li, G. Guan, F. Zhang, G. Nabi, R. K. Wang and Z. Huang, “Laser induced surface acoustic wave combined with phase sensitive optical coherence tomography for superficial tissue characterization: a solution for practical application,” *Biomedical Optics Express,* vol. 5, no. 5, pp. 1403 - 1418, 2014.

[156] A. van den Beukel, “On the theory of the acousto-electric effect,” *Applied Scientific Research,* vol. B, no. 5, pp. 459 - 468, 1955.

[157] G. Weinreich, T. M. Sanders and H. G. White, “Acoustoelectric effect in n-type germanium,” *Physical Review,* vol. 114, no. 1, pp. 33 - 44, 1959.

[158] G. Weinreich, “Acoustodynamic effects in semiconductors,” *Physical Review,* vol. 104, no. 2, pp. 321 - 324, 1956.

[159] G. Weinreich and H. G. White, “Observation of the acoustoelectric effect,” *Physical Review,* vol. 106, no. 5, pp. 1104 - 1106, 1957.

[160] A. R. Hutson and D. L. White, “Elastic wave propagation in piezoelectric semiconductors,” *Journal of Applied Physics,* vol. 33, no. 40, pp. 40 - 47, 1962.

[161] K. A. Ingebrigsten, “Linear and nonlinear attenuation of acoustic surface waves in a piezoelectric coated with a semiconducting film,” *Journal of Applied Physics,* vol. 41, no. 2, pp. 454 - 459, 1970.

[162] K. A. Ingebrigsten, “Surface Waves in Piezoelectrics,” *Journal of Applied Physics,* vol. 40, no. 7, pp. 2681 - 2686, 1969.

[163] A. Esslinger, R. W. Winkler, C. Rocke, A. Wixforth, J. P. Hotthaus, H. Nickel, W. Schlapp and R. Losch, “Ultrasonic approach to the integer and fractional quantum Hall effect,” *Surface Science,* vol. 305, pp. 83 - 86, 1994.

[164] V. I. Fal'ko, S. V. Meshkov and S. V. Iordanskii, “Acoustoelectric drag effect in the two-dimensional electron gas at strong magnetic field,” *Physical Review B,* vol. 47, no. 15, pp. 9910 - 9912, 1993.

[165] M. Rotter, A. Wixforth, W. Ruile, D. Bernklau and H. Riechert, “Giant acoustoelectric effect in GaAs/LiNbO3 hybrids,” *Applied Physics Letters,* vol. 73, no. 15, p. 2128, 1998.

[166] R. Arsat, M. Breedon, M. Shafiei, P. G. Spizziri, S. Gilje, R. B. Kaner, K. Kalantar-zadeh and W. Wlodarski, “Graphene-like nano-sheets for surface acoustic wave gas sensor applications,” *Chemical Physics Letters,* no. 4-6, pp. 344 - 347, 2009.

[167] E. F. Whitehead, E. M. Chick, L. Bandhu, L. M. Lawton and G. R. Nash, “Gas loading of graphene-quartz surface acoustic wave devices,” *Applied Physics Letters,* vol. 103, no. 6, p. 063110, 2013.

[168] D. Ciplys, R. Rimeika, V. Chivukula, M. S. Shur, J. H. Kim and J. M. Xu, “Surface acoustic waves in graphene structures: response to ambient humidity,” in *Proceedings of the IEEE Sensors 2010*, Kona, USA, 2010.

[169] Y. J. Guo, J. Zhang, C. Zhao, P. A. Hu, X. T. Zu and Y. Q. Fu, “Graphene/LiNbO3 surface acoustic wave device based relative humidity sensor,” *Optik,* vol. 125, no. 19, pp. 5800 - 5802, 2014.

[170] P. V. Santos, T. Schumann, M. H. Oliveira, Jr., J. M. J. Lopes and H. Riechert, “Acousto-electric transport in epitaxial monolayer graphene on SiC,” *Applied Physics Letters,* vol. 102, no. 22, p. 221907, 2013.

[171] A. Hernandez-Minguez, A. Tahraoui, J. M. J. Lopes and P. V. Santos, “Acoustoelectric transport at gigahertz frequencies in coated epitaxial graphene,” *Applied Physics Letters,* vol. 108, no. 19, p. 193502, 2016.

[172] S. Okuda, T. Ikuta, Y. Kanai, T. Ono, S. Ogawa, D. Fujisawa, M. Shimatani, K. Inoue, K. Maehashi and K. Matsumoto, “Acoustic carrier transportation induced by surface acoustic waves in graphene in solution,” *Applied Physics Express,* vol. 9, no. 4, p. 045104, 2016.

[173] S. O. Yurchenko, K. A. Komarov and V. I. Pustovoit, “Multilayer-graphene-based amplifier of surface acoustic waves,” *AIP Advances,* vol. 5, no. 5, p. 057144, 2015.

[174] Z. Insepov, E. Emelin, O. Kononenko, D. V. Roshchupkin, K. B. Tnyshtykbayev and K. A. Baigarin, “Surface acoustic wave amplification by direct current-voltage supplied to graphene film,” *Applied Physics Letters,* vol. 106, no. 2, p. 023505, 2015.

[175] L. Shao and K. P. Pipe, “Amplificatoin and directional emission of surface acoustic waves by a two-dimensional electron gas,” *Applied Physics Letters,* vol. 106, no. 2, p. 023106, 2015.

[176] G. Coco, E. Cadelano and L. Colombo, “Gap opening in graphene by shear strain,” *Physical Review B,* vol. 81, no. 24, p. 241412, 2010.

[177] A. J. Vigil, A. W. Hull, L. P. Solie, M. J. Miller, R. J. Kansy and D. A. Fleisch, “Applications of acoustic charge transport,” *IEEE Transactions on Ultrasonics, Ferroelectrics, and Frequency Control,* vol. 40, no. 5, pp. 488 - 495, 1993.

[178] L. Bandhu, “Acoustoelectric Transport in Graphene,” Univeristy of Exeter, 2015.

[179] F. J. Ahlers, O. F. O. Kieler, B. E. Sagol, K. Pierz and U. Siegner, “Quantized acoustoelectric single electron transport close to equilibrium,” *Journal of Applied Physics,* vol. 100, no. 9, p. 093702, 2006.

[180] O. D. D. Couto, Jr, S. Lazic, F. Iikawa, J. A. H. Stotz, U. Jahn, R. Hey and P. V. Santos, “Photon anti-bunching in acoustically pumped quantum dots,” *Nature Photonics,* vol. 3, no. 11, pp. 645 - 648, 2009.

[181] J. Cunningham, V. I. Talyanskii, J. M. Shilton, M. Pepper, A. Kristensen and P. E. Lindelof, “High-frequency single-electron transport and the quantized acoustoelectric effect,” *Physica B,* vol. 280, pp. 493 - 494, 2000.

[182] C. Rocke, S. Zimmerman, A. Wixforth, J. P. Kotthaus, G. Bohm and G. Weimann, “Acoustically driven storage of light in a quantum well,” *Physical Review Letters,* vol. 78, no. 21, pp. 4099 - 4102, 1997.

[183] M. Streibl, C. Rocke, A. O. Govorov and A. Wixforth, “Novel optoelectronic signal processing via the combination of SAW and semiconductor heterostructures,” in *1998 IEEE Ultrasonics Symposium*, Sendai, Japan, 1998.

[184] J. Devkota, P. R. Ohodnicki and D. W. Greve, “SAW sensors for chemical vapours and gases,” *Sensors,* vol. 17, no. 801, pp. 1 - 28, 2017.

[185] X. Li, Y. Zhu, W. Cai, M. Borysiak, B. Han, D. Chen, R. D. Piner, L. Colombo and R. S. Ruoff, “Transfer of large-area graphene films for high-performance transparent conductive electrodes,” *Nano Letters,* vol. 9, no. 12, pp. 4359 - 4363, 2009.

[186] Z. Ni, Y. Wang, T. Yu and Z. Shen, “Raman spectroscopy and imaging of graphene,” *Nano Research,* vol. 1, no. 4, pp. 273 - 291, 2008.

[187] A. Gupta, G. Chen, P. Joshi, S. Tadigadapa and P. C. Eklund, “Raman scattering from high-frequency phonons in supported n-graphene layer systems,” *Nano Letters,* vol. 6, no. 12, pp. 2667 - 2673, 2006.

[188] H. Pinto and A. Markevich, “Electronic and electrochemical doping of graphene by surface adsorbates,” *Beilstein Journal of Nanotechnology,* vol. 5, pp. 1842 - 1848, 2014.

[189] M. Wall, “Raman spectroscopy optimizes graphene characterization,” *Advanced Materials and Processes,* vol. 4, pp. 35 - 38, 2012.

[190] J. Pan and P. Fraud, “Wire bonding challenges in optoelectronics packaging,” Society of Manufacturing Engineers, Dearborn, 2004.

[191] D. Bodas, S. J. Patil, V. N. Krishnamurthy and S. A. Ganal, “PMMA as an etch mask for silicon micromachining - a feasibility study,” *Journal of the Indian Institute of Science,* vol. 81, pp. 645 - 651, 2001.

[192] K. L. Grosse, M. Bae, F. Lian, E. Pop and W. P. King, “Nanoscale Joule heating, Peltier cooling and current crowding at graphene-metal contacts,” *Nature Nanotechnology,* vol. 6, no. 5, pp. 287 - 290, 2011.

[193] K. Nagashio, T. Nishimura, K. Kita and A. Toriumi, “Contact resistivity and current flow path at metal/graphene contact,” *Applied Physics Letters,* vol. 97, no. 14, p. 143514, 2010.

[194] E. Watanabe, A. Conwill, D. Tsuya and Y. Koide, “Low contact resistance metals for graphene based devices,” *Diamond & Related Materials,* vol. 24, pp. 171 - 174, 2012.

[195] D. Roshchupkin, L. Ortega, I. Zizak, O. Plotitcyna, V. Matveev, O. Kononenko, E. Emelin, E. Erko, K. Tynyshtykbayev, D. Irzhak and Z. Insepov, “Surface acoustic wave propagation in graphene film,” *Journal of Applied Physics,* vol. 118, no. 10, p. 104901, 2015.

[196] V. S. Chivukula, D. Ciplys, J. H. Kim, R. Rimeika, J. M. Xu and M. S. Shur, “Surface acoustic wave response to optical absorption by graphene composite film,” *IEEE Transactions on Ultrasonics, Ferroelectrics, and Frequency Control,* vol. 59, no. 2, pp. 265 - 270, 2012.

[197] T. Poole, L. Bandhu and G. R. Nash, “Acoustoelectric photoresponse in graphene,” *Applied Physics Letters,* vol. 106, no. 13, p. 133107, 2015.

[198] O. V. Yazyev and S. G. Louie, “Electronic transport in polycrystalline graphene,” *Nature Materials,* vol. 9, pp. 806 - 809, 2010.

[199] A. Venugopal, J. Chan, X. Li, C. W. Magnuson, W. P. Kirk, L. Colombo, R. S. Ruoff and E. M. Vogel, “Effective mobility of single-layer graphene transistors as a function of channel dimensions,” *Journal of Applied Physics,* vol. 109, no. 10, p. 104511, 2011.

[200] J.-. H. Chen, C. Jang, S. Adam, M. S. Fuhrer, E. D. Williams and M. Ishigami, “Charged-impurity scattering in graphene,” *Nature Physics,* vol. 4, no. 5, pp. 377 - 381, 2008.

[201] Z. Fan, A. Uppstu and A. Harju, “Dominant source of disorder in graphene: charged impurities or ripples?,” *2D Materials,* vol. 4, no. 2, p. 025004, 2017.

[202] M. Lafkioti, B. Krauss, T. Lohmann, U. Zschieschang, H. Klauk, K. v. Klitzing and J. H. Smet, “Graphene on a hydrophobic substrate: doping reduction and hysteresis suppression under ambient conditions,” *Nano Letters,* vol. 10, no. 4, pp. 1149 - 1153, 2010.

[203] S. S. Varghese, S. Lonkar, K. K. Singh, S. Swaminathan and A. Abdala, “Recent advances in graphene based gas sensors,” *Sensors and Actuators B: Chemical,* vol. 218, pp. 160 - 183, 2015.

[204] G. Lu, L. E. Ocola and J. Chen, “Reduced graphene oxide for room-temperature gas sensors,” *Nanotechnology,* vol. 20, no. 44, p. 445502, 2009.

[205] S. Adam, E. H. Hwang, E. Rossi and S. Das Sarma, “Theory of charged impurity scattering in two-dimensional graphene,” *Solid State Communications,* vol. 149, no. 27 - 28, pp. 1072 - 1079, 2009.

[206] M. J. Lee, J. S. Choi, J.-S. Kim, I.-S. Byun, D. H. Lee, S. Ryu, C. Lee and B. H. Park, “Characteristics and effects of diffused water betwen graphene and a SiO2 substrate,” *Nano Research,* vol. 5, no. 2, pp. 710 - 717, 2012.

[207] W. Kim, A. Javey, O. Vermesh, Q. Wang, Y. Li and H. Dai, “Hysteresis caused by water molecules in carbon nanotube field-effect transistors,” *Nano Letters,* vol. 3, no. 2, pp. 193 - 198, 2003.

[208] T. Lohmann, K. v. Klitzing and J. H. Smet, “Four-terminal magneto-transport in graphene p-n junctions created by spatially selective doping,” *Nano Letters,* vol. 9, no. 5, pp. 1973 - 1979, 2009.

[209] J. Moser, A. Verdaguer, D. Jimenez, A. Barreiro and A. Bachtold, “The environment of graphene probed by electrostatic force microscopy,” *Applied Physics Letters,* vol. 92, no. 12, p. 123507, 2008.

[210] J. Moser, A. Barreiro and A. Bachtold, “Current-induced cleaning of graphene,” *Applied Physics Letters,* vol. 91, no. 16, p. 163513, 2007.

[211] S. Kim, P. Zhao, S. Aikawa, E. Einarsson, S. Chiashi and S. Maruyama, “Highly stable and tunable n-type graphene field effect transistors with poly(vinyl alcohol) films,” *ACS Applied Materials & Interfaces,* vol. 7, no. 18, pp. 9702 - 9708, 2015.

[212] B. H. Kim, S. J. Hong, S. J. Baek, H. Y. Jeong, N. Park, M. Lee, S. W. Lee, M. Park, S. W. Chu, H. S. Shin, J. Lim, J. C. Lee, Y. Jun and Y. W. Park,

"N-type graphene induced by dissociative H2 adsorption at room temperature," *Scientific Reports,* vol. 2, no. 690, pp. 1 - 6, 2012.

[213] S. Some, J. Kim, K. Lee, A. Kulkarni, Y. Yoon, S. Lee, T. Kim and H. Lee, "Highly air-stable phosphorus-doped n-type graphene field-effect-transistors," *Advanced Materials,* vol. 24, no. 40, pp. 5481 - 5486, 2012.

[214] X. Wang, X. Li, L. Zhang, Y. Yoon, P. K. Weber, H. Wang, J. Guo and H. Dai, "N-doping of graphene through electrothermal reactions with ammonia," *Science,* vol. 324, no. 5928, pp. 768 - 771, 2009.

[215] C. Baeumer, D. Saldana-Greco, J. M. P. Martirez, A. M. Rappe, M. Shim and L. W. Martin, "Ferroelectrically driven spatial carrier density modulation in graphene," *Nature Communications,* vol. 6, no. 6136, pp. 1 - 8, 2015.

[216] J. H. Davies, The Physics of Low Dimensional Semiconductors, Cambridge, UK: Cambridge University Press, 1998.

[217] Z. Li, Y. Wang, A. Kozbial, G. Shenoy, F. Zhou, R. McGinley, P. Ireland, B. Morganstein, A. Kunkel, S. P. Surwade, L. Li and H. Liu, "Effect of airborne contaminants on the wettability of supported graphene and graphite," *Nature Materials,* vol. 12, pp. 925 - 931, 2013.

[218] D. H. Tian, J.-Y. Park, K. B. Kim, N. Lee and Y. Seo, "Characterization of graphene-based FET fabricated using a shadow mask," *Scientific Reports,* vol. 6, p. 25050, 2016.

[219] A. Fasolino, J. H. Los and M. I. Katsnelson, "Intrinsic ripples in graphene," *Nature Materials,* vol. 6, pp. 858 - 861, 2007.

[220] J. C. W. Song, K. J. Tielrooij, F. H. L. Koppens and L. S. Levitov, "Photoexcited carrier dynamics and impact-excitation cascade in graphene," *Physical Review B,* vol. 87, no. 15, p. 155429, 2013.

[221] J. H. Strait, H. Wang, S. Shivaraman, V. Shields, M. Spencer and F. Rana, "Very slow cooling dynamics of photoexcited carriers in graphene observed by optical-pump terahertz-probe spectroscopy," *Nano Letters,* vol. 11, no. 11, pp. 4902 - 4906, 2011.

[222] B. Y. Sun, Y. Zhou and M. W. Wu, "Dynamics of photoexcited carriers in graphene," *Physical Review B,* vol. 85, no. 12, p. 125413, 2012.

[223] H. Ramamoorthy, R. Somphonsane, J. Radice, G. He, J. Nathawat, C.-P. Kwan, M. Zhao and J. P. Bird, "Probing charge trapping and joule heating

in graphene field-effect transistors by transient pulsing," *Semiconducting Science and Technology,* vol. 32, p. 084005, 2017.

[224] Y. Zhou and K. P. Loh, "Making patterns on graphene," *Advanced Materials,* vol. 22, no. 32, pp. 3615 - 3620, 2010.

[225] T. Okada, S.-. Y. Su, C.-. S. Huang, K. Igarashi, A. Wada, L.-. J. Li, K.-. I. Ho, P.-. W. Li, I.-. H. Chen, C.-. S. Lai and S. Samukawa, "Ultra-low damage fabrication of graphene nanoribbons by neutral beam etching," in *Extended Abstracts of the 2013 International Conference on Solid State Devices and Materials*, Fukuoka, 2013.

[226] P. Simonet, D. Bischoff, A. Moser, T. Ihn and K. Ensslin, "Graphene nanoribbons: relevance of etching process," *Applied Physics Letters,* vol. 117, no. 18, p. 184303, 2015.

[227] T. Poole and G. R. Nash, "Acoustoelectric current in graphene nanoribbons," *Scientific Reports,* vol. 7, no. 1, p. 1767, 2017.

[228] H. Wang, Y. Wu, C. Cong, J. Shang and T. Yu, "Hysteresis of Electronic Transport in Graphene Transistors," *ACS Nano,* vol. 4, no. 12, pp. 7221 - 7228, 2010.

[229] M. Levy, J. Schmidt, A. Schenstrom, M. Revzen, A. Ron, B. Shapiro and C. G. Kuper, "Ultrasonic attenuation and the resistive transition in a superconducting granular lead film," *Physical Review B,* vol. 34, no. 3, pp. 1508 - 1513, 1986.

[230] A. S. Mayarov, N. Hunter, W. Muchenje, C. D. Wood, M. Rosamond, E. H. Linfield, A. G. Davies and J. E. Cunningham, "Surface acoustic wave generation and detection using graphene interdigitated transducers on lithium niobate," *Applied Physics Letters,* vol. 104, no. 8, p. 083509, 2014.

[231] Y. G. Lee, S. K. Lim, C. G. Kang, Y. J. Kim, D. H. Choi, H.-J. Chung, R. Choi and B. H. Lee, "Origin of the channel width dependent field effect mobility of graphene field effect transistors," *Microelectronic Engineering,* vol. 163, pp. 55 - 59, 2016.

[232] B. Chitara, L. S. Panchakarla, S. B. Krupanidhi and C. N. R. Rao, "Infrared photoredetectors based on reduced graphene oxide and graphene nanoribbons," *Advanced Materials,* vol. 23, pp. 5419 - 5424, 2011.

[233] X. Yu, Z. Dong, Y. Liu, T. Liu, J. Tao, Y. Zeng, J. K. W. Wang and Q. J. Wang, “A high performance, visible to mid-infrared photodetector base on graphene nanoribbons passivated with HfO2,” *Nanoscale,* vol. 8, no. 1, pp. 327 - 332, 2015.

[234] J. Schiefele, J. Pedrós, F. Sols, F. Calle and F. Guinea, “Coupling light into graphene plasmons through surface acoustic waves,” *Physical Review Letters,* vol. 111, no. 23, p. 237405, 2013.

[235] M. Farmat, S. Guenneau and H. Bağcı, “Exciting graphene surface plasmon polaritons through light and sounds interplay,” *Physical Review Letters,* vol. 111, no. 23, p. 237404, 2013.